Experimental and Theoretical Studies of Binary Nucleation and Condensation

Thesis by
Sonia Maria Kreidenweis-Dandy

in Partial Fulfillment of the Requirements
for the Degree of
Doctor of Philosophy

California Institute of Technology
Pasadena, California
1989
(Submitted June 28, 1988)

To my husband, David Dandy

Acknowledgments

I wish to thank my research advisor, Professor John Seinfeld, for his support, advice and encouragement during my stay at Caltech. His confidence in my abilities has kept me going through the difficult times. Professor Richard Flagan has been an invaluable source of ideas and advice in the laboratory, and a sympathetic ear when things went wrong with the experiment. Very special thanks to Professor Kikuo Okuyama, who was instrumental in getting me started in lab; I greatly appreciate the attention and concern he has always accorded my work, and especially his continued friendship.

Much of the work reported here has been supported by NSF grant ATM-8503103; I am grateful for this aid.

Thank you, Ken Reardon and Roya Maboudian, for being two very special friends. You have made such a difference in my life. Carol Jones Adkins not only helped me greatly with technical problems, but was a good friend as well. There have been many other people at Caltech whose friendship and help I've appreciated. I'd especially like to acknowledge Hung Nguyen and Ranajit Sahu, who cheerfully answered my many questions in lab. Brian Wong was always willing to answer my questions, listen to my complaints, or just talk; his patience and determination have made a strong impression on me, one I hope I will always remember in my future endeavors.

I would also like to express my gratitude for the loving support of my parents. They have always encouraged me in whatever paths I have chosen, and given me the pep talks I needed. On this Coast, Tom and Shirley Dandy have been wonderful "parents". Thanks to Tommy, who has earned an honest living for a long time before his big sister ever got a real job, but who never rubs it in (unlike Georgie). My college roommates and friends back in Ridgewood have never forgotten me; their friendship — especially Heidi and Donna — has meant so much.

Most of all, love and thanks to my husband Dave. I couldn't have done this without him.

Abstract

Many gas-to-particle conversion processes occurring in the atmosphere (and in technological applications) involve more than one gaseous species. An understanding of how gas-to-particle conversion occurs in multicomponent systems is necessary to predict the evolution of atmospheric aerosols. Of particular interest is the validity of binary nucleation theory in describing particle formation from two interacting vapors.

Chapter II presents a modeling study of heat and mass transfer to aqueous droplets dried under various conditions, and discusses the applicability of common assumptions in describing such processes. A method for the separation, into droplets containing different solutes, of an aerosol composed of two types of aqueous droplets is proposed.

Next, in Chapter III, an experimental study of binary nucleation theory using two similar organics (dibutylphthalate and dioctylphthalate) is presented, and compared with the predictions of an integral model that describes particle formation using binary nucleation theory. It was found that the number concentrations of particles formed in the presence of both vapors was higher than could be attributed to single-component nucleation of either organic, suggesting that binary nucleation was the mechanism for particle formation. Model predictions using the theoretical binary nucleation rates, modified by suitable (species-dependent) enhancement factors, were able to represent the data well.

Attention was next focused on an environmentally-important organosulfur compound, dimethylsulfide, and its oxidation under atmospheric-type conditions. In particular, the aerosol-forming ability of the two major sulfur-containing products, methanesulfonic acid and sulfuric acid, was investigated theoretically. Binary nucleation and multicomponent condensation theories were used to predict particle formation and growth in the chemically reacting system at 36% relative humidity, and model predictions were compared with published experimental smog chamber measurements of dimethylsulfide photooxidation.

It was found that the experimental results could be well represented by a model that allowed for binary nucleation of aqueous sulfuric acid droplets, and ternary growth of these droplets by condensation of water, methanesulfonic acid, and sulfuric acid vapors. This investigation is presented in Chapter IV.

The calculations presented in Chapter IV are some of the first estimates of particle formation in the methanesulfonic acid/water binary vapor system. In order to assess the validity of binary nucleation theory in describing this particle formation, an experimental program was initiated for the investigation of binary nucleation phenomena in this system. A continuous-flow, mixing-type device was proposed that would yield information not only on the critical saturation ratios required for observable particle formation, but the actual variation of nucleation rate with the gas-phase concentration of each species. The experimental apparatus that was constructed and used for this purpose and a summary and analysis of the experimental results are found in Chapter V. Particle formation was observed at moderate relative humidities and undersaturated acid vapor concentrations, demonstrating that methanesulfonic acid is able to undergo binary nucleation with water vapor. The adequacy of classical binary nucleation theory in predicting the nucleation rates is discussed in detail. The second major goal of the experimental program that was realized was the demonstration of the usefulness of this device in the investigation of binary nucleation phenomena, particularly for corrosive materials, which are difficult to work with in conventional systems.

Because of its successful application to the methanesulfonic acid/water vapor system, this device shows great promise for future applications in the study of binary nucleation phenomena. Suggestions for the modification and improvement of the apparatus that emerged from laboratory experience and from the data analysis are presented in Chapter VI.

Table of Contents

Chapter I

Introduction

I. Problem statement

In a number of areas of current scientific interest, both theoretical and applied, gas-to-particle conversion processes are an important aspect of the underlying physics. Such areas include environmental science and pollution control, production of ultrafine ceramic powders, and contamination control in clean rooms. For example, an understanding of how gas-phase pollutants react in the atmosphere to form condensable species, and how these species generate new aerosol particles or condense upon preexisting nuclei in the atmosphere, can lead to an understanding of the formation of photochemical smog and can suggest methods for its abatement. Very high purity gases can be used as a starting material for the production of high quality ceramic powders. In order to control the particle sizes (uniform, spherical particles are the most desirable for processing), the mechanism and kinetics of the particle formation and growth must be understood. As a last example, current state-of-the-art technology in clean rooms has focused on achieving a very high degree of efficiency in filtering out airborne dust particles and particles emitted by workers and equipment. However, it is possible that contaminants, in the form of submicron particles, are actually produced during the semiconductor processing steps by gas-to-particle conversion. As the size scale of features on integrated chips becomes smaller, such contamination represents a significant stumbling block to cost-effective production, and the particle formation processes must be understood to formulate a solution to the problem.

Another feature that the above-mentioned applications have in common is that the gas-to-particle conversion generally involves not one, but a number of species. One has merely to consider the spectrum of pollutants released into the atmosphere—organic and inorganic, gaseous and particulate—to appreciate the necessity for considering the possibility of interaction between species as photochemical smog is produced. In technological applications as well it is rare that a single species alone is of interest. Certainly the ability to describe what

happens when different precursors are combined greatly expands the number of possibly useful applications of a technology.

The motivation for the investigation of multicomponent nucleation and growth undertaken in this thesis is to add to the understanding of gas-to-particle conversion processes in the presence of more than one condensable species, from both fundamental and applied points of view. The salient features of multicomponent condensation and of binary nucleation theories are presented first. Next, previous experimental attempts at verifying the predictions of binary nucleation theory are briefly discussed. These are followed by a description of the theoretical and experimental efforts undertaken in this thesis work. Since the focus of this work has been applications in atmospheric sciences, the examples that are discussed will be taken from this field.

II. Multicomponent condensation and binary nucleation theories

The sizes of particles in an aerosol distribution can be changed by the processes of coagulation (the combining of smaller particles to create a single larger particle) and of condensational growth (the incorporation of gaseous molecules). As an example of the latter process, a particle in the atmosphere consisting of a salt crystal, when transferred from a dry environment into a humid one, may absorb water vapor to form an aqeuous solution and thereby greatly increase its size. Also, in the form of an aqueous droplet, the particle can now act as a site for chemical reactions occurring in aqeuous solution by absorbing other gaseous species, increasing the gas-to-particle conversion in the atmosphere.

In the atmosphere, pollutant species are generally present in concentrations that represent very small mole fractions of the carrier gas (the ambient air). As a consequence, the molar fluxes of such species can be decoupled, and an effective binary diffusion coefficient used to calculate the flux to a surface. Another common assumption in atmospheric modeling is to represent particles as spheres and calculate fluxes in this coordinate system. In the usual case, the change in particle radius is much slower than the flux of gaseous species to the surface, so that the fact that this surface is in motion can be ignored (the "steady-state" assumption) and the fluxes to a stationary interface calculated. The motion of the surface is later re-introduced by considering the change in mass of the particle due to condensation of all the species and computing the corresponding increase in size. The appropriate equations for condensational growth, and a discussion of the justifications for the assumptions made, may be found in Seinfeld (1987).

In certain cases of atmospheric interest, one of the condensing species is present in a much higher concentration than the others. Examples that are considered in this thesis are the sulfuric acid–water or methanesulfonic acid–water systems, in which the partial pressures of the acids are many orders of magnitude smaller than that of the water vapor, even at low relative humidity. For such cases, it is sufficient to calculate only the flux of the acid species to the

droplet, and assume equilibration with water vapor at all times. This assumption is discussed in more detail in the chapters concerning these systems.

As mentioned in the problem statement, in the formation of new particles from a gas phase, the possibility that gaseous species can interact must be considered in order to accurately model the physics. Of particular interest to atmospheric scientists is the idea that two species that can form highly nonideal solutions can interact in the gas phase to create large number concentrations of submicron solution particles. These particles would act as a significant input to the small-diameter end of the atmospheric aerosol size spectrum, thus replenishing the number concentration of the ambient aerosol, which would otherwise decrease with time as the aerosol "ages"—that is, as coagulation combines particles to decrease the concentration, as larger particles are lost to scavenging by rain or to deposition on the ground, and as transport and diffusion disperse the aerosol.

The reason that so-called binary nucleation is of particular interest is that existing theories predict that this particle formation can occur under conditions such that either species is highly undersaturated with respect to single-component nucleation of that species. To understand what this means, one may first consider the metastable equilibrium that exists when a gas-phase species (such as water vapor in the atmosphere) attains a partial pressure that is larger than its saturation vapor pressure under the prevailing conditions. For example, for water vapor, the atmospheric concentration is usually expressed as the relative humidity (RH), which is the ratio of the ambient partial pressure of water vapor to the equilibrium vapor pressure of water over a flat surface (at the ambient temperature). As the atmosphere cools, this equilibrium vapor pressure decreases, until eventually a relative humidity of over 100% is achieved. From equilibrium considerations alone, this should result in a phase change (producing clouds or ultimately rain), but due to kinetic considerations the RH can be increased to over 300% before this phase change occurs.

Single component nucleation theory describes the kinetics of such a phase change from the metastable state (as the number of water droplets produced per cubic centimeter per second). In the general case, the ratio described by RH for water vapor is termed the saturation ratio S; from the discussion above, it is clear that the phase change cannot occur unless $S > 1$.

If this nucleation theory is extended to a binary vapor system, the criterion for supersaturation (the metastable state) is changed. Now, the gas-phase concentrations must be greater than the partial pressures of the two species over their *solution*. The equilibrium solution partial pressure of each species is described thermodynamically as the product of its pure-component vapor pressure over a flat surface and its activity in that solution. If the solution were ideal, for example, Raoult's Law would apply, and the activity would equal the mole fraction. Therefore, for metastable equilibrium of a binary gas phase with a binary solution consisting of equal mole fractions of each species, the partial pressure of each species in the gas phase would need to be only slightly more than half its equilibrium vapor pressure.

Two important implications of this theory for atmospheric systems can be stated immediately. First, emitted pollutants may be condensable species, or may react to form condensable species. Either way, the concentration of the condensables will most likely be small, due to the effects of dilution in the atmosphere, and it is likely that single-component nucleation of these species will not occur. Similarly, relative humidities are usually well below 100%, particularly during sunny days when photochemical reactivity is high. However, it is well known that large numbers of particles (frequently incorporating water vapor as well) are formed as byproducts of these reactions, contributing in a large measure to visibility degradation. Binary nucleation theory can be used to hypothesize how these submicron aerosols are formed, identifying the precursors that contribute most heavily to such visibility degradation.

The second important implication is to the rate at which new particles are

formed. If the binary solution is highly nonideal thermodynamically, it is possible that the solution activities are much smaller than would be predicted by Raoult's Law. In the case, even very small gas-phase concentrations of condensables (orders of magnitude less than the equilibrium vapor pressures) can result in high nucleation rates. The reason that this impacts atmospheric work in particular is that two species that are found universally in polluted air—water vapor and sulfuric acid, a product of SO_2 oxidation—form such a highly nonideal solution. Calculations have shown that ppm levels of sulfuric acid in the presence of moderate RH can produce very high number concentrations of submicron aerosol, and it is possible that other pollutant (or natural) species can show similar behavior.

The first formulation of binary nucleation theory was presented by Reiss (1950) as an extension of classical single-component nucleation theory. The free energy of formation of a cluster containing i molecules of species A and j molecules of species B is given by the change in the chemical potential of each species from the gas phase to the solution plus the energy of the formation of the interface. Reiss showed that a saddle point exists in the free energy surface (expressed as a function of i and j) that represents the energetic barrier to the phase change. Clusters with sizes smaller than the critical size, which is located at the saddle, are unstable, whereas those clusters that pass over the barrier by addition of molecules of either or both species form stable droplets.

The kinetics of the passage through the saddle were first accurately described by Stauffer (1976), who demonstrated that previous approaches—which assumed that growth occurred along the path of steepest descent—were incorrect because they assumed that the free energy surface alone determined the direction of growth. This is not true because there is a contribution due to the bombardment rate of either species onto the cluster, so that if one species is present in a higher concentration than the other, addition of that species is more likely, whether or not it is along the path of lowest energy.

One problem with this "classical" formulation of the binary nucleation rate theory is that, as the concentration of one species becomes large, one would expect that the nucleation rate approach the single-component nucleation rate of that species. Unfortunately, this is not the case. The energy term in the binary theory, as well as the kinetic term, do approach the correct limits. However, the so-called Zeldovich term—which accounts for the departure from equilibrium of the cluster distribution and is based upon the second derivative of the formation free energy—diverges in this limit. As a physical description one may imagine that, as the concentration of one species becomes very small, the free energy surface changes shape, so that the "walls" of the saddle become ever steeper. In the single component case, the surface collapses to a two-dimensional line, so that the curvature in the third dimension is infinite.

This behavior was first observed by Wilemski (1975), who proposed what is essentially an extrapolation formula to avoid the divergent regions. Subsequently Mirabel and Clavelin (1978a) demonstrated that the divergence becomes important only in cases for which the theory, using continuous variables (rather than the integers i and j) to describe nucleation in a more convenient mathematical form, predicted less than one molecule of a species in the critical cluster. By using only integer values of i and j, the binary rate can be made to approach the correct limiting forms. These authors also modified somewhat the limiting form of the direction over the saddle (expressed as the angle ϕ with respect to the axes) that was obtained by Stauffer. The equations given by Mirabel and Clavelin continue to be quoted as the definitive expressions for calculating the rate of binary nucleation. However, the expression they present for the Zeldovich term is actually the limiting form for the case of steepest descent on the free energy surface, and is inconsistent with the definition of ϕ used in the rest of their calculations. (This inconsistency is demonstrated in the Appendix.) Therefore, in this work the equations of Stauffer were used, with the modification that the single-component nucleation rate was used if the critical cluster contained less

than one molecule of a species.

A number of modifications to the theory, in particular to the calculation of the cluster free energy, have been proposed. One of the arguments has concerned the calculation of the size and composition of the critical cluster, which locates the free energy saddle by setting the first derivatives of the free energy with respect to i and j equal to zero. In taking the derivatives, the change in the surface tension with composition has traditionally been included. Recently, the thermodynamic consistency of the resulting equations has been called into question, and arguments advanced that the surface tension derivative term should not be included (Renninger *et al.*, 1981; Wilemski, 1984). It appears that the current consensus is that this term should be omitted from the calculation.

Other modifications have dealt with the specification of the surface tension of a binary cluster that may contain only a few molecules of each species, in particular the validity of using the bulk surface tension of an equilibrium solution (of a flat surface) as the input parameter. The distinction between the surface composition and the composition of the droplet interior is made to determine the correct surface tension. Flageollet-Daniel *et al.* (1983) developed a method to calculate the corrected surface tension of binary droplets and found improved agreement with experimental results than was obtained using the bulk surface tension. Wilemski (1987) employed the Gibbs adsorption isotherm to implicitly account for surface enrichment, and also found better agreement with some experimental data. Other approaches have used a dynamic or size dependent surface tension to improve agreement between theory and experiments (Rasmussen, 1982; Rasmussen, 1986; Spiegel *et al.*, 1986).

In some gas-phase systems, the assumptions made in the classical theory—that the monomer concentration is much larger than the total cluster concentration, for example—are not accurate. This is true in the case of a vapor that is associated to a large extent, so that cluster-cluster interactions must be considered. A theory to account for nucleation in associated vapors has been published

by Studzinski *et al.* (1986). A similar situation is found in the sulfuric acid–water vapor system, where a large number of the acid molecules exist as hydrates rather than free acid. Heist and Reiss (1974) and Shugard *et al.* (1974) have described hydrate formation and nucleation in such a system. The same problem was considered by Suzuki and Mohnen (1981) who used a cluster-cluster interaction model to determine the nucleation rate, with essentially the same results for sulfuric acid and water that were obtained by Reiss and coworkers. Among the other interesting variations to the classical binary nucleation theory is the work of Ray *et al.* (1986) demonstrating that nuclei of two different compositions may be produced under certain conditions if the two species are only partially miscible in the liquid phase.

III. Experimental verification of binary nucleation theory

The efforts focused on the proper formulation of binary nucleation theory, and in particular the prediction of the rate of nucleation of sulfuric acid-water droplets, are evidence of the importance attached to an understanding of these phenomena and their application to atmospheric processes. Further evidence is the number of experimental efforts that have focused on verifying the theoretical predictions, and perhaps distinguishing between different formulations of the cluster free energy. In general, investigations of nucleation phenomena can be categorized into two types of experiment: those that generate condensable species via gas-phase reactions and those that begin with the condensable species directly and supersaturate the gas phase by mechanical means (such as cooling or expansion).

Examples of experiments that use gas-phase chemistry to generate the aerosol precursor are smog chamber investigations (Teflon bags used in photochemical reaction experiments, for example). These initiate photochemical reactions using sunlight or artificial sources of uv radiation. Aerosol formation has been observed in many atmospheric-type systems (NO_H and organics, for example) studied in this manner. If the source rates of the condensable vapors are known, and the number concentration of aerosol measured as a function of irradiation time, the theoretical and experimental rates of conversion of gaseous species to the particulate phase can be compared. Unfortunately, not only are the source rates rarely known to a high degree of accuracy, but the identity of the condensing species are also usually not known.

Devices used in the second type of experiment include the diffusion cloud chamber (Mirabel and Clavelin, 1978b), the expansion cloud chamber (Schelling *et al.*, 1981), and the shock tube (Zahoransky and Peter, 1985). Each of these has been used to measure binary nucleation rates (or, more usually, the critical saturation ratios for which the nucleation rate is first large enough to generate

measurable number concentrations) for sulfuric acid and water or some other aqueous system, and a few have been used for other binary systems. Agreement with theoretical predictions varies widely (particularly depending upon which variation of the surface tension is used), and each type of experiment has disadvantages (these will be discussed in Chapter IV). Nevertheless, the fact that subsaturated (in the single-component sense) vapors can interact in the gas phase to generate measurable particle concentrations has been demonstrated.

IV. Overview of thesis

This work seeks to make two contributions to the current understanding of binary nucleation and multicomponent condensation. The first of these is the development of models that describe these processes in chemically reacting or nonreacting systems to predict the number and size of new particles that are formed. The second is the development and application of a new type of experiment for studying binary nucleation phenomena, of the chemically nonreacting type. This new apparatus addresses some of the shortcomings of previous devices.

In Chapter II, a study is made of the equations for multicomponent condensation (or evaporation), specifically the assumption of isothermal droplet growth. The analysis is applied to salt solution droplets dried by different methods, and the applicability of the isothermal assumption is evaluated for the different conditions. A particular application that is considered is the drying of such particles in a so-called diffusion dryer, a laboratory device typically used to create solid particles from aqueous solutions. It is also shown that, when used in conjuction with two size-classifying instruments (diffusion mobility analyzers), the diffusion dryer can classify particles with respect to composition. Although this principle could not be used for the solutions considered in the experimental part of this thesis, the possibility for future applications exists.

The application of binary nucleation theory to an ideal binary system of two similar organics is discussed in Chapter III. An integral model is presented that uses the classical binary nucleation theory to compute the total number concentration with time. Competition between the nucleation and growth processes is allowed by computing the growth of nucleated particles and consequent depletion of the condensable vapors. This model is used to analyze the results of an experiment performed with a new type of apparatus, a continuous-flow device that rapidly mixes and cools saturated vapors to produce the metastable state; by changing the temperatures at which saturation of the carrier gases occurs and by

varying flow rates, a wide range of initial saturation ratios can be achieved. Furthermore, a direct comparison between single-component and binary nucleation phenomena is possible by repeating the conditions (flow rates and temperatures) of the binary experiments, but replacing one saturated stream with carrier gas only. It was found that the numbers of particles produced in the binary case could not be explained by single-component nucleation alone, verifying the underlying idea of gas-phase interaction between the two species that effectively enhances the ability of a vapor system to form particles. It was also found that the model could predict well the general trends observed for the variation of the number concentration N with saturation ratios, but not the actual magnitude of N. By multiplying the rate of nucleation by a suitable factor, agreement between theory and experiment was obtained. It is postulated that this multiplication factor represents a correction term to the calculation of the cluster energy.

Next, the application of the model and experimental technique to an environmentally important system, the organosulfur system, was undertaken. The atmospheric reactions of organosulfur species have recently been of increasing concern, as it has been postulated that such species make up a significant fraction of the atmospheric sulfur budget (Andreae and Raemdonck, 1983). These reactions are known to generate SO_2, which in turn generates sulfuric acid in the environment. In addition, one of the major sulfur-containing products of the reactions of dimethyl sulfoxide (the most abundant organosulfur species) is methanesulfonic acid, and it has been suggested that this acid may undergo binary nucleation with water vapor.

An experimental smog chamber investigation of dimethyl sulfoxide oxidation was carried out by Hatakeyama *et al.* (1985) in an attempt to elucidate some of the unknown reaction pathways. The production of aerosol during these runs was observed, and measurements were made of the total aerosol number concentrations and the mean sizes. For identical initial conditions of the gaseous precursors, it was observed that aerosol formation depended very strongly on

the relative humidity in the system, an observation consistent with binary nucleation theory for aqueous particles. Analysis of the aerosol identified sulfuric acid and methanesulfonic acid as the major constituents. This is an exciting observation, in light of the previously discussed problem of unidentified organic species comprising the aerosol in other smog-chamber studies. It offers some hope of realistically modeling the aerosol formation and judging the adequacy of classical theory in describing the nucleation and growth processes. Also, a companion effort was underway at Caltech to develop a chemical mechanism for DMS photooxidation (Yin *et al.*, 1986) which could be used to obtain production rates of the two acids, and consequently used in an aerosol model. The companion effort also included a series of experiments in which aerosol measurements were taken, to be compared with theoretical predictions.

Therefore, a model was developed to describe nucleation and growth of aqueous sulfuric acid-methanesulfonic acid-water particles, allowing for binary nucleation of either H_2SO_4 or MSA and ternary condensation. (This work represents one of the first published calculations of the binary nucleation rate for MSA and water; the other published calculations (Hoppel, 1987) appeared nearly simultaneously with ours.) Total aerosol number concentrations and mean particle sizes were predicted by using the production rates of vapors estimated from the work of Hatakeyama *et al.* and compared with their published data. From the comparisons it was postulated that, although MSA was the major S product species, formation of new particles was dominated by sulfuric acid and water nucleation, whereas growth was due largely to condensation of MSA. This work is described in Chapter IV.

The experimental contribution to the understanding of binary nucleation is discussed in Chapter V. The continuous-flow mixing-type device used to investigate the ideal binary organic system was modified for use with the MSA–water system. Modification involved several changes in the method of carrier gas saturation, temperature control, and materials of construction. It was demonstrated

that particles are produced at moderate relative humidities and for undersaturated acid vapor concentrations, thus verifying that binary nucleation does occur for these species, and the experimental results are compared with theoretical predictions. Another contribution that was realized is the demonstration of the usefulness of this type of device for the investigation of binary nucleation phenomena, especially for materials such as acids that are difficult to work with experimentally.

Because the experimental system used in this work was new and untested, suggestions for improvement in the design for future applications have emerged, both from laboratory experience and from the analysis of the data. These are discussed in Chapter VI.

Appendix: The Zeldovitch term

The Zeldovitch term as evaluated by Stauffer (1976) will be here compared with that obtained using the steepest-descent assumption. First, it is necessary to define the angle ϕ that the path of nucleation makes with the n_i, n_j axes. In the case of steepest descent, this angle is the orientation of the saddle in the free energy surface, and is given by

$$\cot 2\phi = (D_{11} - D_{22})/2D_{12}, \tag{1}$$

where the matrix D has been defined by $D_{ij} = \frac{1}{2}\partial^2 G/\partial n_i \partial n_j$. (Note that, at the saddle point, the eigenvectors of D must have opposite signs so that det $D < 0$ always.)

Stauffer showed that the correct definition for ϕ involves not only the curvature of the free energy surface, but the impingement probabilities of molecules onto the clusters, expressed as $R_{11} = a(i,j)\beta_1$, and similarly for R_{22}; here, $a(i,j)$ is the area of the critical cluster. With the shorthand

$$r = R_{22}/R_{11} \tag{2}$$

$$s = \frac{1}{2}\left(\frac{-D_{11}}{D_{12}} + \frac{R_{22}D_{22}}{R_{11}D_{12}}\right), \tag{3}$$

one obtains

$$\tan \phi = s + (s^2 + r)^{1/2}. \tag{4}$$

Now, from his development, Stauffer calculates

$$Z = -D^r_{xx}/(-\det D)^{1/2}, \tag{5}$$

where D^r_{xx} is a component of the matrix D rotated to (x,y) coordinates, using ϕ to determine the rotation matrix.

This definition of Z differs from the steepest-descent results. As written in Mirabel and Katz's (1974) paper, their Z (Z_{MK}) is

$$Z_{MK} = \left(\frac{-(D_{11}\cos^2\phi + 2D_{12}\cos\phi\sin\phi + D_{22}\sin^2\phi)}{D_{11}\sin^2\phi - 2D_{12}\cos\phi\sin\phi + D_{22}\cos^2\phi}\right)^{1/2} \tag{6}$$

$$Z_{MK} = \left(-D^r_{xx}/D^r_{yy}\right)^{1/2}. \tag{7}$$

This result assumes the matrix D^r to be diagonal, which is the case only if the steepest descent theory is used. This is shown by an examination of the off-diagonal components of D^r:

$$D^r_{xy} = D^r_{yx} = -D_{11}\sin\phi\cos\phi + D_{12}\cos^2\phi - D_{12}\sin^2\phi + D_{22}\sin\phi\cos\phi, \tag{8}$$

$$D^r_{xy}/(\sin 2\phi) = \frac{1}{2}\left(D_{22} - D_{11}\right) + D_{12}\cot 2\phi. \tag{9}$$

Substituting the steepest-descent angle [Eq. (1)], one obtains $D^r_{xy} = D^r_{yx} = 0$.

Interestingly, the Mirabel and Katz definition of Z continues to be quoted by many workers. This is due in part to a paper published by Mirabel and Clavelin (1978) in which they acknowledge Stauffer's revised definition of the angle ϕ, but correct his assertion that the quantities $d_A = -D_{11}/D_{12}$ and $d_B = -D_{22}/D_{12}$ are always positive, which alters somewhat the limiting values obtained for ϕ as the concentration of one component approaches zero. However, although employing Stauffer's definition of ϕ, these workers used the Mirabel and Katz definition of Z, which is inconsistent.

References

Andreae, M. O. and Raemdonck, H. (1983) *Science* **221**, 744.

Flageollet-Daniel, C., Garnier, J.P., and Mirabel, P. (1983) *J. Chem. Phys.* **78**(5), 2600.

Hatakeyama, S., Izumi, K., and Akimoto, H. (1985) *Atm. Env* **19**, 135.

Heist, R.H. and Reiss, H. (1974) *J. Chem. Phys.* **61**(2), 572.

Hoppel, W.A. (1987) *Atm. Env.* **21**, 2703.

Mirabel, P. and Clavelin, C. (1978a) *J. Aer. Sci.* **9**, 219.

Mirabel, P. and Clavelin, C. (1978b) *J. Chem. Phys.* **68**(11), 5020.

Mirabel, P. and Katz, J.L. (1974) *J. Chem. Phys.* **60**(3), 1138.

Rasmussen, D. (1982) *J. Crystal Growth* **56**, 45.

Rasmussen, D. (1986) *J. Chem. Phys.* **85(4)**, 2272.

Ray, A.K., Chalam, M., and Peters, L.K. (1986) *J. Chem. Phys.* **85**(4), 2161.

Reiss, H. (1950) *J. Chem. Phys.* **18**, 840.

Renninger, R.G., Hiller, F.C., and Bone, R.C. (1981) *J. Chem. Phys.* **75**(3), 1584.

Schelling, F.J. and Reiss, H. (1981) *J. Coll. Int. Sci.* **83**(1), 246.

Seinfeld, J.H. (1987) *Atmospheric Chemistry and Physics of Air Pollution*, Wiley and Sons, New York.

Shugard, W.J., Heist, R.H., and Reiss, H. (1974) *J. Chem. Phys.* **61**(12), 5298.

Spiegel, G.H., Zahoransky, R.A., and Wittig, S.L.K. (1986) *Shock waves and shock tubes*, D. Bershader and R. Hanson. eds., Stanford University Press.

Stauffer, D. (1976) *J. Aer. Sci.* **7**, 319.

Studzinski, W., Spiegel, G.H., and Zahoransky, R.A. (1986) *J. CHem. Phys.* **84**(7), 4008.

Suzuki, K. and Mohnen, V.A. (1981) *J. Aer. Sci* **12**, 61.

Wilemski, G. (1975) *J. Chem. Phys* **62**(9), 3763.

Wilemski, G. (1984) *J. Chem. Phys* **80**(3), 1370.

Wilemski, G. (1987) *J. Chem. Phys* **91**(10), 2492.

Yin, F., Grosjean, D., and Seinfeld, J.H. (1986) *J. Geophys. Res.* **91**(D13), 14417.

Zahoransky, R.A. and Peter, F. (1985) *J. Chem. Phys.* **83**(12), 6425.

Chapter II

Evaporation and Growth of Multicomponent Aerosols: Laboratory Applications

The text of Chapter II consists of an article which appears in *Aerosol Science and Technology* **6** (1987).

Evaporation and Growth of Multicomponent Aerosols: Laboratory Applications

Sonya M. Kreidenweis, Richard C. Flagan,* and John H. Seinfeld

Department of Chemical Engineering
California Institute of Technology
Pasadena, CA 91125

* Environmental Engineering Science.

Abstract

Design equations for two types of devices used in aerosol growth and evaporation studies, the well-mixed vessel and the diffusion dryer, are developed and their use demonstrated for aqueous salt solution particles. The results of several common simplifying approximations are evaluated. An approximate method for determining residence times required for drying particles that exhibit a hysteresis effect, accurate to within several percent for the cases considered, is suggested.

I. Introduction

There exist several devices in which aerosol properties are measured based on either evaporating or growing particles. Ogren et al. (1985) have reported the design of a cloud sampling probe in which cloud droplets are inertially separated, impacted into a flow of warm air, and evaporated so that the resulting aerosol represents the content of the activated cloud condensation nuclei. The probe consists essentially of a tube through which the evaporating droplets flow. Proper design of the droplet to aerosol converter requires that one be able to predict the residence time necessary to evaporate fully the feed droplets. The aerosol mobility chromatograph, as developed by Liu et al. (1978), is a flow device in which hygroscopic aerosol particles of different compositions are humidified. The resulting preferential growth of different particles can then serve as a means for their separation.

Another application of this general technique related to the cloud sampling probe of Ogren et al. is the so-called diffusion dryer, in which aqueous aerosols equilibrated at ambient conditions are passed in laminar flow through a circular tube with absorbing walls. As the water vapor is depleted from the carrier gas by absorption at the tube wall, a driving force is created for evaporation of water from the particles flowing through the tube. This configuration is commonly used in the laboratory to dry aerosols. The design of such a dryer is based on determining the residence time in, and hence the length required for, the tube in order to ensure a completely dry aerosol at the outlet.

In each of the above-described devices, the central feature of the operation is the controlled evaporation or growth of particles in a flowing system. The object of this work is to develop general design equations for systems in which multicomponent aerosols are to be evaporated or grown and to illustrate the solution of the equations for several representative situations. Although the development is general, aqueous salt aerosols will be focused on because of their

importance in atmospheric studies.

The description of the growth and evaporation of aerosol particles is a key element in aerosol behavior, and as such, has been examined by numerous investigators. Theory and experiments related to single aerosol particle transport processes have been reviewed by Wagner (1982) and Davis (1983). These surveys are of interest in examining the approximations that have been made to the full, coupled equations of heat and mass transfer from a droplet; several of these are discussed below.

The common approach to predicting particle growth or evaporation is to invoke the steady-state assumption for the gas-phase mass and energy conservation equations to determine the fluxes from the droplet. Time dependency is then introduced by equating the instantaneous energy and mass fluxes to the energy and mass changes of the droplet. Twomey (1977) and Pesthy et al. (1981) have given conditions for the applicability of quasi-steady state flux expressions based on continuum equations. Their analysis concludes that the assumption is valid as long as the vapor density is much smaller than the liquid density. Brock (1967) studied the noncontinuum regime and also concluded that, in general, the assumption is a valid one. Wagner (1982) observed that the quasistationary theory appears to be a good approximation, but its applicability can be verified only by comparison with experimental data. Davis (1983) pointed out that "when heat and mass transfer processes are coupled, the criterion for quasi-steady state requires full solution of the problem discussed, but most investigators have assumed quasi-steady state".

Chang and Davis (1974) determined the temperature field in a droplet and the temperature and concentration fields in the continuum surrounding a droplet using the unsteady state equations and compared the results with the quasistationary assumption. Their analysis of water/air and dibutyl phthalate (DBP)/helium systems led to several conclusions. First, conduction within the drop was very rapid and the temperature inside could be reasonably well approximated as uni-

form. Second, it was found that for low vapor pressure species such as DBP and for species with a low heat of vaporization the transient period is short and the wet-bulb temperature is rapidly attained. However, for higher vapor pressure species (such as water) the transient period was much longer, and the applicability of the steady-state assumption was questioned. The unsteady state analysis presented by Nix and Fukuta (1973) allows for mass and heat source functions as exponential functions of time. They obtained closed-form solutions for the concentration and temperature fields around the droplet, and compared the steady-state approximation with their transient droplet growth equations. The error was found to be proportional to the droplet radius and to decrease with increasing time constant for the source functions.

Studies using as their basis the steady state assumption have modified the equations to account for noncontinuum effects, changing ambient conditions, and solution effects. One of the simplest approaches is that of El Golli et al. (1972), which, to find the radius as a function of time, determines the wet-bulb temperature of a pure water droplet evaporating into a turbulent air stream at constant ambient relative humidity and assumes the drop is isothermal at this temperature. A similar approach was used by El Golli et al. (1974) to study the evaporation of saline droplets at various constant ambient relative humidities. Activity and density were allowed to vary, but the drop was assumed to be isothermal and the Kelvin effect was neglected. The continuum analysis presented by Wagner and Pohl (1975) allowed for dependence of the mean ambient temperature and vapor pressure on the drop radius and drop concentration of the growing aerosol by means of a mass balance. Fukuta and Walter (1970) modified the quasi-steady state equation to account for noncontinuum effects and presented growth equations for pure water and solution droplets. However, as discussed by Davis (1983), their treatment requires introduction of numerous correction factors that must be obtained from experimental data. In addition to pure-component and solution droplets, some studies of multicomponent droplet

evaporation have appeared. Ravindran *et al.* (1979) presented theoretical and experimental results for isothermal binary solution droplet evaporation under the assumptions of ideal liquid solution behavior, ideal mixing inside the drop, and dilute vapor-gas behavior outside of the drop. Similar assumptions regarding mixing and solution behavior were employed by Newbold and Amundson (1973), but their analysis allowed for variations in droplet temperature during evaporation and for the effect of Stefan flow. A further extension of this approach was presented by Smolik and Vitovec (1984), who analyzed the case of evaporation of a droplet into a multicomponent gaseous mixture, also employing numerical solution of the generalized Stefan-Maxwell equations, with condensation of a higher-molecular- weight component from the gas and simultaneous absorption of the gaseous component in the droplet. Wagner (1982) pointed out that for the conditions usually encountered in the atmosphere, Stefan flow can be neglected. However, this is not the case for high-temperature conditions such as those in combustion processes, or if the vapor concentration is not small compared with the gas concentration. Also, for atmospheric conditions radiation can be neglected, particularly for small droplets; under high-temperature conditions, however, this assumption may not be a good one.

The objective of the present analysis is the theoretical description of flow devices used in the study of aerosols. Results obtained with various modifications to the steady state equations are compared for two cases of droplet evaporation. The first is the case of a pure or multicomponent mixture droplet evaporating into an ambient environment at fixed, known relative humidity. This type of environment is encountered in a well-mixed vessel, such as a flask containing wet air used to humidify dry aerosols. The second case considers an aerosol particle, equilibrated with a known relative humidity of its carrier gas, introduced into a tube with perfectly absorbing walls. The particle's environment is thus depleted of one or more components also present in the droplet, and evaporation from the drop occurs. This second case may be used to model the operation of the

diffusion dryer. The direct effect of aerosol growth or evaporation processes on the ambient temperature and concentration fields is not taken into account; that is, it is assumed that the quantity of mass or energy transferred to or from the particles is small compared with that in the gas phase.

II. Equations for simultaneous mass and heat transfer to Aerosol particles

Beginning with the equations for gas-phase mass and energy conservation, applying the pseudo-steady state approximation, and equating the fluxes of heat and mass to the drop with the changes in drop temperature and number of moles, we arrive at the following equations for droplet composition and temperature as functions of time:

$$\frac{dn_i}{dt} = -4\pi r^2 J_i \tag{1}$$

and

$$\frac{dT}{dt} = \frac{-4\pi r^2}{\sum_i n_i c_{p,soln}} \left[\frac{a}{e^a - 1} \frac{k}{r} (T - t_\infty) \beta_T(Kn_g) + \sum_i J_i \left(h_{v,i} - \Delta \overline{H_i} \right) \right], \tag{2}$$

where

$$a = \frac{r}{k} \sum_i J_i c'_{p,i},$$

$$J_i = \frac{C_T D_{Im} \ln C}{p_T r} \left[\frac{a_i p_i^o \exp\left(\frac{2\sigma \overline{V_i}}{rRT}\right) C^{D_{Im}/D_{im}} - p_{i,\infty}}{C^{D_{Im}/D_{im}} - 1} \right] \beta_{M,i}(Kn_i),$$

$$C = \frac{p_T - \sum_i p_{i,\infty}}{p_T - \sum_i a_i p_i^o \exp\left(\frac{2\sigma \overline{V_i}}{rRT}\right)},$$

$$\beta_{M,i}(Kn_i) = \frac{1 + Kn_i}{1 + 1.71 Kn_i + 1.333 Kn_i^2},$$

$$Kn_i = \frac{\lambda_{v,i}}{r},$$

$$\beta_T(Kn_g) = \frac{1 + Kn_g}{1 + 1.71 Kn_g + 1.333 Kn_g^2},$$

$$Kn_g = \frac{\lambda_g}{r},$$

where the subscript i refers to the ith component in the droplet, the subscript I refers to the inert gas surrounding the droplet, n_i are moles of i, t is time,

T is drop temperature, T_∞ is ambient temperature, r is drop radius, k is the thermal conductivity of the gas, $h_{v,i}$ is the latent heat of i, $\Delta\overline{H_i}$ is the partial molar enthalpy of mixing, $c_{p,soln}$ is the solution heat capacity, $c'_{p,i}$ is the heat capacity of gaseous i, C_T is total gas concentration, p_T is total pressure, D_{Im} and D_{im} are the effective binary diffusivities of the inert and of i, respectively, in the mixture, p_i^o is the vapor pressure of pure i, $\overline{V_i}$ is the partial molar volume of i, R is the gas constant, λ_g and $\lambda_{v,i}$ are the mean free path of the (inert) gas molecules and of the vapor molecules of i, respectively, and $p_{i,\infty}$ is the partial pressure of i far from the drop.

The development of Eqs. (1) and (2) follows that of Newbold and Amundson (1973) and includes the following assumptions:

(1) The gas-liquid interface is at equilibrium. This assumption implies that the interfacial resistance is negligible compared with diffusive resistance of the gas.

(2) The rigorous Stefan-Maxwell equation for mass transport is simplified using the effective binary diffusivity of component i with respect to the mixture.

(3) The temperature and concentrations are assumed uniform over the volume of the droplet.

(4) Radiation effects are assumed negligible.

(5) The vapor phase behaves as an ideal gas.

The present model differs from that of Newbold and Amundson in that:

(1) Nonidealities in solution behavior are accounted for.

(2) The Kelvin effect on droplet vapor pressure is accounted for.

(3) Deviations from the continuum heat and mass fluxes under transition regime conditions are accounted for.

Equations (1) and (2) can be numerically integrated subject to the initial conditions

$$n_i(0) = n_{i,0} \tag{3}$$

$$T(0) = T_{\infty,0}, \tag{4}$$

and the volume conservation relation

$$r(t) = \left[\frac{3}{4\pi}\sum_i n_i(t)\overline{V_i}\right]^{1/3} \tag{5}$$

to give the history of the particle size and composition as a function of time. To do so one needs to specify the values of $p_{i,\infty}$, $i = 1, ..., n$, as well as the temperature and composition dependence of the physical properties a_i, D_{ij}, $\overline{V_i}$, $\Delta\overline{H_i}$, $h_{v,i}$, k, σ, $c_{p,soln}$, $c_{p,i}$,and p_i^o. The only parameters that are characteristic of the device itself are the ambient partial pressure $p_{i,\infty}$ and the total pressure and ambient temperature, p_T and T_∞. We now consider the specification of $p_{i,\infty}$ in a geometry that is frequently used in diffusion drying and humidification operations.

III. Laminar flow in a tube with constant wall conditions

For purposes of the present analysis, we will assume that evaporation or condensation has negligible effect on depletion or increase of the ambient concentration of the species. The bulk temperature of the flowing gas is assumed to be constant. At time zero the particle is in equilibrium with the ambient partial pressure p_{i,∞_0}:

$$p_{i,\infty_0} = a_i p_i^o \exp\left(\frac{2\sigma \overline{V_i}}{rRT}\right). \tag{6}$$

Then, at $t = 0$, the driving force for evaporation (or condensation) is zero. A driving force is created by allowing for depletion (or augmentation) of the ambient vapor in the device. If the device consists of a well-mixed vessel then, upon introduction, the particles are exposed to a constant $p_{i,\infty}$. A commonly used mode of influencing $p_{i,\infty}$ in diffusion drying or humidifcation operations is by absorption (or evaporation) of the transferring species (usually water) at the surface of the wall of a tube through which the particle-carrying gas is flowing in laminar flow.

If the following assumptions are made, this geometry describes the well-known Graetz problem in heat or mass transfer: the wall is a perfect absorber (or has a constant partial pressure in the case of growth),the particles do not influence the flow, and the flow is laminar. The partial pressure of species i at any axial (z) and radial (r_t) position at steady state in a tube of radius R_t is given by

$$\chi = \frac{p_{i,\infty} - p_{i,wall}}{p_{i,\infty_0} - p_{i,wall}} = \sum_{n=1}^{\infty} c_n Y_n \exp\left(-\lambda_n^2 \varsigma\right), \tag{7}$$

where

$$\varsigma = \frac{z D_{ij}}{R_t^2 \, v_{z,max}}$$

and $c_n(\xi)$, $Y_n(\xi)$, and $\lambda_n(\xi)$ depend on $\xi = r_t/R_t$, and are tabulated (Brown, 1960).

Equation (7) can be used to define the ambient partial pressure of species i as a function of axial and radial position in a laminar flow device. The residence time of a particle at a radial position r_t is related to the axial position in the tube by

$$t = \frac{z}{v_{z,max}[1 - \xi^2]}.$$

It must be noted that the requirement that the wall be a perfect absorber is an idealization of the actual adsorption characteristics of a laboratory dryer. The actual boundary condition is determined by the adsorption characteristics of the dessicant used; thus, while freshly-replaced adsorbent may initially closely approximate a perfect sink for the diffusing species, as it becomes saturated its adsorbing ability (and hence the "true" boundary condition) varies with time and axial position.

Similarly, the assumption of a constant partial pressure at the wall during a humidification operation requires that the medium remain uniformly saturated with the evaporating species. Changes in wall temperature with time or position affect the wall partial pressure.

IV. Drying of a solution particle

The foregoing analysis of droplet evaporation will be applied to the simulation of the drying of an aqueous solution particle in two ambient environments: first, at a constant ambient relative humidity, and second, in a laminar flow device as previously described, with axial and radial water vapor partial pressure profiles. Although Eqs. (1) and (2) include the effect of Stefan flow, it is usually assumed that, at typical atmospheric conditions, this effect is negligible; the validity of this simplification will be examined for the cases considered here. It is also possible to considerably simplify the analysis of droplet evaporation by assuming that the particle quickly attains and remains at its wet-bulb temperature, rather than solving Eq. (2) simultaneously with (1). The applicability of this approach to the present cases will also be investigated.

The example that will be taken is that of a 1-μm salt crystal initially exposed to, and equilibrated with, an environment at 99.8% relative humidity. It is recognized that a solid crystal will in fact be non-spherical in shape, but for purposes of this work it is assumed that treating it as a spherical particle is acceptable. Atmospheric pressure (p_T = 1 atm) and an ambient temperature (T_∞) of 293.15 K will be used, to simulate typical laboratory conditions. Quasi-steady state equations are developed for the following cases, for ambient partial pressure:

(1) coupled mass and heat transfer, including Stefan flow

(2) coupled mass and heat transfer, not including Stefan flow

(3) mass transfer equation with the wet-bulb temperature computed at each step in the integration

(4) mass transfer equation with the initial wet-bulb temperature

(5) isothermal mass transfer with drop temperature equal to the ambient

For the case of the drop in the laminar concentration profile, cases (3) and (4)

will be omitted.

Case (1). For the case of only one diffusing component, J_i becomes

$$J_i = \frac{C_T D_{1m}}{r} \ln\left[\frac{p_T - p_{1,\infty}}{p_T - a_1 p_1^o \exp\left(\frac{2\sigma\overline{V_1}}{rRT}\right)}\right] \beta_M(Kn_1). \tag{8}$$

Equations (1) and (2) are solved simultaneously.

Case (2). Expanding the exponential and logarithmic terms in (1) and setting $C \approx 1$ (valid for a trace component diffusing into air) yield

$$J_i = \frac{C_T D_{im}}{p_T r}\left[a_i p_i^o \exp\left(\frac{2\sigma\overline{V_i}}{rRT}\right) - p_{i,\infty}\right]\beta_{M,i}(Kn_i). \tag{9}$$

When a is small, the criterion

$$\frac{a}{e^a - 1} \approx 1$$

is satisfied, and the Stefan flow can be neglected. In this case, Eq. (2) becomes

$$\frac{dT}{dt} = \frac{-4\pi r^2}{\sum_i n_i c_{p,soln}}\left[\frac{k}{r}(T - T_\infty)\beta_T(Kn_g) + \sum_i J_i(h_{v,i} - \overline{\Delta H_i})\right]. \tag{10}$$

Neglecting Stefan flow appears to be a good assumption under laboratory conditions of temperature and pressure.

Cases (3) and (4). The wet bulb temperature is obtained by equating the steady-state heat flux from the drop to the product of the molar flux and the latent heat transported to or from the sphere:

$$\sum_i J_i h_{v,i} = -\frac{k}{r}(T - T_\infty)\beta_T, \tag{11}$$

which yields the following implicit equation for the wet-bulb temperature T_{wb}, neglecting Stefan flow:

$$\frac{\beta_M}{kRT_\infty\beta_T}\sum_i D_{im} h_{v,i}\left[a_i p_i^o \exp\left(\frac{2\sigma\overline{V_i}}{rRT_{wb}}\right) - p_{i,\infty}\right] - (T_\infty - T_{wb}) = 0. \tag{12}$$

The evaporation of water from an aqueous solution particle can be treated as a continuous process, causing a continuous increase in molality up to the point of solution saturation. After this point, further evaporation of water will result in a decrease in the total amount of saturated solution present, but no further increase in concentration. In order to conserve the initial total number of moles of salt and simultaneously satisfy the saturation concentration constraint when the evaporation process is in this regime, the moles of dissolved salt, in solution at concentration m_{sat} where m is molality, will be adjusted to corespond to the moles of water present. Any salt in excess of that needed to attain m_{sat} is assumed to crystallize in the center of the particle and maintain equilibrium with the saturated solution surrounding it. Thus, although the number of moles of water varies from $n_{w,o}$ to 0 as the particle dries, the molality increases monotonically with time to m_{sat} but then remains at that constant value until drying is complete. If the drop consists of unsaturated solution only, its mass is given by

$$M_{drop} = n_w \left[\frac{m M_{w,w}}{1000} + M_{w,s} \right], \tag{13}$$

where $M_{w,w}$ and $M_{w,s}$ refer to the molecular weights of water and salt, respectively. Then the drop radius is

$$r = \left[\frac{3}{4\pi} \frac{M_{drop}}{\rho} \right]^{1/3}. \tag{14}$$

After the solution in the drop has reached saturation, the drop radius is given by:

$$r_{sat} = \left[\frac{3}{4\pi} \left(\left(\frac{1}{\rho_{sat}} \left[\frac{m_{sat} n_w M_{w,w} M_{w,s}}{1000} + n_w M_{w,w} \right] \right) + \frac{M_{w,s}}{\rho_{salt}} \left[n_{salt,total} - \frac{m_{sat} n_w M_{w,w}}{1000} \right] \right) \right]^{1/3}, \tag{15}$$

where ρ_{salt} and n_{salt} refer to the dry salt density and number of moles in the dry salt crystal, respectively.

A shortcoming of this treatment of aerosol evaporation as applied to salt solutions is that it fails to predict or account for the hysteresis effect exhibited by inorganic salt solutions as the relative humidity is decreased from the value with which the solution is initially in equilibrium (Tang *et al.*, 1977; Pruppacher and Klett, 1978; Richardson and Spann, 1984; Spann and Richardson, 1985). As the humidity is decreased to just below the deliquescence point, immediate recrystallization of the salt and the expected abrupt decrease in particle size (corresponding to the abrupt size increase as the same particle deliquesces) do not occur. Rather, a supersaturated solution forms. Evaporation from this solution causes a continuous, gradual decrease in size. Frequently, an abrupt size change will occur at some relative humidity lower than that for deliquescence, caused by sudden recrystallization of the supersaturated solution. This recrystallization humidity is generally not reproducible, and it is thought that the phenomenon results from a lack of crystallization nuclei in the solution.

Because this effect cannot be accurately predicted, it is not feasible to incorporate it into the evaporation equation for salt solutions. However, it will play a significant role in the design length for a diffusion dryer. In this case, the relative humidity necessary for recrystallization of the supersaturated solution can be estimated experimentally. An approximate method for obtaining the design length under these conditions will be discussed below.

V. Comparison of evaporation rates

The approaches developed in the preceding sections will be used to compare the evaporation rates of an aqueous sodium chloride droplet under various external conditions. The results will also be used to check the validity of the different assumptions discussed concerning the treatment of droplet temperature changes. The initial conditions for the NaCl solution droplet evaporation are determined from the equilibrium relation,

$$RH_0 = \frac{p_{w,\infty_0}}{p_w^o} = a_w \exp\left(\frac{2\sigma\overline{V_w}}{rRT_\infty}\right), \tag{16}$$

where RH_0 denotes the ambient relative humidity at the inlet to the dryer, and all properties are evaluated at the ambient temperature T_∞, which is taken as the initial droplet temperature. The dry salt crystal equivalent radius is also specified, which fixes the total number of moles of salt in the wet particle at any time. An initial guess for the molality of the solution in equilibrium with the given RH_0 is made, and all solution properties and the diameter are computed at this molality. The property data required for the integration were obtained from the International Critical Tables (1926-1930) and Robinson and Stokes (1965) and, where possible, fit to third-order polynomials in concentration at given temperatures. The temperature dependency of the physical properties was obtained by interpolation. If the equilibrium condition in Eq. (16) is satisfied to within a specified tolerance, the current m is correct, and the calculated r, m, and n_w become the initial conditions. If the equation is not satisfied, Newton's method is used to generate a new guess.

The time dependence of the diameter of an aqueous salt solution of a 1-μm dry salt particle, initially at a relative humidity of 99.8% at 293.15 K and placed at $t = 0$ in an environment at zero ambient partial pressure of water, is shown in Figure 1 for the various assumptions discussed previously. It can be seen that

the Stefan flow term has negligible effect on the drying time at this temperature. In addition, the simplified treatment of case (4) differs from the more rigorous solution of cases (1) and (2) by less than 2%.

The effect of various ambient relative humidities on the drying process is shown in Figure 2, for ambient RH of 60%, 75%, and 80% and an ambient temperature of 293.15 K, using the method of case (2). At a relative humidity of 75%, the particle can dry completely but takes approximately five times as long to do so as at $RH = 60\%$. For RH greater than approximately 75%, the particle diameter approaches a value greater than the diameter of the original dry particle because the partial pressure over the drop has equilibrated with the ambient partial pressure while the particle still contains moisture.

Next, particles at an initial temperature of 293 K and initial relative humidities of 99.8% and 85% are assumed to be placed in the laminar flow concentration profile to simulate diffusion drying. We consider a particle on the centerline the tube. The results, appearing in Figures 3 and 4, indicate that the assumption that the particle remains at temperature T_∞ throughout the drying process is a much better approximation in computing total drying time than in the case where the particle is instantaneously exposed to zero ambient RH; in Figures 3 and 4, the differences between the isothermal and nonisothermal assumptions are less than 2.5%. This behavior is consistent with the observation that the time constant for changes in the ambient environment in the laminar flow case is much larger than that for changes associated with the concentration and temperature profiles around the droplet, so that these adjust quickly to the slow changes of the environment.

The profiles are qualitatively different from those at constant ambient relative humidity, due to the changing ambient partial pressure as well as the behavior as the solution comprising the particle becomes saturated. At this point,

and for all times greater than this, further decreases in the moles of water in the drop will decrease the total amount of solution, and hence wet particle size, but will not increase the concentration, which remains fixed at m_{sat}. Likewise, the activity of the solution, $a_{w,sat}$, remains constant. Thus, the vapor pressure over the saturated drop is a function only of diameter in this regime. The behavior shown in Figures 3 and 4 suggests different regimes for the aqueous salt solution aerosols during evaporation, which depend on the relationship between molality and ambient partial pressure as functions of time. We can define t^{sat} as the time at which the solution in the particle reaches its saturation concentration, and t^* as the time at which the ambient partial pressure equals the vapor pressure over the saturated drop. In the present case, these times occur within a few hundreths of a second of each other; for convenience, only t^* is marked. Results of d_p vs. t show that for $t > t^*$ complete drying of the drop occurs very rapidly in comparison with the time required to reach the point t^*.

Thus, if $p_{w,\infty} = a_{w,sat}p_w^o$ occurs at a time t^* that is greater than the time t^{sat} at which the particle reached saturation, the condition of zero driving force can occur, implying that the particle size remains essentially constant in some time interval centered at t^*.

At the entrance to the tube, the partial pressures of water over the drop and in the carrier gas are equal. For $0 < t < t^*$, p_{w,∞_o} and $a_w p_w^o$ are both decreasing functions of time, but evaporation occurs because the ambient partial pressure is always less than that over the drop at any time. For $t > t^*$, p_{w,∞_o} decreases with t, but $a_{w,sat}p_w^o$ (the partial pressure over the drop, excluding the Kelvin effect) remains fixed. The results suggest that, for particles of such size that the Kelvin and noncontinuum effects can be neglected, the major contribution to the drying time is the time required for the solution in the drop to become saturated. This also corresponds to the time for which the ambient partial

pressure of the evaporating species has become nearly equal to the saturation vapor pressure over the droplet. In general, then, for application to the design of aerosol drying equipment for this type of particle, the residence time required is a strong function of initial relative humidity and the size of the dry salt crystal.

The results also suggest an approximate method for taking into account the hysteresis effect exhibited by a drying salt particle, if the relative humidity at which the recrystallization finally occurs can be estimated. It is necessary to assume that the drop temperature is the same as that of the ambient gas. The length required to achieve the relative humidity for recrystallization in the carrier gas (at the streamline of interest) is determined from the solution of the ambient partial pressure (χ). Since, generally, we have shown that the solution particles respond quickly to changes in the ambient environment, this will be approximately the length required to dry the humid aerosol. Application of this approximation for the length to the case of Figure 3 (but using the theoretical RH for recrystallization) gives an error of $\approx 3\%$ in the length required for drying as compared to that calculated from the equations of case (2).

VI. The Aerosol mobility chromatograph

Liu et al. (1978) proposed a device termed an aerosol mobility chromatograph for the separation of aerosols of different composition by preferential growth. The aerosol to be investigated is generated, given a Boltzmann equilibrium charge distribution, and then is introduced into the first of two differential mobility analyzers (DMA). The DMA is used to render the aerosol monodisperse by allowing selective passage through the device of only those particles of a selected electrical mobility, which can be related to size. The monodisperse aerosol is then grown via humidification, and the new size distribution is measured with the second DMA in conjunction with an electrometer current sensor. By varying the particle size selected by the second DMA, which is accomplished by scanning the range of applied voltages, and measuring the electrometer current at each voltage, which is proportional to the number concentration, the size distribution of the final aerosol can be inferred. Although in the original design, the humidification was carried out in the vapor space of a flask containing water at a given temperature, we wish to examine here also the feasibility of designing an aerosol mobility chromatograph in the laminar flow mode.

Whereas up to now we have been discussing devices based on particle evaporation, we turn now to particle humidification. We assume that at time zero particles that are equilibrated to their environment at a certain vapor concentration are introduced into a region of higher vapor concentration. In the laminar flow device with aqueous aerosols, the higher RH is accomplished by having a uniformly wetted tube wall at which $RH = 1$. The separation of different aqueous solution particles occurs as the particles grow selectively as the humidity in the device increases with particle residence time. The general design equations already developed, with some minor modifications, can be applied directly to the design of the aerosol mobility chromatograph.

The case that will be considered is that of an initially dry monodisperse aerosol entering a tube with walls saturated with water. For this application, the dimensionless quantity χ is rewritten:

$$\chi = \frac{p_{w,\infty} - p_w^o}{p_{w,\infty_o} - p_w^o}. \tag{17}$$

At any point in the tube, we can relate χ to the local relative humidity by

$$\chi = \frac{RH - 1}{RH_o - 1}, \tag{18}$$

and, if $RH_o = 0$,

$$RH = 1 - \chi. \tag{19}$$

The driving force on the particle will be positive only when the local RH satisfies the condition:

$$RH_{local} \geq a_w p_{w,s}, \tag{20}$$

where $p_{w,s}$ is the vapor pressure at the drop surface. Thus, for some length into the tube, a particle at the centerline remains dry, until the centerline relative humidity increases to the deliquescence point.

The growth of a 1-μm dry particle down such a tube was computed for two types of aerosols: sodium chloride and ammonium sulfate. Figure 5 compares the growth curves along the centerline of the tube for these two cases. Since NaCl has a lower deliquescence point, it humidifies first, and also grows to a larger final size. This result illustrates that a mixed aerosol composed of these two types of particles can be separated into two chemical fractions by this technique, by first growing the aerosol and then classifying the humid aerosol by size.

VII. Conclusions

The design equations for the well-mixed and laminar diffusion dryers have been developed, and the illustrative calculations for NaCl and $(NH_4)_2SO_4$ aqueous solution droplets lead to several conclusions. First, for the conditions (atmospheric) considered, it appears that the Stefan flow term and its energy analogue may be safely neglected in considering aqueous solution evaporation. For the case of constant ambient relative humidity, treating the droplet temperature as equal to that of the surrounding gas is a poor assumption, but the assumptions of instantaneous wet-bulb temperature throughout the evaporation process and of the initial wet-bulb temperature being maintained constant during the process each lead to total drying times within several percent of that obtained by solving the coupled equations. For a multicomponent drop, the wet-bulb temperature is a function of composition and hence a single constant value for this temperature cannot be strictly accurate. As discussed by Davis (1983), "the depression of the interfacial temperature depends strongly on the dimensionless group $\Delta H_{vap} D_{ij} C_T / k T_\infty$ and the vapor pressure". In general, the growing or evaporating drop cannot be assumed to be at the ambient gas pressure unless the vapor pressure above the drop is extremely low (as in the case of DBP) or the heat of vaporization is small. For the case of the laminar flow dryer, assuming the droplet temperature is equal to the bulk gas temperature results in a total drying time within a few percent of that computed using the coupled set of mass and energy equations. A special problem associated with the evaporation of salt solutions, the hysteresis effect, was considered, and an approximate method for obtaining the length of a drying tube under such conditions was proposed.

We have also demonstrated that a laminar-flow humidifying system, by controlling the vapor partial pressure along the humidifying tube in a known manner, can be used to preferentially grow one component of an external aerosol

mixture, thus providing a means for the separation of the mixture into its component aerosols. In the system considered, the size of the NaCl particle, initially with the same dry diameter as that of the $(NH_4)_2SO_4$ particle, doubles several seconds before the $(NH_4)_2SO_4$ particle deliquesces; after both have deliquesced, their sizes differ by about 20%. This technique is the basis for the operation of the aerosol mobility chromatograph, and the equtions developed may be used in the design of such a device.

Acknowledgement

This work was supported by National Science Foundation grant ATM-8503103.

References

Brown, G. M. (1960). *AIChE J.***1**:179–183.

Brock, J. R. (1967). *J. Coll. Int. Sci.***24**:344–351.

Chang, R. and Davis, E. J. (1974). *J. Coll. Int. Sci.***47**:65–77.

Davis, E. J. (1983). *Aer. Sci. Tech.***2**:121–144.

El Golli, S., Bricard, J., Turpin, P.-Y., and Armaud, G. (1972). *Aer. Sci.***3**:255–274.

El Golli, S., Bricard, J., Turpin, P.-Y., and Treiner, C. (1974). *Aer. Sci.***5**:273–292.

Fuchs, N. A. and Sutugin, A. G. (1971). In *Topics in Current Aerosol Research*(Hidy and Brock, eds.). Pergamon Press, London, pp. 4–75.

Fukuta, N. and Walter, L. A. (1970). *J. Atm. Sci.***27**:1160–1172.

Liu, B. Y. H., Pui, D. Y. H., Whitby, K. T., Kittelson, D. B., Kousaka, Y., and McKenzie, R. L. (1978). *J. Atm. Sci.***12**:99–104.

National Research Council (1926-1930). *International Critical Tables* (Edward W. Washburn, ed.). McGraw-Hill, New York.

Newbold, F. R., and Amundson, N. R. (1973). *AIChE J.***19**:22–30.

Nix, N. and Fukuta, N. (1973). *J. Chem. Phys.***58**:1735–1740.

Ogren, J. A., Heintzenberg, J., and Charlson, R. J. (1985). *Geophys. Res. Let.***12**:121–124.

Pesthy, A. J., Flagan, R. C., and Seinfeld, J. H. (1981). *J. Coll. Int. Sci.***82**:465–479.

Pruppacher, H. R. and Klett, J. D. (1978). *Microphysics of Clouds and Precipitation.* Reidel, Dordrecht, p. 155.

Ravindran, P., Davis, E. J., and Ray, A. K. (1979). *AIChE J.***25**:966–975.

Richardson, C. B. and Spann, J. F. (1984). *J. Aer. Sci.* **15**:563–571.

Robinson, R. A. and Stokes, R. H. (1965). *Electrolyte Solutions.* Butterworths, London, pp. 476, 510.

Smolik, J. and Vitovec, J. (1984). *J. Aer. Sci.***15**:545–552.

Spann, J. F. and Richardson, C. B. (1985). *Atm. Env.***19**:819-825.

Tang, I. N., Munkelwitz, H. R., and Davis, J. G. (1977).*J. Aer. Sci.***8**:149–159.

Twomey, S. (1977). In *Developments in Atmospheric Science.* Elsevier, Amsterdam, Vol. 7, p. 71.

Wagner, P. E. (1982). In *Aerosol Microphysics. II. Chemical Physics of Microparticles*(W. H. Marlowe, ed.). Springer-Verlag, Berlin, pp. 129–178.

Wagner, P. E. and Pohl, F. G. (1975). *J. Coll. Int. Sci.***53**:429–438.

Figure Captions

Figure 1. Particle evaporation rates at constant relative humidity. NaCl solution particle, dry diameter = 1 μm. Initial humidifying RH = 99.8%. Drying RH = 0%.

Figure 2. Particle evaporation rates at constant relative humidity. NaCl solution particle, dry diameter = 1 μm. Initial humidifying RH = 99.8%.

Figure 3. Particle evaporation rates in laminar flow dryer. NaCl solution particle, dry diameter = 1 μm. Initial humidifying RH = 99.8%.

Figure 4. Particle evaporation rates in laminar flow dryer. NaCl solution particle, dry diameter = 1 μm. Initial humidifying RH = 85%.

Figure 5. Particle growth rates in laminar flow humidifier.

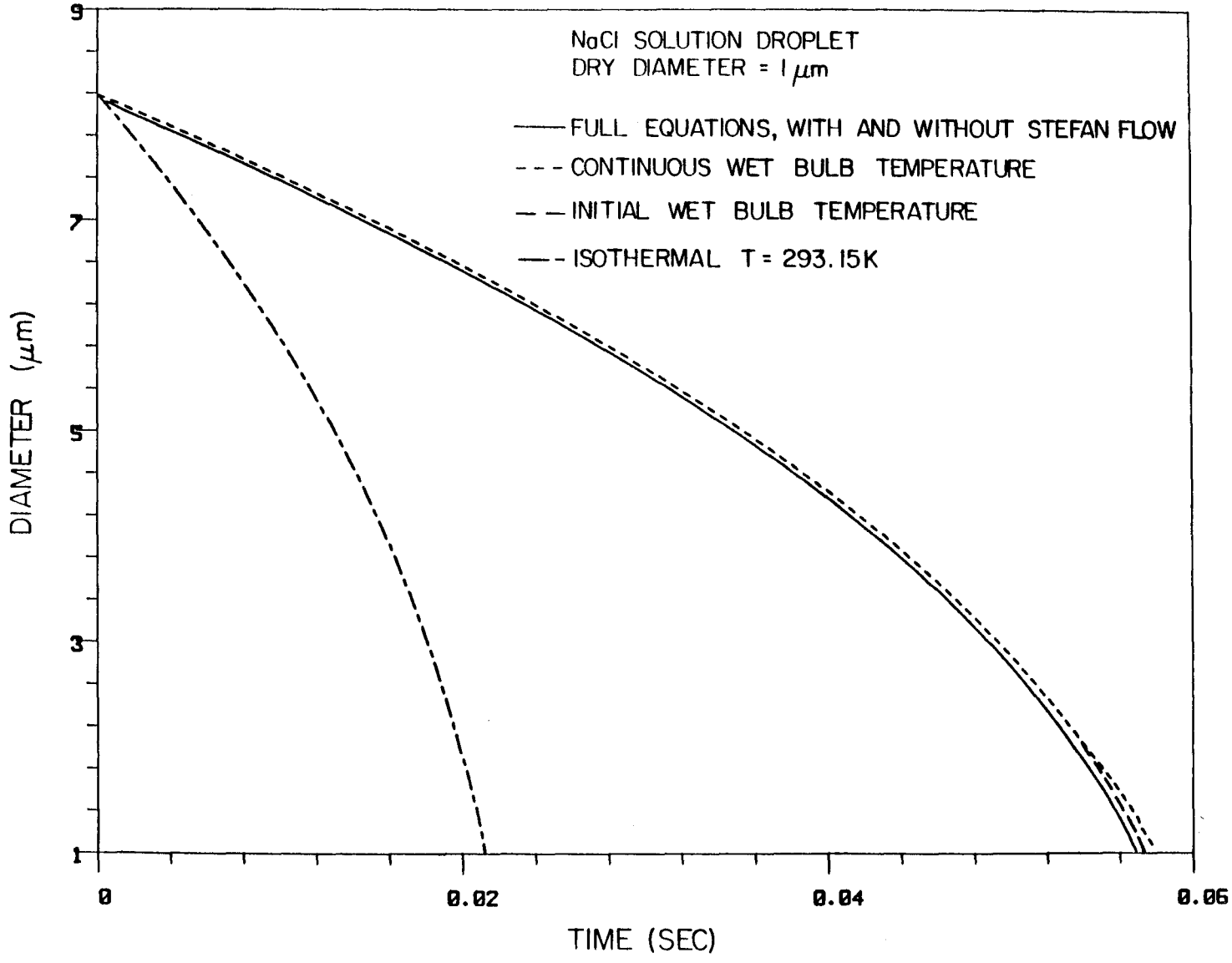
NaCl SOLUTION DROPLET
DRY DIAMETER = 1 μm
FULL EQUATIONS, WITH AND WITHOUT STEFAN FLOW
CONTINUOUS WET BULB TEMPERATURE
INITIAL WET BULB TEMPERATURE
ISOTHERMAL T = 293.15K
DIAMETER (μm)
9
7
5
3
1
0
0.02
0.04
0.06
TIME (SEC)

Figure 1

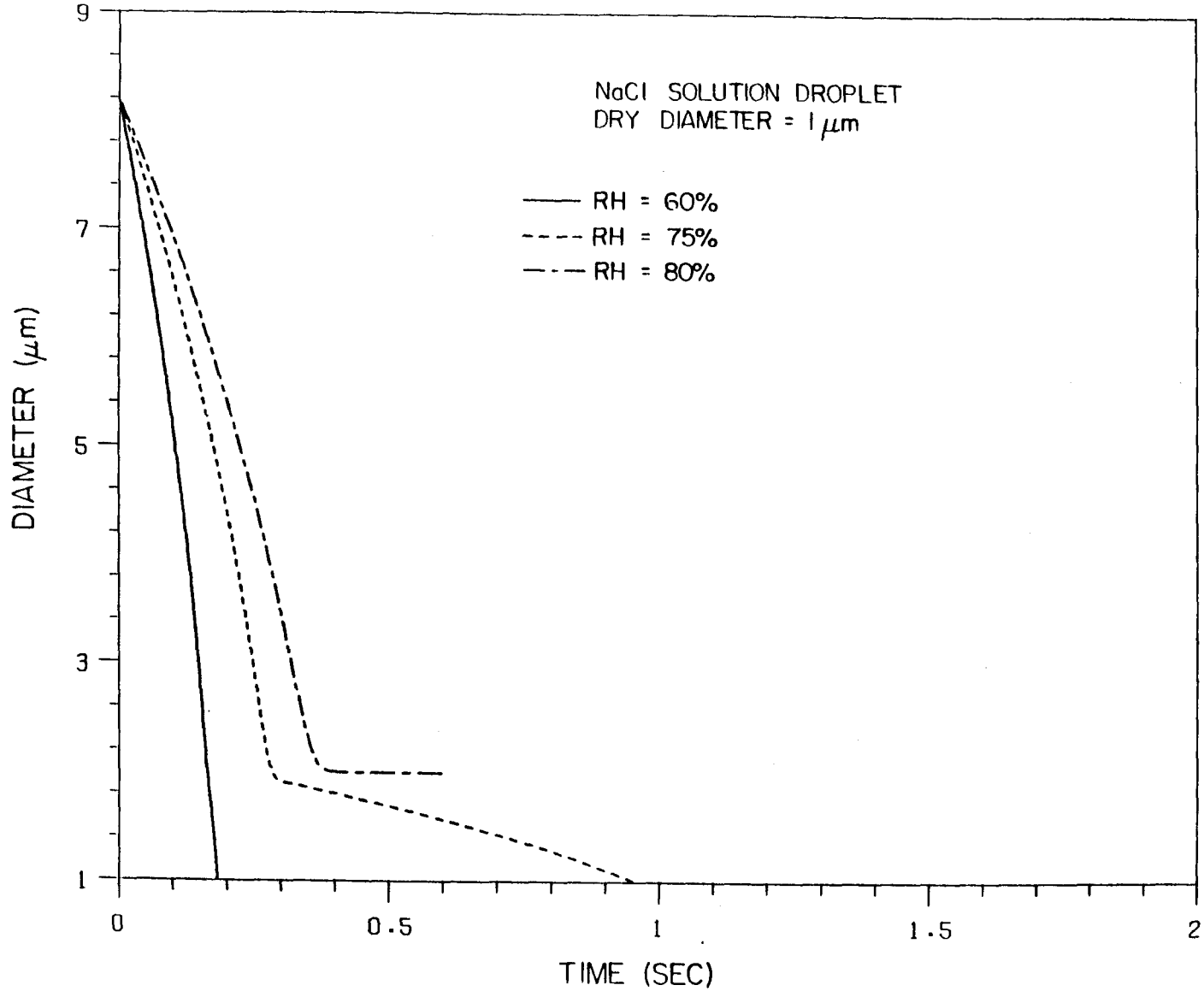
NaCl SOLUTION DROPLET
DRY DIAMETER = 1 μm
RH = 60%
RH = 75%
RH = 80%
DIAMETER (μm)
TIME (SEC)
9
7
5
3
1
0
0.5
1
1.5
2

Figure 2

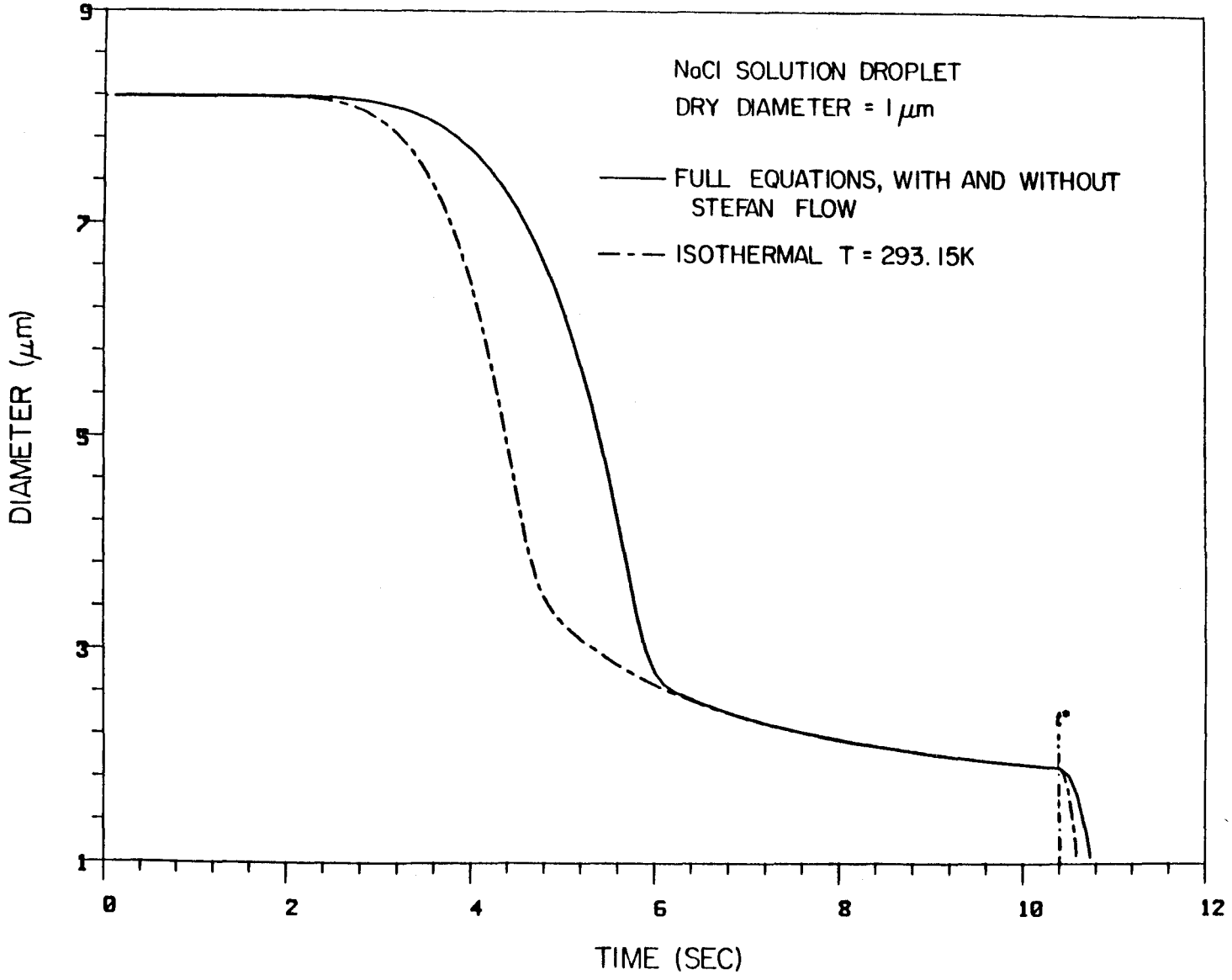
NaCl SOLUTION DROPLET
DRY DIAMETER = 1 μm
FULL EQUATIONS, WITH AND WITHOUT STEFAN FLOW
ISOTHERMAL T = 293.15K
DIAMETER (μm)
TIME (SEC)
t*
9
7
5
3
1
0
2
4
6
8
10
12

Figure 3

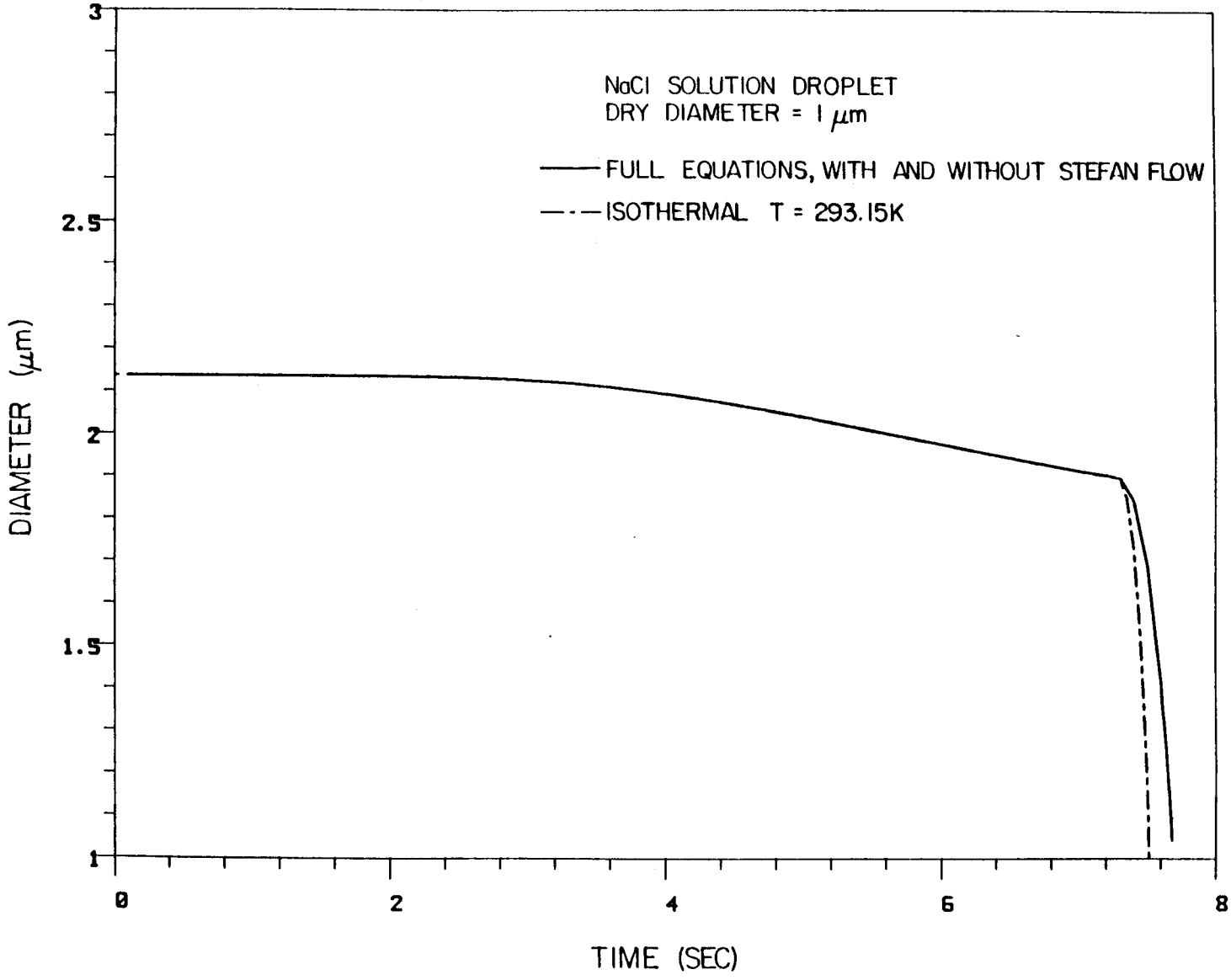
NaCl SOLUTION DROPLET
DRY DIAMETER = 1 μm
FULL EQUATIONS, WITH AND WITHOUT STEFAN FLOW
ISOTHERMAL T = 293.15K
DIAMETER (μm)
3
2.5
2
1.5
1
0
2
4
6
8
TIME (SEC)

Figure 4

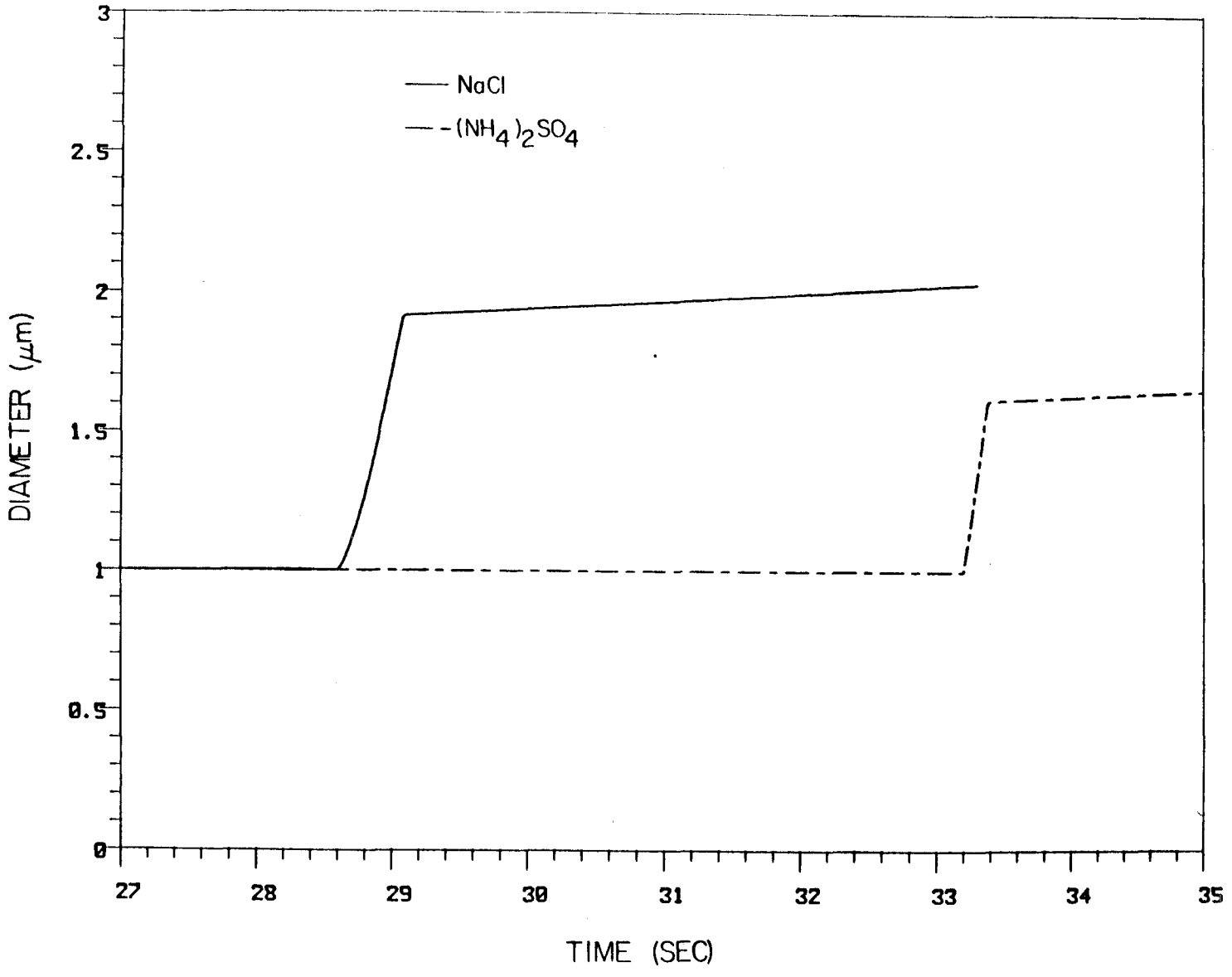
NaCl
(NH4)2SO4
DIAMETER (μm)
TIME (SEC)
0
0.5
1
1.5
2
2.5
3
27
28
29
30
31
32
33
34
35

Figure 5

Chapter III

Studies in Binary Nucleation: The Dibutylphthalate/Dioctylphthalate System

The text of Chapter III consists of an article which appears in the *Journal of Chemical Physics* **89** (10), 6442–6453.

Studies in Binary Nucleation:

The Dibutylphthalate/Dioctylphthalate System

Sonia M. Kreidenweis,* Kikuo Okuyama and Yasuo Kousaka

Department of Chemical Engineering
University of Osaka Prefecture, Osaka, Japan

and

Richard C. Flagan and John H. Seinfeld

Department of Chemical Engineering
California Institute of Technology
Pasadena, California 91125

* Department of Chemical Engineering, California Institute of Technology, Pasadena, California.

Abstract

A continuous-flow mixing apparatus has been developed for the study of binary nucleation. This apparatus has been used to investigate the nucleation of mixed dibutylphthalate/dioctylphthalate vapors, and the interaction of the two vapors in particle formation has been demonstrated. A model that considers competition between nucleation and condensation processes during particle formation is applied in the analysis of the experimental results, allowing comparison of the magnitudes of the theoretical and actual nucleation rates in both the single-component and mixed vapor systems.

I. Introduction

The formation of particles by homogeneous nucleation from a vapor phase containing two condensable components, so-called binary nucleation, has received much attention from both theoretical and experimental points of view. The most distinctive aspect of binary nucleation is the formation of particles at supersaturations of either component that are insufficient to support significant homomolecular homogeneous nucleation.

Previous theoretical analyses of particle formation in two-component systems have been, for the most part, based on modifications of the original theory for binary nucleation as developed by Reiss[1]. This theory is an extension of the classical homomolecular (Becker-Döring-Zeldovich) nucleation theory to two components, and contains similar inherent assumptions (for example, the equilibrium cluster distribution assumption and determination of the critical cluster size by equating liquid- and gas-phase chemical potentials, allowing for the change in free energy due to formation of the interface). Supersaturations with respect to the composition over a solution droplet are smaller (or larger) than those with respect to a pure phase, depending on the deviation from ideality of the solution behavior. The critical cluster size, and hence nucleation rate, are greatly affected by such nonidealities. The classical example of greatly enhanced nucleation due to solution nonidealities is the sulfuric acid-water system, for which large rates of nucleation have been theoretically predicted at low relative humidities and for trace amounts of acid vapor.

Limited data are available with which to evaluate the theories; most laboratory studies of binary nucleation have been carried out using equipment originally developed for the study of homomolecular nucleation, such as the piston cloud chamber[2], the diffusion cloud chamber[3], and the supersonic nozzle[4]. These systems allow one to determine the critical supersaturation ratio for nucleation, but usually do not give information about the dependence of the aerosol number concentration on the supersaturations of the two component vapors.

An additional disadvantage is that those which rely on expansion to produce supersaturations operate at low temperatures.

Recently, the device referred to as the particle size magnifier (PSM) has been employed[5,6] to study the homogeneous nucleation of single-component vapors without introducing the complications inherent in many of the traditional systems. In the PSM, a saturated, high-temperature vapor stream is rapidly mixed with room-temperature gas to generate large supersaturations, with nucleation and growth subsequently occurring in an isothermal region downstream. A wide range of saturation ratios and mixed temperatures in a range of atmospheric interest (for example, 30°C.), can be achieved by adjusting the temperatures and relative flow rates of the streams. By observing the total number of particles produced for various supersaturations, both the critical supersaturation and the dependence of the number of particles formed upon saturation ratio can be determined. This dependence can be related to that predicted theoretically using an appropriate model. Experiments performed in a PSM, therefore, can potentially yield more information about the nucleation process, especially at conditions of atmospheric interest, than those performed using other types of apparatus.

We present here the first measurements of binary nucleation rates in the particle size magnifier. Two organic species, dibutylphthalate (DBP) and dioctylphthalate (DOP), were chosen for this study. Previous single-component experiments in the PSM[5,6] investigated the homomolecular nucleation behavior of DBP, and a number of other researchers have studied nucleation of either of these compounds. Advantages of this choice of species include the following: most of the physical properties of both compounds are known, and since they are similar organics they are expected to form ideal solutions, thus simplifying the theoretical analysis. Because of the low saturation vapor pressures, the droplets formed are expected to be stable, minimizing losses during the counting.

The experimental procedure used in this study was designed to allow for

direct comparison between the numbers of particles produced in the case of mixed vapor and those that would have been produced in the presence of either species alone. This was achieved by performing a mixed vapor experiment at a particular set of temperatures and flow rates, then replacing in turn each of the organic vapor streams by a dry air stream and repeating the experiment at the same conditions, but in the presence of only one of the condensable vapors. The number of droplets formed via the different nucleation mechanisms is measured and compared with those predicted from a dynamic model that combines expressions for classical nucleation and steady-state particle growth.

II. Experimental Apparatus and Method

Figure 1 shows a schematic of the experimental apparatus used in the binary nucleation experiments, which is similar to that used in the previous nucleation studies of single-component DBP vapor. A high purity, particle-free air stream is split into three gas flows: one is a room temperature diluent gas flow and the other two are high temperature carrier gas flows that are saturated with either DBP or DOP vapor after passing through each saturator. The two high temperature flows are preliminarily mixed. The resulting DBP-DOP vapor flow is turbulently mixed with the room temperature flow in the mixing unit, and then held at constant temperature through the residence volume, where the supersaturated vapor is given time to homogeneously nucleate. The resulting aerosol stream then goes to particle measurement instrumentation.

Each saturator consists of a column filled with silica gel that has been impregnated with liquid DBP or DOP as shown in Figure 2. The flow rate of carrier air may range from 0.1 to 0.5 ℓ/min. Temperatures measured by alumel-chromel thermocouples at five positions in the saturators were consistent to within 0.1°C.

Figure 3 depicts the mixing unit that is used to rapidly mix the high temperature DBP-DOP vapor with low-temperature diluent gas. The temperatures of the DBP and DOP streams are denoted T_{sh1} and T_{sh2}, respectively, and T_l represents the temperature of the diluent gas flow. The particle-free air saturated with the organic vapors flows horizontally into a tube and meets low-temperature gas blown in through eight 0.08 cm diameter holes. The flow rates of the vapor streams from each saturator are denoted Q_{sh1} and Q_{sh2}, and the flow rate of room-temperature gas is Q_l. The mixing ratios, R_{h1} and R_{h2}, are expressed as Q_{sh1}/Q_m for DBP and Q_{sh2}/Q_m for DOP, where Q_m is the total flow rate of mixed gas. For these experiments, a mixing ratio of either 0.1 or 0.2 was used for both R_{h1} and R_{h2}. The vapor temperatures from the saturators were varied from 100°C. to 155°C., and the flow rate of room-temperature gas

Q_l ranged from 0.8 ℓ/min. to 2.0 ℓ/min.

The residence volume unit, which shall be referred to as the reheater, consists essentially of a temperature-controlled tube. The DBP-DOP vapor and air mixture flows from the mixing unit directly into the reheater, which provides the desired residence time, t_r, for homogeneous nucleation and condensational growth to occur. A temperature controller is used to maintain the temperature, T_r, equal to the adiabatic mixing temperature of the vapor-air stream, T_m, in order to maintain constant conditions for nucleation. In the case of DBP and DOP vapors, the vapor pressures and latent heats are sufficiently small that the increase in temperature of the gas after condensation is negligible, so that the temperature of the reheater can be maintained constant down its length. The volume of the reheater is 190 cm^3, giving a residence time of 5.7 s for a gas flow rate $Q_m = 2$ ℓ/min. Part of the total flow is drawn through a TSI 3020 condensation nucleus counter (CNC), which measures the total particle number concentration.

In starting up the PSM, the three air flows were first set to the desired values, and the temperatures of the saturators were increased gradually to the desired values. The temperature of the reheater was simultaneously controlled so that it would be at the mixed temperature determined by heat and mass balances. Assuming that the hot air-vapor mixture is combined rapidly and adiabatically with the room temperature air, in the supersaturated atmosphere produced, the temperature of the mixed gas, T_m, and the absolute masses of DBP and DOP per kilogram of dry air, H_{m1} and H_{m2}, respectively, are given by heat and mass balance equations:

$$T_m = \left(C_{sh1}T_{sh1}Q_{sh1} + C_{sh2}T_{sh2}Q_{sh2} + C_lQ_lT_l\right)/C_{si}\,Q_T, \tag{1}$$

$$H_{m1} = H_{sh1}Q_{sh1}/Q_T, \tag{2}$$

$$H_{m2} = H_{sh2}Q_{sh2}/Q_T, \tag{3}$$

$$Q_T = Q_{sh1} + Q_{sh2} + Q_l, \tag{4}$$

where C is the the specific heat, kcal/kg(dry air)K, Q the mass flow rate, kg(dry air)/s, and the vapor content H can be related to the vapor pressure of DBP or DOP, p in mm Hg:

$$H = M\,p\,/\left(28.966(760-p)\right). \tag{5}$$

The saturation ratios S_{o1} and S_{o2} for DBP and DOP vapors can be found from

$$\begin{aligned} S_{o1} &= p_1/p_1^o \\ S_{o2} &= p_2/p_2^o, \end{aligned} \tag{6}$$

where p_1^o and p_2^o are the saturated vapor pressures of DBP and DOP at the temperature T_m. In the calculation of these saturation ratios, the physical properties listed in Table 1 were used.

Figure 4 shows the values of the initial saturation ratios S_o in the mixing zone for both DBP and DOP vapors. It can be seen that the value of S_o depends strongly on the temperatures of both gas streams and on the mixing ratio. It is also seen that S_o attains high values when R_h is between 0.05 and 0.3. For the same temperatures and mixing conditions, DOP attains higher values of S_o than does DBP, due to the higher boiling point of DOP. A relatively small value of R_h (0.1) was selected to maintain the temperature of the mixed gas only slightly above room temperature. This ratio led to high supersaturations in the reheater and prevented a significant temperature drop between the reheater and the room temperature detector, which could have led to additional homogeneous nucleation.

In the experiment, a particular set of flow rates was used for all the runs; the variation in saturation ratio was achieved by changing the temperatures of the vapor streams, T_{sh1} and T_{sh2}. These were selected so that there was no possibility of particle formation during the preliminary mixing process, before dilution with cool air. The number concentration of homogeneously nucleated binary droplets was measured at steady state. By then replacing one saturator containing the impregnated silica gel with one filled with dry gel, homogeneous

nucleation of a single-component vapor was observed for comparison with binary nucleation at the identical temperatures and mixing conditions.

A typical set of experimental data is given in Table 2. In all the experiments, the flow through each saturator was one-tenth of the total mixed flow rate (as indicated by $R_{h1} = R_{h2} = 0.1$), and the dilution air stream temperature was approximately 21°C. This condition resulted in a mixed-gas temperature T_m of approximately 42°C. For the particular experiment of Table 2, the temperature of the DOP saturator remained fixed at 130°C. as the temperature of the DBP saturator was increased stepwise. The first block of data shows results in the mixed-vapor case; in the second block, the DOP saturator was replaced by a dry column, resulting in nucleation of DBP particles; and in the third, the DBP column was replaced by dry gel. These data are shown as a function of the saturation ratio of DBP in Figure 5, with the closed circles representing the binary results, and the closed squares and triangles representing homomolecular DBP and DOP nucleation, respectively. It is not possible to also show the saturation ratio of DOP; the homomolecular DOP results are shown as a function of the saturation ratio of DBP that would have been obtained if the DBP saturator had not been replaced by a dry column.

It is immediately evident from Figure 5 that the numbers of particles produced in the mixed-vapor cases cannot be explained by homogeneous nucleation of DBP or DOP alone. However, as the saturation ratio of DBP becomes very small or very large, the mixed-vapor results tend towards those for single-component nucleation. Both of these observations support qualitatively the predictions of binary nucleation theory. In the next section we present a model to be used for quantitative comparisons.

III. Integral Model for Binary Nucleation and Growth

To analyze the measured particle number concentrations for both single-component and binary nucleation, one must account for nucleation, depletion of the vapor, and growth of particles by condensation. An integral model, for example, that developed by Warren et al.[7,8] for single-component particles, and extended to binary systems by Kreidenweis and Seinfeld[9], can be used. In such an integral model it is assumed that the total number of aerosol particles is divided into sets; each set consists of monodisperse particles at a specified diameter, and is referred to as a mode and is given the index i. For example, if there are preexisting particles in the system of diameter d_{p_1} and new particles of diameter d_{p_2} are nucleated, two modes are used in describing the aerosol. (No preexisting particles were present in the experiments reported here.) The aerosol is further described by its moments, total number concentration in each mode, N_i, and total mass concentration of each condensable species in each mode, M_{ji}, and the vapor phase by the saturation ratio of each species, S_j.

The condensation rate of each component j is approximated by a continuum expression modified for noncontinuum effects by the expression developed by Dahneke[10], and incorporating a factor α that accounts for polydispersity and is defined by

$$R_{c_{ij}} = \frac{2\pi D_j p_j^o}{RT} \int_{d_{p_i}^*}^{\infty} d_{p_i} \left[S_j - a_{ji} \exp\left(\frac{4\sigma \overline{V}_j}{d_{p_i} RT} \right) \right] n_i(d_{p_i})\, f(Kn_{ji})\, dd_{p_i} \qquad (7)$$

$$= \alpha_{ji} N_i \left\{ \frac{2\pi D_j p_j^o}{RT} \overline{d_{p_i}} \left[S_j - a_{ji} \exp\left(\frac{4\sigma \overline{V}_j}{\overline{d_{p_i}} RT} \right) \right] f(\overline{Kn}_{ji}) \right\} \qquad (8)$$

$$f(Kn_{ji}) = \frac{1 + Kn_{ji}}{1 + 2Kn_{ji}(1 + Kn_{ji})}, \qquad (9)$$

$$Kn_{ji} = \frac{2\lambda_j}{d_{p_i}},$$

where D_j is the diffusion coefficent of species j in the mixture, d_{p_i} is the particle diameter, a_j is the activity of species j in the solution, σ is the surface tension, $\overline{V}_j$ is the partial molar volume of species j, Kn_{ji} is the Knudsen number, and

λ_j is the mean free path of species j. The polydispersity factor α_{ji} is somewhat less than one, but will be taken as equal to one in these simulations. This assumes the aerosol to be monodisperse and will tend to somewhat overpredict the condensation rate, thus underpredicting the total number of particles formed. The significance of α is discussed in more detail in the Appendix.

The rate of formation of particles will be described by the binary nucleation rate expression of Mirabel and Katz[11], as modified by Stauffer [12],

$$R_{J_{BIN}} = C_J \exp(-\Delta G^*/kT), \tag{10}$$

$$\Delta G^* = \frac{4}{3}\pi\sigma r^{*2}, \tag{11}$$

$$C_J = \frac{\beta_1\beta_2}{\beta_1 \sin^2\phi + \beta_2 \cos^2\phi} \frac{(S_1 p_1^o + S_2 p_2^o)}{kT} 4\pi r^{*2} Z, \tag{12}$$

where β_i is the impingement rate of species i onto the cluster of radius r^*, ϕ is the angle between the unrotated coordinates and the rotated coordinates through the saddle point, and Z is the binary Zeldovitch factor. These expressions are directly analogous to those for the single-component case. The quantities Z and ϕ are determined from the second derivatives of the free energy:

$$\tan\phi = s + \left(s^2 + \frac{\beta_1}{\beta_2}\right)^{1/2}, \tag{13}$$

$$s = \frac{1}{2} \frac{\left(\frac{\partial^2 \Delta G}{\partial n_1^2} - \frac{\beta_1}{\beta_2}\frac{\partial^2 \Delta G}{\partial n_2^2}\right)}{\frac{\partial^2 \Delta G}{\partial n_1 \partial n_2}}, \tag{14}$$

$$Z = \frac{-1\left(\frac{\partial^2 \Delta G}{\partial n_1^2}\cos^2\phi + \frac{\partial^2 \Delta G}{\partial n_2^2}\sin^2\phi + 2\frac{\partial^2 \Delta G}{\partial n_1 \partial n_2}\cos\phi\sin\phi\right)}{\left[\left(\frac{\partial^2 \Delta G}{\partial n_1 \partial n_2}\right)^2 - \frac{\partial^2 \Delta G}{\partial n_1^2}\frac{\partial^2 \Delta G}{\partial n_2^2}\right]^{1/2}}. \tag{15}$$

It was assumed for this study that DBP and DOP form ideal solutions[13], which is expected to be a reasonable estimate for two similar organic compounds. Therefore, the partial molar volumes are equal to the molar volumes of the pure components. It was also assumed that the vapor pressure of the solution obeys Raoult's law over the complete composition range, so that the activity of each

component in solution is equal to its mole fraction. Due to lack of solution data, a simple linear relation was assumed for the mixture surface tension:

$$\sigma = x_{DBP}\sigma_{DBP} + x_{DOP}\sigma_{DOP}.$$

The assumption that DBP and DOP form ideal solutions can be invoked to simplify the equations used to determine the properties of the critical cluster. For ideal binary solutions ($j = 1, 2$), the composition of the critical embryo can be determined by

$$\ln\frac{S_2}{x_2} = \ln\frac{S_1}{x_1}\frac{\left(V_2 + \frac{3}{2}\frac{V}{\sigma}x_1\frac{d\sigma}{dx_2}\right)}{\left(V_1 - \frac{3}{2}\frac{V}{\sigma}x_2\frac{d\sigma}{dx_2}\right)}, \tag{16}$$

which defines the critical size to be

$$r^* = \frac{2\sigma V_1 - 3x_2 V\frac{d\sigma}{dx_2}}{RT\ln(S_1/x_1)}. \tag{17}$$

Recent work[14] has suggested that the surface tension derivatives should not be included in Eqs. (16) and (17). The effect of this revision was checked by repeating some of the simulations presented in this work with the surface tension derivatives set equal to zero. The resulting number concentrations were lower than those obtained using Eqs. (16) and (17) by less than a factor of three.

One difficulty with the binary nucleation rate expression, which was pointed out by Wilemski[15], is the failure to approach the classical single-component rate as the supersaturation of either component approaches zero. This behavior is attributed to the divergence of the non-equilibrium (Zeldovitch) term as the curvature of the free energy surface, in the denominator, becomes undefined. Our approach to this problem follows the suggestion of Mirabel and Clavelin[16]. First, Eqs. (16) and (17) were used to determine the number of molecules of each species in the critical cluster. If one of these was found to be less than one, it was assumed that single-component nucleation, not binary, would occur. The homomolecular nucleation rate was taken to be the classical Becker-Döring-Zeldovitch rate:

$$R_j = S_j^2\left(\frac{p_j^o}{kT}\right)^2 2v_j\left(\frac{\sigma_j}{2\pi m_j}\right)^{1/2}\exp\left(\frac{-16\pi\sigma_j^3 v_j^2}{3k^3T^3\ln^2 S_j}\right). \tag{18}$$

Insight into the theoretical behavior of binary nucleating systems can be gained by considering a simplified ideal mixture of two species A ($j = 1$) and B ($j = 2$) that will be considered to have the same physical properties, including vapor pressure. Therefore, the composition and size of the critical cluster are given by

$$x_1 = \frac{S_1}{S_1 + S_2} \tag{19}$$

$$r^* = \frac{2\sigma V}{RT \ln(S_1/x_1)}. \tag{20}$$

Nonidealities of solution behavior affect the free energy of formation of the embryo. The effect of varying the formation free energy from that of an ideal system,

$$\Delta G = kT\left(x_1 \ln x_1 + x_2 \ln x_2\right) \tag{21}$$

is shown in Figure 6 for the hypothetical A-B system. The single-component nucleation rates are also shown for comparison. It is immediately seen from Figure 6 that the ideal binary system behaves as though a single component were present: the nucleation rate is constant and equal to the rate expected for a saturation ratio equal to the sum of the individual ratios, $S_1 + S_2$. Therefore, considering binary nucleation of two similar species leads to a larger predicted rate than would be expected for either species alone. Also, if the two species form a (favorably) nonideal solution, even larger rates are predicted by binary nucleation theory. The shape of the curves will be somewhat different for A and B having different physical properties (as is the case with DBP-DOP).

For modeling the DBP-DOP single-component and mixed-vapor experiments, a number of inputs are required. First, the initial saturations in the mixing chamber, S_{j_o}, are evaluated at the adiabatic mixing temperature calculated for the experimental conditions. This temperature is assumed constant throughout the nucleation and growth processes, neglecting the effects of latent heats, heats of mixing, and possible radial variations in the flow tube.

No seed particles were introduced into the mixed vapor stream, and therefore we need consider only one mode containing the nucleated particles. We

can therefore omit the subscript i. In order to compute the mean diameter required for evaluation of Eq. (8), it is assumed that the mass of each component per particle can be estimated by M_j/N. These masses, with the density of the solution, are used to obtain the diameter.

The rate of generation of new particles is given by Eq. (10) in the mixed-vapor cases, and by Eq. (18) when only one vapor is present; the appropriate source term is denoted by R_J in the equations that follow. The condensation rate for each component is given by Equation (8). The remaining variables in the integral model are the saturation ratios of each condensable species. The total particle number concentration N varies due only to nucleation; the total particle mass concentration M_j, $j = 1, 2$, varies from both nucleation and condensation; and the saturation ratios S_j, $j = 1, 2$, of each species decreases as gas-to-particle conversion takes place. The integral model expresses these changes by:

$$\frac{dN}{dt} = R_J E_J \tag{22}$$

$$\frac{dM_j}{dt} = MW_j \left(g_j^* \frac{dN}{dt} + R_{C_j} \right) \tag{23}$$

$$S_j(t) = S_{j_o} - M_j(t) \frac{RT}{MW_j p_j^o} \tag{24}$$

$j = 1$ for DBP

$j = 2$ for DOP.

Measured nucleation rates frequently do not agree with those predicted by classical nucleation theory; thus we introduce a factor to be experimentally determined that brings the two into agreement. That factor, E_J, can be termed an enhancement factor. It has been found that the integral model, using classical theory modified by such a factor, can predict the trends in the data quite well[5,17]. In general, the enhancement factor is different for different condensing species; a key contribution of this work is the determination of the best-fit enhancement factors for DBP, DOP, and the mixed vapor cases.

IV. Comparison of Measured and Predicted Nucleation Rates

The experimental data shown in Figure 5 are repeated in Figure 7, where the closed symbols again represent the number concentrations of particles observed experimentally. The corresponding open symbols of the same shape are the model predictions for the experimental temperatures and saturation ratios. Also indicated in Figure 7 are the enhancement factors used in Eq. (22) for the binary, DBP, and DOP nucleation simulations. The value of $E_{DBP} = 10^7$ used here agrees well with values of the DBP enhancement factor previously observed for conditions of temperature and saturation ratios similar to those used in this study[5]. The model predictions shown in Figure 7 agree well with the trends in the experimentally observed total number of particles, and can predict closely the total number as well with the appropriate enhancement factor.

A summary of the saturation ratios in all the mixed-vapor cases studied is shown in Figure 8. Each of these points has a corresponding single-component DBP point and a single-component DOP point that was used for comparison of homomolecular nucleation rates. Many of the measured number concentrations are shown in Figures 9 through 11.

The experimental procedure used to obtain the data shown in Figure 9 was similar to that described previously, but in this case the DOP saturator was maintained at 120°C. as the DBP saturator temperature was varied, resulting in somewhat lower values of saturation ratio than those in Figure 7. Again, the predicted number concentrations agree within an order of magnitude with those observed, for values of the enhancement factors $E_{BIN} = 10^3$, $E_{DBP} = 10^7$, and $E_{DOP} = 10^5$.

Figures 10 and 11 show data obtained for constant temperatures in the DBP saturators of 124 and 130°C., respectively, and stepwise variation of the DOP saturator temperature. The variation of the DOP saturator temperature results in a stronger dependence upon S_{DOP}, and therefore the data are plotted against this abscissa. Similar enhancement factors were used for the binary

and DOP simulations, but a slightly smaller enhancement factor ($E_{DBP} = 10^6$) than was found for the experiments shown in Figures 7 and 9 was required to accurately represent the DBP nucleation data. As in all the studies, the total number concentration of particles measured in the binary vapor system exceeds those expected via homomolecular nucleation alone, except in the case of very small or very large saturation ratio of DOP. For small S_{DOP}, nucleation of DBP alone dominates, and the mixed vapor number concentrations tend towards those found for DBP only. However, in Figures 10 and 11 it appears that the binary experimental data do not tend towards those for single-component DOP as the saturation ratio of DOP becomes large, although the binary simulations do approach the DOP-only case; the reason for this behavior of the model will be explained in the discussion of the enhancement factor which follows. The reasons for the apparently anomalous behavior of the experimental data may be explained in part by the difficulty of showing a three-dimensional function on a two-dimensional plot. That is, it is not evident from this representation what the saturation ratio of DBP is for the mixed vapor case at high S_{DOP}. If the DBP concentration is still high enough to significantly impact the nucleation rate, the mixed vapor data will not approach the single-component DOP data. In fact, the detection limit of the particle counter is 10^7 cm^{-3}, so that the number concentration at which the binary and single-component DOP curves converge may not be experimentally observable.

The inadequacies of the two-dimensional representation can be clarified by consideration of Figures 12 and 13, in which the data of Figures 10 and 11, respectively, have been replotted. In Figure 12a, the DBP-only and mixed vapor results of Figure 10 are shown as functions of S_{DBP}, and in Figure 12b, the DOP-only and mixed vapor results are shown as functions of S_{DOP}; similar comments apply to Figures 13a and 13b. It is now clear, from Figure 12a, why the binary data do not tend toward the DOP-only data: the minimum saturation ratio of DBP is about 150, evidently still high enough to affect the

binary particle formation. (From Figures 7 and 9, one sees that DBP is undersaturated with respect to single-component particle formation only below about $S_{DBP} = 100$, so one might expect its effect on the binary rate to be significant even below $S_{DBP} = 100$, depending upon the vapor concentration of DOP; if the concentration of DOP overwhelms that of DBP, single-component nucleation of DOP may dominate kinetically.) These arguments also apply to Figures 13a and 13b.

The use of an enhancement factor to reconcile theoretically predicted and experimentally observed nucleation rates is at present simply a convenient means for representing such deviations. The enhancement factor found for the mixed-vapor cases, $E_{BIN} = 10^3$, is significantly lower than those found to represent the homomolecular nucleation of either organic. A possible explanation for this observation lies in the assumptions made for the physical properties of the binary solution. The ideal mixture assumption for the molar volume of the solution is probably adequate, and, in any case, the nucleation rate does not depend very strongly on density. The equilibrium calculations will be affected by the values assumed for the activity of each species over the solution; Raoult's Law may not be valid over the full composition range. Probably the most important assumption, however, and the one most likely to be in error, is the surface tension assumed for the liquid mixture. The free energy of the critical cluster, and hence the calculated nucleation rate, is very sensitive to this parameter: a two percent reduction in surface tension can produce an order of magnitude increase in the nucleation rate. The surface tension also affects the magnitude of the Kelvin term, and hence will modify the condensation rate onto existing particles. Since nucleation and condensation are competing processes, errors in σ will also impact the total number of particles that are predicted to be produced.

One of the consequences of using a binary enhancement factor that is much smaller than those used for the single-component species in the model is that the model predictions in the binary case, as the saturation ratio of one component

becomes small, will no longer go smoothly to the single-component limit; this can be seen by lowering the $\Delta G = \Delta G^{id}$ curve in Figure 6 by three orders of magnitude in R_J, and considering its points of intersection with curves A and B. Similar behavior is found for the model results; in Figure 7, for example, binary nucleation predictions at low S_{DBP} fall below those of single-component DBP, whereas the binary experiments go smoothly to the single-component experiments in this limit. It is somewhat difficult to obtain the "best-fit" binary enhancement factor, since the mixed-vapor results depend upon two variables. For example, the same binary model and experimental results are shown in Figures 12a and 12b, but the model appears to fit the data better when shown as a function of S_{DBP} than when plotted against S_{DOP}. A single, non-adjustable factor E_{BIN} may be inadequate to describe the behavior over the entire experimental range.

V. Conclusions

The particle size magnifier, which has previously been used to study homomolecular nucleation, has been extended to investigate binary nucleation phenomena. This work concerns the binary nucleation of two organic vapors, dibuytlphthalate and dioctylphthalate, for a wide range of saturation ratios. The nucleation behavior of mixed-vapor systems was compared with that observed in the presence of either organic alone. The number of particles formed in the binary case is larger than would be expected via homomolecular nucleation, confirming the interaction between the two organic species during particle formation. In the mixed-vapor case, however, as the saturation ratio of one species became very large or very small, the numbers of particles produced tended towards those observed in the single-vapor cases.

Observed aerosol number concentrations were compared with the predictions of an integral model that allows for competition between nucleation and growth processes in gas-to-particle conversion, and that uses as particle source rates the predictions of classical homomolecular nucleation theory and binary nucleation theory, modified by suitable experimentally-determined enhancement factors; a key contribution of this work is the measurement of the DBP, DOP, and binary DBP/DOP enhancement factors. When these enhancement factors are employed, the total numbers of particles as well as the trends in number concentration with saturation ratio that are predicted compare favorably to those observed experimentally.

Acknowledgement

This work was supported by National Science Foundation Grant ATM-8503103.

Appendix: The parameter α

In this appendix we demonstrate the origin of the condensation equation for a binary aerosol, Eqs. (7) and (8), by considering first the appropriate distribution function for a multicomponent aerosol. We show that the correct equation is analogous to that written for homomolecular condensation. We next discuss the origin of the factor α as a correction for the diameter used in the integral model, and show how to calculate α for the special case of a lognormal aerosol for which the Kelvin effect is negligible.

The aerosol size-composition probability density function is defined[18]

$$dN = N_\infty \, g(m_1, m_2, \ldots, m_k) \, dm_1 \, dm_2 \ldots dm_k, \tag{25}$$

where N_∞ is the total number of particles and m_i are the moles of species i in a particle. A size distribution function $\tilde{n}(m_1)$ can be obtained by integrating over all but one of the species:

$$\tilde{n}(m_1) = N_\infty \int_{m_2} \ldots \int_{m_k} g(m_1, m_2, \ldots, m_k) \, dm_2 \ldots dm_k \tag{26}$$

In the single component case, the total moles in the aerosol phase are

$$\begin{aligned} M &= \int_{d_p} m(d_p) n(d_p) \, dd_p \\ &= \frac{\rho\pi}{6} \int_{d_p} d_p^3 \, n(d_p) \, dd_p \\ &= \frac{\rho\pi}{6} N_\infty \, \overline{d_p}_m^3, \end{aligned} \tag{27}$$

where $\overline{d_p}_m$ is the mass (or mole) mean diameter. The mass mean diameter is defined as the diameter of a particle having the mean mass of the distribution. This is exactly the definition used to determine $\overline{d_p}$ of Eq. (8).

In the case of a binary aerosol, the total moles of each component must be computed. Considering first species 1,

$$\begin{aligned} M_1 &= \int_{m_1} m_1 \tilde{n}(m_1) \, dm_1 \\ &= N_\infty \int_{m_1} \int_{m_2} m_1 \, g(m_1, m_2) \, dm_1 \, dm_2 \\ &= N_\infty \, \overline{m}_1, \end{aligned} \tag{28}$$

where M_1 are the total moles of species 1 in the aerosol and $\overline{m}_1$ is the average moles of species 1 per particle.

To determine the change in the total aerosol moles with time for a single-component aerosol,

$$\frac{dM}{dt} = \int_{d_p} \frac{dm}{dt} n(d_p)\, dd_p, \tag{29}$$

whereas for the binary case, for species 1,

$$\begin{aligned} \frac{dM_1}{dt} &= N_\infty \int_{m_1} \int_{m_2} \frac{dm_1}{dt} g(m_1, m_2)\, dm_2\, dm_1 \\ &= \int_{m_1} \frac{dm_1}{dt} \tilde{n}(m_1)\, dm_1. \end{aligned} \tag{30}$$

From the properties of size distributions it can be shown that

$$n(d_p)\, dd_p = \tilde{n}(m_1)\, dm_1, \tag{31}$$

so that Eq. (30) is equivalent to

$$\frac{dM_1}{dt} = \int_{d_p} \frac{dm_1}{dt} n(d_p)\, dd_p. \tag{32}$$

Similar arguments can be used for the change in M_2 with time. Eq. (32) is identical to Eq. (29) for the single component case, except that in Eq. (32) the rate of change of mass per particle refers to the condensation rate of species 1 only.

Since the binary and single-component cases are similar, for simplicity we will discuss the factor α referring to the single-component case only. In the discussion that follows the assumption will be made that the Kelvin effect, $\exp\left(4\sigma V/d_p RT\right)$, which is the factor by which the vapor pressure over a droplet is enhanced due to the curvature of the surface, is approximately equal to one. For large particles (continuum regime), this assumption is usually a good one, but it can be in error for small particle sizes or large values of σ. We will consider the two limiting cases of growth in the continuum and kinetic regimes.

Continuum Regime. The condensation rate onto a single particle is given by

$$\frac{dm}{dt} = \frac{2\pi D p^o}{RT} d_p (S-1). \tag{33}$$

Note that in the binary case, for component 1, we can write

$$\frac{dm_1}{dt} = \frac{2\pi D_1 p_1^o}{RT} d_p a_1 \left(\frac{S_1}{a_1} - 1\right). \tag{34}$$

Summing over all diameters of the distribution, the total rate of change of moles is

$$\begin{aligned} \frac{dM}{dt} &= \frac{2\pi D p^o}{RT}(S-1)\int_{d_p} d_p n(d_p)\, dd_p \\ &= \frac{2\pi D p^o}{RT}(S-1) N \overline{d_{p_n}}, \end{aligned} \tag{35}$$

where $\overline{d_{p_n}}$ is the number mean diameter of the distribution. Using the definition of α given in Eqs. (7) and (8),

$$\frac{dM}{dt} = \frac{2\pi D p^o}{RT}(S-1)\alpha N \overline{d_{p_m}}. \tag{36}$$

Comparison of Eqs. (35) and (36) shows that α is given by

$$\alpha_c = \overline{d_{p_n}} \;/\; \overline{d_{p_m}}. \tag{37}$$

Kinetic Regime. The condensation rate onto a single particle is given by

$$\frac{dm}{dt} = \frac{\bar{c}\pi p^o}{RT} d_p^2 (S-1), \tag{38}$$

with the total rate onto all particles

$$\begin{aligned} \frac{dM}{dt} &= \frac{\bar{c}\pi p^o}{RT}(S-1)\int_{d_p} d_p^2 n(d_p)\, dd_p \\ &= \frac{\bar{c}\pi p^o}{RT}(S-1) N \overline{d_{p_s}}, \end{aligned} \tag{39}$$

where $\overline{d_{p_s}}$ is the surface area mean diameter of the distribution. By comparison with the expression used in the integral model, it can be shown that in this case

$$\alpha_k = \left(\overline{d_{p_s}} \;/\; \overline{d_{p_m}}\right)^2. \tag{40}$$

Magnitude of α. Equations (37) and (40) can be written

$$\alpha_c = \frac{\int_0^\infty d_p n(d_p) dd_p}{\left[\int_0^\infty d_p^3 n(d_p) dd_p\right]^{1/3}} \tag{41}$$

$$\alpha_k^{1/2} = \frac{\left[\int_0^\infty d_p^2 n(d_p) dd_p\right]^{1/2}}{\left[\int_0^\infty d_p^3 n(d_p) dd_p\right]^{1/3}}. \tag{42}$$

For simplicity in the following analysis, let $x = d_p$ and consider a normalized distribution function $n(x)$, so that

$$\int_0^\infty n(x)\, dx = 1. \tag{43}$$

We will make use of Hölder's inequality, where $1/p + 1/q = 1$:

$$\int_a^b \left|f(x)g(x)\right| dx \;\le\; \left(\int_a^b \left|f(x)\right|^p dx\right)^{1/p} \left(\int_a^b \left|g(x)\right|^q dx\right)^{1/q}. \tag{44}$$

In applying Eq. (44), the absolute value signs will be omitted, since the distribution functions we consider are always positive.

Using Hölder's inequality with $f(x) = xn(x)^{1/3}$, $g(x) = n(x)^{2/3}$, $p = 3$, and $q = 3/2$,

$$\int_0^\infty xn(x)\, dx \;\le\; \left(\int_0^\infty x^3 n(x)\, dx\right)^{1/3} \left(\int_0^\infty n(x)\, dx\right)^{2/3}. \tag{45}$$

The last term in Eq. (45) is equal to unity [Eq. (43)]. Thus we obtain the relation

$$\alpha_c = \frac{\int_0^\infty xn(x) dx}{\left(\int_0^\infty x^3 n(x)\, dx\right)^{1/3}} \;\le\; 1. \tag{46}$$

Similarly, applying Eq. (44) with $f(x) = x^2 n(x)^{2/3}$, $g(x) = n(x)^{1/3}$, $p = 3/2$, and $q = 3$,

$$\int_0^\infty x^2 n(x)\, dx \;\le\; \left(\int_0^\infty x^3 n(x)\, dx\right)^{2/3} \left(\int_0^\infty n(x) dx\right)^{1/3}, \tag{47}$$

from which one obtains

$$\alpha_k^{1/2} = \frac{\left(\int_0^\infty x^2 n(x)\,dx\right)^{1/2}}{\left(\int_0^\infty x^3 n(x)\,dx\right)^{1/3}} \leq 1. \tag{48}$$

The factor α is less than one, or equal to one in the case of a monodisperse aerosol, for any continuous distribution function, and the assumption of monodispersity therefore maximizes the condensation rate.

In the special case of a lognormal aerosol, α can be written in terms of the variance of the distribution, σ_g:

$$\alpha_c = \alpha_k = \exp\left(-\ln^2 \sigma_g\right). \tag{49}$$

It is seen that $\alpha = 1$ is true only in the case of a monodisperse aerosol, for which the variance is equal to unity. For a lognormal aerosol with $\sigma_g = 1.3$, $\alpha = 0.93$. Thus the assumption of monodispersity results in a condensation rate about seven percent too large.

References

[1] H. Reiss, *J. Chem Phys.* **18(6)**, 840 (1950).

[2] H. Reiss, D.I. Margolese, and F.J. Schelling, *J. Coll. Int. Sci.* **56(3)**, 511 (1976).

[3] P. Mirabel and J.L. Clavelin, *J. Chem. Phys.* **68(11)**, 5020 (1978).

[4] W. Studzinski, G.H. Spiegel, and R.A. Zahoransky, *J. Chem. Phys.* **84(7)**, 4008 (1986).

[5] K. Okuyama, Y. Kousaka, D.R. Warren, R.C. Flagan, and J.H. Seinfeld, *Aer. Sci. Tech.* **6(1)**, 15 (1987).

[6] D.R. Warren, K. Okuyama, Y. Kousaka, J.H. Seinfeld, and R.C. Flagan, *J. Coll. Int. Sci.* **116(2)**, 563 (1987).

[7] D.R. Warren and J.H. Seinfeld, *Aer. Sci. Tech.* **3**, 135 (1984).

[8] D.R. Warren and J.H. Seinfeld, *J. Coll. Int. Sci.* **105(1)**, 136 (1985).

[9] S.M. Kreidenweis and J.H. Seinfeld, *Atm. Env.*, **22(2)**, 283 (1988).

[10] B. Dahneke, in *Theory of Dispersed Multiphase Flow* (Academic Press, New York, 1983).

[11] P. Mirabel and J.L. Katz, *J. Chem. Phys.* **60(3)**, 1138 (1974).

[12] D. Stauffer, *J. Aer. Sci.* **7**, 319 (1976).

[13] P. Ravindran and E.J. Davis, *J. Coll. Int. Sci.* **85(1)**, 278 (1982).

[14] G. Wilemski, *J. Chem. Phys.* **80(3)**, 1370 (1984).

[15] G. Wilemski, *J. Chem. Phys.* **62(9)**, 3763 (1975).

[16] P. Mirabel and J.L. Clavelin, *J. Aer. Sci.* **9**, 219 (1978).

[17] R. Strey, P.E. Wagner, and T. Schmeling, *J. Chem. Phys.* **84(4)**, 2325 (1986).

[18] S.K. Friedlander, *Smoke, Dust and Haze* (Wiley and Sons, New York, 1977).

Table 1

Property Data for DBP and DOP

	DBP	DOP
molecular weight	278.35	390.56
vapor pressure[a], torr	$\ln p = 16.27 - \frac{5099}{T+163.5}$	$\ln p = 29.31 - \frac{13408}{T+273.15}$
density[a], g cm^{-3}	$1.063 - 0.00083\ T$	0.98
surface tension[a], dynes cm^{-1}	$35.3 - 0.0863\ T$	$32.2 - 0.0737\ (T - 25)$

[a] T in °C.

Table 2

EXPERIMENTAL CONDITIONS AND MEASURED NUMBER CONCENTRATIONS

$R_{h1} = R_{h2} = 0.1 \qquad T_{sh2} = 130°C$

T_{sh1}	T_l	T_m	S_{o1}	S_{o2}	N
100	21.0	39.8	30.8	1454.0	2.784×10^5
104	21.0	40.2	39.1	1376.3	2.292×10^5
108	21.8	41.3	45.6	1194.2	2.088×10^5
112	22.0	41.8	56.0	1106.4	1.186×10^5
116	20.8	41.3	78.0	1192.7	1.236×10^5
120	21.0	41.8	94.2	1104.6	3.018×10^5
124	20.4	41.8	122.2	1115.3	5.496×10^5
128	21.0	42.7	139.8	988.9	7.886×10^5
132	21.2	43.2	165.4	915.5	2.248×10^6
124	21.2	42.4	113.0	-	1.140×10^2
126	21.2	42.6	124.6	-	5.582×10^2
128	21.0	42.5	142.5	-	3.258×10^3
130	21.0	42.9	153.7	-	3.082×10^4
132	21.0	43.1	168.6	-	9.220×10^4
134	21.2	43.4	181.2	-	6.932×10^5
136	21.0	43.5	202.0	-	8.750×10^6
100	20.0	39.0	-	1622.8	1.140×10^2
108	20.0	39.8	-	1453.0	5.582×10^2
116	20.4	40.9	-	1245.7	3.258×10^3
120	20.8	41.7	-	1128.8	3.082×10^4
124	21.0	42.2	-	1045.3	9.220×10^4
128	21.4	43.0	-	947.4	6.932×10^5
132	21.6	43.5	-	877.1	8.750×10^6
136	21.8	44.1	-	811.9	8.750×10^6

Figure Captions

Figure 1. Schematic of experimental apparatus.

Figure 2. Schematic of saturator.

Figure 3. Schematic of mixing unit.

Figure 4. Initial saturation ratio, S_o, as a function of mixing ratio for two dilution temperatures.

Figure 5. Total number concentrations of particles for DBP only, DOP only, and mixed vapor cases, $T_{sh2} = 130°C$.

Figure 6. Single-component and binary nucleation rates in idealized $A - B$ system with various assumptions for free energy of mixing.

Figure 7. Predicted and measured total particle number concentrations, $T_{sh2} = 130°C$.

Figure 8. Summary of binary experiments performed.

Figure 9. Predicted and measured total particle number concentrations, $T_{sh2} = 120°C$.

Figure 10. Predicted and measured total particle number concentrations, $T_{sh1} = 124°C$.

Figure 11. Predicted and measured total particle number concentrations, $T_{sh1} = 130°C$.

Figure 12. Predicted and measured total particle number concentrations, $T_{sh1} = 124°C$.

Figure 13. Predicted and measured total particle number concentrations, $T_{sh1} = 130°C$.

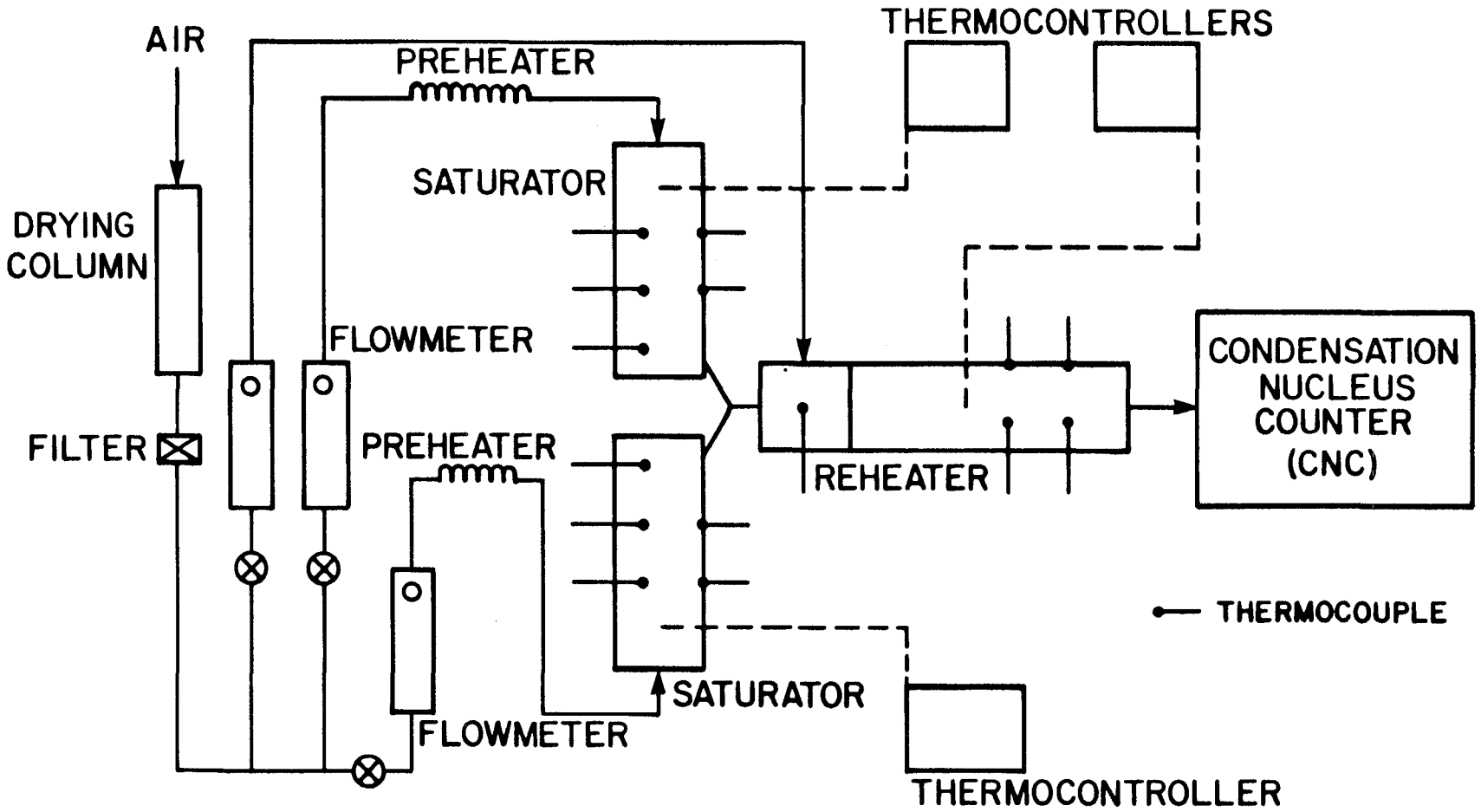

SCHEMATIC DIAGRAM OF THE EXPERIMENTAL APPARATUS

Figure 1

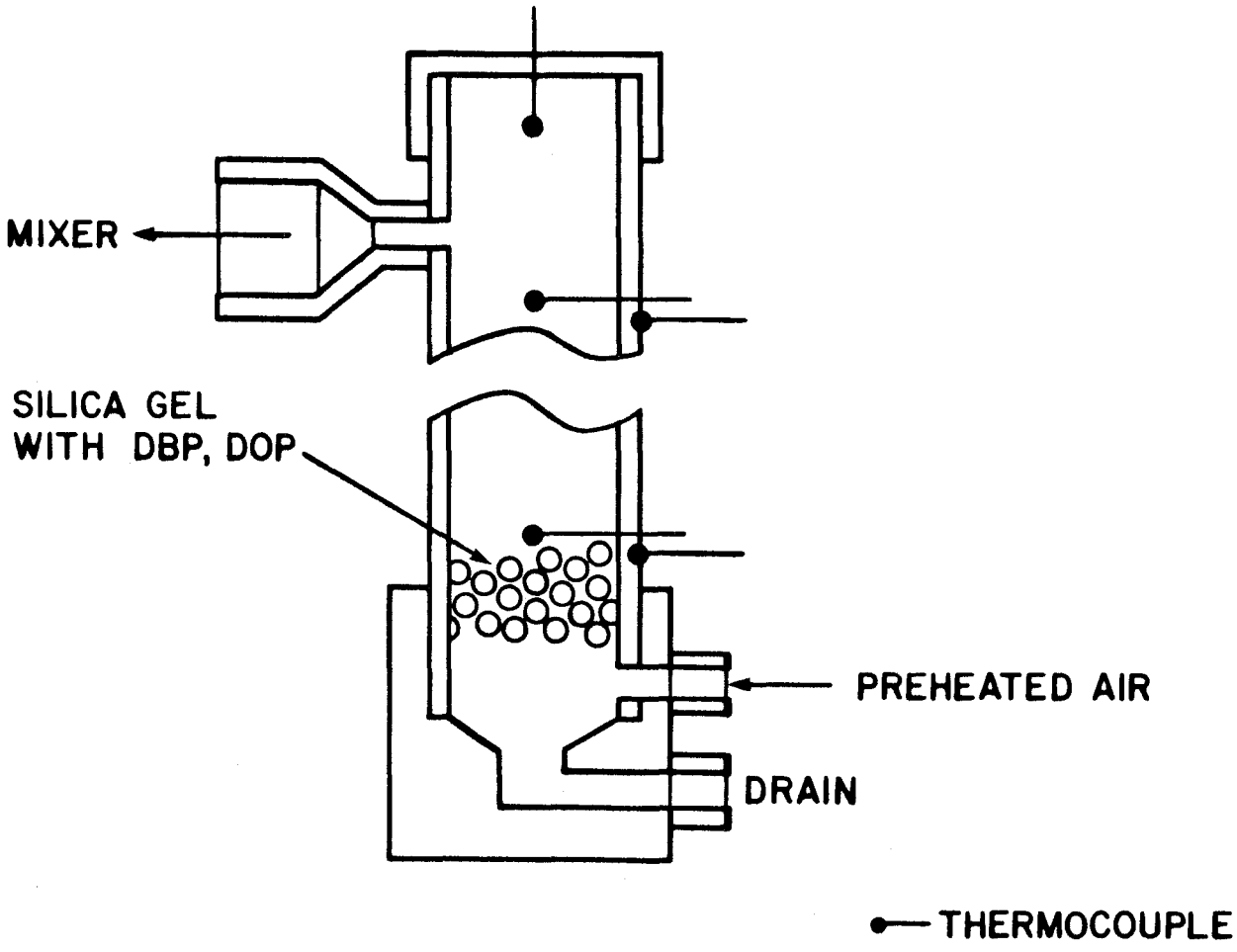
MIXER
SILICA GEL
WITH DBP, DOP
PREHEATED AIR
DRAIN
THERMOCOUPLE

Figure 2

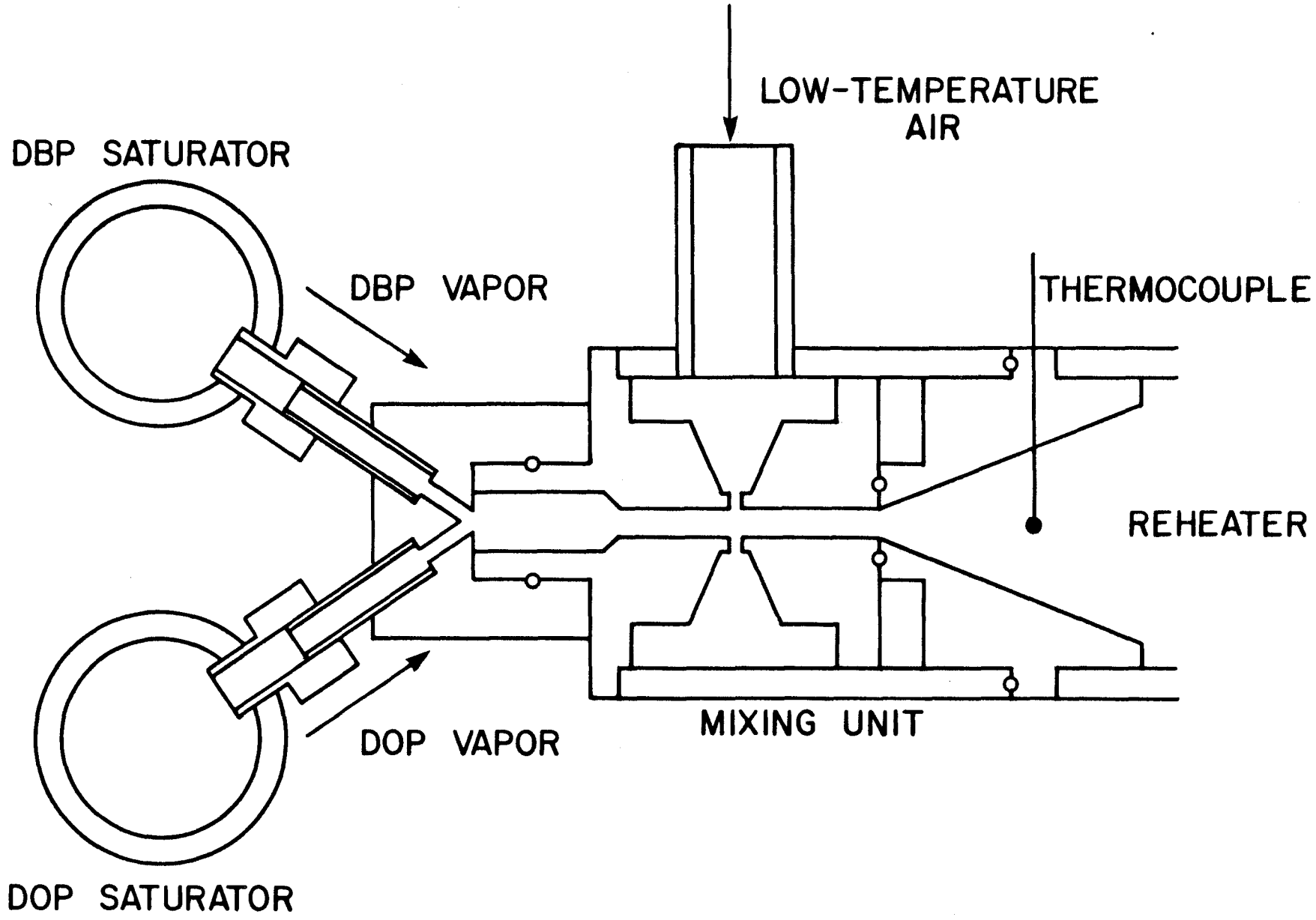
LOW-TEMPERATURE
AIR
DBP SATURATOR
DBP VAPOR
THERMOCOUPLE
REHEATER
MIXING UNIT
DOP VAPOR
DOP SATURATOR

Figure 3

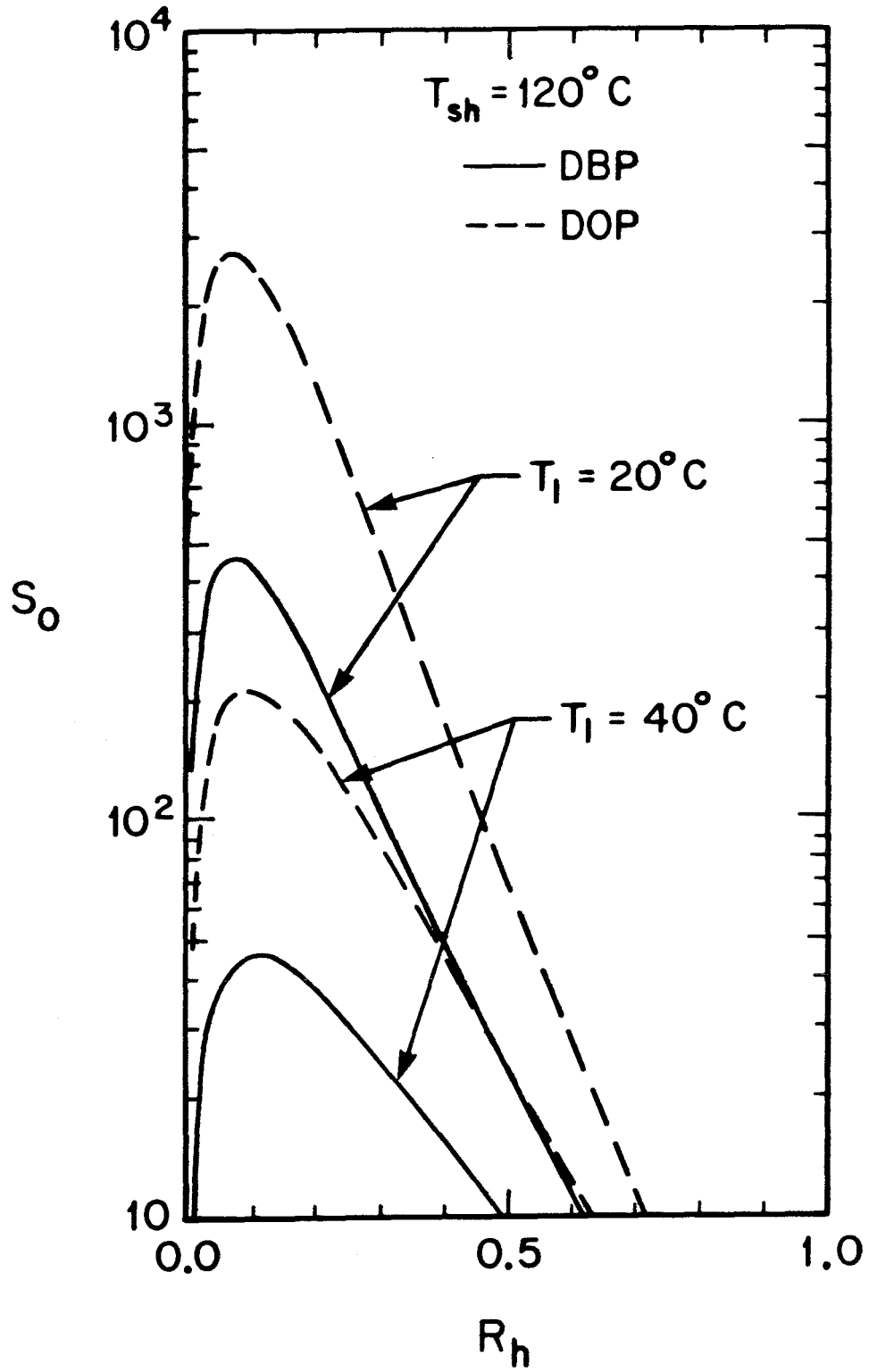

Figure 4

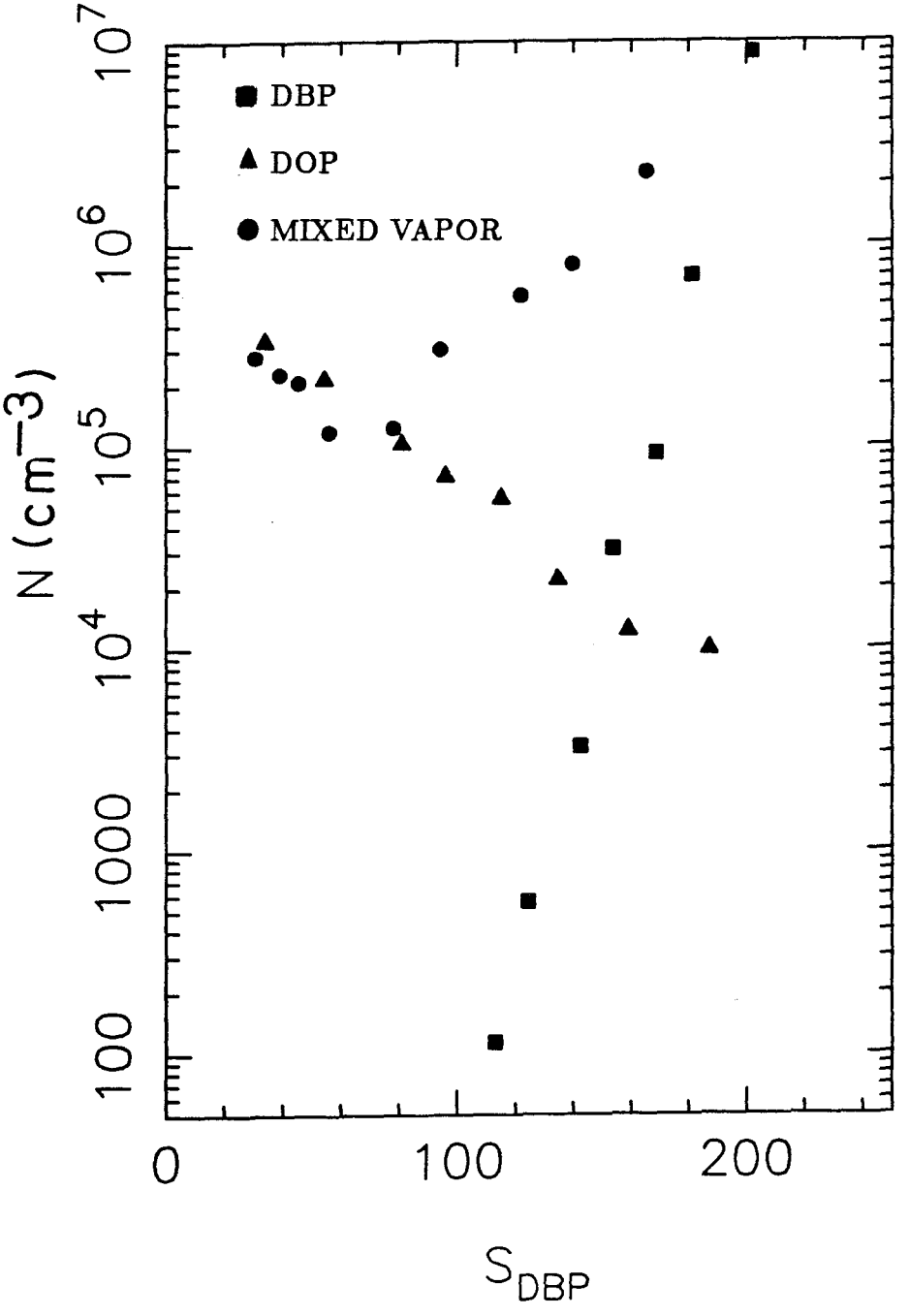
DBP
DOP
MIXED VAPOR
N (cm⁻³)
10⁷
10⁶
10⁵
10⁴
1000
100
0
100
200
S_DBP

Figure 5

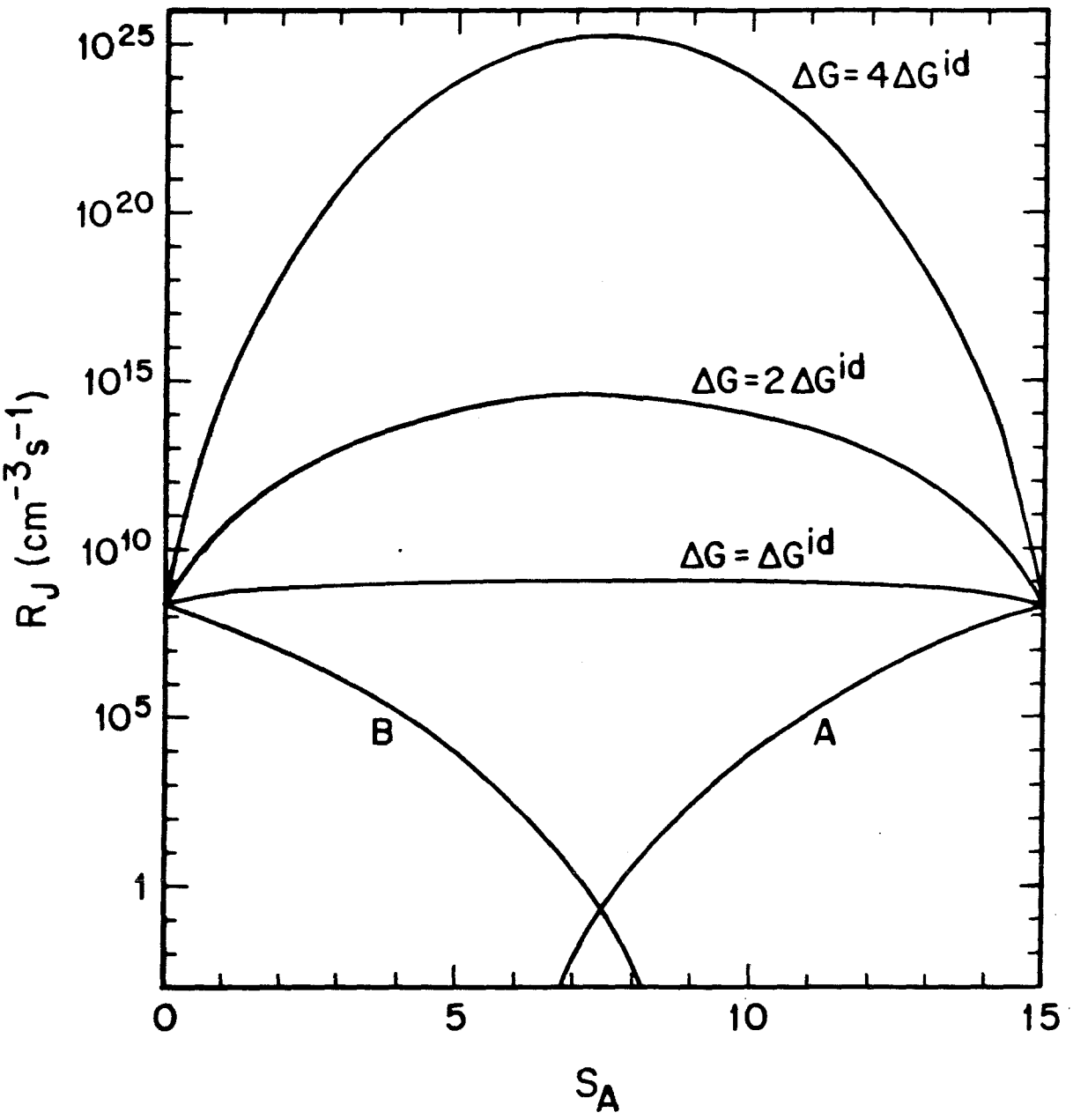
10^{25}
10^{20}
10^{15}
10^{10}
10^{5}
1
R_J ($cm^{-3}s^{-1}$)
$\Delta G = 4\Delta G^{id}$
$\Delta G = 2\Delta G^{id}$
$\Delta G = \Delta G^{id}$
B
A
0
5
10
15
S_A

Figure 6

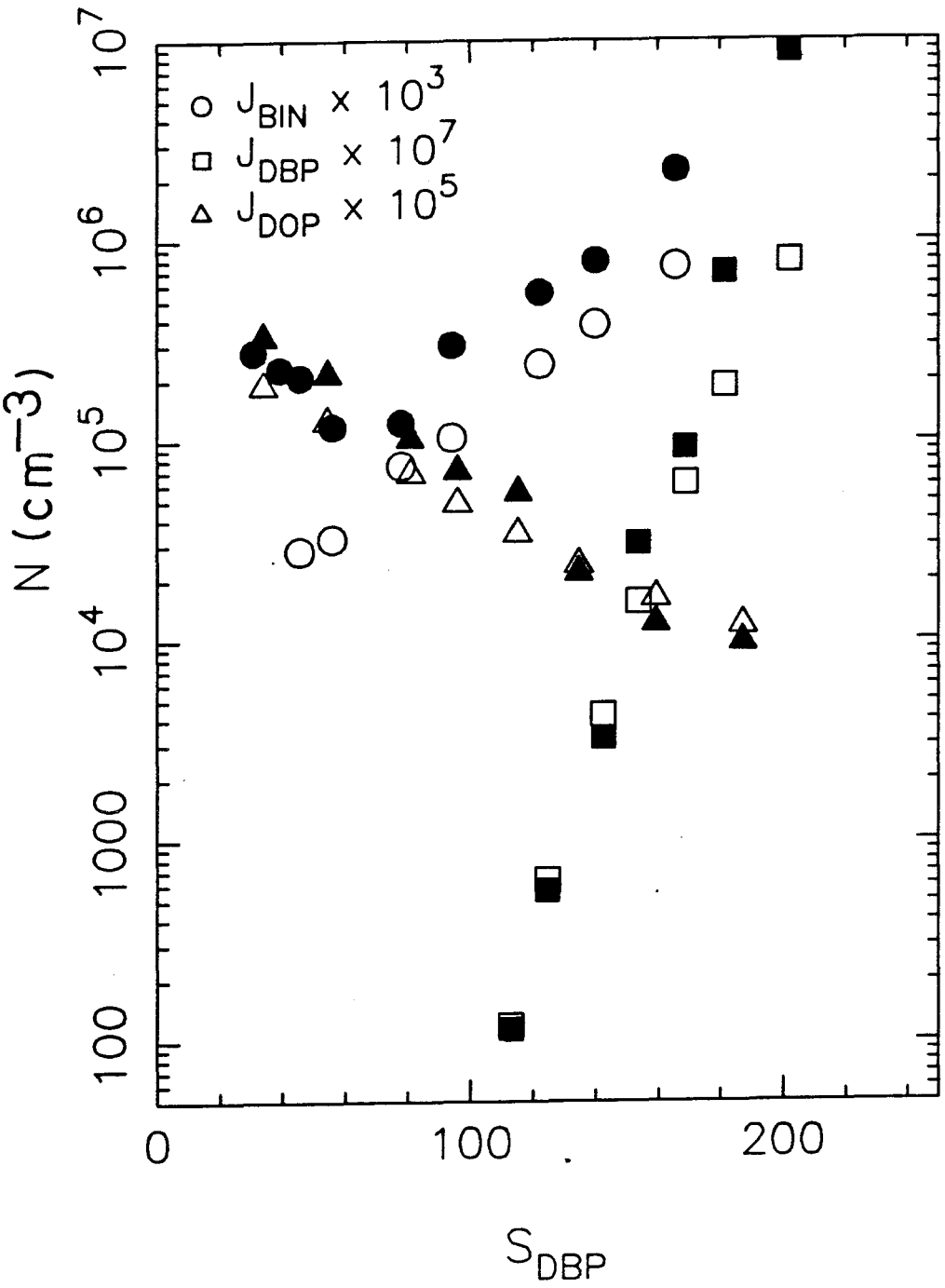
$J_{BIN} \times 10^3$
$J_{DBP} \times 10^7$
$J_{DOP} \times 10^5$
N (cm^{-3})
10^7
10^6
10^5
10^4
1000
100
0
100
200
S_{DBP}

Figure 7

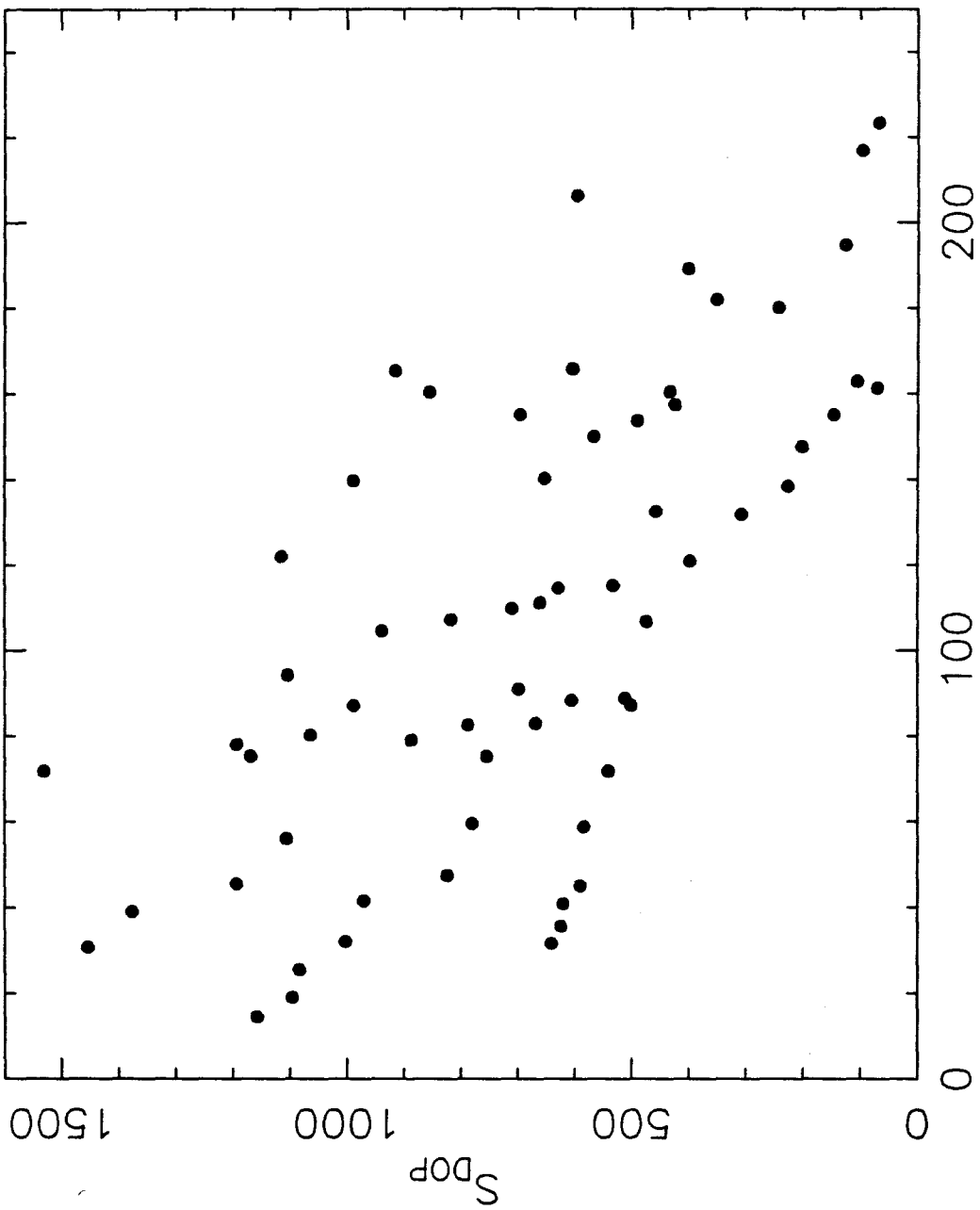

Figure 8

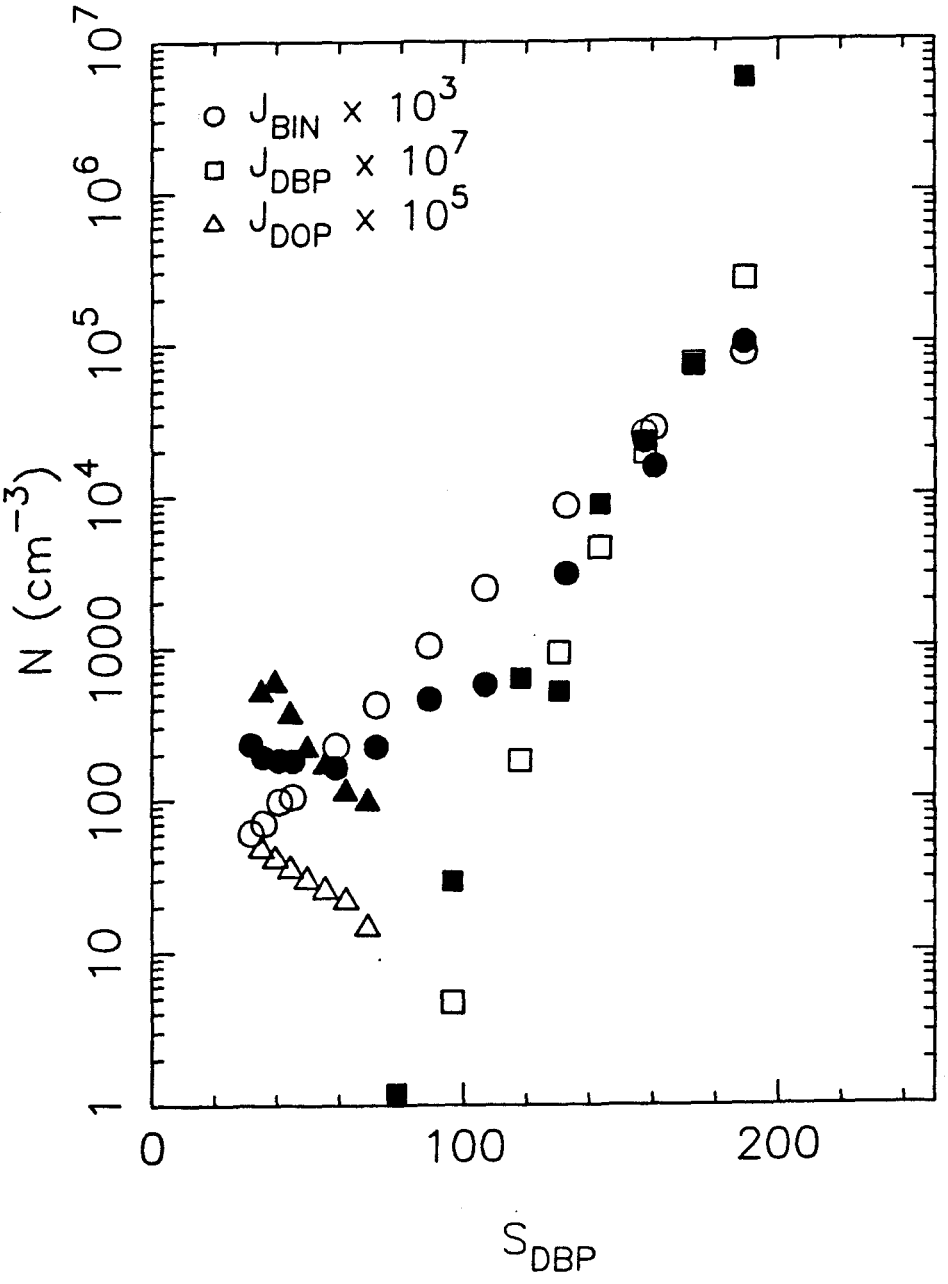
$J_{BIN} \times 10^3$
$J_{DBP} \times 10^7$
$J_{DOP} \times 10^5$
N (cm^{-3})
1
10
100
1000
10^4
10^5
10^6
10^7
0
100
200
S_{DBP}

Figure 9

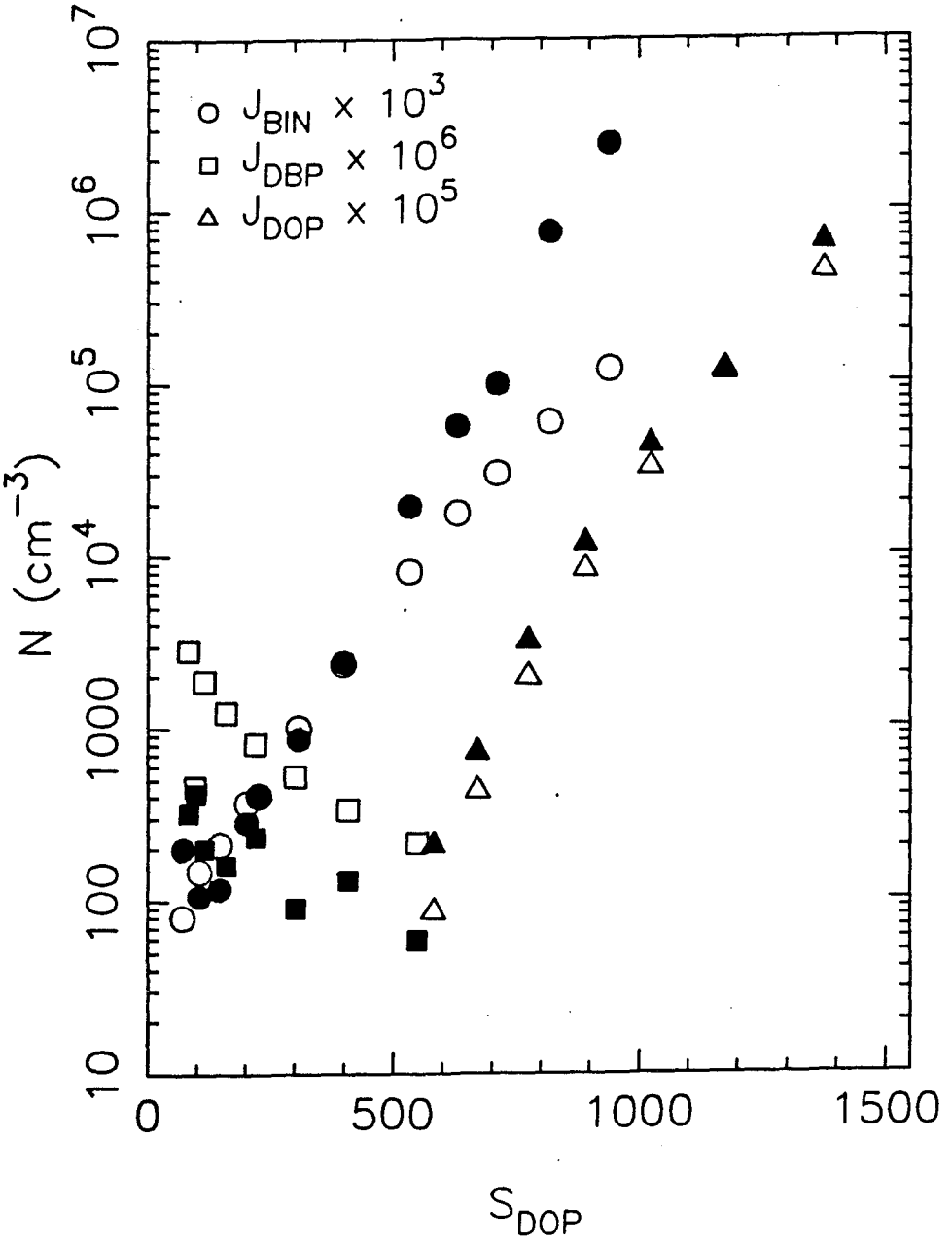
o J_{BIN} x 10^3
□ J_{DBP} x 10^6
△ J_{DOP} x 10^5
N (cm^{-3})
10
100
1000
10^4
10^5
10^6
10^7
0
500
1000
1500
S_{DOP}

Figure 10

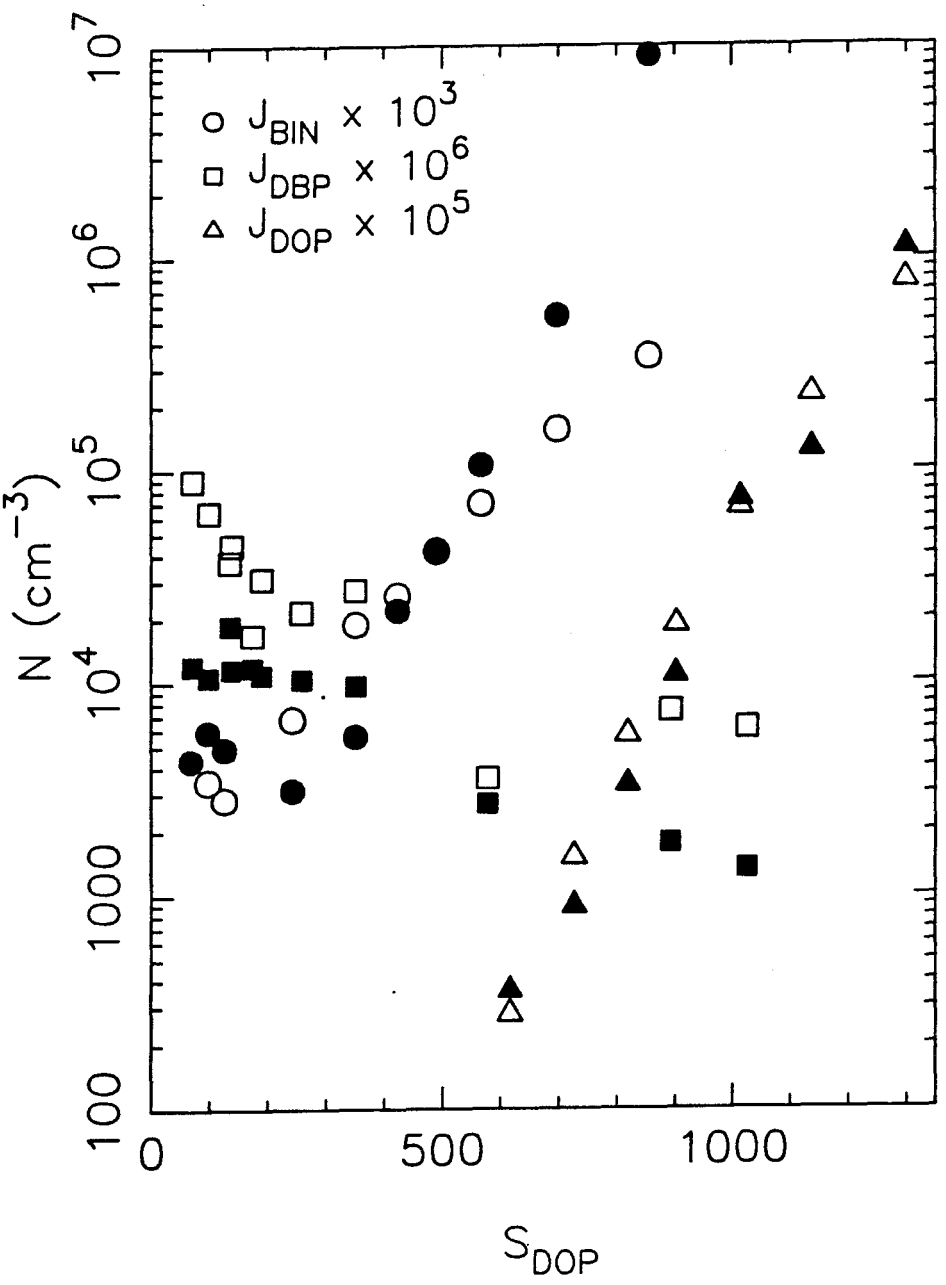
$J_{BIN} \times 10^3$
$J_{DBP} \times 10^6$
$J_{DOP} \times 10^5$
N (cm^{-3})
100
1000
10^4
10^5
10^6
10^7
0
500
1000
S_{DOP}

Figure 11

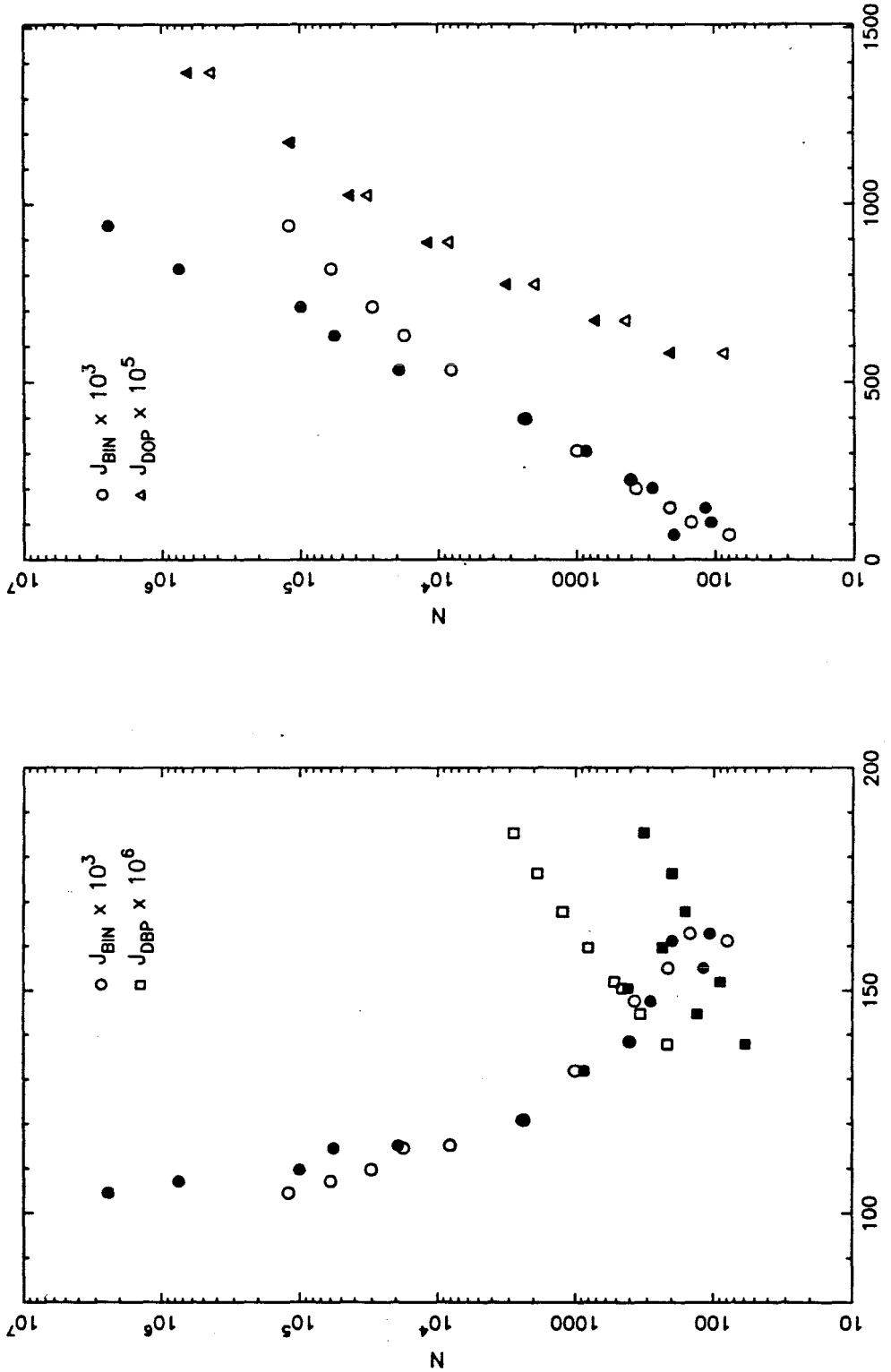

Figure 12

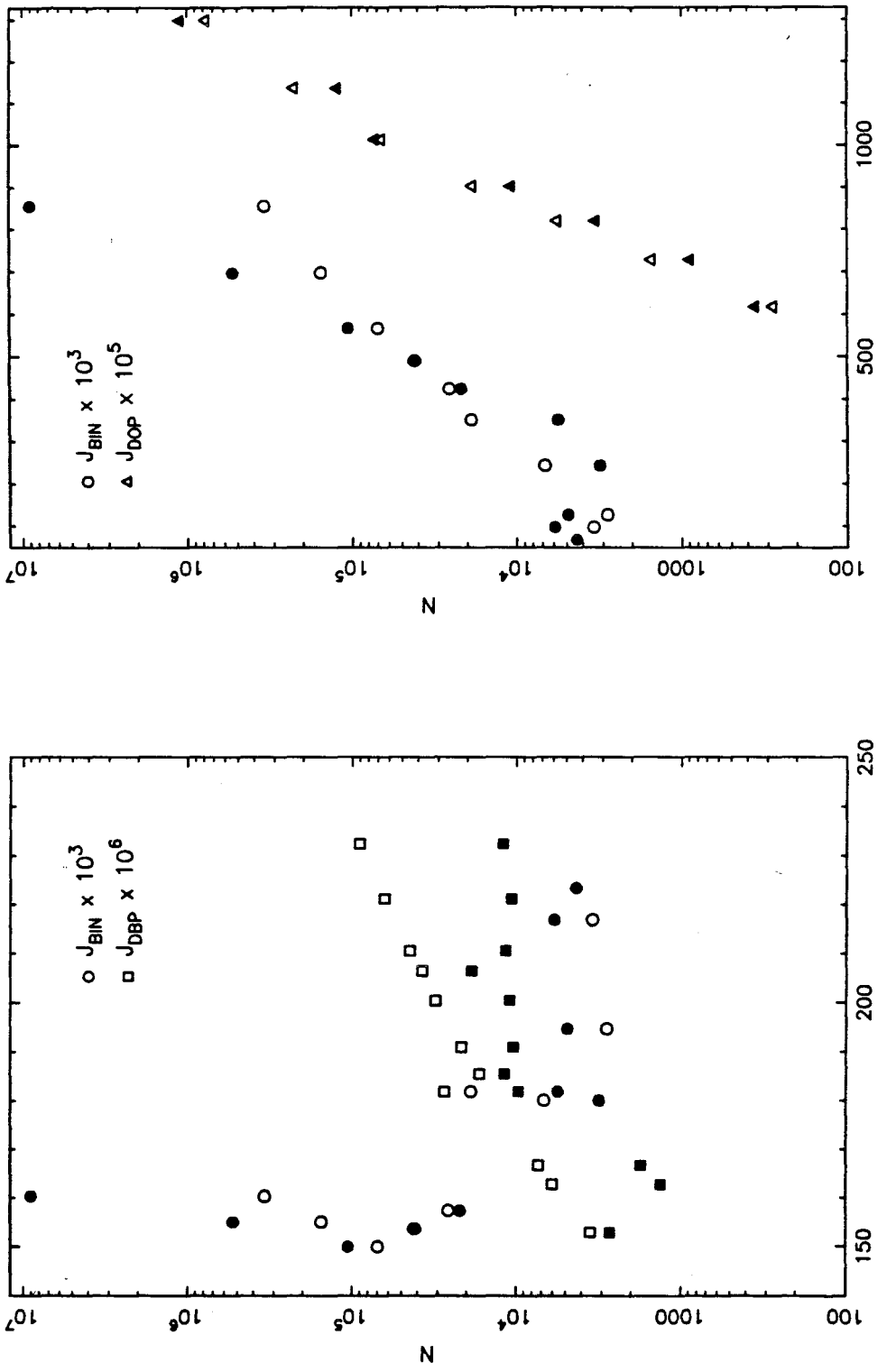
o J_{BIN} x 10^3
▵ J_{DOP} x 10^5
N
100
1000
10^4
10^5
10^6
10^7
500
1000
S_{DOP}
(b)
o J_{BIN} x 10^3
□ J_{DBP} x 10^6
N
100
1000
10^4
10^5
10^6
10^7
150
200
250
S_{DBP}
(a)

Figure 13

Chapter IV

Nucleation of Sulfuric Acid-Water and Methanesulfonic Acid-Water Particles: Implications for the Atmospheric Chemistry of Organosulfur Species

The text of Chapter IV consists of an article which appears in *Atmospheric Environment* **22** (1988)

Nucleation of Sulfuric Acid-Water and Methanesulfonic Acid-Water Solution Particles: Implications for the Atmospheric Chemistry of Organosulfur Species

Sonya M. Kreidenweis and John H. Seinfeld

Department of Chemical Engineering
California Institute of Technology
Pasadena, California 91125

Abstract

Binary nucleation theory is applied to the formation of aqueous sulfuric acid and aqueous methanesulfonic acid particles and the relative rates of aerosol formation in humid atmospheres are compared. An integral model is presented which allows for nucleation of solution particles, aerosol growth, and condensable vapor source and depletion rates. To extend this model, the water activities of the ternary solution, sulfuric acid-methanesulfonic acid-water, are estimated, and growth of the nucleated aerosol by incorporation of both types of acid is considered. Predictions of both forms of the model are compared with the experimental results of Hatakeyama et al. (1985) for the photooxidation of dimethylsulfide in humid air.

I. Introduction

Since the publication of Doyle's (1961) calculations applying Reiss' (1950) theory of binary nucleation to the sulfuric acid-water system, there has been considerable interest in homogeneous heteromolecular nucleation as a process for generating condensation nuclei in the atmosphere. The sulfuric acid-water system has been the focus of such research for two reasons. First, it is known that sulfuric acid is generated in the oxidation of SO_2, exists in the atmosphere in trace amounts, has an extremely low vapor pressure, and has been detected in atmospheric particles (as sulfates). Second, Doyle's and subsequent calculations (for example, Mirabel and Katz, 1974) demonstrated that, due to the highly non-ideal nature of sulfuric acid solutions, large numbers of submicroscopic particles could be generated in ppb concentrations of the acid at relative humidities as low as 10%. As a result, the sulfuric acid-water system has frequently been the focus of investigations of the aerosol-forming properties of atmospheric sulfur systems.

An important aspect of the atmospheric sulfur cycle is the fate of organosulfur compounds. Reduced-sulfur compounds emanating from biogenic sources are of particular importance in the global sulfur budget. In particular, dimethyl sulfide (DMS) is the most abundant and its emission into the atmosphere from oceanic sources is estimated to be about 30 TgS y^{-1} (Andreae and Raemdonck, 1983). Moreover, condensation nuclei resulting from DMS oxidation have been suggested as possibly contributing to cloud formation over the oceans.

The evidence for the importance of DMS in atmospheric chemistry has led to a number of studies of the chemistry of DMS under atmospheric-type conditions (Hatakeyama et al., 1982; Grosjean and Lewis, 1982; Hatakeyama et al., 1985) which attempt to elucidate reaction pathways and to identify the yields of SO_2 and other major sulfur-containing oxidized products. Hatakeyama et al. (1982, 1985) identified the major product of the oxidation of DMS to be methanesulfonic acid (MSA), with a yield of greater than 50 percent, rather than SO_2 (ultimately

H_2SO_4), as was previously expected. In addition, both these investigators and Panter and Penzhorn (1980) detected MSA in the aerosol phase. Hatakeyama et al. observed the formation of aerosol in both dry and humid smog-chamber photooxidation of DMS and postulated that binary nucleation of MSA-water solution droplets was responsible for the particulate formation in humid air, whereas self and/or co-condensation of MSA and H_2SO_4 was proposed to have produced the aerosol observed in the dry runs. Understanding the aerosol-forming potential of the DMS system is a key link in understanding the oxidation of atmospheric organosulfur systems. Since both MSA and H_2SO_4 are observed in the aerosol phase, models that predict, for example, whether this aerosol is an internal mixture (one type of particle containing both acid species) or external mixture (two types of particles, each containing only one of the acid species) will support some vapor production mechanisms over others.

There have been a number of attempts to experimentally verify the the binary nucleation rates predicted by binary nucleation rate theories for the sulfuric acid-water system. Experiments have been carried out in batch or continuous systems, in which the H_2SO_4 is generated by a chemical reaction such as the oxidation of SO_2 in the presence of water vapor, or in diffusion or expansion chambers. Cox (1973) observed aerosol formation during the photoylsis of ppm concentrations of SO_2 at relative humidities less than one percent and studied the effects of varying SO_2 and water vapor contents. Boulaud et al. (1977) mixed controlled amounts of SO_3 and water vapor in a batch system and measured particle number as a function of time for semiquantitative comparison with theoretical nucleation rates. Mirabel and Clavelin (1978) observed binary nucleation of H_2SO_4-H_2O at relative humidities greater than 100% in a diffusion cloud chamber and found good agreement with the hydrate theory of Shugard *et al.* (1974) in predicting the minimum acid partial pressure required for observable nucleation rates. A summary of experiments performed in expansion chambers and a discussion of the difficulties associated with studying the sulfu-

ric acid-water system were presented by Schelling and Reiss (1981). An overall conclusion that can be drawn from these and the numerous other experimental results published is that, while it may be readily demonstrated that H_2SO_4, even in trace amounts, is a good nucleating agent in the presence of water vapor, the relationship of nucleation rates to gas-phase concentrations is extremely difficult to verify; thus, it is difficult to test theoretical predictions of the number concentrations produced. Nevertheless, the theory has been used in atmospheric modeling (Middleton and Kiang, 1978; Hamill et al., 1982; and others), noting these uncertainties; the qualitative conclusions that can be drawn are valuable in comparing particle formation mechanisms under varied atmospheric conditions.

The object of this work is to apply binary nucleation theory to the MSA-water system and compare calculated particle formation rates with those predicted for H_2SO_4-H_2O. A model is developed to predict total numbers of particles produced at constant relative humidity for given vapor source rates of the acidic species, accounting for mass balances and droplet growth. Based on these results, some observations can be made regarding the mechanisms operating in the organosulfur system.

II. Prediction of binary nucleation rates

The development of an expression for the binary nucleation rate is analogous to that for classical, single-component nucleation. In the binary case, however, the embryo free energy is minimized with respect to both cluster size and composition. This minimum represents a saddle point in the free energy surface; the rate of passage of the critical clusters through this saddle point determines the binary nucleation rate. The expressions used here for calculating the rates of binary nucleation are those given by Stauffer (1976) and Mirabel and Katz (1974). While it is also possible to compute the rates predicted by the hydrate theory of Shugard et al. (1974), the simpler nonhydrated theory is sufficient for comparison between the two acids and does not deviate substantially from the hydrated theory at low RH. The procedure for calculating the nucleation rates is as follows. First, an equilibrium calculation is carried out to satisfy the constraints that the partial molar free energy of each component (acid and water) over the solution droplet equals the partial molar free energy of the vapor phase. This determines (uniquely) the composition and size of the critical cluster. These values are then used in the expressions for the total change in free energy, frequency factor, and "Zeldovich factor" that make up the total nucleation rate. The equations used are summarized in Appendix A.

Prediction of binary nucleation rates requires detailed solution property data at the temperatures of interest over the entire range of compositions, including the partial pressures of water and acid vapor over the solution. Many data exist for aqueous sulfuric acid solutions, although the vapor pressure of the pure acid has still not been determined absolutely. As pointed out by Hamill et al. (1982), the present uncertainty in the vapor pressure of pure H_2SO_4 would account for an uncertainty of perhaps two orders of magnitude in the predicted rates of nucleation. A summary of values used in this study and the sources of the property data are given in Appendix B.

In contrast to H_2SO_4, relatively few property data exist for methanesulfonic acid (MSA). It is known to dissolve readily in water, and its dissociation constant in aqueous solution (K_a), estimated at 73 mol ℓ^{-1} by Clarke and Woodward (1966), shows it to be a stronger acid than nitric acid. The partial pressure of MSA over concentrated aqueous solutions at 25°C. was measured by Clegg and Brimblecombe (1985) and used to estimate the Henry's Law constant. Solution density data at a few temperatures were taken by Bascombe and Bell (1959) and Teng and Lenzi (1975), and the surface tension of the pure acid was measured by Berthoud (1929). Gregor et al. (1963) and Covington et al. (1973) measured osmotic and activity coefficients at 25°C. up to 40 molal. We have used these data to estimate the physical properties of aqueous MSA over the full concentration range, as discussed in Appendix B, which were used to predict nucleation rates and critical cluster properties. Figures 1 and 2 compare the property values used for MSA with those used for H_2SO_4.

Figure 3 summarizes the nucleation rates for the sulfuric acid-water and methanesulfonic acid-water systems at various relative humidities in terms of the relative acidities of each acid. The definition of the relative acidity is similar to that of the relative humidity: it is defined as the partial pressure of acid vapor in the gas phase divided by the vapor pressure of the pure acid at that temperature, p_a/p_a^o. It is seen that homogeneous homomolecular (i.e., single-component) nucleation of the two acids proceeds at very similar conditions of relative acidity (the RH here is zero). This similarity is due to the similar physical properties for the pure phases, most importantly the surface tension. As the relative humidity is increased, the deviation in nucleation rates calculated for the two acids becomes more pronounced. A comparison of the free energies of mixing for the two solutions and for a hypothetical ideal solution (Figure 4) illustrates why this is so. The larger the free energy of mixing, the lower is the barrier to formation of the liquid phase.

The contrast between the behavior of the two binary systems is shown even

more clearly on the upper scales of Figure 3, where the relative acidities have been converted to partial pressures of acid vapor. The much lower vapor pressure of H_2SO_4 compared with that of MSA translates a given relative acidity into a lower partial pressure.

III. Modeling of aerosol production in dynamic systems

The production of aerosol particles in the organosulfur system we are considering in this work involves a series of steps. The process is initiated by the production of condensable species via gas-phase chemical reactions. These condensable species may then either nucleate (homomolecular or binary nucleation) to form new particles, condense onto preexisting particles, or remain as gaseous species if the gas phase is thermodynamically favored. The simplest model incorporating vapor-phase source and depletion rates and allowing for competition between nucleation and condensation processes is an integral model, for example, the model used by Warren et al. (1984, 1985). This model describes the aerosol by its moments (total number N and total aerosol mass M) and describes the vapor phase as homogeneous, with a vapor supersaturation S. The condensation rate is approximated by a continuum expression modified for noncontinuum effects by the expression due to Dahneke (1985), and incorporating a factor α that accounts for polydispersity and is defined by

$$\begin{aligned} R_c &= 2\pi D_{ij} p^o \int_{D_p^*}^{\infty} f(D_p) D_p \Big[S - \exp\Big(\frac{4\sigma V}{D_p RT} \Big) \Big] f(Kn)\, dD_p \\ &= \alpha \Big\{ 2\pi D_{ij}\, p^o\, \overline{D_p} \Big[S - \exp\Big(\frac{4\sigma V}{\overline{D_p} RT} \Big) \Big] f(\overline{Kn}) \Big\} N, \end{aligned} \tag{1}$$

where α is somewhat less than one. Here, the mean particle diameter is obtained from the mean mass per particle, M/N.

In this work, the factor α will be taken as one, which corresponds to a monodisperse aerosol (of diameter $\overline{D_p}$). As discussed by Warren and Seinfeld (1985), it can be shown that, for given fixed total mass and total number, a monodisperse aerosol has the maximum total surface area, as well as the maximum number mean diameter of any possible aerosol distribution. Since the condensation rate is proportional to $\overline{D_p}$ to $\overline{D_p}^2$, depending on the magnitude of $\overline{Kn}$, the monodisperse model will systematically overpredict the condensation rate and thus underpredict the total number formed, as these two processes are in competition.

For the binary systems considered here, the integral model is formulated as follows. The vapor phase is described by the relative acidity RA and the gas-phase source rate of acid vapor, R_g. It is assumed that the relative humidity remains constant; this can be shown to be a good assumption, even at high rates of nucleation, because of the large partial pressure of water (on the order of 10^4 ppm) as compared with either acid. The particle source term is given by binary nucleation rate theory, at a given temperature and RH, for RA as a function of time. The aerosol can be characterized by the mass of acid in the aerosol phase M_a , with the mass of water in the aerosol determined by assuming equilibration with the ambient relative humidity. The mean particle size is determined by finding the mean acid mass per drop (M_a/N) and performing an equilibrium calculation so that the partial pressure of water over the drop equals the water vapor pressure in the surrounding gas. The composition so determined, with the mass of acid per drop, determines droplet size and properties to be used in the condensation equation. Because the relative amount of water vapor is so much greater than that of acid vapor, it is assumed that growth is determined by the impingement rate of acid molecules onto the droplet as the rate-determining step. The droplet then re-equilibrates with the ambient RH after each addition of acid. Aspects of this treatment are similar to the approaches used by Hamill (1975) and Takahashi et al. (1977) to describe H_2SO_4-H_2O systems. The model then takes the form

$$\begin{aligned} \frac{dRA}{dt} &= \left(R_g - N_{AV} g^* R_{J_b} - R_c\right) RT \,/\, p_a^o \\ \frac{dM_a}{dt} &= M w_a (g^* R_{J_b} + R_c) \\ \frac{dN}{dt} &= R_{J_b}, \end{aligned} \tag{2}$$

with

$$\begin{aligned} R_c = \;& \alpha \Big\{ 2\pi D_{ij}\, p_a^o\, \overline{D_p} \Big[S - a_a \exp\Big(\frac{4\sigma \overline{V_a}}{\overline{D_p} RT} \Big) \Big] f(\overline{Kn}) \Big\} N \\ f(\overline{Kn}) = \;& \left(1 + \overline{Kn}\right) / \left(1 + 2\,\overline{Kn}\left(1 + \overline{Kn}\right)\right), \end{aligned} \tag{3}$$

where

R_g = source rate of condensable (acid) vapor

R_c = condensation rate of (acid) vapor onto existing particles

J_b = rate of binary nucleation

g^* = number of acid molecules in a nucleating cluster, $g^* > g^{crit}$

$\overline{Kn}$ = Knudsen number of particle with mean diameter, $\frac{2\lambda_a}{\overline{D_p}}$

a_a = acid activity in solution.

IV. Discussion of model input parameters and results

In order to implement the model, source rates of acid vapor are needed. These may be obtained from measurement of product concentrations, or from a kinetic mechanism of the gas-phase chemistry (Yin et al., 1986). For this study we will use simplified vapor production rates corresponding to the conditions used in the runs of Hatakeyama et al. (1985) (hereafter referred to as Hatakeyama) and summarized in Table 1. Briefly, runs were carried out at 30°C. at either 36% relative humidity or in very dry air, for two initial DMS concentrations: 1.3 ppm amd 0.012 ppm. The product concentrations were not measured in these runs, and some important rate constant data are as yet unknown. Therefore, the following procedure was used to estimate acid vapor source rates.

First, we note that Hatakeyama estimates the final yield of SO_2 to be approximately 29%, and that of MSA to be greater than 50% (we will use 60%). For an initial dimethyl sulfide concentration of 1.3 ppm, this ultimately gives 0.377 ppm SO_2 and 0.78 ppm MSA. Furthermore, an unknown percentage of the SO_2 is converted to H_2SO_4; we will show results assuming both 1% and 10%. Similar arguments are used for an initial DMS concentration of 0.012 ppm. Based upon Figure 1 of Hatakeyama, the original DMS is consumed over 3.5 hours, so the production of the total amounts of product vapors is assumed to occur at constant rates over 3.5 hours. The source rates so derived are given in Table 2. Since, for a given relative humidity, all other variables (such as temperature) remain the same for different conversion rates, and for different initial DMS concentrations, the cases considered here provide a comparison of the effect of varying acid source rates.

Figure 5 shows the nucleation rates of both acids at 30°C. at relative humidities of 36% and 0% as functions of acid partial pressure. The nucleation rates were calculated using saturation vapor pressures and property data described in the Appendix B. The results will differ substantially with changes in these data, particularly surface tension and p_i^o. Therefore, those conclusions drawn

from this study must be considered in light of the data used. Two observations concerning the experimental results can be made immediately. First, for those runs for which the initial concentration of DMS is 1.3 ppm, for a final yield of MSA of $> 50\%$ and a final yield of H_2SO_4 of 29% (if all the SO_2 were converted) the final partial pressures of each acid, assuming consumption of all of the original DMS, are sufficient to obtain measurable nucleation rates. However, for an initial concentration of DMS of 0.012 ppm, insufficient MSA vapor is produced for any appreciable nucleation of MSA to occur, but binary nucleation of sulfuric acid and water is predicted. In dry air, the total acid produced from an initial concentration of 1.3 ppm of DMS, as estimated by the assumed total conversions described above, represents saturation ratios of less than one for both MSA and H_2SO_4, and classical nucleation theory does not predict aerosol formation in a single-component system unless the vapor is supersaturated. Thus, according to the model presented here, no aerosol is expected to be detected in the "dry-air" run conditions of Hatakeyama, unless there are preexisting condensation nuclei in the system, other condensable vapors are produced, and/or the relative humidity is greater than zero. With respect to this last point, water vapor is postulated to be formed as part of the reaction sequence. In his experiments Cox (1973) observed nucleation at 30°C. at 1% relative humidity (corresponding to several hundred ppm water) for irradiation of initial SO_2 concentrations as low as 5 ppm. Perhaps the role of product water in the production of aerosols in the organosulfur system should be experimentally examined to determine its importance.

Figures 7 through 10 present the aerosol properties – total number, mean diameter, and gas-phase concentration of acids – which were obtained using the input source rates described in Table 2. These results assume no interaction between the two acids; that is, we consider, for given acid source rates, nucleation of only MSA or H_2SO_4 solution droplets. Only H_2SO_4 and H_2O condense on an aqueous H_2SO_4 droplet, and only MSA and H_2O condense on an aqueous

MSA droplet. Thus, if both types of droplet were produced in an experimental run according to this mechanism, the result would be an externally mixed MSA-H_2SO_4-H_2O aerosol. No calculations were performed for the dry runs of Hatakeyama, as single-component nucleation is not predicted for these conditions by the present model. Figures 7 and 8 compare total number produced and mean diameter for the same SO_2 source rate, but for 1% and 10% conversion of SO_2 to H_2SO_4, respectively. As expected, the higher H_2SO_4 source rate results in a higher number concentration of smaller particles. The results for a much slower source rate, for $[DMS]_o = 0.012$ ppm but with other parameters the same as the $[DMS]_o = 1.3$ ppm run, as shown in Figure 9, indicate a delay of approximately 1 hour in particle formation, as compared with the immediate nucleation observed in Figures 7 and 8, several orders of magnitude fewer particles, and a mean droplet diameter approximately twice that of the other runs. As expected, the source rate has a large impact on the model results.

Figures 7 and 8 compare favorably with the aerosol measurements of Hatakeyama, who detected particles almost immediately after irradiation began and observed particle formation continuing over a period of about 10 minutes. Their experimental results are reproduced in Figure 11. The final number counts were on the order of 10^5, and mean diameters ranged from 0.01 to 0.2 μm. However, these investigators also observed number counts on the order of 10^4, with nucleation occurring over the first 10 minutes of irradiation, for an initial DMS concentration of only 0.012 ppm (corresponding to our Figure 9), whereas our simplified source rate gave quite different results. In view of the importance of the vapor source rate to the final number counts and the simplified approach taken here to estimate what this source rate may be, this discrepancy re-emphasizes the need for accurate chemical mechanisms and the possibility of using the interaction between chemistry and aerosol processes to gain a greater understanding of the total system.

Finally, Figure 10 presents the predictions for $[DMS]_o$=1.3 ppm at a rela-

tive humidity of 36%, assuming methanesulfonic acid and water constitute the aerosol phase. Although the source rate of MSA expressed as ppm per second is many times that of H_2SO_4, the formation of particles is delayed because of two effects. First, the vapor pressure of MSA is higher than that of H_2SO_4, so that it takes longer to achieve a partial pressure high enough for nucleation to occur. Second, the MSA-water system is not as strongly interacting as the H_2SO_4-water system, so that a higher relative acidity is required for appreciable nucleation. The mean droplet diameter for the MSA aerosol is much larger than that for sulfuric acid; this is due partially to the slow nucleation rate, so that condensation on the few droplets formed initially dominates over formation of new droplets, and partially to a higher growth rate because of the larger partial pressure of MSA in the ambient gas, since the growth is controlled by collision of acid molecules with the droplet.

V. Droplet growth by ternary condensation

Acid-acid interactions have been neglected in the above examples. Clegg and Brimblecombe (1985) found that MSA is extremely soluble not only in water, but also in acidic solutions. Thus, a sulfuric acid aerosol that has formed by gas-to-particle conversion may grow not only by addition of sulfuric acid and water but also by dissolution of MSA in the droplet, resulting in an internally mixed aerosol. If enough MSA is produced so that an equilibrium can be established between the droplet solution and the gas phase, this may explain the observations of Hatakeyama, who detected the presence of MSA in both phases. In order to determine the gas-liquid partitioning, estimates of the ternary properties for MSA-H_2SO_4-H_2O systems must be made.

Since the assumption is made that the solution droplet is in equilibrium with the ambient relative humidity, the most important property of the ternary solution for our purposes is the water activity as a function of the droplet composition. The water activity was estimated using the mixing rules of Kusik and Meissner (1978) from correlations for the MSA-H_2O activity coefficient and using the HSO_4^--H_2O and SO_4^{2-}-H_2O activity coefficients of Stelson et al. (1984). The partial pressures of the acids over the solution are obtained from the equilibria

$$\begin{aligned} K_1 &= \frac{p_{H_2SO_4}}{\gamma_{12}^2 m_1 m_2} \\ K_2 &= \frac{p_{MSA}}{\gamma_{16}^2 m_1 m_6} \\ K_1(298\text{K}) &= 3.28 \times 10^{-18} \\ K_2(298\text{K}) &= 1.5 \times 10^{-14}, \end{aligned} \tag{4}$$

where the subscript 1 refers to H^+ ion, the subscript 2 to HSO_4^-, 4 to SO_4^{2-}, and 6 to $CH_3SO_3^-$. The activity coefficients are those "mixed" according to the Kusik-Meissner rules, evaluated at the total ionic strength of the solution. Figure 12 shows the variation of the solution water activity with molality of each acid at 25°C., as data were available at this temperature only.

When the two acids can interact it is necessary to expand the integral model

to account for the interaction (see Table 3). We define two modes in the aerosol phase: the first produced by H_2SO_4 nucleation, the second by MSA nucleation. The droplets in either mode then grow by impingement of both H_2SO_4 and MSA molecules. For a given number of H_2SO_4 and MSA molecules in a drop, a ternary solution equilibrium calculation can be performed so that the vapor pressure of water over the drop, including the Kelvin effect, is equal to the relative humidity:

$$RH = a_{w_{ternary}} \exp\left(\frac{4\sigma_{ternary} V_{w_{ternary}}}{\overline{D_p} RT}\right). \tag{5}$$

From the composition so determined, we can also find the activities of the acids in solution, which are used in the condensation equations. Due to lack of information, the ternary solution densities and surface tensions were computed by simply proportioning them by the mole fractions:

$$\begin{aligned} \rho_{ternary} &= x_{H_2O}\,\rho^o_{H_2O} + x_{MSA}\,\rho^o_{MSA} + x_{H_2SO_4}\,\rho^o_{H_2SO_4} \\ \sigma_{ternary} &= x_{H_2O}\,\sigma^o_{H_2O} + x_{MSA}\,\sigma^o_{MSA} + x_{H_2SO_4}\,\sigma^o_{H_2SO_4}, \end{aligned} \tag{6}$$

where the superscript ^{o} refers to the pure property. Errors in these quantities will affect the Kelvin effect, which is strongly dependent on the surface tension, and the droplet size, which varies with the density.

Figures 13 and 14 display results for the same conditions as those shown in Figures 7 and 8, but allowing for condensation of both acid species. It is immediately obvious that the effect of the ternary condensation is to increase the mean particle size and decrease the total number produced, both a result of the increased condensation rate. It is expected that the partial pressure of H_2SO_4, for example, over a ternary solution at a given water activity will be less than that over a binary H_2SO_4-H_2O solution at the same water activity, due to the presence of the MSA. Thus the growth rate due to the incorporation of H_2SO_4 molecules is enhanced, as the driving force for condensation of H_2SO_4 is larger. Since H_2SO_4 vapor depletion occurs faster, fewer particles can nucleate. In addition, the MSA is present in higher gas-phase concentrations than the

H_2SO_4, and so has a higher condensation rate; the addition of this species also greatly increases the droplet growth rate.

It is interesting to note that, for Figures 8 and 14, which correspond to 36% relative humidity, 10% conversion of SO_2 to H_2SO_4, and 60% conversion of DMS to MSA, the total number and mean droplet size predicted by the binary and ternary condensation models bracket the experimental results of Hatakeyama for the same conditions. The effect of varying the MSA vapor source rate is shown in Figure 15, for which a 30% conversion of DMS to MSA was assumed, with the other conditions the same as in Figures 8 and 14. In this case the total number and mean diameter agree quite well with those measured, although this agreement in itself cannot determine what the actual conversion rates are, given the many assumptions made; however, the observation of such trends is of importance.

VI. Conclusions

The nucleation rates of methanesulfonic acid-water solution droplets have been estimated using binary nucleation theory and available property data for the binary system. Particles may be formed for sub-saturation levels of MSA in the gas phase and at relative humidities below 100%, and the predicted rates were compared with those calculated for the sulfuric acid-water system. Although both predictions are susceptible to errors, particularly due to uncertainties in property data, some important differences are noted, and these observations were applied to recent experimental smog chamber results for organosulfur chemistry systems.

The results of the binary nucleation rate calculations were used as particle source terms in an integral, dynamic model of particle formation from gas-phase chemical reactions. The model was tested using temperature, relative humidity, and vapor (H_2SO_4 and MSA) source rates corresponding approximately to those of the photooxidation experiments performed by Hatakeyama et al. (1985), and the effect of varying vapor source rates was shown. As expected, higher source rates lead to the formation of higher number concentrations of smaller particles than those obtained from lower source rates. Increases in relative humidity greatly increase the particle source rates. An important conclusion based on these model results is that particle formation in the DMS system, for conditions such as those used here, is a result of binary nucleation of sulfuric acid, with little or no contribution to the total number resulting from binary nucleation of methanesulfonic acid.

To test the effect of interactions between the two acids, a model for the water activity over a ternary solution of H_2SO_4-MSA-H_2O was developed. The activity as a function of acid concentrations was used to calculate droplet growth rates and droplet sizes in equilibrium with a given relative humidity. When used in the integral model, the ternary condensation rates for the same ambient conditions as described above resulted in increased particle growth and lower

total number concentration for given vapor source rates. Support for a ternary condensation mechanism is found in the observed presence of both H_2SO_4 and MSA in experimental and ambient aerosols.

The objective of this work is to provide a framework for studying the interaction of these two acids during particle formation. Although this study was limited to low-humidity cases for purposes of comparison with existing data, the models presented here can easily be applied to higher-humidity systems as found in the atmosphere. Further tests of the models under more widely varying conditions, and using accurate gas-phase data, will be necessary. The applications of the models described here, therefore, have direct bearing on the analysis of these experimental results and in the modeling of atmospheric chemistry, in particular, the homogeneous heteromolecular formation of ultrafine aerosols in the atmosphere that can act as condensation nuclei for other species.

Acknowledgement

This work was supported entirely by National Science Foundation grant ATM-8503103.

Appendix A: Binary nucleation rate equations

The total binary nucleation rate is given by (Stauffer, 1976)

$$J_{total} = R_{av}\, c_{sp}\, Z, \tag{7}$$

where

R_{av} = the average growth rate

c_{sp} = the droplet equilibrium concentration,

$= N\exp(-G_{sp}/kT)$

Z = Zeldovich factor, given by free energy derivatives at the saddle point.

Further, we will denote the two vapor species as A (acid) and W (water). Then N is the total number of molecules in the vapor phase, $N_A + N_W$ and G_{sp} is the free energy of formation of droplets from the vapor phase, which reduces to

$$G_{sp} = \frac{4}{3}\pi\sigma r^{*2}, \tag{8}$$

where σ is the surface tension of the binary droplet and r^* is the critical cluster size. These two quantities are determined by solving for the energy minimum:

$$\left(\frac{\delta\Delta G}{\delta n_A}\right)_{n_W} = 0 \tag{9}$$

$$\left(\frac{\delta\Delta G}{\delta n_W}\right)_{n_A} = 0. \tag{10}$$

These equations may be written explicitly in the following form:

$$RT\ln\frac{RA_A}{a_A} = \frac{2\sigma\bar{V}_A}{r^*} \tag{11}$$

$$RT\ln\frac{RH}{a_W} = \frac{2\sigma\bar{V}_W}{r^*}, \tag{12}$$

where $\bar{V}_i$ is the partial molar volume of water or acid in the binary solution. In writing these equations we have adopted the suggestion of Wilemski (1987) that the derivative of the surface tension with respect to composition be taken as

zero. This assumption was tested for both H_2SO_4 and MSA nucleation rates and found to not significantly alter the computed rates. In view of the uncertainties in the mixture surface tensions, it was decided to use the Wilemski theory in our model.

The Zeldovich factor is computed from

$$Z = \frac{(-1)(D_{AA}\cos^2\phi + D_{WW}\sin^2\phi + D_{AW}\cos\phi\sin\phi)}{(-\det D)^{1/2}}. \tag{13}$$

The elements of the matrix D are the second derivatives of the free energy (divided by two):

$$\frac{8\pi r^3}{3}D_{AA} = V(1-x_A)\left(\frac{d\mu_{A,l}}{dx_A}\right) + (\mu_{A,l}-\mu_{A,g})\frac{\bar{V}_A}{3} + \frac{2\sigma V(1-x_A)}{r}\left(\frac{d\bar{V}_A}{dx_A}\right) \tag{14}$$

$$\frac{8\pi r^3}{3}D_{WW} = \frac{V x_A^2}{(1-x_A)}\left(\frac{d\mu_{A,l}}{dx_A}\right) + (\mu_{W,l}-\mu_{W,g})\frac{\bar{V}_W}{3} + \frac{2\sigma V x_A}{(1-x_A)r}\left(\frac{d\bar{V}_A}{dx_A}\right) \tag{15}$$

$$\frac{8\pi r^3}{3}D_{AW} = -V x_A\left(\frac{d\mu_{A,l}}{dx_A}\right) + (\mu_{A,l}-\mu_{A,g})\frac{\bar{V}_A}{3} - \frac{2\sigma V x_A}{r}\left(\frac{d\bar{V}_A}{dx_A}\right) = \frac{8\pi r^3}{3}D_{WA}. \tag{16}$$

The average growth rate is defined by

$$R_{av} = \det R \,/\, \left(R_{AA}\sin^2\phi + R_{WW}\cos^2\phi - 2R_{AW}\sin\phi\cos\phi\right), \tag{17}$$

with the elements of the matrix R giving the impingement probabilities. We will take the elements $R_{AW} = R_{WA} = 0$, valid for nonassociated vapors. Then $R_{AA} = S(n_A n_W)\beta_{1A}$, the impingement rate of single molecules on the surface area of the cluster ($S(n_A n_W)$), with an analogous expression for R_{WW}.

The expression for the angle ϕ of the nucleation current direction through the saddle point, for nonassociated vapors, was derived by Stauffer (1976):

$$\tan\phi = s + \left(s^2 + r\right)^{1/2}, \tag{18}$$

with

$$r = R_{WW}/R_{AA}$$

$$s = -\frac{1}{2D_{AW}}\left(D_{AA} - rD_{BB}\right).$$

Appendix B: Sources of property data used in model

Sulfuric acid-water solutions

The densities at a given temperature were fit to polynomials in weight fraction. All other properties were fitted to cubic splines in appropriate concentration variables at a given temperature. When necessary, linear interpolation between two temperatures at a given mole fraction was used to get solution data at other temperatures than the literature values, except for activity data, which were fit to composition data at 25 ° C only.

- Osmotic coefficient: Rard (1983)
- Surface tension: Morgan and Davis (1916); Sabinina and Terpugow (1935); International Critical Tables (1934); CRC Handbook (1980).
- Density: International Critical Tables (1934); CRC Handbook (1980).
- Activity coefficient of acid: Giauque et al. (1960); Pitzer et al. (1977).
- Vapor pressure:* Roedel (1979); Gmitro and Vermeulen (1964).

Methanesulfonic acid-water solutions

All data used was at 25°C and not corrected for temperature, due to lack of information. The densities were fit to polynomials in weight fraction. A linear relation was used for the surface tension, with the surface tension of methanesulfonic acid taken as 53 dynes cm^{-1}. This value was based on Berthoud's (1929) measurement at 32.4°C of 49.39 dynes cm^{-1} and on an estimate using parachors. All other properties were fitted to cubic splines in appropriate concentration variables.

---

* Considerable disagreement still exists over the saturation vapor pressure of sulfuric acid. The following values for the vapor pressure of pure sulfuric acid were used in this study:

at T = 25 ° C, p_a° = 0.04 ppm.

at T = 30 ° C, p_a° = 0.06867 ppm.

- Activities: Activity and osmotic coefficients to 40 molal were measured by Covington et al. (1973). This data set was extended using the acid activities measured by Clegg and Brimblecombe (1985), by fitting a polynomial to $\ln \gamma$ as a function of ln(molality) and using this polynomial to calculate the osmotic coefficients.
- Density: Bascombe and Bell (1959) and Teng and Lenzi (1975).
- Vapor pressure of pure acid: Two vapor pressure measurements from the CRC Handbook (1980) and one from Clegg and Brimblecombe (1985) were found to be well represented by the function

$$\ln p_a^\circ = \frac{-8.00648 \times 10^3}{T} + 2.14237 \ln T + 7.45208. \qquad (19)$$

Appendix C

The text of Appendix C consists of a Letter to the Editor which will appear in *Atmospheric Environment*

Letter to the Editor

After submission of the final version of our paper, "Nucleation of Sulfuric Acid-Water and Methanesulfonic Acid-Water Solution Particles: Implications for the Atmospheric Chemistry of Organosulfur Species", Kreidenweis S.M. and Seinfeld J.H. (1987), *Atmospheric Environment* **22**, 283-296, the following report came to our attention:

Hoppel W.A., Fitzgerald J.W., Frick G.M., Larson R.E., and Wattle B.J. (1987) "Preliminary Investigation of the Role that DMS and Cloud Cycles Play in the Formation of the Aerosol Size Distribution", *NRL Report 9032*, July 29, 1987, Naval Research Laboratory, Washington, D.C.

The report includes a theoretical study of the nucleation properties of methanesulfonic acid (MSA), undertaken to analyze the results of dimethyl sulfide (DMS) photolysis experiments carried out in an environmental chamber. In agreement with our findings, the authors conclude that nucleation of new particles in DMS oxidation is most likely due to heteromolecular nucleation of H_2SO_4, whereas subsequent growth is due largely to MSA and H_2O condensation. The binary nucleation rate predictions are similar; however, an important difference in the NRL analysis is that the surface tension of MSA-H_2O solutions was measured, whereas we estimated the solution surface tension as:

$$\sigma = 53\, x_{\mathrm{MSA}} + 72\, x_{\mathrm{H_2O}}, \tag{20}$$

where x_i refers to the mole fraction of the species in solution.

To evaluate the effect of the measured surface tension on the predictions of our model, we have recalculated two of the cases presented in our paper using the curve fit given as Eq. 8 in Hoppel *et al.*:

$$\begin{aligned}\sigma = {} & 51.777 - 3.7628 \ln(x + 0.1) - 4.51915 \left[\ln(x + 0.1)\right]^2 \\ & - 2.93893 \left[\ln(x + 0.1)\right]^3,\end{aligned} \tag{21}$$

where here x refers to the mole fraction of MSA in solution. The calculations using both the previous and revised correlations for σ are shown in Figure 15. Cases 1 and 2 correspond to the following assumed conditions:

Case 1. $[DMS]_o = 1.3$ ppm, 60% conversion of DMS to MSA, RH=36%, $T =$ 30°C, MSA$-H_2O$ nucleating and condensing. (1a) linear estimate of solution surface tension. (1b) NRL correlation for surface tension.

Case 2. $[DMS]_o = 1.3$ ppm, 30% conversion of DMS to MSA, 10% conversion of SO_2 to H_2SO_4, RH=36%, $T = 30$°C, $H_2SO_4 - H_2O$ nucleating, $H_2SO_4 - MSA - H_2O$ condensing. (2a) linear estimate of solution surface tension. (2b) NRL correlation for surface tension.

In both cases, the total number concentration produced using the revised σ is larger than that predicted using our estimate. As expected, Case 1, which involves the nucleation and growth of aqueous MSA droplets, shows the largest effect due to the revised surface tension, with particle formation occuring earlier in the run. However, the total number produced is still much smaller than that observed by Hatakeyama *et al.* The source rates represented by Case 2 are those that gave best agreement with the experimental results. For this case, the previous and revised surface tensions give qualitatively similar nucleation and growth behavior. The overall conclusions of our previous paper are thus not affected by this variation in surface tension. However, depending upon the relative source rates of condensable vapors, the increased MSA$-H_2O$ nucleation rates that are a consequence of the revised σ may represent a significant source of new particles in organosulfur systems.

Sonia Kreidenweis
John H. Seinfeld
California Institute of Technology

References

Andreae M. O. and Raemdonck H. (1983) Dimethyl sulfide in the surface ocean and the marine atmosphere: a global view. *Science* **221**, 744-747.

Bascombe K.N. and Bell R.P. (1959) Acidity functions of some aqueous acids. *J. Chem. Soc.*, 1096-1104.

Berthoud, A. (1929) Quelques proprietes physico-chimiques des acides ethane- et methane-sulfonique. *Helv. Chim. Acta* **12**, 859-865.

Boulaud D., Madelaine G., Vigla D. and Bricard J. (1977) Experimental study on the nucleation of water vapor sulfuric acid binary system. *J. Chem. Physics* **66**, 4854-4860.

Clarke J.H.R. and Woodward L.A. (1966) Raman spectrophotometric determination of the degrees of dissociation of methanesulfonic acid in aqueous solution at 25°C. *Trans. Faraday Society* **62**, 2226-2233.

Clegg S.L. and Brimblecombe P. (1985) The solubility of methanesulphonic acid and its implications for atmospheric chemistry. *Environmental Technology Letters* **6**, 269-278.

Covington A.K., Robinson R.A. and Thompson R. (1973) Osmotic and activity coefficients for aqueous methane sulfonic acid solutions at 25 C. *J. Chem. Eng. Data* **18**, 422-423.

Cox, R.A. (1973) Some experimental observations of aerosol formation in the photo-oxidation of sulphur dioxide. *J. Aerosol Science* **4**, 473-483.

Dahneke B. (1983) Simple kinetic theory of brownian diffusion in vapors and aerosols. In *Theory of Dispersed Multiphase Flow*, R.E. Meyer (Ed.), Academic Press, New York, 97-138.

Doyle G.J. (1961) Self-nucleation in the sulfuric acid–water system. *J. Chem. Phys.* **35**, 795-799.

Giauque W.F., Hornung E.W., Kunzler J.E., and Rubin T.R. (1960) The thermodynamic properties of aqueous sulfuric acid solutions and hydrates from

15 to 300 K. *J. Amer. Chem. Soc.* **82**, 62-70.

Gmitro J.I. and Vermeulen T. (1964) Vapor–Liquid Equilibria for Aqueous Sulfuric Acid. *A.I.Ch.E. J.* **10**, 740-746.

Gregor H.P., Rothenburg M. and Fine N. (1963) Molal activity coefficients of methane- and ethanesulfonic acids and their salts. *J. Phys. Chem.* **67**, 1110-1112.

Grosjean D. and Lewis R. (1982) Atmospheric photooxidation of methyl sulfide. *Geophys. Res. Lett.* **9**, 1203-1206.

Hamill P. (1975) The time dependent growth of $H_2O - H_2SO_4$ aerosols by heteromolecular condensation. *J. Aerosol Science* **6**, 475-482.

Hamill P., Turco R.P., Kiang C.S., Toon O.B. and Whitten R.R. (1982) An analysis of various nucleation mechanisms for sulfate particles in the stratosphere. *J. Aerosol Science* **13**, 561-585.

Hatakeyama S., Izumi K. and Akimoto H. (1985) Yield of SO_2 and formation of aerosol in the photooxidation of DMS under atmospheric conditions. *Atmospheric Environment* **19**, 135-141.

Hatakeyama S., Okuda M. and Akimoto H. (1982) Formation of sulfur dioxide and methane-sulfonic acid in the photooxidation of dimethyl sulfide in the air. *Geophys. Res. Lett.* **9**, 583-586.

International Critical Tables of Numerical Data, Physics, Chemistry and Technology (1926-1930), E.W. Washburn (Ed.), McGraw-Hill, New York.

Kusik C.L. and Meissner, H.P. (1978) Electrolyte activity coefficients in inorganic processing. *Am. Inst. Chem. Eng. Symp. Ser.* **173**, 14-20.

Middleton P. and Kiang C.S. (1978) A kinetic aerosol model for the formation and growth of secondary sulfuric acid particles. *J. Aerosol Science* **9**, 359-385.

Mirabel P. and Clavelin J.L. (1978) Experimental study of nucleation in binary mixtures: the nitric acid-water and sulfuric acid-water systems. *J. Chem. Phys.* **68**, 5020-5027.

Mirabel P. and Katz J.L. (1974) Binary homogeneous nucleation as a mechanism for the formation of aerosols. *J. Chem. Phys.* **60**, 1138-1144.

Morgan J.L.R. and Davis C.E. (1916) The properties of mixed liquids. I. Sulfuric acid-water mixtures. *J. Amer. Chem. Soc.* **38**, 555-568.

Panter R. and Penzhorn R.-D. (1980) Alkyl sulfonic acids in the atmosphere. *Atmospheric Environment* **14**, 149-151.

Pitzer K.S., Roy R.N. and Silvester L.F. (1977) Thermodynamics of electrolytes. 7. Sulfuric acid. *J. Amer. Chem. Soc.* **99**, 4930-4936.

Rard J.A. (1983) Isopiestic determination of the osmotic coefficients of aqueous H_2SO_4 at 25 C. *J. Chem. Eng. Data* **28**, 384-387.

Rard J.A., Habenshuss A., and Spedding F.H. (1976) A review of the osmotic coefficients of aqueous H_2SO_4 at 25 C. *J. Chem. Eng. Data* **21**, 374-379.

Reiss H. (1950) The kinetics of phase transitions in binary systems. *J. Chem. Phys.* **18**, 840-848.

Roedel W. (1979) Measurement of sulfuric acid saturation vapor pressure; implications for aerosol formation by heteromolecular nucleation. *J. Aerosol Science* **10**, 375-386.

Sabinina L. and Terpugow L. (1935) Die Oberflachenspannung des Systems Schwefelsäure-Wasser. *Z. phys. Chem.* **A 173**, 237-241.

Schelling F.J. and Reiss H. (1981) Expansion cloud chamber observations on the nucleation and growth of sulfuric acid-water droplets. *J. Colloid Interface Science* **83**, 246-264.

Shugard W. J., Heist R.H., and Reiss H. (1974) Theory of vapor phase nucleation in binary mixtures of water and sulfuric acid. *J. Chem. Phys.* **61**, 5298-5305.

Stauffer D. (1976) Kinetic theory of two-component ("heteromolecular") nucleation and condensation. *J. Aerosol Science* **7**, 319-333.

Stelson A.W., Bassett M.E. and Seinfeld J.H. (1984) Thermodynamic equilib-

rium properties of aqueous solutions of nitrate, sulfate and ammonium. In *Chemistry of Particles, Fogs and Rain*, J.L. Durham, ed., Butterworth, MA, pp. 1-52.

Takahashi K., Kasahara M. and Itoh M. (1975) A kinetic model of sulphuric acid aerosol formation from photochemical oxidation of sulfur dioxide vapor. *J. Aerosol Science* **6**, 45-55.

Teng T.T and Lenzi F. (1975) Methanesulfonic and trichloroacetic acids: densities of aqueous solutions at 20, 25, and 35°C. *J. Chem. Eng. Data* **20**, 432-434.

Warren D.R. and Seinfeld J.H. (1984) Nucleation and growth of aerosol from a continuously reinforced vapor. *Aerosol Science and Technology* **3**, 135-153.

Warren D.R. and Seinfeld J.H. (1985) Prediction of aerosol concentrations resulting from a burst of nucleation. *J. Colloid Interface Science* **105**, 136-142.

Weast R. C. (ed.) (1978) *Handbook of Chemistry and Physics*, 58th Edn. CRC Press, Boca Raton.

Wilemski G. (1984) Composition of the critical nucleus in multicomponent vapor nucleation. *J. Chem. Phys.* **80**, 1370-1372.

Yin F., Grosjean D. and Seinfeld J.H. (1986) Analysis of atmospheric photooxidation mechanisms for organosulfur compounds. *J. Geophys. Res.* **91**, 14417-14438.

Table 1

Experimental conditions of Hatakeyama et al. (1985)

Run*	Figures**	$(DMS)_o$	RH	Max [CN]	Time for nucleation
1	6,7	1.3 ppm	36%	1.2×10^5	0–10 min. into run
2	1,6,7	1.3 ppm	0	2.2×10^3	50–70 min. into run
3	3,4	0.012 ppm	36%	3.3×10^5	0–10 min. into run

* Run number assigned by us.

** Figure numbers refer to Hatakeyama et al. (1985).

Table 2

Conditions for simulations

$(DMS)_o$	% SO_2 to H_2SO_4	H_2SO_4 source rate, ppm s^{-1}	MSA source rate, ppm s–1	*RH*
1.3 ppm	1%	2.992×10^{-7}	–	36%
	10%	2.992×10^{-6}	–	36%
	1%	2.992×10^{-7}	–	0
	10%	2.992×10^{-6}	–	0
1.3 ppm	–	–	6.19×10^{-5}	36%
	–	–	6.19×10^{-5}	0
1.3 ppm	1%	2.992×10^{-7}	6.19×10^{-5}	36%
	10%	2.992×10^{-6}	6.19×10^{-5}	36%
	10%	2.992×10^{-6}	3.1×10^{-5}	36%
0.012 ppm	1%	2.762×10^{-9}	–	36%
	10%	2.762×10^{-8}	–	36%
	–	–	5.71×10^{-7}	36%

* Figure numbers in this work.

Table 2, continued

Conditions for simulations

Hatakeyama run no.	Figure No.*	$[CN]_{max}$ predicted	time for nucleation
1	7	2.4×10^4	0 to 15 min
1	8	1.0×10^6	0 to 5 min
2	not shown	0	–
2	not shown	0	–
1	10	5	30 to 40 min
2	not shown	0	–
1	13	100	0 to 10 min
1	14	2.3×10^4	0 to 5 min
1	15	6×10^4	0 to 5 min
3	not shown	0	–
3	9	500	60 to 90 min
3	not shown	0	–

Table 3

Expanded integral model for acid–acid interactions

$$\frac{d}{dt}N_1 = R_{J_b,\mathrm{H_2SO_4–H_2O}}$$

$$\frac{d}{dt}N_2 = R_{J_b,\mathrm{MSA–H_2O}}$$

$$\frac{d}{dt}M_{\mathrm{H_2SO_4},1} = MW_{\mathrm{H_2SO_4}}\left(N_{AV}g^*_{\mathrm{H_2SO_4}}R_{J_b,\mathrm{H_2SO_4–H_2O}} + R_{C_{\mathrm{H_2SO_4},1}}\right)$$

$$\frac{d}{dt}M_{\mathrm{MSA},1} = MW_{\mathrm{MSA}}R_{C_{\mathrm{MSA},1}}$$

$$\frac{d}{dt}M_{\mathrm{H_2SO_4},2} = MW_{\mathrm{H_2SO_4}}R_{C_{\mathrm{H_2SO_4},2}}$$

$$\frac{d}{dt}M_{\mathrm{MSA},2} = MW_{\mathrm{MSA}}\left(N_{AV}g^*_{\mathrm{MSA}}R_{J_b,\mathrm{MSA–H_2O}} + R_{C_{\mathrm{MSA},2}}\right)$$

$$\frac{p^o_{\mathrm{H_2SO_4}}}{RT}\frac{d}{dt}RA_{\mathrm{H_2SO_4}} = R_{g_{\mathrm{H_2SO_4}}} - N_{AV}g^*_{\mathrm{H_2SO_4}}R_{J_b,\mathrm{H_2SO_4–H_2O}} - R_{C_{\mathrm{H_2SO_4},1}} - R_{C_{\mathrm{H_2SO_4},2}}$$

$$\frac{p^o_{\mathrm{MSA}}}{RT}\frac{d}{dt}RA_{\mathrm{MSA}} = R_{g_{\mathrm{MSA}}} - N_{AV}g^*_{\mathrm{MSA}}R_{J_b,\mathrm{MSA–H_2O}} - R_{C_{\mathrm{MSA},1}} - R_{C_{\mathrm{MSA},2}}$$

subscript 1 = mode 1 (H_2SO_4–H_2O nucleation mode)

subscript 2 = mode 2 (MSA–H_2O nucleation mode)

Figure Captions

Figure 1. Properties of aqueous sulfuric acid solutions at 25° C.

Figure 2. Properties of aqueous methanesulfonic acid solutions at 25° C.

Figure 3. Nucleation rates of aqueous acid droplets at 25° C. at various relative humidities as a function of acid relative acidity. Upper scales: corresponding acid partial pressures in ppm.

Figure 4. Free energy of mixing.

Figure 5. Nucleation rates at 30° C of aqueous acid droplets at $RH = 36\%$ and of pure acid droplets at zero relative humidity.

Figure 6. Total number of particles predicted, mean diameter, and gas-phase concentrations in ppm of H_2SO_4 and MSA for $[DMS]_o$ =1.3 ppm, 1% conversion of SO_2 to H_2SO_4, $RH = 36\%$, $T = 30°C$ and $H_2SO_4 - H_2O$ nucleating and condensing.

Figure 7. Total number of particles predicted, mean diameter, and gas-phase concentrations in ppm of H_2SO_4 and MSA for $[DMS]_o$ =1.3 ppm, 10% conversion of SO_2 to H_2SO_4, $RH = 36\%$, $T = 30°C$. and $H_2SO_4 - H_2O$ nucleating and condensing.

Figure 8. Total number of particles predicted, mean diameter, and gas-phase concentrations in ppm of H_2SO_4 and MSA for $[DMS]_o$ =0.012 ppm, 10% conversion of SO_2 to H_2SO_4, $RH = 36\%$, $T = 30°C$. and $H_2SO_4 - H_2O$ nucleating and condensing.

Figure 9. $[DMS]_o$ Total number of particles predicted, mean diameter, and gas-phase concentrations in ppm of H_2SO_4 and MSA for $[DMS]_o$ =1.3 ppm, 60% conversion of DMS to MSA, $RH = 36\%$, $T = 30°C$. and MSA–H_2O nucleating and condensing.

Figure 10. Experimental results of Hatakeyama et al. (1985). Total number

of particles produced and mean diameter for $[DMS]_o$ =1.3 ppm,T = 30°C. – , $RH = 36\%$; $\cdots$, $RH = 0$.

Figure 11. Water activity of the ternary solution H_2SO_4–MSA–H_2O as a function of sulfuric acid molality for various molalities of methanesulfonic acid.

Figure 12. Total number of particles predicted, mean diameter, and gas-phase concentrations in ppm of H_2SO_4 and MSA for $[DMS]_o$ =1.3 ppm, 1% conversion of SO_2 to H_2SO_4 , 60% conversion of DMS to MSA, $RH = 36\%$, $T = 30°C$. $H_2SO_4 - H_2O$ nucleating and H_2SO_4–MSA–H_2O condensing.

Figure 13. Total number of particles predicted, mean diameter, and gas-phase concentrations in ppm of H_2SO_4 and MSA for $[DMS]_o$ =1.3 ppm, 10% conversion of SO_2 to H_2SO_4 , 60% conversion of DMS to MSA, $RH = 36\%$, $T = 30°C$. $H_2SO_4 - H_2O$ nucleating and H_2SO_4–MSA–H_2O condensing.

Figure 14. Total number of particles predicted, mean diameter, and gas-phase concentrations in ppm of H_2SO_4 and MSA for $[DMS]_o$ =1.3 ppm, 10% conversion of SO_2 to H_2SO_4 , 30% conversion of DMS to MSA, $RH = 36\%$, $T = 30°C$. $H_2SO_4 - H_2O$ nucleating and H_2SO_4–MSA–H_2O condensing.

Figure 15. Total number concentration (cm^{-3}) of particles and mean particle diameter (cm). Cases 1 and 2 are as described in text.

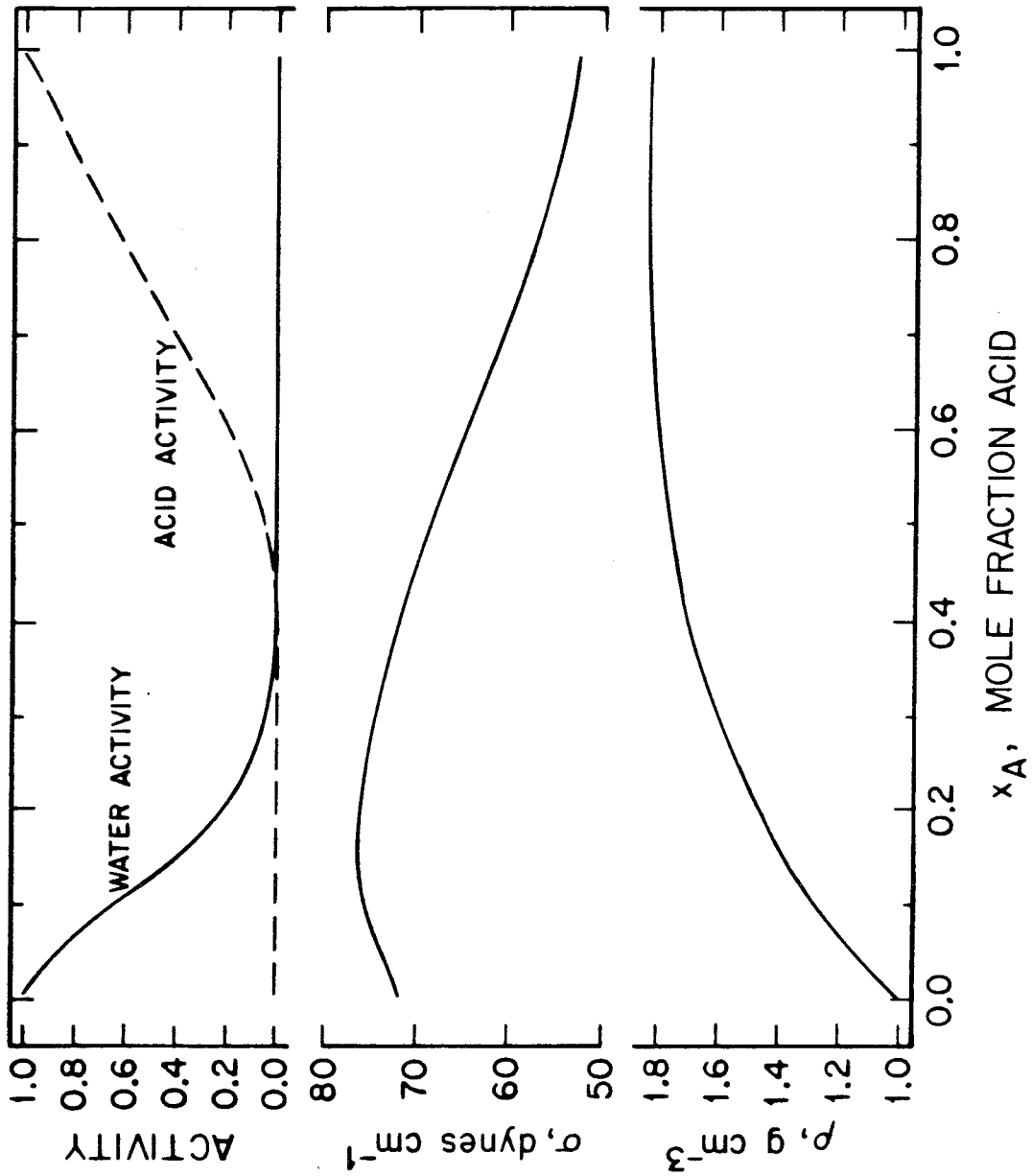
ACTIVITY
1.0
0.8
0.6
0.4
0.2
0.0
WATER ACTIVITY
ACID ACTIVITY
σ, dynes cm⁻¹
80
70
60
50
ρ, g cm⁻³
1.8
1.6
1.4
1.2
1.0
0.0
0.2
0.4
0.6
0.8
1.0
x_A, MOLE FRACTION ACID

Figure 1

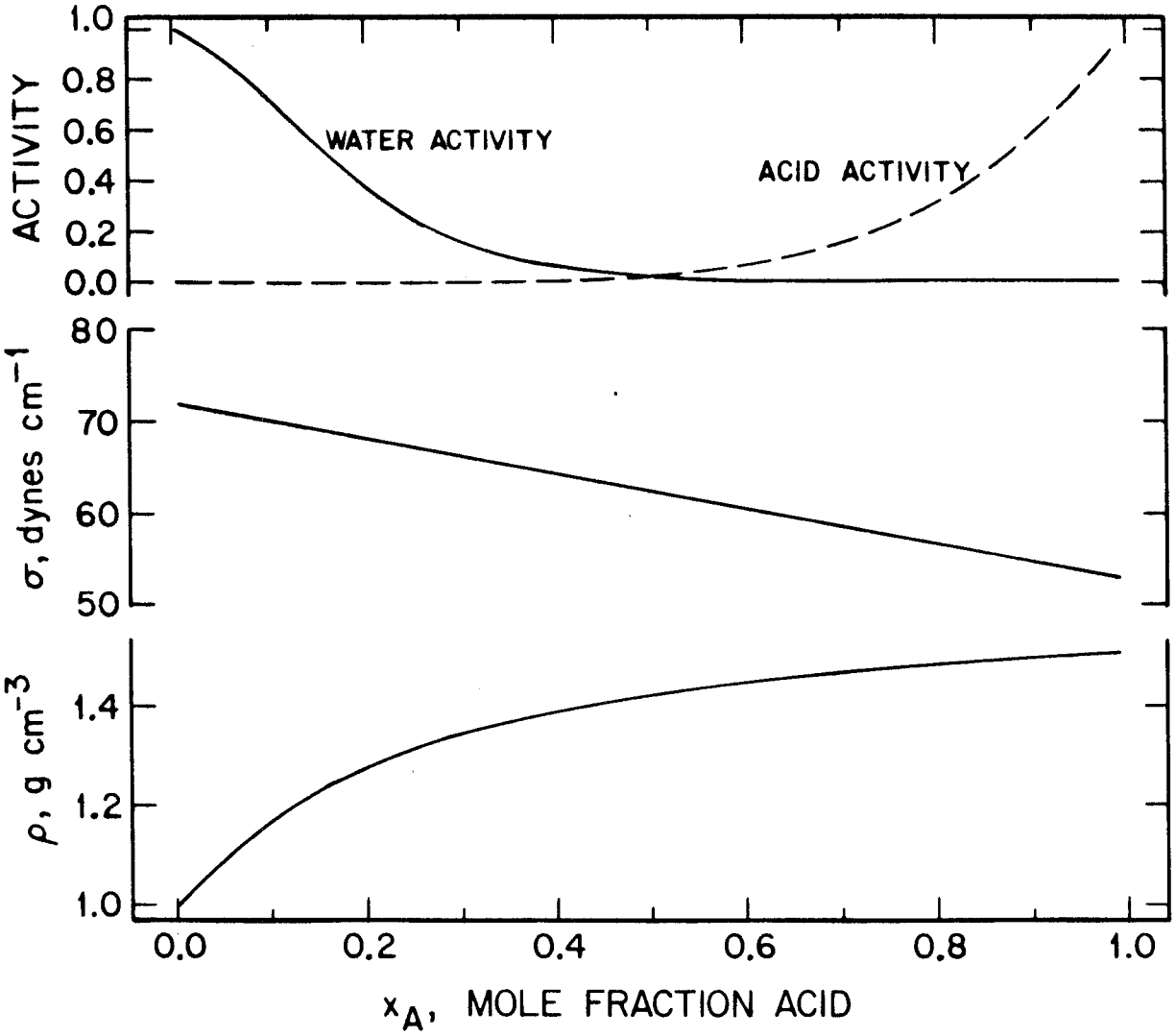
ACTIVITY
1.0
0.8
0.6
0.4
0.2
0.0
WATER ACTIVITY
ACID ACTIVITY
σ, dynes cm⁻¹
80
70
60
50
ρ, g cm⁻³
1.4
1.2
1.0
0.0
0.2
0.4
0.6
0.8
1.0
x_A, MOLE FRACTION ACID

Figure 2

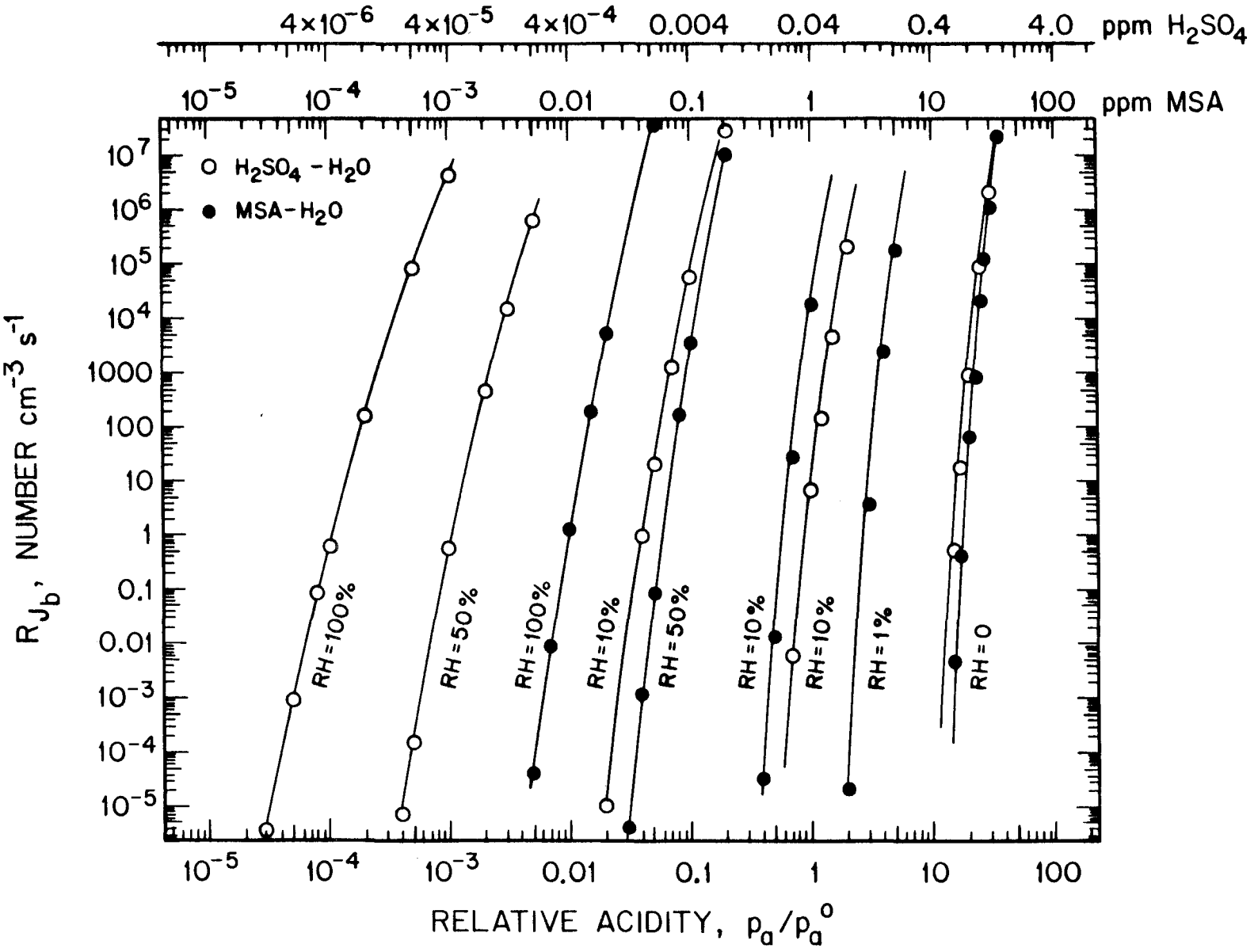
4×10⁻⁶ 4×10⁻⁵ 4×10⁻⁴ 0.004 0.04 0.4 4.0 ppm H₂SO₄
10⁻⁵ 10⁻⁴ 10⁻³ 0.01 0.1 1 10 100 ppm MSA
O H₂SO₄ - H₂O
● MSA-H₂O
RH=100%
RH=50%
RH=100%
RH=10%
RH=50%
RH=10%
RH=10%
RH=1%
RH=0
R_Jb, NUMBER cm⁻³ s⁻¹
RELATIVE ACIDITY, p_a/p_a^o

Figure 3

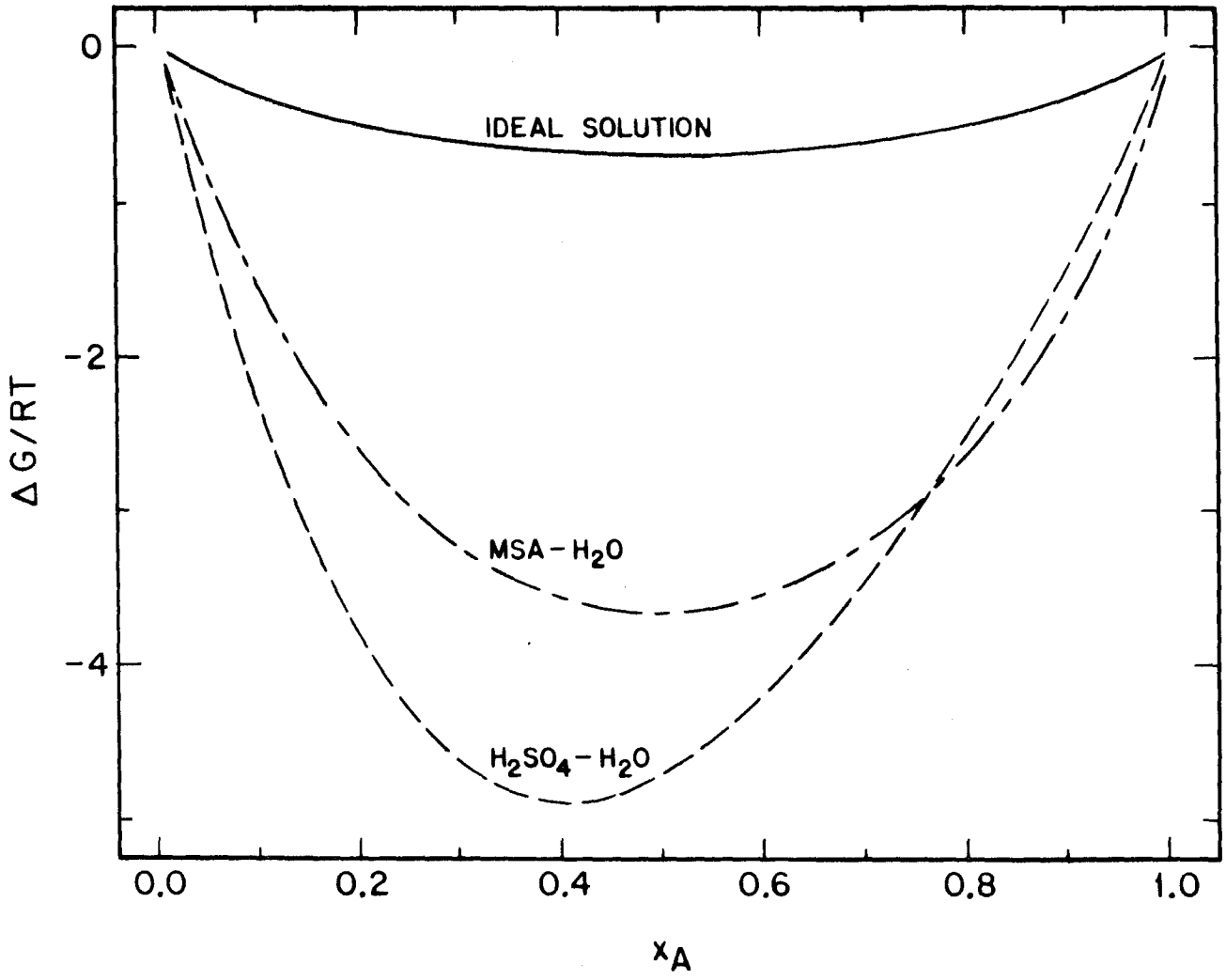

Figure 4

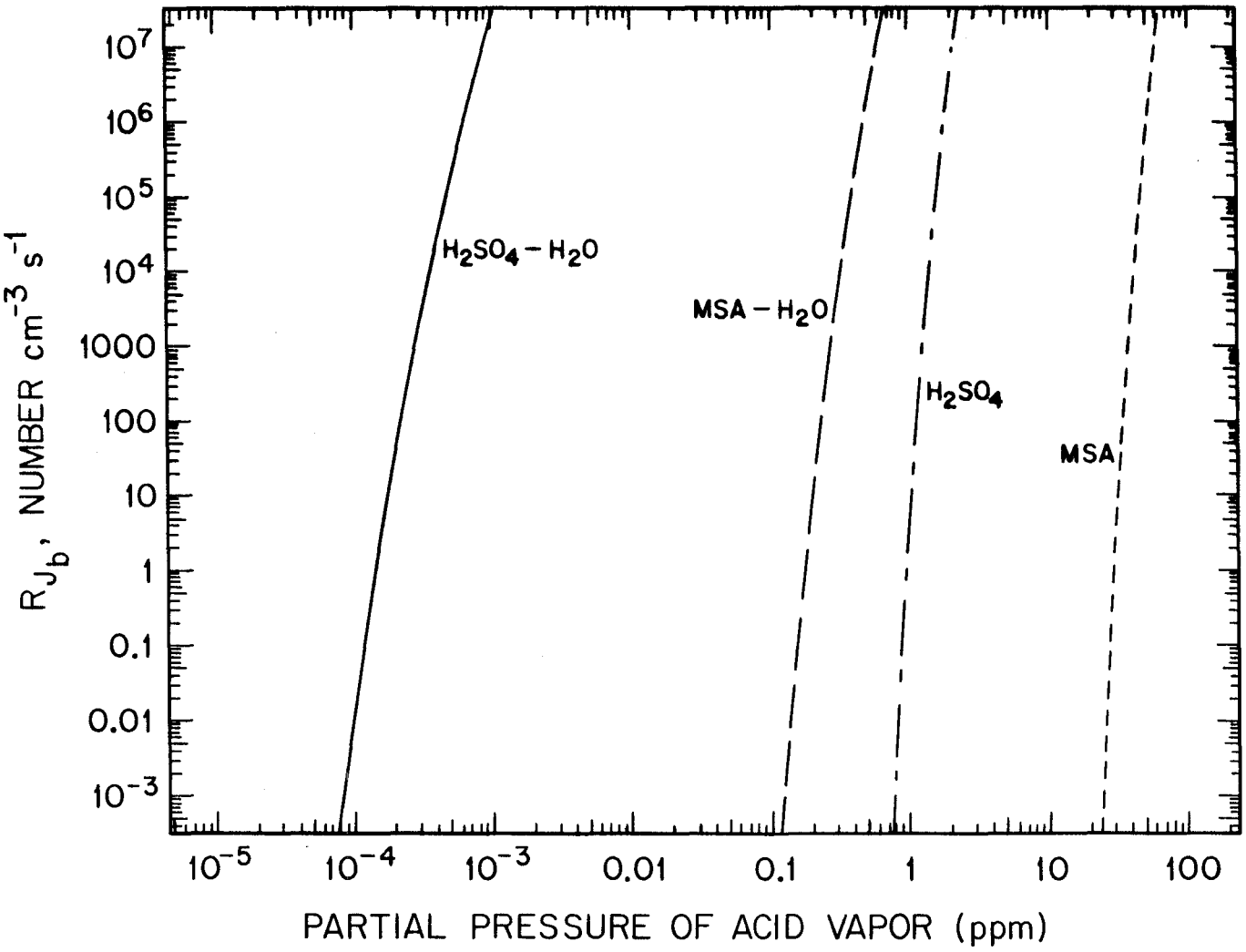
10^7
10^6
10^5
10^4
1000
100
10
1
0.1
0.01
10^{-3}
R_{J_b}, NUMBER cm^{-3} s^{-1}
$H_2SO_4 - H_2O$
MSA – H_2O
H_2SO_4
MSA
10^{-5}
10^{-4}
10^{-3}
0.01
0.1
1
10
100
PARTIAL PRESSURE OF ACID VAPOR (ppm)

Figure 5

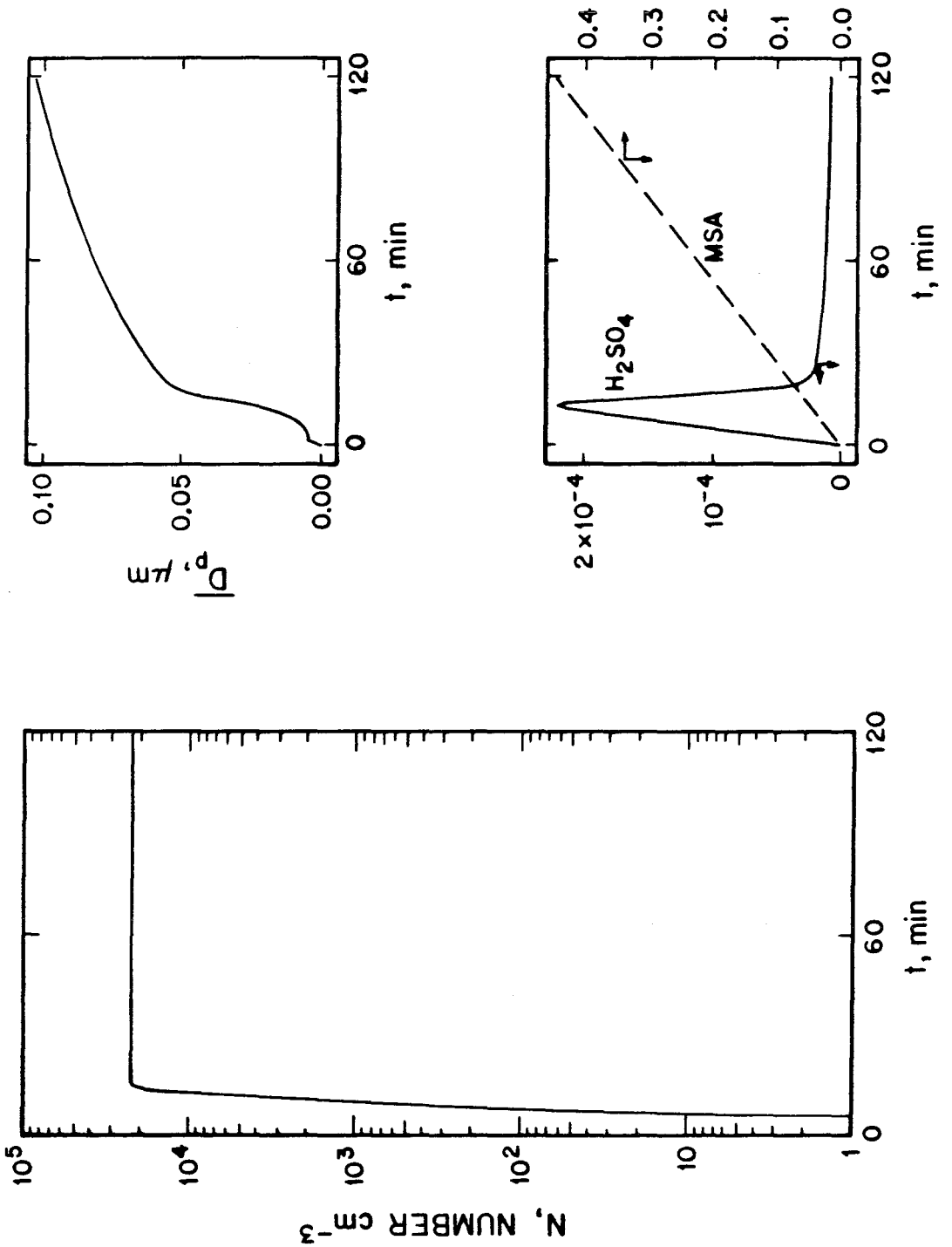
N, NUMBER cm⁻³
10⁵
10⁴
10³
10²
10
1
0
60
120
t, min
D̄p, μm
0.10
0.05
0.00
0
60
120
t, min
2×10⁻⁴
10⁻⁴
0
0.4
0.3
0.2
0.1
0.0
H₂SO₄
MSA
0
60
120
t, min

Figure 6

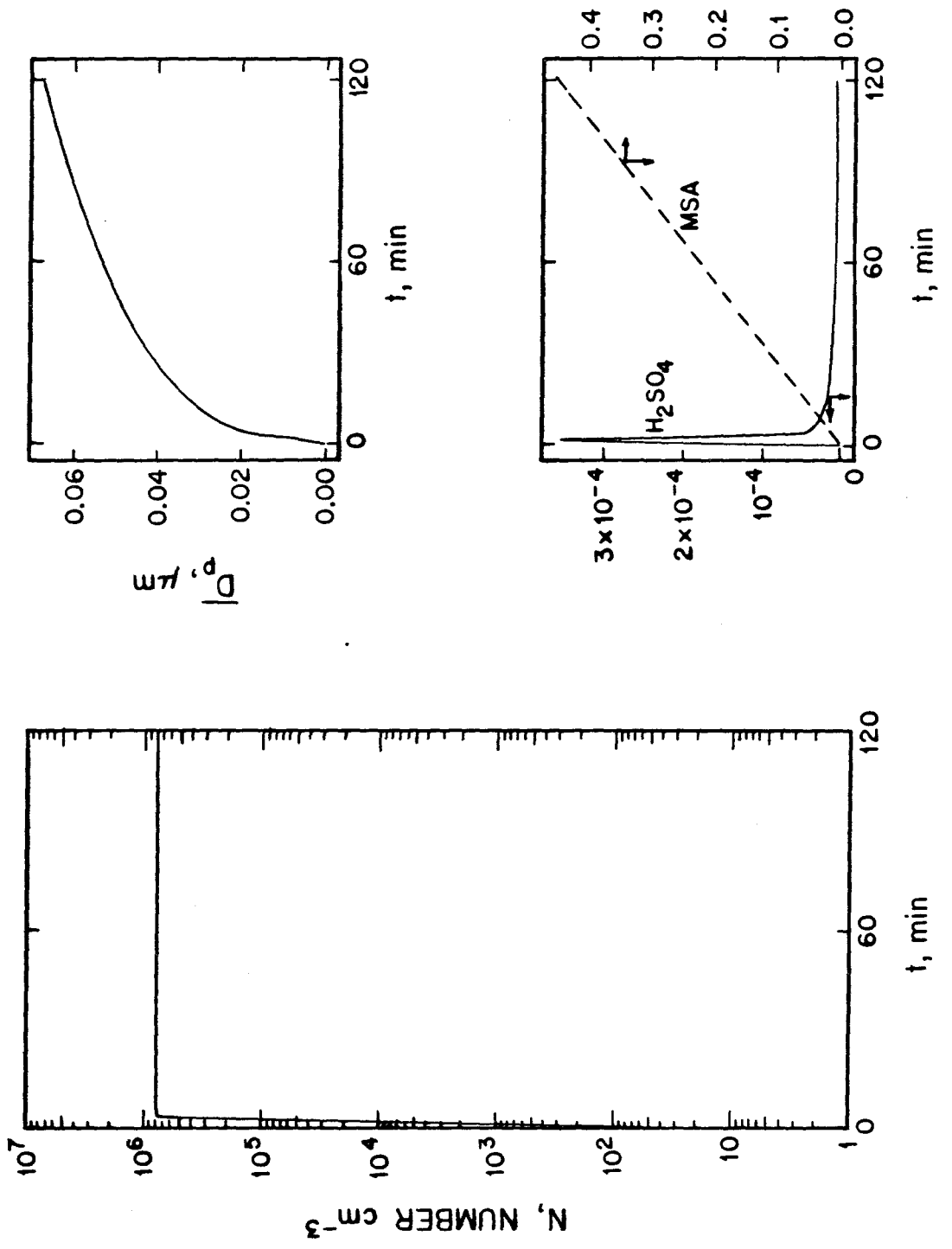
N, NUMBER cm⁻³
10⁷
10⁶
10⁵
10⁴
10³
10²
10
1
0
60
120
t, min
D_p, μm
0.06
0.04
0.02
0.00
0
60
120
t, min
H_2SO_4
MSA
3x10⁻⁴
2x10⁻⁴
10⁻⁴
0
0.4
0.3
0.2
0.1
0.0
0
60
120
t, min

Figure 7

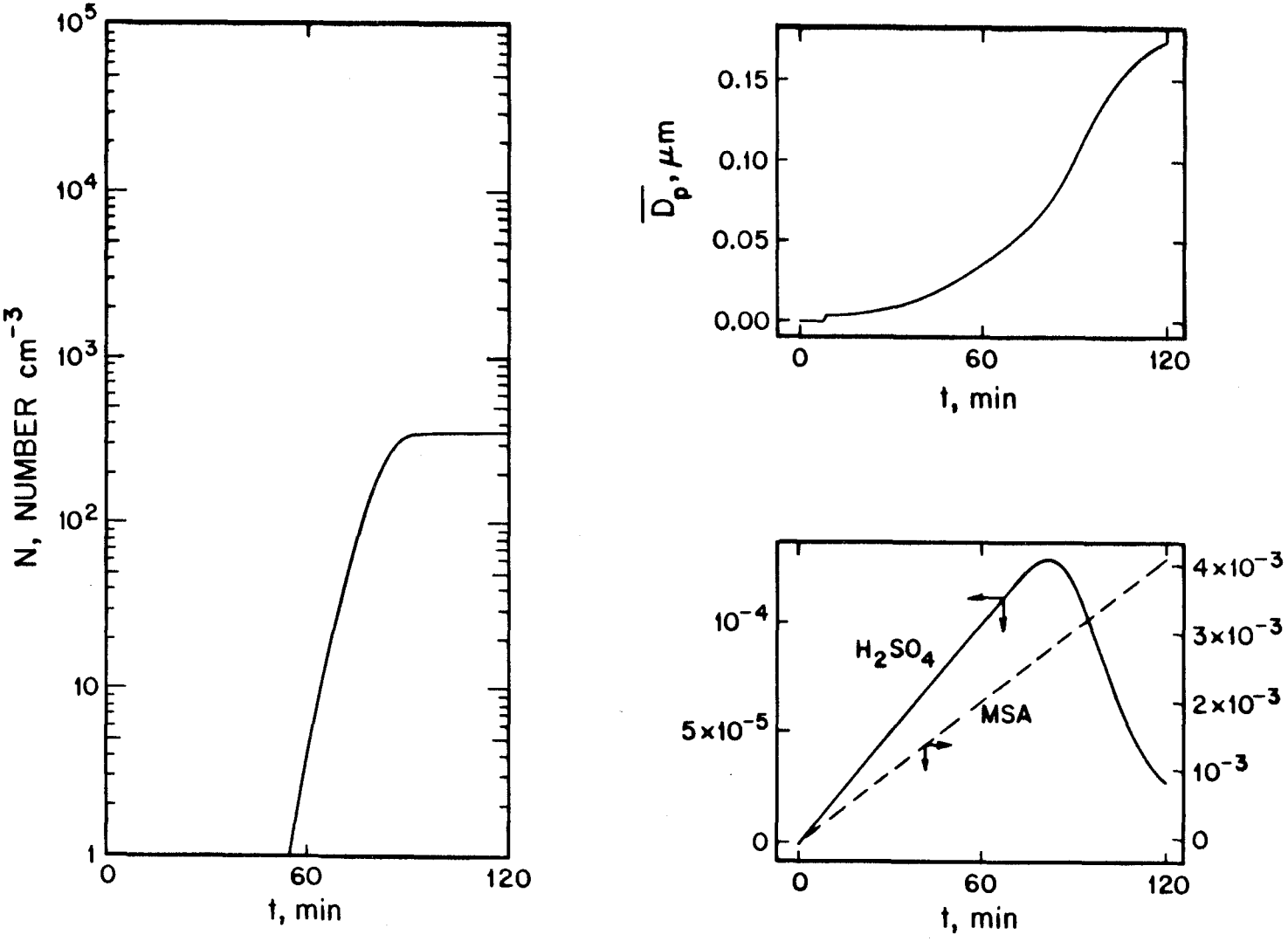
N, NUMBER cm^{-3}
10^5
10^4
10^3
10^2
10
1
0
60
120
t, min
$\overline{D_p}$, μm
0.15
0.10
0.05
0.00
0
60
120
t, min
10^{-4}
5×10^{-5}
0
H_2SO_4
MSA
4×10^{-3}
3×10^{-3}
2×10^{-3}
10^{-3}
0
0
60
120
t, min

Figure 8

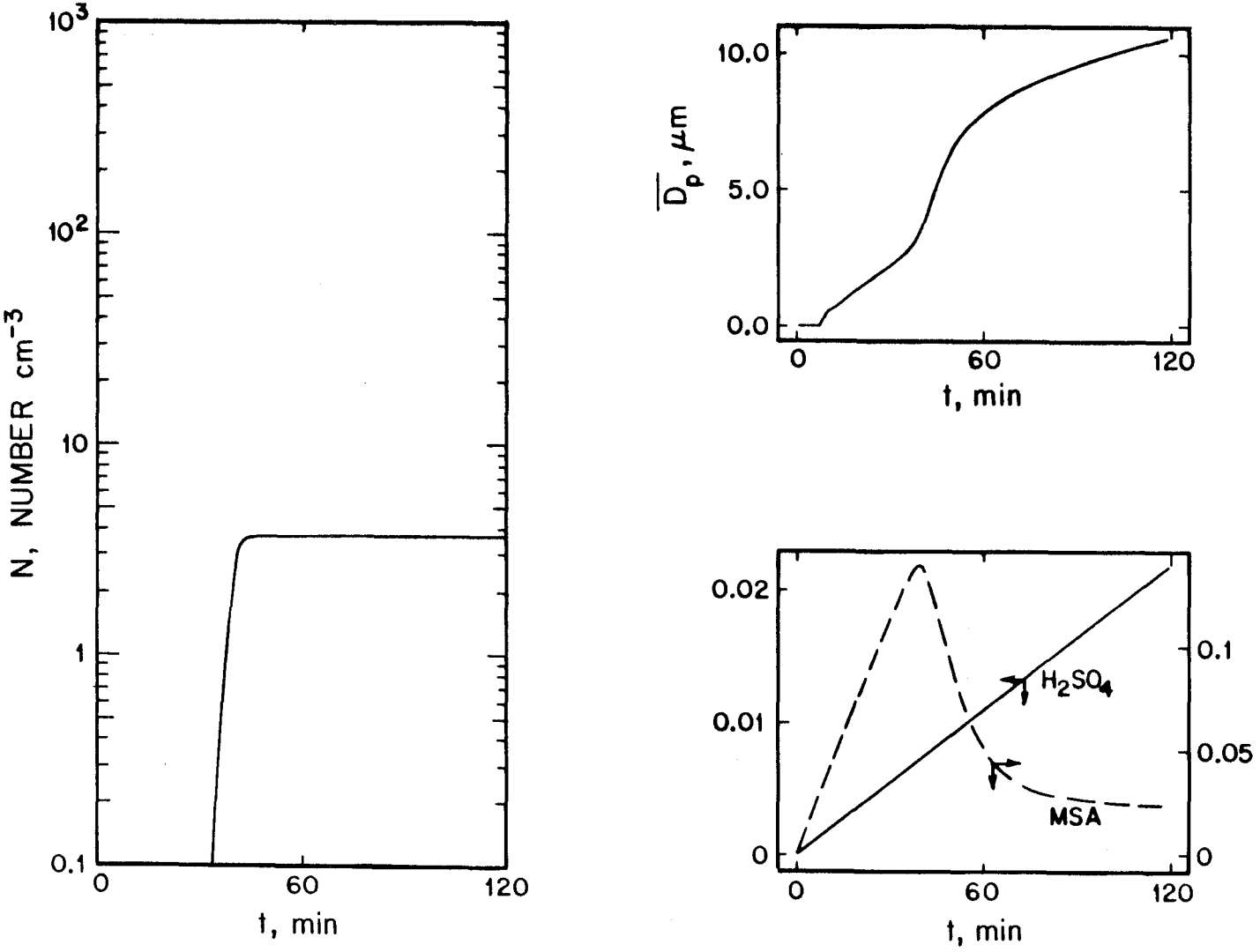
N, NUMBER cm^{-3}
10^3
10^2
10
1
0.1
0
60
120
t, min
$\overline{D_p}$, μm
10.0
5.0
0.0
0
60
120
t, min
0.02
0.01
0
0.1
0.05
0
H_2SO_4
MSA
0
60
120
t, min

Figure 9

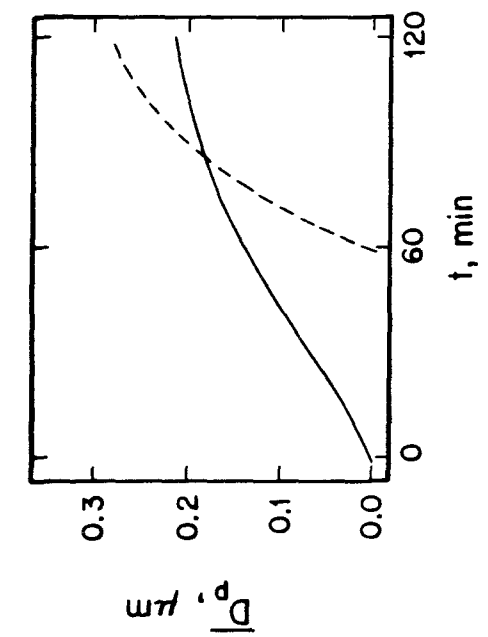
$\overline{D_p}$, μm
0.0
0.1
0.2
0.3
0
60
120
t, min

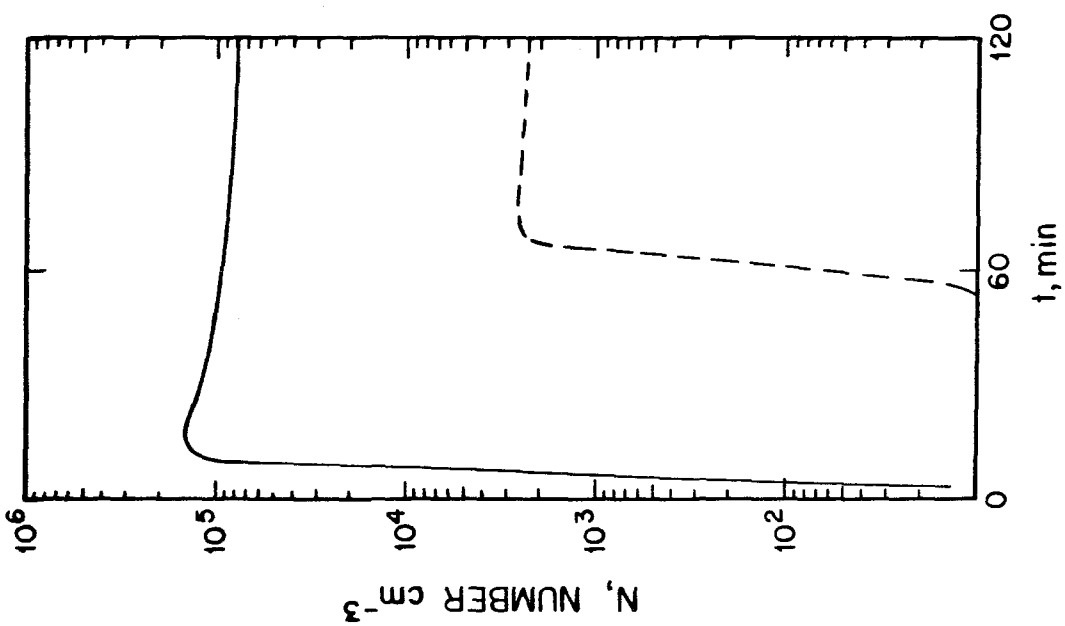
N, NUMBER cm^{-3}
10^2
10^3
10^4
10^5
10^6
0
60
120
t, min

Figure 10

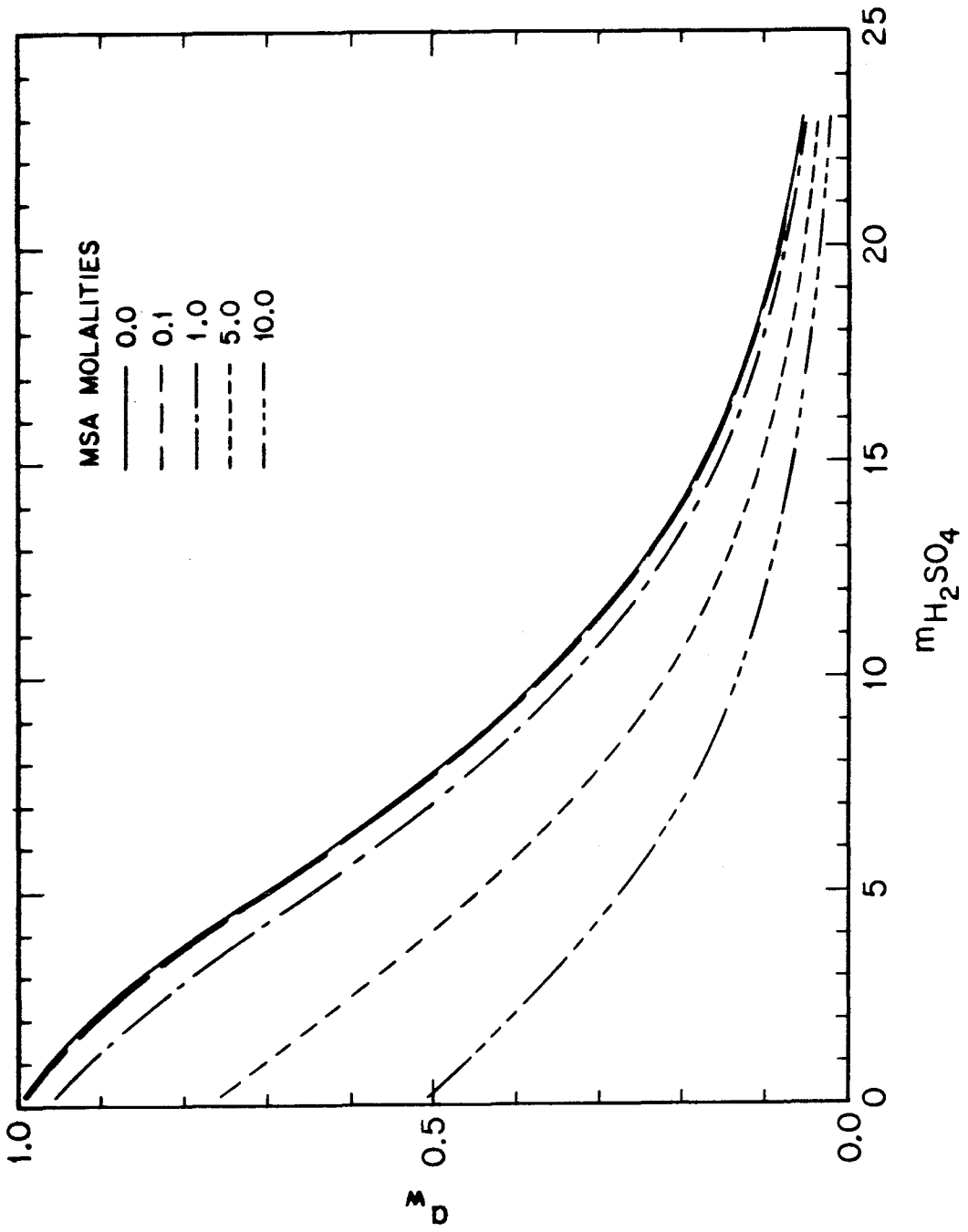

Figure 11

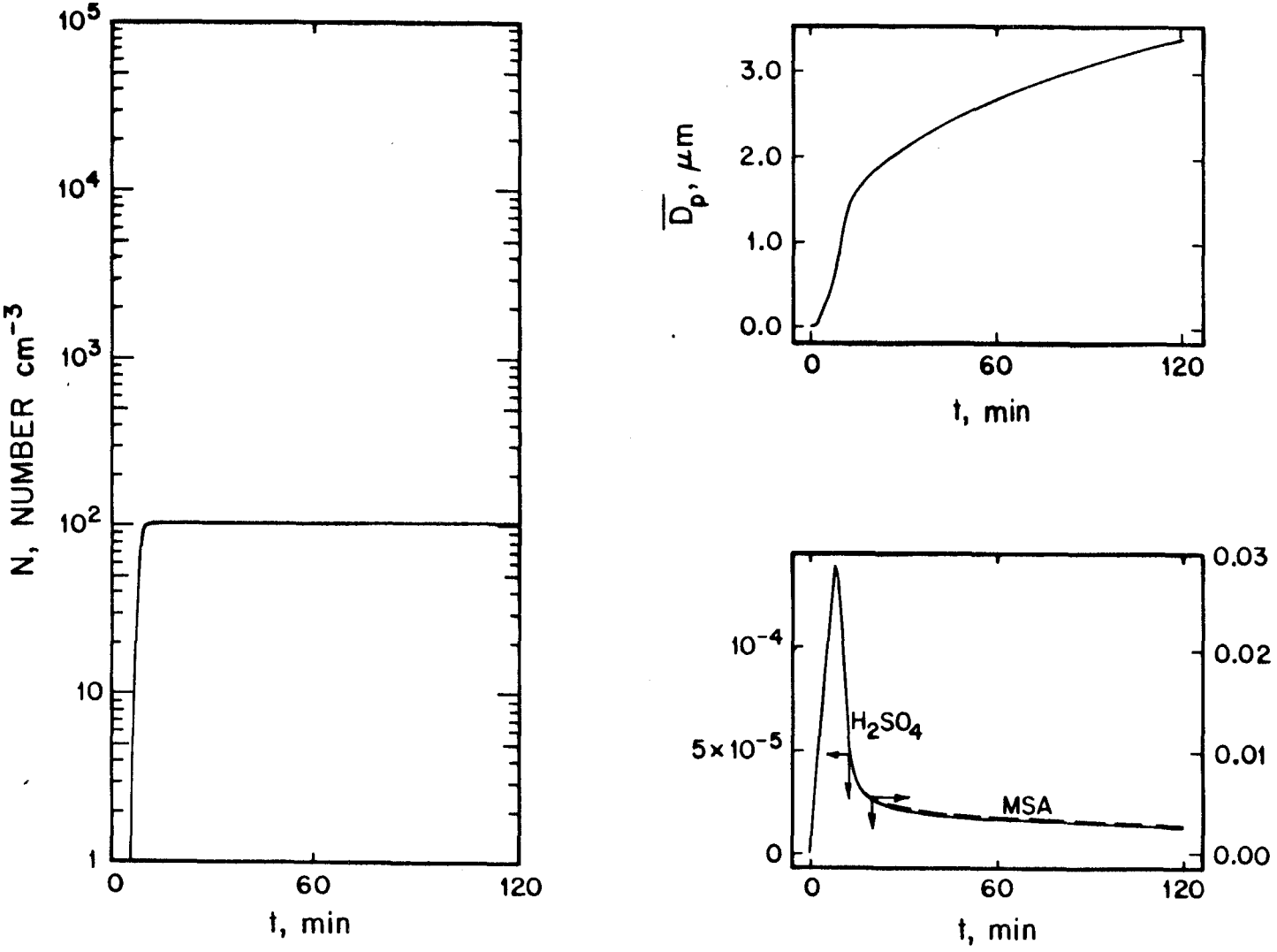
N, NUMBER cm^{-3}
10^5
10^4
10^3
10^2
10
1
0
60
120
t, min
$\overline{D_p}$, μm
3.0
2.0
1.0
0.0
0
60
120
t, min
10^{-4}
5×10^{-5}
0
H_2SO_4
MSA
0.03
0.02
0.01
0.00
0
60
120
t, min

Figure 12

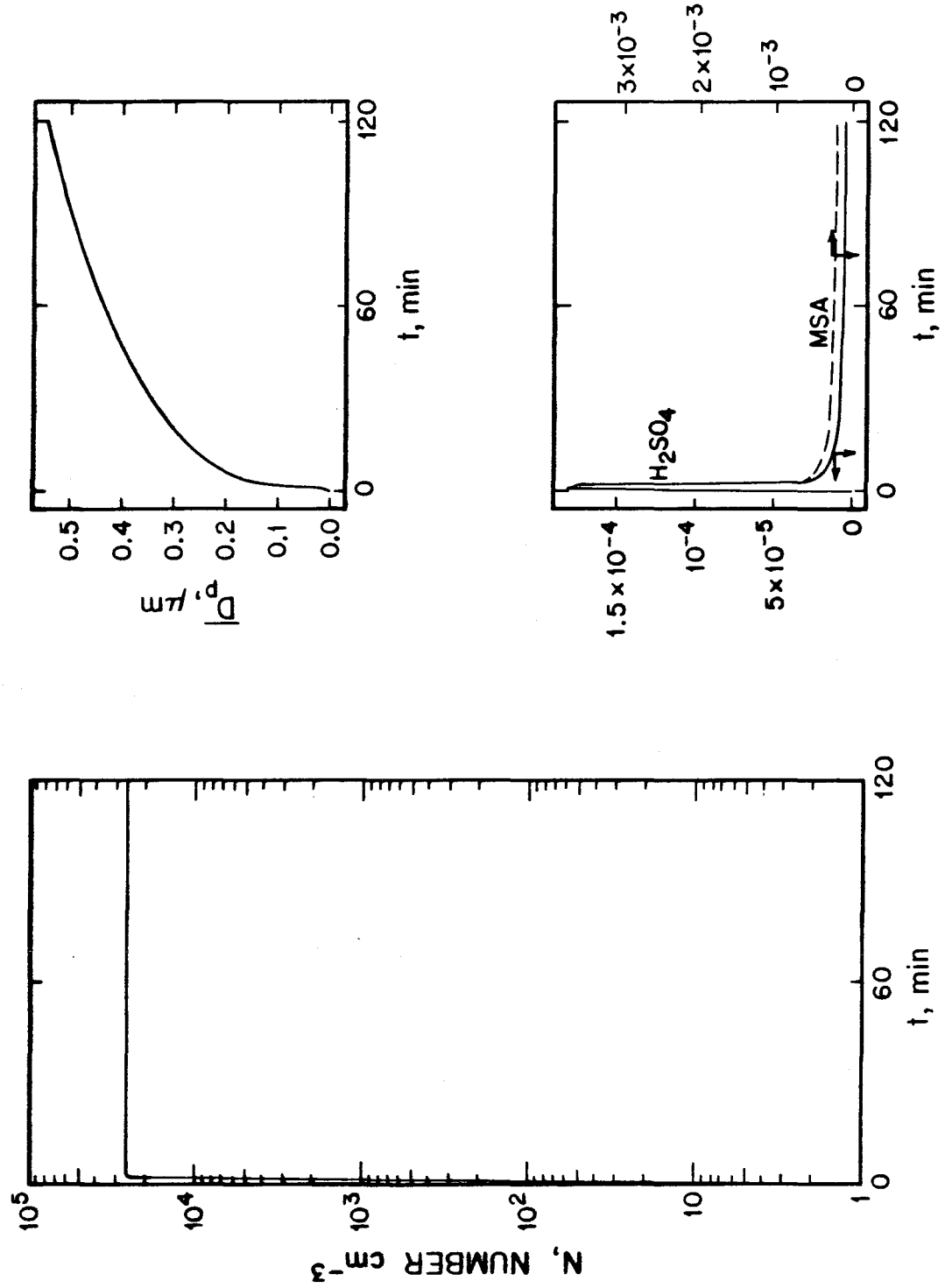
N, NUMBER cm⁻³
10⁵
10⁴
10³
10²
10
1
0
60
120
t, min
D_p, μm
0.5
0.4
0.3
0.2
0.1
0.0
0
60
120
t, min
H_2SO_4
MSA
1.5×10⁻⁴
10⁻⁴
5×10⁻⁵
0
3×10⁻³
2×10⁻³
10⁻³
0
60
120
t, min

Figure 13

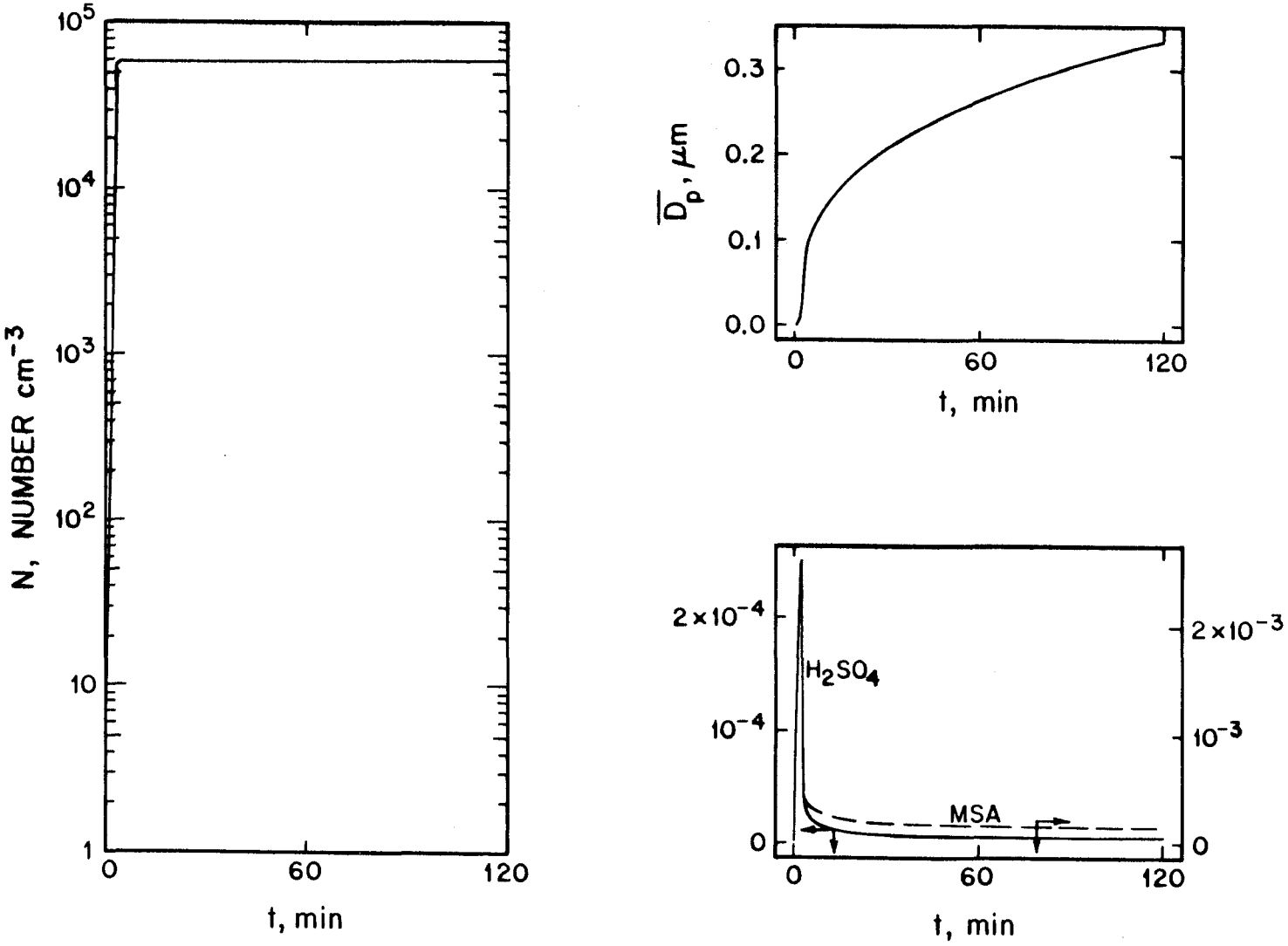
N, NUMBER cm^{-3}
10^5
10^4
10^3
10^2
10
1
0
60
120
t, min
$\overline{D}_p$, μm
0.3
0.2
0.1
0.0
0
60
120
t, min
2×10^{-4}
10^{-4}
0
H_2SO_4
MSA
2×10^{-3}
10^{-3}
0
0
60
120
t, min

Figure 14

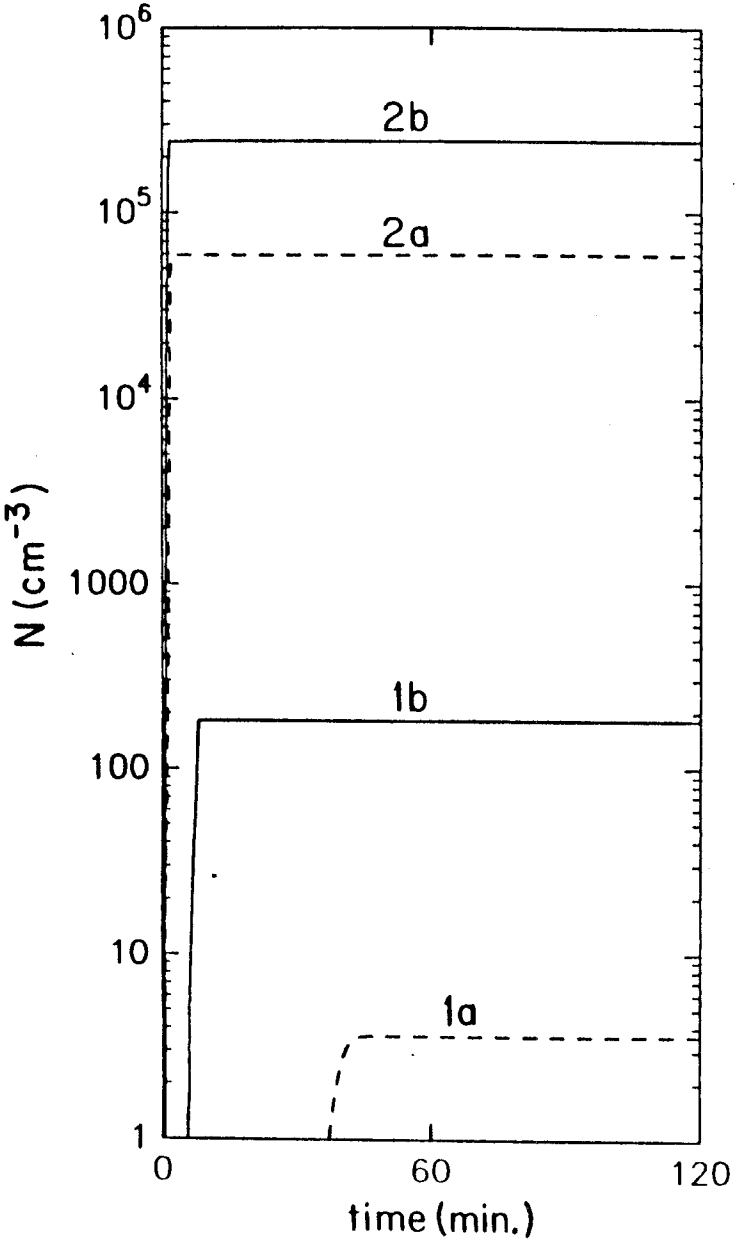
10^6
10^5
10^4
1000
100
10
1
N (cm^{-3})
2b
2a
1b
1a
0
60
120
time (min.)

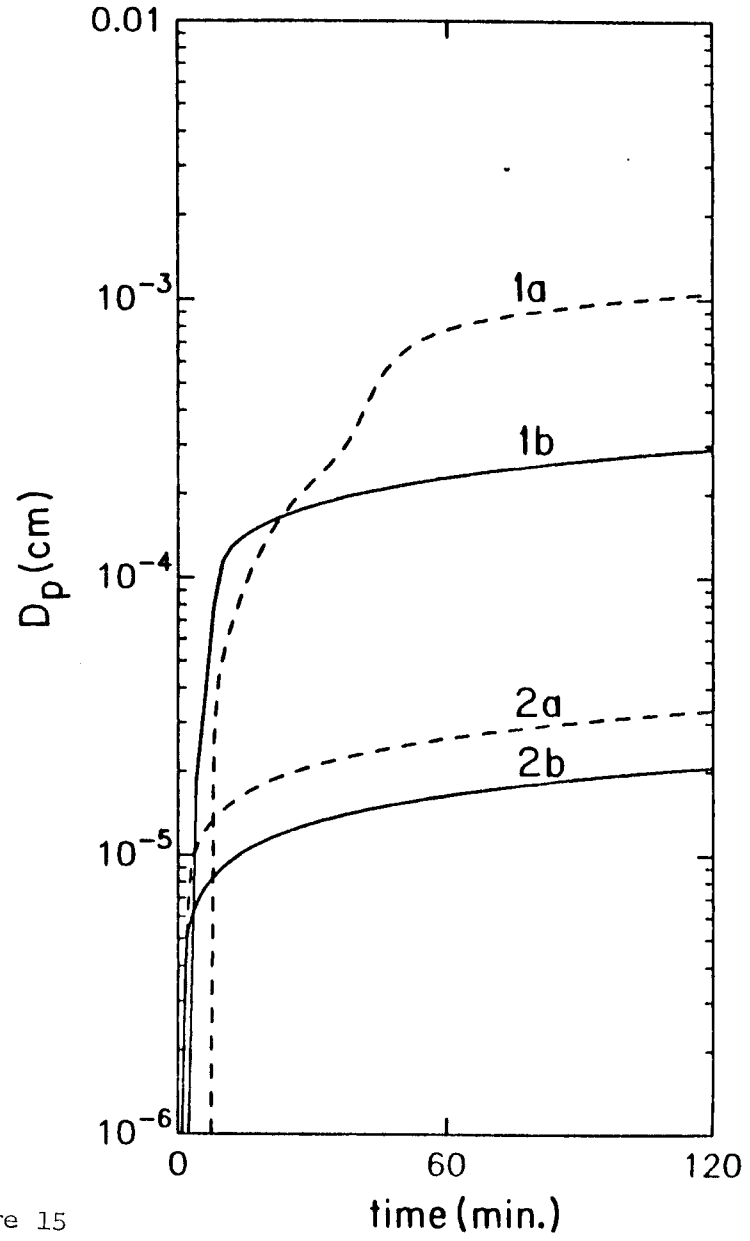
0.01
10^{-3}
10^{-4}
10^{-5}
10^{-6}
D_p (cm)
1a
1b
2a
2b
0
60
120
time (min.)

Figure 15

Chapter V

Experimental Investigation of Binary Nucleation of Methanesulfonic Acid and Water Vapors

The text of Chapter V consists of an article which has been accepted in the *Journal of Aerosol Science.*

I. Introduction

Measurements of binary nucleation rates have taken a number of forms, most of which can be classified into two broad categories: those employing chemical reactions to generate one or both condensable species, and those that begin with the condensable species directly but use external means to bring about conditions favorable for gas-to-particle conversion.

An example of the former category is the experiment reported by Cox (1973). Sulfur dioxide was photolyzed by irradiation with u.v. in a flow reactor containing varying amounts of SO_2 and water vapor. In this manner "threshold" values for the SO_2 concentrations required for significant particle formation at specified relative humidities were determined. However, quantitative comparison with binary nucleation theory is limited by the accuracy with which the conversion rate of SO_2 to H_2SO_4 is known. This example illustrates the main disadvantage of using a chemical reaction-controlled experiment for determination of the rate of nucleation: unless the chemical kinetics are known with a high degree of accuracy, or the concentration of condensable species can be measured directly, the gas-phase concentrations and hence the nucleation driving force are subject to a large uncertainty that is carried over into the comparison of predicted and measured number concentrations.

Another drawback to using a chemical source rate of the condensing vapor is the relative insensitivity of such a system to the nucleation rate expression employed when modelling the particle formation. That is, one can vary the instantaneous nucleation rate (for a given partial pressure) by several orders of magnitude without observing a corresponding variation in the total number predicted theoretically. This weak dependence upon the magnitude of the nucleation rate is a result of the natural "balancing" that occurs in a chemically-reacting system between the rate of vapor production and the combined rates of depletion due to both nucleation and condensation (Warren and Seinfeld, 1985; Warren *et al.*, 1987). In a nucleating system driven by a steady vapor

source rate, the saturation ratio S (the ratio of the gas-phase partial pressure of the nucleating species to its saturation vapor pressure) builds up coincident with increasing the nucleation and condensation rates to maxima, after which gas-to-particle conversion processes deplete the vapor. Condensation is essentially linear in the gas-phase concentration of the condensing species, whereas nucleation is a very strong function of this concentration; however, as will be discussed later, the rate of vapor loss to particles due to condensation quickly dominates over the rate of loss due to nucleation. Thus, faster nucleation will just shift this maximum S to a slightly lower value (occurring slightly earlier), resulting in a very small increase in total number. For example, Warren and Seinfeld (1985) found that multiplying the nucleation rate of the "classical" theory by 10^{20} resulted in an increase in total particle number of less than three orders of magnitude. A chemically-reacting system can therefore not be used to distinguish between alternative nucleation rate expressions that differ greatly in magnitude.

Diffusion cloud chambers, expansion cloud chambers, shock tubes and supersonic nozzles are familiar examples of apparati that generate supersaturation of the condensable species by thermal or mechanical means and which have been used in single-component as well as binary nucleation studies. They are limited, however, to determination of the critical saturation ratios (nucleation onset conditions) and cannot give detailed information on the rate as a function of the saturation ratio. In the diffusion cloud chamber (Mirabel and Clavelin, 1978) the onset conditions correspond to a nucleation rate of about 1 cm^{-3} s^{-1} and are determined visually as a height within the chamber, which can be related to partial pressures by a calculated composition-temperature profile. This instrument has the advantage of operation near room temperature, a temperature range for which most of the physical property data needed for theoretical calculations have been reported in the literature. However, for the sulfuric acid-water system, relative humidities below 100% cannot be achieved within the confines

of stable chamber operation temperatures, and for atmospheric applications a moderate relative humidity range is of most practical interest. The last three devices mentioned have the disadvantage of operating at low temperatures. This requires extrapolation of physical property data, in some cases actually below the solution freezing point (Zahoransky and Peters, 1985), introducing further uncertainty into the theoretical comparisons. The "onset" conditions for these systems are estimated to correspond to nucleation rates of 10^{10} cm^{-3} s^{-1}, which are generally not achievable in atmospheric-type systems where a natural balancing tends to occur between condensable species production and consumption even at relatively high source rates.

In order to address the inadequacies of the present methods for experimental studies of nucleation, a continuous-flow mixing-type device was developed (Okuyama *et al.*, 1987) and extended to binary systems (Kreidenweis *et al.*, 1988). This device uses rapid mixing of carrier gas streams that have been saturated with the species of interest at known temperature and pressure to generate desired initial gas-phase concentrations. The mixed stream is then passed into a reactor volume to allow particles to nucleate and grow to detectable size. Because the initial saturation ratio is the maximum, no natural "balancing" occurs between vapor production and depletion; the number of particles generated is quite sensitive to the nucleation rate and, therefore, can be employed to distinguish between competing theories. In addition, a wide range of initial partial pressures can be investigated by appropriate manipulation of the saturation temperatures and relative flow rates of each stream, so that the "onset" condition for nucleation may be determined by scanning the range of partial pressures of one species by holding the other fixed. Moreover, because the mixing system operates at steady state, high resolution particle counters can be used to determine the number concentration formed during the nucleation burst. Temperatures can be selected so that available property data can be used in the model evaluation.

The goal of the present work is the improvement of the continuous-flow mixing-type experiment designed for the observation of binary nucleation phenomena and its application to acid-water systems. Results are presented for the nucleation of methanesulfonic acid (MSA) and water near 25° C. This particular binary system was chosen in the interest of elucidating the aerosol-forming properties of organosulfur species in the atmosphere; recent laboratory experiments and chemical mechanisms developed indicate that the major sulfur-containing products of the photooxidation of dimethyl sulfide (the most abundant organosulfur species in the environment) are MSA and sulfuric acid, both of which have been detected in the aerosol phase. The theoretical formation rates of aerosol in such a system have been recently investigated (Kreidenweis and Seinfeld, 1987), and the present work is intended to complement the theoretical predictions by determining the applicability of binary nucleation rate theory to the MSA–water system.

II. Description of the experimental apparatus and procedure

A schematic of the experimental apparatus used is shown in Figure 1. High purity nitrogen is filtered through a 0.1 μm pore Teflon filter to a regulator that steps the pressure down to 1.76 $\times 10^4$ kg m^{-2} (25 psig). From this point the flow is split to seven on/off, and then seven metering, valves, three of which are connected to rotameters and four of which are connected to capillary flowmeters, allowing for achievement of a wide range of flow rates. The outputs are directed to one of the final three streams: the one flowing through the water bubblers (designated as the flow rate F_H), the one flowing through the acid bubbler (F_A), and the one that becomes the dilution stream (F_D). All of the lines in the metering system are of dehydrated copper tubing and brass or stainless steel Swagelok. All subsequent lines are Teflon, unless otherwise noted, with Teflon or stainless steel Swagelok fittings.

The stream to be humidified passes first through a bubbler, filled with ultrapure (Milli-Q) water and held at room temperature, to increase the humidity to near its target value, thereby limiting the evaporative cooling in the final humidification stage. The flow then passes through a second bubbler (Figure 2), also containing Milli-Q water, which is immersed in a water-filled tank W_H held at constant temperature with a copper coil through which water is pumped from a Neslab refrigerated circulating constant temperature bath. A thermistor (T_6) enclosed in a glass tube protruding into the bubbler liquid monitors the temperature at which the final humidification occurs. A Teflon filter assembly, containing two Gelman TF-200 0.2 micron pore size Teflon filters, is fitted to the mouth of the bubbler to capture particles entrained during the bubbling process. The efficiencies of this double-filter arrangement were measured and found to be about 99.999999% for NaCl particles of 40 to 75 nm diameter (see Appendix). A pressure tap in the filter assembly just before the filter monitors the pressure inside the bubbler, p_{bw}. The entire assembly as shown in Figure 2 is immersed to the top of the filter holder, which is fitted with a glass cap that is joined to

a glass tee with a three-way Teflon valve; these glass parts are wound with a heating tape maintained at a temperature high enough to prevent condensation of the humidified nitrogen.

At the tee the humid nitrogen is mixed with the dry dilution stream. A thermistor T_2 encased in a Teflon fitting is used to monitor the temperature of the output stream, in order to be sure it is high enough to prevent condensation. (In cases where mixing of the two is not desired, the three-way valve can permit selection of dry flow only or humid flow only.) The mixed stream then flows through about a meter of Teflon tubing wound inside a second water-filled tank (W_A) containing the acid bubbler (Figure 3) in order to assure isothermal conditions upon mixing. Dry nitrogen enters the acid bubbler in the lowest chamber and is bubbled through a frit that supports a pool of liquid acid. A tap over the acid pool monitors the pressure p_{ba} at which the nitrogen becomes saturated with acid, and a glass-enclosed thermistor measures the liquid temperature. Two coarse frits help remove entrained particles, after which the acidified stream is filtered through two Gelman 0.2 μm pore size Teflon filters and passes into the central chamber of the mixing apparatus,also made of Teflon.

The water vapor/nitrogen mixture temperature T_3 is measured just before the stream is injected into the mixing apparatus through eight 0.5 mm holes surrounding the central chamber, causing rapid mixing between the humid and acidic streams. The initial relative humidity and relative acidity are calculated for the conditions at this point of mixing.

A glass tube of inside diameter 40 mm and length approximately 25 cm is fitted by a flange onto the top of the Teflon mixer, and acts as a reactor volume for nucleation and growth of particles. The entire assembly of acid bubbler, mixer, and reactor tube is immersed in the tank W_A, which is maintained at constant temperature by heating with a copper coil, through which water from a Neslab constant-temperature bath is pumped. At its exit, the reactor tube reduces to 9.5 mm (three-eighths inch) glass tubing connected to a tee, one outlet of which

is vented to the laboratory exhaust. A thermistor T_p is located near the tee to monitor bath temperature at this position. The other outlet passes outside of the tank and is connected to a glass tee with a Teflon three-way valve. The valve can be adjusted to draw flow from the experimental apparatus to measure the number of nucleated particles, or to draw room air through a total particle filter connected to one of the legs of the tee. This filtered air is sampled between data points to reduce the exposure of the CNC to acid nuclei. The three-way valve is connected to the CNC inlet by means of a Teflon fitting enclosing a thermistor T_5. The condensation nuclei counter (CNC) is a TSI model 3020; its characteristics are discussed in the Appendix. A list of equipment used, diagrams of the thermistor configurations, a description of the procedure used for filling the acid bubbler, and calibrations for the thermistors and flow rates are also found in the Appendix.

In order to reduce the possibility of contamination when the experiment was not in use, the dry line was flushed continuously with a small purified air flow, which also helped to keep the equipment particle-free. To begin an experiment, this air flow was replaced with dry nitrogen for several hours before data were taken, during which time the CNC and constant-temperature baths were also turned on. The CNC was checked for a zero on the filtered lab air; typical readings were 0.00 to 0.01 particles cm^{-3}. Particle counts for the individual dry, humidified, and acidified streams were also taken prior to a run. The dry and humidified streams generally gave readings similar to those for the filtered lab air.

The acidified stream contained some particles that escaped capture by the bubbler afterfilter. The possibility that these particles resulted from nucleation of the acid vapor with either trace moisture contamination or contact with the butanol inside the CNC was investigated as follows. First, a flow containing only the acid vapor was sampled by the CNC. The flow rate through the bubbler was varied and the corresponding steady state particle concentration was measured.

If the particles were due to nucleation, the counts should be independent of flow rate, since the CNC samples a constant flow rate of about 300 cm^{-3} min^{-1} and the vapor concentration would not change with flow rate, or perhaps decrease slightly if the nitrogen flow did not equilibrate with the acid pool at the higher flow rates. The counts were found, however, to increase with increasing flow rate (see Figure 4). The acid flow was also mixed with dry nitrogen flow to check the effect on the particle counts. The number concentrations measured corresponded closely to what was expected from dilution effects alone, whereas a nucleation mechanism would be expected to show a stronger dependence on the concentration of acid in the sampled stream. The number counts obtained at even the highest flow rates of acid vapor used in the experiments were small (less than about 100 cm^{-3}), several orders of magnitude lower than the numbers produced at the high nucleation rates studied, and were, thus, judged to be acceptable.

An experiment was begun after the temperature readings of the water and acid bubblers reached a steady state. Two types of experiments were performed: in the first, the relative humidity of the mixed stream was kept constant, and in the second, the relative acidity was kept constant. Although individual flow rates were varied, the total flow through the system was maintained at $2\,\ell\,min^{-1}$(measured at STP) to eliminate residence time variations. The flow rate of the constant stream (acid or water vapor) was first set, along with the appropriate flow of dry nitrogen to make up the balance of the $2\,\ell\,min^{-1}$without the addition of the second vapor stream, and the number concentration, which is expected to be zero or small for these conditions, was measured. Next, a small flow of the varying vapor stream was added, with a corresponding decrease in the dry flow, and the steady state number concentration was recorded. This was repeated for decreasing percentages of dry nitrogen in the total flow, until no dry makeup flow was present, and then the procedure was reversed. Temperature and bubbler pressures were measured for each of these conditions. Last, some

points were repeated in arbitrary order to check the reproducibility of the results. Each constant-humidity or constant-acidity experiment was repeated on at least two different days.

III. Calculation of relative humidity and relative acidity

The "nominal" value of the relative humidity (RH) or relative acidity (RA) is the fraction of the total $2\,\ell\,\mathrm{min}^{-1}$ flow that the humid or acidified stream constitutes. The actual RH and RA depend upon the measured temperatures and pressures in the system.

In order to calculate the relative humidity achieved upon mixing of all three streams, one must determine the moles of water evaporated during the humidification process per mole of dry nitrogen flowing into the bubbler. The flow calibrations give the volume (the measured volumetric flow converted to STP) of dry nitrogen that passes through the bubbler. To convert to moles, one simply uses the ideal gas law:

$$\text{moles } \mathrm{N}_2 = F_H \frac{(1013250)}{(298.15)(8.31696 \times 10^7)} \,. \tag{1}$$

Since the temperature of the water inside the bubbler T_{bw} is measured (by the thermistor T_6), the partial pressure of water vapor at this temperature, $p_w^o(T_{bw})$, is equal to the partial pressure of water vapor in the humidified stream, assuming equilibrium between the liquid and gas. The absolute pressure inside the bubbler p_{wb} is also measured, and by difference the partial pressure of dry nitrogen is $p_{N_2} = p_{wb} - p_w^o(T_{bw})$. The "absolute humidity", or ratio of moles of water vapor to moles of dry nitrogen, Y_W, is calculated from

$$Y_W = \frac{p_w^o(T_{bw})}{p_{N_2}} = \frac{p_w^o(T_{bw})}{[p_{bw} - p_w^o(T_{bw})]} \,, \tag{2}$$

and this ratio, assuming ideal gases, is also equal to the ratio of the volumes. Therefore, for all streams measured at STP, the factors for conversion to moles cancel, and the volume of water vapor is equal to $F_W = Y_W F_H$.

The flow rates of the dilution (F_D) and acidified (F_A) streams are also given at STP from the calibrations. Therefore, after mixing of all streams, the total moles of water vapor per total moles of humidified N_2, X, is

$$X = \frac{F_W}{F_W + F_H + F_D + F_A} = \frac{Y_W F_H}{(1 + Y_W)F_H + F_D + F_A} \,. \tag{3}$$

Note that the volume of acid vapor contributing to the total flow has been neglected. This correction is very small, as will be shown in the calculation of the relative acidity.

Again assuming ideal gases, the partial pressure of water vapor in the total flow is equal to the mole fraction of water vapor, multiplied by the total stream pressure (which is assumed to be equal to lab pressure, since no large pressure drops occur between the reactor volume and the exhaust): p_w(mixed stream) = Xp_{lab}. This vapor pressure of water fixes the dew point of the mixed stream. To calculate the relative humidity, the temperature of the mixed stream T_m must be known: $RH = p_w/p_w^o(T_m)$. T_m is assumed to be equal to the bath temperature as measured by thermistors T_3 and T_p, since the mixing is isothermal and the reactor is also maintained at this temperature.

The complete formula for calculating the relative humidity is therefore:

$$RH = \frac{p_{lab}}{p_w^o(T_m)} \frac{Y_W F_H}{[(1+Y_W)F_H + F_D + F_A]} \tag{4}$$

$$Y_W = \frac{p_w^o(T_{bw})}{p_{bw} - p_w^o(T_{bw})} \, . \tag{5}$$

A similar development is used to calculate the relative acidity. However, the partial pressure of acid vapor is on the order of 1 ppm, and is therefore much less than the total pressure inside the acid bubbler, and one obtains

$$Y_A \approx \frac{p_a^o(T_{ba})}{p_{ba}} \tag{6}$$

$$1 + Y_A \approx 1 \, , \tag{7}$$

where T_{ba}, p_{ba} refer to conditions inside the acid bubbler. Then

$$\begin{aligned} RA &= \frac{p_{lab}}{p_a^o(T_m)} \frac{Y_A F_A}{[(1+Y_W)F_H + F_D + F_A]} \\ &= \frac{p_{lab}}{p_{ba}} \frac{p_a^o(T_{ba})}{p_a^o(T_m)} \frac{F_A}{[(1+Y_W)F_H + F_D + F_A]} \, . \end{aligned} \tag{8}$$

An interesting advantageous feature of the experimental design is revealed in the formula for the relative acidity. If the acid bubbler temperature can be

maintained at the same temperature as the mixed stream (T_m), knowledge of the variation of the acid vapor pressure with temperature—and indeed even the actual vapor pressure at the mixed temperature—is not required in order to compute the relative acidity in the mixed stream. This is of great value in investigating the nucleation rates for species for which the vapor pressures are not accurately known (such as methanesulfonic and sulfuric acids): it allows construction of the binary nucleation rate curve as a function of relative humidity and relative acidity (at constant temperature) independent of detailed knowledge of the actual acid vapor pressure. Comparison with theory, however, requires a value for the vapor pressure, since the nucleation rate depends on the bombardment rate of acid molecules, which is a function of the gas-phase concentrations. Unfortunately, in the experiments performed, the temperature measured inside the acid bubbler was somewhat lower than that measured in the rest of the bath (usually about 0.5° C.), so that the term $p_a^o(T_{ba})/p_a^o(T_m)$ had to be included. As discussed in the following sections, a temperature difference of this size results in a change in the calculated RA of about 5 percent, and therefore could not be neglected.

IV. Presentation of experimental data

Experiments were performed at constant nominal relative acidities of 30, 50, and 60 %, and constant nominal relative humidities of 15, 40, and 50 %. The total number concentrations of particles measured as a function of the non-constant species are summarized in Figures 5 through 10, with data taken on different days indicated by separate symbols. The calculated RH and RA are used for plotting, with horizontal error bars used to indicate the computed uncertainty (5%) in these values. Tables of the raw data, the program used to convert these to plottable form, and the resulting plotted data are found in the Appendix. Several immediate observations can be made from the figures. First, the trends in the data are as expected: the RH for which significant nucleation is first observed at a constant RA decreases as the value of RA is increased (and similarly for the constant RH experiments). Second, the measured number concentrations show a strong dependence upon the saturation ratio of the varying species, with orders of magnitude increase in particle number occurring for small changes in the RA or RH. The plotted data are also consistent from day to day and from plot to plot, i.e., the values of N at a given (RA, RH) in a constant RA run are comparable to the values of N at similar coordinates in a constant RH run. The consistency is especially encouraging in that three separate MSA samples were used to generate the data, with parts of the apparatus being disassembled and cleaned each time the sample was changed.

Some comments on the data reproducibility must be made. First, although every attempt was made to reproduce as nearly as possible the value of the constant species when each experiment was repeated, this was difficult for several reasons. First, the lab temperature varies during the day and changes slightly the steady-state temperature attained in the baths. The temperature of the bath containing the water bubbler was the more stable throughout a run, and from day to day, because a smaller mass of water was heated by a coil that fitted closer around the bubbler itself. Fortunately, the temperature of the bath containing

the acid bubbler varied only slowly during a run, due in part to the large mass of water held in the tank. The stirrer located inside this bath did an excellent job of mixing the water to a uniform temperature, as was observed from the close agreement between the temperatures measured by the probe T_p and the thermistor T_3.

Variations in bubbler pressures also contributed to the deviations in the "constant" RA or RH values. First, pressure at the outlet of the water bubbler is dependent upon the total flow at the tee where the humid and dry streams meet. When a flow rate through the water bubbler is set and a bubbler pressure recorded for humid-only flow, this pressure increases when dry flow is added to the system, and depends upon the actual flow rate of the dry stream as well. Therefore, with all other variables kept constant, the relative humidity decreases with increasing dry flow, although the humid stream is maintained at a constant fraction of the total flow, simply because the pressure at which saturation occurs is increased. Second, it was observed that the pressure inside the acid bubbler increased slowly throughout the course of the experiments. This was thought to be due to wetting of the filters or frits. As a result the same flow setting for the acidified stream on different days produced slightly different values for the RA.

Although all of these effects were taken into account in the data analysis and the actual values are indicated on the plots, they resulted in some deviations in the chosen constant values (RH or RA) Since, as will be discussed, the confidence in the calculated RA and RH is within about 5%, these smaller deviations are seen to be acceptable.

In the next section, the impact of experimental error and uncertainty upon the interpretation of the data will be evaluated. Appropriate comparisons of the experimental results with the predictions of binary nucleation theory are made in a subsequent section.

V. Estimation of uncertainty and error

There are five possible sources of uncertainty and error in the measurement and interpretation of the data: uncertainty in readings from the equipment, such as thermistors, pressure gauges, and the counting efficiency of the CNC; uncertainty in the reproducibility of the flow rates; the question of the purity of the acid throughout the course of the experiments; losses of vapor and/or particles to surfaces or to evaporation; and the effect of the flow pattern, including mixing as well as the flow in the reactor chamber.

Uncertainty in the relative humidity and relative acidity

The uncertainties in temperature and pressure readings and in the reproducibility of flow rates impacts the computed values of relative humidity and relative acidity, and may be quantified by the following analysis. By taking the logarithm of the expression for the relative humidity and differentiating, one obtains the relation

$$\frac{dRH}{RH} = \frac{dY_W}{Y_W} + \frac{dF_H}{F_H} + \frac{dF_T}{F_T} + \frac{dp_{lab}}{p_{lab}} + \frac{dp_w^\circ(T_m)}{p_w^\circ(T_m)} \ . \tag{9}$$

The flow rates of the acidified and dry streams are generally reproducible to within 1.5 percent and that of the humidified stream to within about three percent. The uncertainty in the total flow is less than or equal to the maximum uncertainty and may therefore be taken as 3 percent as an upper bound. The uncertainty associated with the thermistor measurement of the temperatures is approximately 0.04 °C. The laboratory pressure is read from a mercury manometer to the nearest 0.1 mm Hg; therefore the lab pressure is known to better than $0.1/760 \approx 10^{-4}$, and its error can be neglected relative to the other errors (as will be shown). The variation in Y_W may be expressed as

$$\frac{dY_W}{Y_W} = \frac{dp_w^\circ(T_{ba})}{p_w^\circ(T_{ba})} + \frac{dp_{ba}}{p_{ba}} \ , \tag{10}$$

where the approximation $p_{bw} - p_w^\circ(T_b) \approx p_{bw}$ has been made. The uncertainty in the saturation vapor pressures must be related to the uncertainty of the

temperature measurement. This is done by assuming that, over the temperature interval of interest, the saturation vapor pressure may be expressed as

$$\ln p_w^o(T) = \frac{A}{T} + B \tag{11}$$

$$\frac{dp_w^o(T)}{p_w^o(T)} = -A\frac{dT}{T^2} \, . \tag{12}$$

For a representative value of $T = 23°\text{C}.$ and the interval $20°\text{C}. < T < 30°\text{C}.$, $A \approx -5216$. Then

$$\frac{dp_w^o(T)}{p_w^o(T)} \approx -5216\frac{.04}{(296.15)^2} = 2.4 \times 10^{-3} \, . \tag{13}$$

If the uncertainty in the temperatures was as high as 0.1°C., the relative error would be $\approx 6 \times 10^{-3}$, still less than one percent.

The pressure inside the water (and acid) bubbler is read as a gauge pressure, and therefore $p_{bw} = p_{lab} + p_{bw,gauge}$, and

$$\frac{dp_{bw}}{p_{bw}} = \frac{dp_{bw,g}}{p_{lab} + p_{bw,g}} \, . \tag{14}$$

This gauge pressure is read on a scale of 0 to 5 psig (3.446×10^4 N m^{-2}) with 0.1 psig (689.3 N m^{-2}) divisions, and therefore with an uncertainty of approximately 0.03 psig (206.8 N m^{-2}). For a typical laboratory pressure of 14.2 psia (9.788×10^4 N m^{-2}),

$$\frac{0.03}{14.2+5} < \frac{dp_{bw}}{p_{bw}} < \frac{0.03}{14.2+0}$$

$$0.0016 < \frac{dp_{bw}}{p_{bw}} < 0.0021 \, . \tag{15}$$

Therefore, a reasonable estimate of this uncertainty is $dp_{bw}/p_{bw} = 0.002$.

The total uncertainty in the relative humidity can thus be approximated as

$$\frac{\sigma_{RH}^2}{RH^2} = 2\left(\frac{dp_w^o(T)}{p_w^o(T)}\right)^2 + \left(\frac{dp_{bw}}{p_{bw}}\right)^2 + \left(\frac{dF_H}{F_H}\right)^2 + \left(\frac{dF_T}{F_T}\right)^2$$

$$\frac{\sigma_{RH}}{RH} = 0.0048^2 + 0.002^2 + 0.03^2 + 0.03^2 = 0.043 \, . \tag{16}$$

A conservative estimate of the total uncertainty is that the relative humidity is known to within five percent.

Using similar arguments for the calculation of uncertainty in the relative acidity, one obtains

$$\frac{dRA}{RA} = \frac{dp_{ba}}{p_{ba}} + \frac{dF_A}{F_A} + \frac{dF_T}{F_T} + 2A\frac{dT}{T^2} + 2B\frac{dT}{T} \ . \tag{17}$$

The acid vapor pressure curve has been estimated as

$$\ln p_a^o(T) = \frac{-8006}{T} + 2.14237 \ln T + 7.45208 \ . \tag{18}$$

Again using a representative temperature of 23 °C., for an uncertainty of ±0.04 °C., the sum of the two terms relating to the uncertainty of the vapor pressure is approximately equal to 0.008; for an uncertainty of ±0.1°C., this is approximately 0.02. Also, for a temperature difference of ±0.5° C. between the acid pool and the bath, the contribution to the change in RA is 0.046; therefore, as indicated earlier, the measured temperature of the acid pool must be used in calculating RA.

The acid bubbler pressure is also read as a gauge pressure, on a scale of 0 to 15 psig (1.034×10^5 N m^{-2}) with 0.5 psig (3346 N m^{-2}) divisions, so that the uncertainty is approximately 0.2 psig (1379 N m^{-2}). Thus

$$\frac{0.2}{14.2 + 15} < \frac{dp_{ba}}{p_{ba}} < \frac{0.2}{14.2}$$

$$0.007 < \frac{dp_{ba}}{p_{ba}} < 0.0141 \ . \tag{19}$$

For the total uncertainty, one computes

$$\frac{\sigma_{RA}^2}{RA^2} = 0.008^2 + 0.014^2 + 0.03^2 + 0.03^2$$

$$\frac{\sigma_{RA}}{RA} = 0.045 \ . \tag{20}$$

It can therefore be estimated that the relative acidity is also known to within five percent.

Effect of acid purity

Methanesulfonic acid from Alfa Chemical Company, with an assayed purity of 99.5%, was used without further purification. The nitrogen used in the experiment contains a moisture content of not greater than 10 ppm. This corresponds to 0.01 cm^3 of water vapor per liter of nitrogen, or 4.1×10^{-7} moles of water vapor per liter of nitrogen. Assuming two weeks of a constant nitrogen flow of $1\,\ell\,min^{-1}$through the acid bubbler (the actual total nitrogen flow over a series of experiments is smaller than this), at the end of the two weeks the acid will have absorbed 2.5×10^{-4} moles of water vapor. Since about 300 cm^3 of acid are held in the bubbler (about 4.7 moles acid), the mole fraction of acid will have decreased to 0.999 after this time. Thus the change in activity that results from the bubbling process alone is only about 0.1%, and is not important. Since acids are, in general, hygroscopic, the sample may pick up moisture during the runs (from diffusion of water vapor from the mixing chamber into the acid bubbler) or in handling. However, the reproducibility of the data with different acid samples, and with the same sample on different days, justifies the assumption that no measurable degradation of acid quality occurred over the course of the experiments.

Effect of CNC response characteristics

The response characteristics for the CNC used have been measured by Bartz et al. (1985). The counting efficiencies (based on the front panel readings) for 3 nm and 20 nm particles, respectively, were reported to be 0.06 $\pm$0.03 and 0.86 $\pm$0.05. The counting efficiency for particles having diameters above about 30 nm is essentially 100%. Since the aerosol sizes are not measured in this experiment, the effect of the counting efficiencies upon the data can be estimated only by comparison with the theoretical predictions for particle size; these are summarized in Figure 11 .

These predictions of Figure 11 were generated using the integral model (to be described later) and assuming a residence time in the reactor of 12 seconds.

Both the aqueous diameter (at the prevailing RH) and the diameter based on the acid content alone (that is, as if the aqueous particle were dried completely) are shown. The dry diameter is approximately half of the aqueous. Most of the calculated aqueous diameters are seen to be above 30 nm (0.03 μm), except for large nucleation rates (generally above 10^8 cm^{-3} s^{-1}), which occur at the higher RH and RA values.

Interestingly, particle formation in the experiments was observed at the higher RA and RH ranges, but the number concentrations were much smaller than would be predicted theoretically form nucleation rates $> 10^8$ cm^{-3} s^{-1} (the model results will be discussed more thoroughly in a following section). Therefore, one can interpret Figure 11 in two ways: first, by checking the grown droplet size for the experimental RH and RA, although the computed rate may be much larger than the apparent measured rate, and determining whether losses are likely to occur; or second, by checking the droplet sizes at nucleation rates (for the given constant RA or RH) that correspond more closely to the measured number concentrations (nucleation rates less than 10^6 cm^{-3} s^{-1}). Since nucleation and condensation compete for available acid vapor, the final D_p will be different for each of these approaches. If the second approach is chosen, one does not expect to see losses due to counting efficiency, as the grown sizes are rather large. If the first approach is taken, the predicted particle sizes are quite small and losses due to decreases in counting efficiency, as well as possible evaporative losses, may be significant.

Below particle concentrations of 1000 cm^{-3}, the CNC counts particles individually. Since more than one particle may occasionally be in the viewing volume, a correction must be made to the front panel readings for this coincidence error. The formula is

$$N_{actual} = N_{indicated} \exp(N_{actual} Q t) \ , \qquad (21)$$

where $Q = 5$ cm^3 s^{-1} and $t = 35$ μs spent in the viewing volume. N_{actual} in the exponential term may be approximated by $N_{indicated}$. At higher concentra-

tions the CNC operates in the photometric mode, using total scattered light to determine particle concentration. The instrument is calibrated from the factory for the counting in this mode, and losses should be negligible as long as the butanol used for detection has not been overly diluted; this is assured by frequent draining and replacement of the alcohol pool. Also, the preset zero of the instrument in the photometric mode was checked after the series of experiments was completed, and found to be correct.

The possibility also exists that aqueous particles, flowing through the CNC saturator tube, which is maintained at 35 °C., may lose water by evaporation before reaching the condenser tube. (The acid may be considered as nonvolatile over the experimental time scale.) If the quantity of acid in the particle is such that it would form a particle with a diameter of at least 30 nm, this would have no effect on the ultimate counting efficiency. However, if the particle evaporates to below 30 nm, this could result in low measured number counts. Again, the importance of this effect can only be evaluated by comparison with theory; Figure 11 summarizes the expected impact of evaporation.

Effect of particle and vapor losses to surfaces

In order to obtain estimates of the particle and vapor losses to surfaces in the apparatus, one should first calculate the Reynolds numbers inside the tubing and inside the reactor. For a $2\,\ell\,\mathrm{min}^{-1}$ flow rate and $\nu = 0.15\ \mathrm{cm}^2\ \mathrm{s}^{-1}$, one finds that the Re inside 1/4" O.D. Teflon tubing (3/16" (0.476 cm) I.D.) is about 600, and inside the reactor it is equal to about 70. Thus the flow can be adequately characterized as laminar.

The problem of convective mass (or heat) transfer in laminar flow through a circular pipe is known as the Graetz problem, and the solution is well known. Friedlander (1977) uses this solution to determine the fractional particle number concentration remaining suspended in the carrier gas as a function of the aerosol and flow properties. If the walls are considered to be perfect sinks for the vapor or particles, the mixed mean concentration n_{av} can be related to the initial

concentration n_0 by

$$\frac{n_{av}}{n_0} = 8 \sum_{n=0}^{\infty} \frac{G_n}{\lambda_n^2} \exp\left(-\lambda_n^2 x_l\right) , \tag{22}$$

where G_n and λ_n are terms in the series solution, and x_l is the dimensionless length. For particle diffusion,

$$x_l = \frac{x}{a^2} \frac{D}{2U} , \tag{23}$$

and for vapor diffusion

$$x_l = \frac{x}{a^2} \frac{D_A}{2U} . \tag{24}$$

Here, x is the axial length, D is the particle diffusivity, d_p is the particle diameter, D_A is the vapor diffusivity, and U is a characteristic velocity. The relationship between D and d_p is given by the Stokes-Einstein relation; values of D tabulated by Friedlander (1977) were used here.

Representative values for n_{av}/n_0 for vapor and particles in both the tubing and reactor are shown in Table 1. It is seen that the walls are predicted to be effective sinks for particles smaller than about 0.01 μm, and also effective in reducing the vapor concentration. It is hoped that the glass and Teflon materials used in the apparatus will not in fact act as perfect sinks for these species, but the calculation does show that diffusional losses may become important for very small particles. Since the size of the particles was not measured, one can only estimate the importance of this effect by recourse to theoretical calculations of particle sizes (Figures 11 and 12).

The sizes of critical nuclei, shown in Figure 12, are on the order of 0.001 μm for the conditions of the experiment. (The total number of molecules in the critical cluster, $n_a + n_w$, are also indicated.) If these critical nuclei are formed in the mixing chamber (with a characteristic length scale of about 1 cm), some losses of the nuclei to the chamber walls may occur. However, theory indicates that the critical nuclei grow very rapidly initially, and the grown droplet sizes at the reactor outlet (Figure 11) are, for the most part, larger than 0.01 μm,

Table 1

Reduction in particle and vapor concentrations due to diffusional losses

a. Distance (cm) traveled to achieve indicated reduction in particle concentration

n_{av}/n_0	0.96	0.84	0.40	0.0005
$D_p = .001\ \mu m$	0.41	4.1	41	410
$D_p = .01\ \mu m$	40	400	4000	4×10^4
$D_p = .1\ \mu m$	3100	3.1×10^4	3.1×10^5	3.1×10^6
$D_p = 1\ \mu m$	7.6×10^4	7.6×10^5	7.6×10^6	7.6×10^7

b. Distance (cm) traveled to achieve indicated reduction in vapor pressure

p_{av}/p_0	0.96	0.84	0.40	0.0005
MSA	0.18	1.8	18	180
H_2O	0.085	0.85	8.5	85

and usually larger than 0.1 μm. The calculations summarized in Table 1 indicate that the losses will be minimal under these conditions. Even if $n_{av}/n_0 = 0.5$, the outlet concentration would differ by only a factor of 2 from the true number formed, not a very large error considering the order of magnitude changes in N that occur due to small changes in the initial RH or RA. Since the losses would be largest for smaller particles, which are associated with large N, this factor of 2 or 3 would help explain why explain why the slope of the data is smaller than that predicted theoretically, in some cases almost leveling off at higher vapor concentrations. This last point will be discussed more thoroughly subsequently.

The vapor losses are of greater concern, since a 5% change in RA or RH can change the predicted N by an order of magnitude; Table 1 indicates that such vapor losses may be rapid. It is very difficult to quantify the vapor or particle losses, either experimentally or theoretically, more accurately than the above simple analysis, particularly if the absorptivity of acid and water vapors on the materials used in the apparatus are unknown. However, the adsorptivities are expected to be low, since very inert materials—Teflon and glass—were used.

Effect of imperfect mixing

One of the critical assumptions in this experiment, and the modeling of the data, is that the mixing of the acidic and humid streams occurs on a very fast time scale and results in a perfectly homogeneous mixture. To justify this assumption, the characteristic mixing time can be evaluated using Taylor microscale arguments and compared with the residence time in the mixing chamber. This is followed by a detailed study of the effect of imperfect mixing upon the initial nucleation rates and upon the overall observed rate of particle formation.

The characteristic mixing time in the mixing chamber is given by

$$\tau_M = \left(\frac{ML^2}{KE}\right)^{1/3}, \tag{25}$$

where M is the vapor mass in the mixing chamber, L is an appropriate length,

and KE is the kinetic energy of the entering vapors:

$$KE = \rho Q \frac{1}{2} u^2 \ . \tag{26}$$

Here ρ is the vapor density, Q the volumetric flow rate, and u the linear velocity. In the Teflon mixing chamber used in this experiment, the combined dry and humidifed nitrogen streams are injected into the cylindrical mixing chamber (which has a volume of about 1 cm^3) by means of eight 0.5 mm holes. The linear velocity can be readily calculated for various total (dry+humid) flow rates (since the velocity of the acidified stream, entering the mixing volume from the bottom via a relatively large opening, is much less, its contribution to the total kinetic energy can be ignored), and from this one computes the corresponding τ_M. Since the total flow rate through the mixer is kept constant at $2\,\ell\,min^{-1}$, the residence time in the mixing chamber (τ_R) is also constant, and equal to approximately 30 ms.

Table 2 shows the values of the mixing time and the ratio τ_R/τ_M for various (dry+humid) flow rates. For purposes of rapid and complete mixing, the quantity τ_R/τ_M should be large. The smallest (dry+humid) flow used in the experiments (for $RH_{nom} = 15\%$) was 300 $cm^3\ min^{-1}$, and it is seen from the table that the mixing time is on the order of tens of milliseconds and the ratio τ_R/τ_M is actually order one. For higher (dry+humid) flow rates, the mixing would appear to be adequate.

The effect of segregation on the overall observed nucleation rate should be investigated. This can be done by assuming different "mixedness" ratios (corresponding to the degree of mixing in individual fluid packets) and computing the initial theoretical nucleation rate for that packet. The parameter X is defined as the fraction of the packet that consists of acidified flow. Then the relative humidity and acidity inside the packet are calculated from

Table 2

Characteristic mixing time, τ_M, and the ratio of residence to mixing times, τ_R/τ_M

$F_H + F_D$ (cm^3 min^{-1})	τ_M (ms)	τ_R/τ_M
300	16	1.9
600	7.9	3.8
800	5.9	5.1
1000	4.7	6.3
1200	4.0	7.6
1400	3.4	8.9
1800	2.6	11

Table 3

Experimental conditions used in mixing analysis

	case 1	case 2	case 3
F_A	1011	1011	1011
F_H	396	808	1004
F_D	607	198	–
p_{b_w} (psig)	0.44	0.63	0.73
p_{b_a} (psig)	5.75	5.75	5.80
T_{b_a} °C.	24.88	25.01	25.00
T_{b_w} °C.	23.81	23.85	23.86
T_m °C.	25.23	25.35	25.34
RA_{calc}	0.344	0.341	0.340
RH_{calc}	0.179	0.357	0.440

$$RH = \frac{p_{lab}}{p_w^o(T_m)} \frac{(1-X)Y_w F_H}{(XF_A + (1-X)[(1+Y_w)F_H + F_D])}$$
$$RA = \frac{p_{lab}}{p_{ba}} \frac{p_a^o(T_{ba})}{p_a^o(T_m)} \frac{XF_A}{(XF_A + (1-X)[(1+Y_w)F_H + F_D])} . \quad (27)$$

A value of $X = 0.5$ indicates perfect mixing.

Representative calculations were performed for three experimental conditions used in the $RA_{nom} = 50\%$ run, summarized in Table 3 and Figure 13, for which RH varied from 0.179 to 0.440. Since the total (dry+humid) flow is constant, the mixing should be similar in all three runs; the effect of the mixing on the desired RH and RA will be investigated. The values of RH and RA were calculated for X ranging from 0 through 1 (Figure 13); from these initial vapor concentrations, the theoretical initial binary nucleation rate was computed. The variation of J_B with X is shown in Figure 14. It is seen that the peak nucleation rate is shifted from the desired conditions ($X = 0.5$) toward the region of lower acid content, and drops off rapidly for X greater than 0.5. Thus fluid packets that contain concentrations of acid vapor somewhat smaller than the perfectly mixed concentration experience initial nucleation rates similar to, or slightly higher than, the expected value, whereas packets relatively rich in acid vapor exhibit sharply decreased nucleation rates.

In order to evaluate the overall observed initial nucleation rate, the following approximate analysis was made. It was assumed that a Gaussian distribution of X exists in the mixing chamber, centered about the desired value of $X = 0.5$,

$$G(X) = \frac{1}{(2\pi)^{1/2}} \frac{1}{\sigma_X} \exp\left(\frac{-(X-0.5)^2}{2\sigma_X^2}\right) , \quad (28)$$

where σ_X is the standard deviation of the distributed variable. By normalizing the computed nucleation rate at X with the desired rate, $J_B(0.5)$, the nucleation rate relative to the expected is obtained. Then the total relative nucleation rate is

$$\tilde{J}_{total} = \int_{X=0}^{1} \frac{J(X)}{J(0.5)} G(X)\, dX . \quad (29)$$

Table 4

Overall dimensionless nucleation rate, $\tilde{J}(X)$, for various σ_X

	$\sigma_X = 0.05$	$\sigma_X = 0.1$	$\sigma_X = 0.2$	$\sigma_X = 0.45$
case 1	1.022	0.984	0.743	0.390
case 2	1.061	1.093	0.934	0.532
case 3	1.018	1.017	0.886	0.518

The integrand was evaluated using $\Delta X = 0.02$ and a simple trapezoidal rule was used for the integration. Although this method is not highly accurate, it will provide some measure of the importance of segregation in the system.

The overall dimensionless nucleation rates for the three experimental conditions discussed above, and assuming various values of σ_X, are shown in Table 4. The value of $\sigma_X = 0.05$ corresponds to nearly perfect mixing, whereas a value of 0.45 represents a highly nonideal mixing situation. It is seen that the overall nucleation rate for small σ_X is within a few percent of the expected rate, but can be less than half of the desired at higher σ_X. However, the calculated total rate is still within an order of magnitude of $J(0.5)$, which is acceptable, particularly when compared to other sources of error in the experiment. For example, a $\pm 5\%$ variation in RH or RA results in an order of magnitude variation in total number of particles. It is difficult to determine experimentally the degree of mixing achieved, or its impact upon the experimental results, but from this analysis it would appear that, for the experiments performed, the mixing was adequate, except perhaps for $F_H = 300$ cm^3 min^{-1}; even in this case, the effect of moderately imperfect mixing on the observed results should be negligible.

Effect of flow pattern in reactor

The experiment is modeled using an integral model that applies to either a batch reactor or a plug flow reactor (at constant temperature and volume). As discussed above, the Reynolds number inside the reactor is not large, and even after accounting for entrance effects (a few diameters in the axial direction) it would appear that the flow through most of the reactor is laminar. However, no tracer experiments have been done to estimate the actual behavior inside the reactor. Instead, a simple analysis is presented here to discuss the impact upon the experimental results of the assumption of the two extreme cases of chemical reactor: the plug flow (PFR) and the perfectly mixed continuous stirred tank (CSTR). The actual conversion of a reactor will be somewhere between the conversions predicted for each of these.

First, the integral model (SNM model) that will be described later in this work was used to find the total number concentration and mean particle size at the outlet of a plug flow reactor after a residence time τ. This involves the numerical integration in time of the reaction rate equation

$$dRA/dt = -R_J - R_c \ , \tag{30}$$

where R_J and R_c are the rates of nucleation and condensation, respectively, converted to the appropriate units. In other words, dRA/dt measures the conversion rate of acid vapor to acid in the aerosol phase.

Next, in order to model the CSTR, its design equation was written in the form

$$\tau = \frac{(RA_o - RA)}{(-dRA/dt)} \ , \tag{31}$$

where again τ is the residence time in the reactor and RA_o is the initial acid vapor concentration. To find the acid vapor concentration RA at the CSTR outlet, the rate equation (Eqn. (30)) was integrated numerically and the value of τ was printed out at each timestep. The conditions at the reactor outlet are those for which τ is equal to the residence time of the reactor used.

For these simulations, the residence time of the experimental reactor was estimated to be 12 s. Three different combinations of initial RH and RA were tested, and the results are shown in Figures 15 and 16, which show the conversion χ (equal to $(S_{A_o} - S_A)/S_A$) and total particle number N as functions of τ for both types of reactor. An interesting feature is immediately observed: the total predicted number concentrations at $\tau = 12$ s is the same for both the PFR and CSTR, whereas the total conversion to the aerosol phase—measured in part by the mean particle size—is somewhat different. These results suggest that the unknown flow field in the reactor will not have an effect upon the experimentally measured variable N.

Cases 1 and 2 of Figures 15 and 16 correspond to moderate rates of nucleation ($R_J = 150$ and 1000 cm^{-3} s^{-1}, respectively), whereas Case 3 corresponds

to a high nucleation rate ($R_J = 10^8$). For the first two cases, very few particles are formed for residence times on the same order as the mixing time (10^{-3} s), but significant particles are already formed for both the CSTR and PFR cases for the high nucleation rate of Case 3.

The relative (dimensionless) rates of nucleation and condensation are presented in Figure 17 for Cases 1 and 3 as discussed above. These rates have been converted to relative acidity units, and so measure the importance of each mechanism in depleting the initial gas-phase MSA concentration. The nucleation rate is seen to be approximately constant initially, as the condensation rate increases to a maximum. Near this maximum, the vapor has been depleted to an extent such that the nucleation rate drops off sharply and condensation is the only important gas-to-particle conversion mechanism. Except for the initial stage of nucleation, the dimensionless condensation rate is much larger than the dimensionless nucleation rate; this is especially true in the slower-nucleation Case 1, in which a smaller number of larger droplets are formed that are more effective in scavenging the acid vapor.

Estimation of the time lag for nucleation

The experimental results are to be analyzed with the classical binary nucleation rate theory, which assumes a steady-state distribution of clusters. In order to evaluate the applicability of the steady-state assumption, the time lag for attainment of the steady state must be calculated and compared with the other time scales in the experiment.

An expression for the time lag needed to attain steady-state nucleation in binary vapors was derived by Wilemski (1975). The general definition of the time lag used is

$$\tau_n = \int_0^\infty \left[1 - (I_n(t)/I_{ss})\right] dt \ , \tag{32}$$

where $I_n(t)$ is the net rate of formation of clusters of size n from size $(n-1)$, and I_{ss} is the value of this net rate at steady state. First, rather than using the true nucleation path orientation with respect to the axes n_1, n_2, rotated

coordinates (s_1, s_2) are defined using the angle θ, $\tan\theta = n_2/n_1$ (here, n_i is the number of molecules of species i, and * denotes critical cluster properties). The approximation is made that the current component in the s_2 direction (perpendicular to the approximate nucleation path) is negligible. One can then transform the equation for $f(t)$ (the nonequilibrium cluster concentration),

$$\frac{\partial f}{\partial t} = \frac{\partial I_1}{\partial n_1} - \frac{\partial I_2}{\partial n_2} , \tag{33}$$

where I_i are the components of the current vector in the (n_1, n_2) coordinate system, substituting for I_i and using the rotated coordinates, to obtain

$$\frac{\partial f}{\partial t} = \frac{\partial}{\partial s_1}\Big(D(s_1, s_2)c(s_1, s_2)\frac{\partial}{\partial s_1}(f/c)\Big) , \tag{34}$$

$$D(s_1, s_2) = \frac{\beta_1\beta_2 a(s_1, s_2)}{\beta_1 \sin^2\theta + \beta_2 \cos^2\theta} , \tag{35}$$

where $a(s_1, s_2)$ is the area of the critical cluster and $c(s_1, s_2)$ is the equilibrium cluster concentration. Since only the path $s_2 = 0$ is considered, Eqn. (34) is effectively reduced to a function of only one variable, and the technique of Frisch and Carlier (1971) for single-component systems could be applied to compute the time lag. In this manner, Wilemski found an approximate expression for the time lag in a binary system:

$$\tau_n = 3(n_1^* + n_2^*)(D^* \ln S^*)^{-1} L(\alpha) , \tag{36}$$

$$D^*(x) = 4\pi {r^*}^2 \beta_1\beta_2\big(x^2\beta_1 + (1-x)^2\beta_2\big)^{-1} , \tag{37}$$

$$\ln S^*(x) = (1-x)\ln S_1(x) + x \ln S_2(x) . \tag{38}$$

Here, x refers to the mole fraction of species 2, and the saturation ratios $S_i = p_i/a_i p_i^\circ$. $L(\alpha)$ is a slowly varying function of the free energy of critical nucleus formation, approximated by Wilemski as equal to 1.8.

Eqn. (36) was used with parameter values for the MSA–H_2O system for fixed $RA = 0.34$ and $RH = 0.36$, corresponding to conditions in two of the experiments performed. The time lag was found to be on the order of milliseconds

to tens of milliseconds (Figure 18). This time is quite large, particularly when compared with that for single component systems such as supersaturated water vapor, for which the time lag is on the order of microseconds. The most important contribution to the large time lag is the low concentration of acid molecules in the mixed system; since the steady state is established by molecular collisions, and these are less frequent for low-vapor-pressure species (that are here highly undersaturated as well), the steady state will take longer to be established.

The estimated time lags are of the same order as the characteristic mixing time, and at high nucleation rates can be longer than characteristic times for changes to occur in the gas phase. For example, in Figure 16, for Case 3, a large number of particles are predicted to be formed in 10^{-3} s. This is undesirable: the model is formulated assuming that the cluster distribution responds quickly to changes in the gas phase, and so the time lag should be much shorter than any other experimental time constants. Therefore, interpretation of the experimental data must be done cautiously, with the limitations of the steady-state theory in mind; comparison of the experimental measurements with the predictions of a kinetic model of nucleation and growth (Huang and Seinfeld, 1988) would be very useful. The effect of the time lag upon the experimental results will be discussed in more detail in the following section.

VI. Comparison of experiments and simulations

Gas-to-particle conversion in the continuous-flow mixing apparatus occurs by two mechanisms: nucleation of new particles and vapor condensation onto these particles. As was shown in the discussion of the PFR vs. CSTR approach to modeling (Figures 16 and 17), condensation quickly becomes the dominant means of mass transfer between the two phases after particles are formed by nucleation in the mixing section. To relate the predictions of the rate of binary nucleation (the rate of new particle formation) to the experimental results (total number concentrations at steady state), the competition between nucleation and growth processes for the available condensable vapors and its effect on the steady-state number concentrations must be considered.

Integral model for nucleation and growth

The model that is used here is an integral model, abbreviated the SNM model, since in the single-component case three variables are used to describe the vapor-aerosol system: the saturation ratio S, the total number of particles N, and the total mass in the aerosol phase (related to the mean diameter) M. Previous works have described the extension of this model to ideal binary systems (Kreidenweis *et al.*, 1988) and its application to the methanesulfonic acid–sulfuric acid–water system (Kreidenweis and Seinfeld, 1988). This last reference, Chapter IV in this thesis, also discusses in detail the property data used in evaluating the model parameters for the acid–water binary and ternary systems, so that only a brief description of the model will be presented here.

It is assumed that, because the partial pressure of water is so much greater than that of the acids, the relative humidity remains constant throughout the nucleation and condensation processes. The change in total number of particles is given by the binary nucleation rate at the instantaneous RA and the constant RH. The rate of condensation of acid vapor onto existing particles is computed by assuming a monodisperse aerosol, of a mean size calculated by dividing the total aerosol mass of acid vapor by the total number (yielding a

mass mean diameter of the distribution) and adding water to this acid droplet so that the droplet is in instantaneous equilibrium with the ambient RH, and computing the flux of acid vapor based on a driving force proportional to the difference between the acid vapor activity in the gas phase and over the droplet solution. Noncontinuum effects are accounted for by multiplying the continuum flux expression by the transition regime formula due to Dahneke (1983).

The resulting set of simultaneous, coupled, ordinary differential equations, comprising the model, is

$$\frac{dRA}{dt} = -(N_{AV} g^* R_{J_b} + R_c) RT/p_a^\circ \ , \tag{39}$$

$$\frac{dM_a}{dt} = Mw_a (g^* R_{J_b} + R_c) \ , \tag{40}$$

$$\frac{dN}{dt} = R_{J_b} \ , \tag{41}$$

with

$$R_c = \alpha \left(2\pi D_{ij} p_a^\circ \overline{D}_p \left[RA - a_a \exp\left(\frac{4\sigma \overline{V}_a}{\overline{D}_p RT} \right) \right] f(\overline{K}n) \right) N \tag{42}$$

$$f(\overline{K}n) = (1 + \overline{K}n)/(1 + 2\overline{K}n(1 + \overline{K}n)) \ . \tag{43}$$

As written, the model applies to an isothermal, constant-volume plug flow (or batch) reactor, but as discussed earlier, the results will be valid regardless of the flow pattern in the reactor tube. The equations were integrated for 12 seconds of simulation time (the approximate PFR residence time), using the mean "constant" RH or RA value, as indicated in Figures 19 through 24. The computed total numbers of particles for each set of experiments, along with the experimental data (from which the points corresponding to entrained particles have been removed), are shown in Figures 19 through 24.

It is seen immediately that the SNM model, using the predictions of the "classical" binary nucleation theory, greatly overpredicts the numbers of particles that are formed under the experimental conditions. Two possible explanations for this discrepancy must be considered. First, classical binary nucleation

theory may not be a valid representation of the particle formation in this system, either because of errors in the way the free energy of the critical cluster is calculated (the most frequently used explanation for the failure of classical theories to predict experimental data), or because of errors in the property data used. The second explanation is that the experimental design does not provide the ideal conditions assumed in the model, and has imposed restrictions upon the range of conditions for which particle formation can be *observed.* Evaluation of this second hypothesis requires detailed consideration of the model assumptions, for example, the assumption of a steady-state nucleation rate may not be valid for this system at the experimental conditions. One must also consider the experimental limitations (discussed in general terms in the section dealing with the analysis of errors), such as the various time constants inherent in the equipment design, the detection limits of the instruments, and the possibility of vapor and particle losses.

Applicability of classical binary nucleation theory

Sensitivity to property data

In considering the applicability of binary nucleation theory to the experimental conditions, the first step should be to investigate the sensitivity of the calculated nucleation rate to changes in the input parameters. The effect of errors in the property data upon the predictions of total number concentration can be considered quickly. First, it is well known that the surface tension (σ) used in computing the critical cluster size has a substantial impact upon the predicted nucleation rate. This can be readily seen from the single-component nucleation rate expression (the binary expression is a direct analogy to this), which contains the surface tension raised to the third power in the exponential term. Because nucleation theory rarely agrees with experimental data, a great deal of attention has been focused on the formulation of this exponential (energy) term, particularly on the validity of using the macroscopic surface tension to describe clusters containing fewer than 100 molecules. The possibility of a size-dependent

or non-equilibrium surface tension has been discussed (Rasmussen, 1982; Rasmussen, 1986; Spiegel *et al.*, 1986). Recent investigations (Flageollet-Daniel *et al.*, 1983; Wilemski, 1987) of surface enrichment effects have involved attempts to calculate corrections to the bulk surface tension for binary clusters. In the computations presented in this work, the compositions of the critical nuclei are determined using equations which are claimed to implicitly account for surface enrichment of clusters through the use of the Gibbs adsorption equation in their derivation (Wilemski, 1984).

The problem of specifying the surface tension of a cluster is even more difficult in the binary case than in the single-component case, because of the dependence upon the composition of the critical cluster; frequently, detailed information on even the macroscopic surface tension as a function of composition is not available. Fortunately, for the simulations presented here, macroscopic surface tensions for aqueous methanesulfonic acid solutions, obtained by Hoppel (1987), were available, so that accurate values of the bulk property could be used in the model. It would undoubtedly be possible to fit the data quite well by varying the surface tension within acceptable limits, especially so since essentially two adjustable parameters – the actual magnitude of σ and the variation of σ with composition – could be manipulated.

In order to demonstrate the importance of the value of σ in computing the nucleation rate, the following calculations were performed. The surface tension for MSA–water solutions was assumed to follow the simple relationship

$$\sigma = 53x + 72(1 - x) \ , \tag{44}$$

where x is the mole fraction of acid in the solution. This is the estimate used in a previous study of MSA-water nucleation (Kreidenweis and Seinfeld, 1988), before the measurements of Hoppel (1987) were published. Although the linear relation and Hoppel's correlation are similar for $x = 0$ and $x = 1$, the linear estimate predicts higher surface tensions over the concentration range. Figures 25 through 30 compare the model predictions using Hoppel's correlation and

using the linear estimate with the measurements, demonstrating the large shift in formation free energy (which impacts the theoretical "critical" RH or RA) that occurs due to the change in the surface tension. (The "critical" saturation ratio is defined as the minimum saturation ratio at which measurable nucleation occurs, and is usually approximated as the saturation ratio for which the nucleation rate is about 1 cm^{-3} s^{-1}.) The linear relationship better reproduces the values of N as well as the slope of the data for RA_{nom} = 50% and 60% and for RH_{nom} = 40% and 50%, but overpredicts the data for RA_{nom} = 30% and underpredicts for RH_{nom} = 15%; the agreement could probably be made better by changing slightly the dependence of σ upon x. The conclusions to be drawn from Figures 25 through 30 are first, that the model predictions are very sensitive to σ, and second, that more theoretical work is required in understanding the correct formulation of the embryo free energy in nucleation theories, in particular the surface energy term. In the rest of the analysis presented here, the binary nucleation rate will be computed using the correlation of Hoppel for consistency.

Other physical property data, such as density, have less effect on the computed nucleation rate; however, the value of the acid vapor partial pressure can impact the rate if it is varied by several orders of magnitude. The critical cluster properties can be evaluated from only RA and RH, so that the absolute values of the partial pressures do not play a role in the energy term. However, the preexponential term in the rate expression can be simplified for the case of one component having a much lower vapor pressure than the other:

$$C \approx \frac{p_w \beta_a}{kT \sin^2\phi} \pi D_p^{*2} Z \ . \tag{45}$$

At a given relative humidity (p_w) the frequency factor is thus proportional to the impingement rate of acid molecules, β_a, which is, in turn, proportional to the partial pressure of acid vapor. For the simulations presented here, the saturation vapor pressure of MSA was estimated to be about 1 ppm at 25 °C. This estimate is based upon the measurements of Clegg and Brimblecombe (1985) at 25 °C. and published data at 122 °C. and 167 °C. (Weast, 1977). These three values

were found to be well represented by Eqn. (18); it is unlikely that this estimate is far enough off to have a measurable impact upon the calculations.

Applicability of the steady-state assumption

One of the key assumptions in the derivation of the "classical" nucleation theories is that a steady-state Boltzmann distribution of clusters exists in the gas phase, so that the number of clusters containing g molecules (for the single-component case) is given by

$$n_g = n_1 \exp(-\Delta G_g / kT) \ . \tag{46}$$

In writing Eqn. (46), it is assumed that the monomers (n_1) greatly outnumber the molecules associated with clusters. Therefore, it can be seen that the energy "barrier", ΔG_g, must be much greater than zero for $g \geq 2$ for this assumption to hold. In other words, if no significant energy barrier for the phase change from vapor to liquid droplet exists, then steady state nucleation theory cannot be applied.

Warren *et al.* (1987) have developed a criterion, for the single-component case, to approximate when the activation energy barrier is large enough so that the monomer concentration is the predominant fraction of the total cluster concentration. This criterion takes the form

$$\ln S < 0.4\sigma^* \ , \tag{47}$$

where S is the saturation ratio of the single component and σ^* is a dimensionless surface tension, defined by writing the exponential term in the nucleation rate expression as

$$\exp(-\sigma^{*3} / 2 \ln^2 S) \ . \tag{48}$$

Since the number of molecules in a critical cluster, g^*, is given by

$$g^* = (\sigma^* / \ln S)^3 \ , \tag{49}$$

this criterion implies (approximately) $g^* \geq 16$. This criterion was chosen, somewhat arbitrarily, since for clusters smaller than this, the cluster-cluster interactions (and not just monomer-cluster collisions, as assumed in the classical theory) begin to impact the nucleation rate.

In the binary case, the formation free energy can be written as

$$\Delta G_B^* = \frac{16\pi\sigma^3 V^2}{3(RT \ln S^*)^2} , \tag{50}$$

where V is the molar volume of the solution and where the effective binary saturation ratio S^* has been defined as (writing this for the case of aqueous acid aerosol)

$$S^* = \left(\frac{RH}{a_w}\right)^{1-x^*} \left(\frac{RA}{a_a}\right)^{x^*} . \tag{51}$$

Here, x^* is the mole fraction of acid in the critical cluster solution.

By analogy, then, one may define a dimensionless surface tension in the binary case as

$$(\sigma_B^*)^3 = \frac{32}{3}\frac{\pi}{kT}\left(\frac{V}{RT}\right)^2 \sigma^3 , \tag{52}$$

with the corresponding criterion for the applicability of the classical theory:

$$\frac{\ln S^*}{\sigma_B^*} < 0.4 . \tag{53}$$

The ratio $\ln S^*/\sigma_B^*$ has been computed for the experimental conditions, and is shown in Figure 31 as a function of the relative humidity or acidity. (Since this criterion is related to the size of the critical clusters, similar information, but in a less convenient form, is given by Figure 12, which shows the approximate total number of molecules, $g_B^* = n_a^* + n_w^*$, for MSA-water critical clusters.) It is seen that only the conditions for $RH_{nom} = 15\%$ fall well within the bound, but for the other experiments most of the conditions fall within or near the bound. Interestingly, the data for $RH_{nom} = 15\%$ do not give the best agreement with the model predictions; rather, the data for $RA_{nom} = 60\%$ are closest to the theoretical values. It is also seen that the related formation free energies (Figure

32) are very similar for all runs except $RH_{nom} = 15\%$, which has higher energies and therefore lower nucleation rates (Figure 33).

Based upon these observations, one would expect that, if all of the model predictions were displayed on a single plot (again, with the exception of $RH_{nom} = 15\%$), measurable N values would be expected to lie within relatively narrow ranges of the variables RA and RH (that is, the "critical" RA and RH values are similar). This is indeed observed when the model results are superimposed, and also if all of the experimental data are superimposed, with the exception of $RA_{nom} = 30\%$. For $RA_{nom} = 30\%$, the experimental observations are shifted to higher relative humidity than might be expected from theoretical considerations of the embryo free energy. In other words, the model does predict that nucleation for $RH_{nom} = 15\%$ will occur at noticeably higher RA than in the other constant-RH runs, but does not predict the observation that nucleation at $RA_{nom} = 30\%$ will be shifted to higher relative humidities than in the other constant-RA runs.

Care must be taken in evaluating the significance of these observations. First, the formation free energies (and the energy barrier criteria) have been evaluated assuming that the parameters used in the binary nucleation rate expression are appropriate; as was demonstrated above, changes in the parameters, especially in the solution surface tension, can dramatically alter these predictions. On the other hand, the observation of apparently anomalous results for the case of $RA_{nom} = 30\%$ suggests that it may be of interest to explore other reasons for this behavior, rather than ascribing it to errors in the rate calculation, to determine whether any other consistent explanations can be hypothesized; these explanations may be helpful in evaluating the influence of other effects on the experimental observations.

Applicability of the integral model

The integral model is based upon a number of assumptions, the validity of which must be evaluated. These are properly considered as relating to the experimental limitations, rather than the theoretical, because one is testing

whether or not the experiment conforms to the idealized conditions of the model, and how greatly any nonconformities impact the comparison with the model results.

Effect of the isothermal assumption

First, classical nucleation theories are derived assuming isothermal conditions, and the model does not take into account any latent heat released during nucleation or condensation processes. The increase in temperature of the surrounding gas would have the effect of lowering the local RA or RH, decreasing the overall nucleation rate. The increase in temperature of a liquid droplet during growth would raise the vapor pressures of water and acid at the surface, lowering the driving force for condensation and thereby favoring nucleation. These two effects thus act in opposite directions and will cancel each other out to some extent.

Since the latent heat of water is large, and MSA and water have a high heat of mixing (this is observed when MSA is diluted with water in a beaker, but no measurements of ΔH_{mix} exist), a ballpark estimate of the maximum temperature change that could occur during nucleation and growth would be useful in quantifying the effect of the isothermal assumption. The latent heat of water (all quantities will be estimated at 25 °C.) is about 189 kcal gmol^{-1}, and from the estimated vapor pressure curve of MSA, its latent heat is about 15.9 kcal gmol^{-1}. Neglecting for the moment the heat of mixing, and assuming that all released heat goes into raising the ambient gas temperature, a worst-case calculation will be made for $RA = 0.6$ and $RH = 0.6$. If all of the acid vapor condensed at once, and formed a solution in equilibrium with the relative humidity ($a_w = 0.6$), this solution would have a mole fraction of MSA of approximately 0.13, so that about 6.7 moles of water would condense for every mole of acid. For a gas-phase heat capacity of 7 cal gmol^{-1} °C.$^{-1}$, the corresponding temperature rise of the ambient gas is $\Delta T = 0.11$°C. Essentially the same result is obtained if the heat of mixing of sulfuric acid and water are included as an

estimate for ΔH_{mix} for MSA and water, since the latent heat of water is the dominant contributor to the energy released. For an acid concentration closer to that used in the experiments ($RA = 0.23$), the corresponding temperature rise is about 0.04 °C., about the same as the uncertainty in the temperature measurements. A rise of 0.04 °C. decreases the relative humidity and relative acidity by less than one percent; a rise of 0.11 °C. decreases RH by about 1.3% and decreases RA by about 2%. These changes have negligible impact on the nucleation rate (much less than an order of magnitude). Therefore, the isothermal assumption is a valid one.

Effect of coagulation

The integral model does not consider the effect of coagulation on the ultimate number concentrations predicted. Coagulation is difficult to include in a model that assumes a monodisperse aerosol, particularly since the coagulation coefficient (K_{12}) depends very strongly on the sizes of the colliding particles. For the special case of constant K_{12}, the solution of the coagulation equation is

$$N(t) = N(0) / \left[1 + t\frac{K_{12}N(0)}{2}\right] . \tag{54}$$

The rate of coagulation is minimized for particles of the same size, and is largest for very small particles coagulating with very large ones; theoretical coagulation coefficents have been calculated (Friedlander, 1977) for 6 different particle size combinations (D_p between 0.01 and 1 μm, Table 5); these range from about 10 $\times 10^{-10}$ to 3200 $\times 10^{-10}$ cm^3 s^{-1}.

To estimate the effect of coagulation in the experiment, the final number concentrations at time $t = 12$ s, assuming $N(0) = 10^4$ to 10^{11}, were calculated from Eqn. (54), for four different values of K_{12} (Table 6). (It should be noted that $RA = 0.6$ corresponds to about 10^{13} acid molecules cm^{-3}, so that an initial number concentration of 10^{11} implies very small particles, containing only about 100 acid molecules each.) For values of K_{12} up to 1000 $\times 10^{-10}$, coagulation has very little effect for initial particle concentrations up to about 10^6 cm^{-3}; for

Table 5

Estimates of the coagulation coefficient, $K_{12} \times 10^{-10}$

D_{p_2}, μm	0.01	0.1	1.0
$D_{p_1} = 0.01$ μm	18		
$D_{p_1} = 0.1$ μm	240	14.4	
$D_{p_1} = 1.0$ μm	3200	48	6.8

Table 6

Final number concentration N (cm^{-3}) after 12 s coagulation time for various initial $N(0)$ and constant $K_{12} \times 10^{-10}$

$N(0)$	$K_{12} = 10$	$K_{12} = 100$	$K_{12} = 1000$	$K_{12} = 10000$
10^4	1.00×10^4	9.99×10^3	9.94×10^3	9.43×10^3
10^5	9.99×10^4	9.94×10^4	9.43×10^4	6.25×10^4
10^6	9.94×10^5	9.43×10^5	6.25×10^5	1.43×10^5
10^7	9.43×10^6	6.25×10^6	1.43×10^6	1.64×10^5
10^8	6.25×10^7	1.43×10^7	1.64×10^6	1.66×10^5
10^9	1.43×10^8	1.64×10^7	1.66×10^6	1.67×10^5
10^{10}	1.64×10^8	1.66×10^7	1.67×10^6	1.67×10^5
10^{11}	1.66×10^8	1.67×10^7	1.67×10^6	1.67×10^5

higher $N(0)$ (and for $K_{12} = 10^{-6}$), the final number concentrations can be greatly reduced, and one actually finds that a wide range of initial particle concentrations (10^8 through 10^{12}, for example) produce the same final number concentration after 12 s.

To apply these calculations to the experimental results, two extreme possibilities can be considered for what is occurring in the experimental apparatus, for which the maximum measured N was about 10^5 cm^{-3}. First, very rapid nucleation may occur in the mixing section, resulting in a large number of particles that coagulate to a final N of about 10^5 cm^{-3}. For small K_{12}, this is not supported by the calculations shown in Table 6, since high initial number concentrations also result in relatively high ($> 10^7$ cm^{-1}) final number concentrations. If a very large number of initial particles are formed very rapidly, these will be very small and very nearly monodisperse. From Table 5, it is seen that large K_{12} are calculated only for polydisperse systems. Therefore, the coagulation results shown in Table 6 for large K_{12} do not realistically describe coagulation of a rapidly formed, nearly monodisperse, high-number-concentration aerosol. The second case that may be considered is that a highly polydisperse aerosol will be formed in the experiment, and consequently the results for large K_{12} can be applied to state that, for large $N(0)$, coagulation will greatly reduce the observed number concentration. However, for a polydisperse aerosol, the number concentrations cannot be large enough for appreciable coagulation ($> 10^7$ cm^{-1}) since the total number of acid molecules is limited, and a large number of these are needed to produce each large particle; in addition, as the large particles are formed, these will be very effective in scavenging the acid vapor, suppressing nucleation of new, small particles. In other words, polydispersity and large particle sizes are associated with smaller total number concentrations, whereas higher number concentrations and smaller particle sizes are associated with more nearly monodisperse aerosols. Therefore, it may be concluded that neglecting coagulation in the analysis of the experimental results is a reasonable

approximation.

Effect of polydispersity

For the calculations using the integral model that are presented in this work, the parameter α, which accounts for the polydispersity of the aerosol in evaluating the total condensation rate onto all particles, was set equal to one. This is the equivalent of assuming that the aerosol is monodisperse, which maximizes the condensation rate (and hence tends to underpredict nucleation somewhat) (Kreidenweis *et al.*, 1988). For the special case of a lognormal aerosol,

$$\alpha = \exp(-\ln^2 \sigma_g) \ , \tag{55}$$

where σ_g is the variance of the distribution. For a moderate degree of polydispersity, for example $\sigma_g = 1.3$, $\alpha = 0.93$, so that the predicted condensation rate is about 7 percent too large; this will not have a very large effect upon the final computed number concentration. At any rate, the effect would be to increase N, whereas the model predictions with $\alpha = 1$ are already much larger than the measured N.

Polydispersity of the aerosol can have another effect, however, in the measurement of the total number concentrations by the CNC. The CNC has a distribution of efficiencies depending upon the particle size; the efficiency is reduced for particle diameters below 0.03 μm. One may postulate that, although the theoretical mass mean diameter computed using the integral model is large enough to be counted with high efficiency by the CNC, a significant number of the particles in the size-distributed aerosol that is actually produced in the experiment may have diameters less than the mass mean and may be counted with much lower efficiency. The result would be that the measured number concentrations are much less than the true number concentrations, because the CNC has "missed" counting a large number of small particles.

If the assumption of a lognormal aerosol is again invoked, some estimates can be made as to when the CNC counting efficiency significantly affects the

observed number concentration. As a worst case scenario, it is assumed that no particles less than 0.03 μm are counted. If the measured concentrations are, for example, two orders of magnitude lower than the true concentrations, 99% of the particles must have diameters less than 0.03 μm. The cumulative size distribution $F(D_p)$ (written here for a lognormal aerosol) expresses the fraction of the total aerosol population having diameters less than or equal to D_p:

$$F(D_p) = \frac{1}{2} + \frac{1}{2}\,\mathrm{erf}\left(\frac{\ln\,(D_p/\overline{D}_{p_g})}{\sqrt{\ln\sigma_g}}\right)\,, \tag{56}$$

where $\overline{D}_{p_g}$ is the geometric mean diameter of the distribution, which can be related to the mass mean diameter $\overline{D}_{p_m}$:

$$\overline{D}_{p_m} = \overline{D}_{p_g}\exp(1.5\ln^2\sigma_g)\,. \tag{57}$$

Substituting the values $F(D_p) = 0.99$, D_p=0.03 μm, and a representative σ_g of 1.3, one computes $\overline{D}_{p_m} = 0.016$ μm. This implies that, if the mass mean diameter calculated from the integral model is less than or equal to about 0.016 μm, and if the CNC does not count any particles less than 0.03 μm, the measured number concentrations will be about two orders of magnitude too low. For the same σ_g, if $\overline{D}_{p_m} = 0.01$ μm, the measured concentrations are about 3×10^{-4} those of the true.

The first point that should be made is that this calculation is unrealistic to the extent that it assumes the CNC will not detect any particles smaller than 0.03 μm, whereas in practice there will be some finite efficiency for even extremely small (< 0.005 μm) particles. Furthermore, such very small particles are associated with large number concentrations ($O(10^{10})$ cm^{-3}), so even for an efficiency of 10^{-4}, a measured concentration of 10^6 cm^{-3} would be indicated. Thus it is extremely unlikely that many undetected particles were formed in cases where the measured concentrations were very low (less than 1000 cm^{-3}, for example).

Second, from Figure 11 one can estimate that an aqueous particle with D_p = 0.01 μm is equivalent to an acid-only diameter of about 0.005 μm, from which

the moles of acid per particle can be calculated. For RA between about 0.2 and 0.6, as in the experiment, if all of the acid vapor is converted to the aerosol phase, one would expect number concentrations on the order of 10^9 to 10^{10} cm^{-3} for $\overline{D}_{p_m} = 0.01$ μm. Applying the computed efficiencies, one may conclude that the measured counts will be on the order of 10^6 cm^{-1}. Thus it is possible that, for the highest number concentrations measured, a drop in CNC counting efficiency has influenced the measurements. By "correcting" the measured number concentrations (those $> 10^5$ cm^{-3}, for example) for this effect, the slope of the data would be increased, in better agreement with the model predictions. However, the data would not be appreciably "shifted" to smaller RA or RH (that is, the "critical" RA or RH would not agree better with the model predictions) unless the CNC efficiency correction could also be applied to the measured low number concentrations ($< 10^4$ cm^{-3}). As discussed above, the applicability of this correction to the low measured number concentrations is unlikely, since the grown particle diameters computed by the model at smaller number concentrations are relatively large ($> 0.1\mu$m), and the efficiency of counting would be large. In fact, for $\overline{D}_{p_m} = 0.04$ μm, only about 15% of the total particles have diameters less than 0.03 μm; $\overline{D}_{p_m} = 0.04$ μm is the acid-only diameter computed for $RA = 0.2$ and $N = 10^7$ cm^{-3} assuming that all of the acid vapor is converted to aerosol. Even if only one-third of the available acid vapor were converted, the final $\overline{D}_{p_m}$ would be about 0.027 μm, only 58% of the total particles would have diameters less than 0.03 μm, and the measured concentrations would therefore be low by only about a factor of two (that is, the measurements would be very close to $N = 10^7$ cm^{-3}).

To summarize the expected effects of polydispersity, the assumption of a monodisperse aerosol is not expected to significantly affect the model predictions, since α will not differ greatly from one for the experimental aerosol. For high number concentrations and small particle sizes, the polydispersity can affect the measurement of particle concentrations if the mass mean diameter is

less than about 0.016 μm. In this case, a significant number of particles will have diameters small enough that the efficiency of the CNC in counting these particles is greatly reduced. The expected effect is that the measured number concentrations at high N (greater than about 10^5 cm^{-3}) may be low by several orders of magnitude; if the measurements are corrected for this effect, the slope of the data will become steeper, but the intercept (the "critical" RA or RH) will not be affected, since the efficiency correction is shown not to apply at low particle number concentrations.

Effect of rate of condensation

Since nucleation must compete with condensation for the available acid vapor, it is possible that errors in the computed condensation rate can overpredict (or underpredict) the final number concentrations. (This effect is considered separately from the effect of α, which is discussed above.) The condensation rate is given by Eqn. (42), and for large particles (continuum regime, $Kn \longrightarrow 0$) and small particles (free molecular regime, Kn large) can be written

$$R_c(\text{continuum}) = 2\pi D_{ij} p_a^o \overline{D}_p \Big(RA - a_a \Big) N \tag{58}$$

$$R_c(\text{free molecular}) = 2\pi D_{ij} p_a^o \frac{\overline{D}_p^2}{4\lambda} \left(RA - a_a \exp\left(\frac{4\sigma \overline{V}_a}{\overline{D}_p RT}\right) \right) N \; . \tag{59}$$

The polydispersity factor α has been omitted in the above equations since its effect has already been considered, and the effect of N upon R_c will also not be discussed here. Of the remaining parameters in the condensation rate expressions, it is unlikely that D_{ij} will be in error by more than a few percent, so that the parameters that will be focused on are p_a^o, $\overline{D}_p$, and the driving force, $(RA - a_a \times$ Kelvin effect).

To test the impact of variations in R_c, the condensation rate was increased by an order of magnitude. In the continuum case, this would correspond to an order of magnitude increase in p_a^o, $\overline{D}_p$, or the driving force. It is unlikely that the estimates of the saturation vapor pressure or the diameter will be incorrect

by such a large factor, although if each of these were low by a factor of three the total error would be about an order of magnitude. If the computed acid activities are higher than the true activities, the computed driving force is too small, conceivably by an order of magnitude. (Of course, such errors in the acid activities would also affect the computed nucleation rates.) The continuum flux expression is expected to apply for large particle sizes, which have grown at the expense of the ambient RA; however, if RA has been reduced significantly, nucleation will be quenched, and changes in R_c(continuum) will merely affect the final size and have little impact on the total number.

In the free molecular regime, R_c has a $\overline{D}_p^2$ dependence on diameter, so a factor of three increase in $\overline{D}_p$ would increase the condensation rate by a factor of almost ten. In addition, increasing the diameter would decrease the Kelvin term, increasing the driving force for condensation. The impact of such changes is especially important for the free molecular flux, since this is the limiting form which is expected to apply in the early stages of condensational growth, when new particles are still being formed and changes in the growth equation can significantly affect the competition for acid vapor, and thereby the total number concentration.

Values of N generated by the integral model for $RH = 0.113$ and $RH = 0.345$ at various RA are shown in Table 7 for R_c computed from Eqn. (42) and for $10 \times R_c$. It is seen that the order of magnitude increase in R_c results in about five times fewer particles. Therefore, a change in the condensation rate produces a roughly proportional change in the total number of particles. In most of the comparisons between experiment and predictions, the predicted number concentrations are high by many orders of magnitude; errors in the condensation rate are unlikely to be this large, and are therefore not of great importance in explaining the observed differences.

Table 7

Number concentrations N (cm^{-3}) after 12 s from integral model with R_c and $10 \times R_c$

$RH = 0.113$

RA	N using R_c	N using $10 \times R_c$
0.20	3.7	3.2
0.25	730	163
0.30	8.84×10^3	1.83×10^3
0.35	6.20×10^4	1.20×10^4

$RH = 0.345$

RA	N using R_c	N using $10 \times R_c$
0.07	2.1	1.9
0.10	6.65×10^3	1.37×10^3
0.12	1.37×10^5	2.59×10^4

Effect of entrained particles

As noted in the discussion of the experimental procedure, low ($< 100\ \mathrm{cm}^{-3}$) number concentrations of entrained particles were present in some of the experiments. Since these particles are capable of scavenging acid vapor and thereby affecting the rate of nucleation, their impact upon the final number concentrations was examined using the integral model. For this study, one additional differential equation was included to describe the growth of particles in the preexisting mode; nucleation and growth of a second mode was allowed as before. The preexisting particles were assumed to have diameters of about 0.5 μm and N=100 cm^{-3}. Table 8 summarizes the final number concentrations produced in the presence and absence of the entrained particles at $RH = 0.113$ and $RH = 0.345$. As expected, the presence of the preexisting particles has very little effect upon the number of new particles nucleated for final number concentrations significantly larger than that of the entrained droplets.

Impact of experimental design

The final explanation for the differences between the observed and predicted number concentrations in the experiments reported here is that they are due to the design, and consequently the behavior, of the apparatus itself. The two major effects that will be discussed here are the possible losses (of particles or vapors) that can occur in the apparatus, and the comparison of the experimental time constants, particularly the characteristic mixing time, with the characteristic time scales of the phenomena being investigated.

Effect of particle and vapor losses to surfaces

As discussed in a previous section, particle and vapor losses are difficult to predict. The analysis presented using the solution of the Graetz equation, assuming the surfaces are perfect sinks, suggested that losses of very small particles (essentially, the critical clusters) may occur, but these are not expected to be very great. Also, the materials used in the construction of the apparatus—exclusively Teflon and glass, with some necessary Viton O-rings, in the

Table 8

Number concentrations in nucleated mode N (cm^{-3}) after 12 s with and without preexisting particles N_{pe}

$RH = 0.113$

RA	N $N_{pe} = 0$	N $N_{pe} = 100$
0.20	3.7	2.2
0.25	730	552
0.30	8.84×10^3	8.32×10^3
0.35	6.20×10^4	6.05×10^4

$RH = 0.345$

RA	N $N_{pe} = 0$	N $N_{pe} = 100$
0.07	2.1	1.1
0.10	6.65×10^3	6.21×10^3
0.12	1.37×10^5	1.35×10^5

nucleation and growth sections—were carefully chosen to minimize chemical interactions, and the assumption of a perfect sink at the surface is unrealistic. If one computes as a characteristic time for vapor diffusion the quantity $\tau_{diff} \approx R_t^2/D_{ij}$, where R_t is the tube radius and D_{ij} the vapor diffusivity, a characteristic time on the order of 20 s is obtained. Thus it is unlikely that vapor losses in the reactor will significantly affect the nucleation rate, particularly in that, for most cases, new particles will be formed during a nucleation burst that occurs primarily in the mixing section, and very little vapor (or particle) loss will occur on this length scale (about 1 cm).

Water or acid vapor may be lost to surfaces prior to the mixing chamber, resulting in decreased nucleation rates. An attempt was made to evaluate what corrections would have to be applied to the relative humidities to obtain agreement between the theoretical predictions and the experimental data. (This assumes, of course, the validity of the computed nucleation rate, which has been called into question in the preceding discussions.) First, the "shift" (along the RH axis) for the constant RA experiments (Figures 19, 20 and 21) was measured. This was accomplished by taking each experimental data point for these experiments, noting the experimental RH, and finding the theoretical RH that produced the same total number concentration. Plotting RH_{theory} as a function of RH_{expt} gave an approximately linear relationship, correlated by

$$RH_{theory} = 0.136 RH_{expt} + 0.055 \ . \tag{60}$$

Next, the experimental constant RH values (Figures 22, 23 and 24) were "corrected" according to this relationship, and the SNM model was applied using these new RH values. The experimental data and model results for both RH_{expt} and RH_{theory} are shown in Figures 34 through 36. The corrected RH values produce total number concentrations that are in surprisingly good agreement with the measured. Not only the values of N, but the slope of the data, appear to be better represented. The same technique was attempted for a correction to the constant-RA experiments, but RA_{theory} and RA_{expt} could not be correlated.

There are two possible explanations for the success of the RH correction. The more obvious of these is that extensive losses of water vapor to tubing walls occurred before the stream entered the mixing chamber (the correlation suggests that $RH_{expt} = 10\%$ be corrected to $RH_{theory} = 7\%$, and $RH_{expt} = 60\%$ be corrected to $RH_{theory} = 13\%$). Losses may have indeed been a problem, since a rather long Teflon line was used inside the bath in order that the temperature of the mixed dry/humid streams would equilibrate with that of the bath. However, checks on the relative humidity were made before the data were taken, and the measured RH was found to agree with the calculated to within experimental error. (The RH was not measured during the runs because the presence of acid vapor might damage the sensor in the humidity meter.) Also, the correlation suggests that losses were greater for the higher-humidity runs; this is not supported theoretically, since the dimensionless length x_l in the Graetz formula will be the same for all initial humidities (as long as the velocity remains the same), which results in the same dimensionless mixed mean concentration p_{av}/p_0. Therefore, the losses from all initial humidities will be of the same relative proportion, unlike the predictions of the correlation. Last, if extensive vapor losses occurred, condensation would be observed in the Teflon lines, and a hysteresis effect (slow response to changes in the input RH) would be observed in the measured number concentrations. Neither of these effects was observed during the course of the experiments.

The second and more plausible explanation for the success of Eqn. (60) is that the shift in RH represents a correction to the theoretical nucleation rates. A lower RH will result in a lower nucleation rate, slower particle formation, and increased importance of condensation. Therefore, decreasing the humidity will change the energetics of the nucleation rate and the kinetics of the growth process, both of these acting in the same direction to lower the final number concentration. The success of this "correction" may then be viewed as further evidence that, in applying steady-state binary nucleation theory to

this experiment, the formation free energies of the critical nuclei are somewhat underpredicted by using the available macroscopic thermodynamics, and the condensation rate is also somewhat underpredicted (when the theoretical nucleation rates are large). By decreasing the humidity, one may also be effectively "eliminating" particles that are actually formed in the experiment, but are not counted because of evaporative or diffusional losses, thereby obtaining better *apparent* agreement between theory and experiment. Exploration of these ideas is an interesting possibility for future theoretical and experimental efforts.

Effect of experimental time scales

As discussed earlier, an important consideration when applying classical nucleation theory is the time lag for the cluster distribution to reach steady state. If the time lag is longer than the experimental observation time, the steady-state nucleation rate will not be observed. (For example, the effect of long time lags on experiments using expansion chambers, which have very short experimental time scales, has been discussed in detail by Schelling and Reiss (1981).) Since the residence time for nucleation and growth is of the order of 12 s in our experiments, the time lag (expected, and found, to be much shorter than this) will not prevent observation of nucleation phenomena. However, it is possible that, if the time lag is of the same order of magnitude as other experimental time constants, it can affect the kinetics of the nucleation rate. The steady-state nucleation rate is not established until after this transient, but the integral model assumes that no gas-to-particle conversion occurs during the mixing process and that the steady-state theory applies immediately after the vapors have been mixed and the initial RA and RH have been established.

The time lags for the establishment of the steady-state cluster distribution have been calculated for the experimental conditions and are presented in Figure 37. (Again, it must be stated that these were computed assuming that the classical binary nucleation theory and the macroscopic property data values were adequate in describing this system.) From this Figure, $RA_{nom} = 30\%$ can

be readily distinguished as different from the other constant-RA runs, in that the time lags for this case are much higher, although the estimated nucleation rates (Figure 33) are similar to those for $RA = 50\%$ and $RA = 60\%$. This is an interesting observation, since it was mentioned earlier (in the discussion of the applicability of the steady-state assumption) that the disagreement between theory and experiment for $RA = 30\%$ was larger than might be expected from energy considerations alone. The time lags also suggest an explanation of why $RA_{nom} = 60\%$ shows the best agreement between theory and experiment: the time lags are the lowest within the constant-RA set of experiments, and are lower than most of those computed for the constant-RH experiments. Those few conditions for which the constant-RH time lags are shorter correspond to large initial nucleation rates (and an energy barrier that falls outside the criterion discussed above). These observations reinforce the point that not only must the applicability of the steady-state nucleation theory be tested using energy criteria, but the kinetic limitations, described by the time lag, must also be considered.

Another interesting observation regarding the time lags can be made: if one estimates the RA or RH at which measurable particle formation first occurs for each set of experiments and computes the corresponding time lags at these "critical" RA and RH values, one finds that these time lags are between about 2.5 and 3.5 ms. The time lags are replotted in Figure 38 with numbers indicating the approximate theoretical initial nucleation rates, R_{J_o}. For time lags longer than about 3.5 ms, no particles were observed experimentally, although from Figure 38 it is seen that in some cases large initial nucleation rates are predicted above this cutoff. The reason for this may be related to the mixing times in the apparatus, which may be considered to be between 3 and 8 ms for most of the experimental conditions. The initial conditions (RA and RH in the completely mixed stream) that are used as inputs for the integral model are not established until after the streams have been in contact for the mixing time (about 3 to 8 ms); if the time lag is of the same order, the cluster distribution cannot respond

quickly to the changes in RA and RH during mixing. Of course, the steady-state cluster distribution can be established in a few milliseconds after complete mixing has been achieved, so that the fact that the mixing time and lag time are of the same order will have no consequence unless other changes occur over these time scales. For example, if particle formation occurred as soon as acid and water vapors were brought into contact, this formation could not be described by steady-state nucleation theory, and if a significant number of particles were formed during this contact time, these could affect the subsequent gas-to-particle conversion that did occur after complete mixing (by scavenging vapors).

It is important to note that the analysis of the effect of imperfect mixing presented earlier, suggesting that the overall nucleation rate would not be greatly affected by moderate degrees of segregation, used the predictions of the classical theory and therefore assumed that the steady-state cluster distribution was valid, equivalent to assuming that the time lag was much shorter than the mixing time scale. Since this is not the case, the imperfect mixing analysis cannot be applied to the initial stages of the mixing process. Without detailed knowledge of the flows during mixing and without a theoretical description of particle formation as an unsteady-state process, it is not possible to rigorously compute the effect of the mixing and lag times on the observed particle concentrations. The best that can be done in this case is to use the classical theory and estimate the time scales over which significant particle formation and gas-phase changes occur, compare these to the mixing and lag times, and attempt to draw conclusions.

As the rate of nucleation increases, the time over which significant particle formation occurs decreases rapidly, as can be seen from Figure 16, which shows total number as a function of reactor residence times. For Case 3, with a high initial rate of nucleation (on the order of 10^8 cm^{-3} s^{-1}), a large number of particles ($> 10^5$ cm^{-3}) have been formed on a time scale of the same order as τ_M. This is contrasted with the behavior of Case 1 (Figure 16), for which a

lower initial nucleation rate (about 150 cm^{-3} s^{-1}) is predicted, and for which negligible numbers of particles are formed on the τ_M timescale. Therefore, the mixing and lag times should have little effect on experimental observations if the initial rate of nucleation is low.

The time lag can also be compared with another characteristic time scale in the experiment: the time scale for changes in the gas phase, $(d \ln RA/dt)^{-1} = \tau_{RA}$. The time scale for changes in RA depends very strongly on the initial RA—how many vapor molecules are available for transfer to the aerosol phase—and the rates at which nucleation and growth accomplish this transfer. To estimate $(d \ln RA/dt)^{-1}$, the integral model was applied to two experimental conditions: first, a point from the $RA_{nom} = 60\%$ data set (which showed the closest agreement with theory), $RA = 0.387, RH = 0.2$; and second, a point from the $RA_{nom} = 30\%$ data set (which was not at all well represented by the model), $RA = .228, RH = 0.5$. At each timestep, the values of RA and $(d \ln RA/dt)^{-1}$ (from differencing) were computed. In this way, numerical estimates of τ_{RA} as a function of time were generated.

In the first case ($RA = 0.387, RH = 0.2$), the initial nucleation rate is approximately 5×10^9, the time lag is estimated to be 2.4 ms, and the energy barrier criterion is 0.32 (within the limits for applicability of the steady-state theory). The numerical estimates of τ_{RA} for short times (from 0 to 0.02 s) range from about 10 s initially to about 1 s. Large numbers of particles—on the order of 10^8—are predicted to be formed over this time range, but condensation has not yet become dominant and the mean particle size is about 0.006 μm; since a large number of very small particles do not comprise much mass, the acid vapor is not heavily depleted in the first 0.02 s, and τ_{RA} is much larger than the characteristic mixing and lag times.

This is contrasted with the behavior in the second case ($RA = 0.387, RH = 0.2$). Here, the initial nucleation rate is somewhat larger—10^{13} cm^{-3} s^{-1}—but the lag time, 2.3 ms, is comparable to that for the first case. The energy barrier

criterion is calculated to be about 0.4, at the limits of applicability of steady-state nucleation theory. Since the initial acid vapor concentration is considerably less for this case than for the first, the rapid formation of a large number of particles (about 10^{10} cm^{-3} within the first 0.005 s) quickly depletes the vapor, and the final particle size is only about 0.0056 μm. Consequently, over the first 0.02 s of simulation time, τ_{RA} was computed to be about 5 ms initially and about 15 ms at 0.02 s. These estimates are of the same order as the lag and mixing times, and when the energy barrier criterion is also considered, it is not surprising to find that the SNM model, using steady-state nucleation theory, cannot predict the experimental observations in this case (but does do a better job for the first (higher-RA) case). However, the question still remains: why was nucleation not observed at lower relative humidities for $RA_{nom} = 30\%$, for which the nucleation rates would be smaller and τ_{RA} would be longer than the other time scales?

Summary of effects upon the comparison of data with theory

The primary objective of the experiments described in this work is to evaluate the applicability of the classical binary nucleation rate theory to the methanesulfonic acid–water system. This is approached at two levels: first, it must be demonstrated that particles are formed under conditions such that both acid and water vapor are highly undersaturated with respect to single-component nucleation, verifying the interaction of the two species in gas-to-particle conversion. This was unambiguously shown by our measurements of N. Second, the magnitudes of the predicted nucleation rates, as well their dependence upon RA and RH, must be checked against the experimental data. In order to make this comparison, a model must be used to describe the gas-to-particle conversion.

The assumptions made in formulating the integral model that was used were examined to determine their impact upon the comparison between theory and experiment. The model assumes isothermal conditions, no coagulation of

particles, and monodispersity of the aerosol. Arguments were given that indicate these are adequate assumptions for the conditions of the experiment. Also, it was shown that the number concentrations of entrained particles present in some of the experiments were too low to significantly affect the nucleation of new particles.

However, it was also shown that polydispersity of the aerosol, while not greatly affecting the model predictions, may affect the *measured* value of N, and hence the comparison between theory and experiment, if a significant fraction of the particles are below the detection limit of the condensation nuclei counter. The overall effect upon the measured N is to change the slope, but not the intercept, of the data.

Consideration was also given to other likely causes of biasing of the experimental measurements. One possibility is that large losses of vapor and/or particles occur in the apparatus. Although it cannot be conclusively demonstrated that these losses did not occur, several arguments against this possibility were presented, and it is believed that such losses were negligible. The characteristic time scales inherent in the apparatus and in the observed phenomena were compared to determine their influence upon the data. It was concluded that unsteady-state nucleation may occur in the mixer as a consequence of the relatively long lag times in the acid/water system, with an unknown effect upon the final number concentrations.

Finally, the sensitivity of the model predictions to the parameters used in the calculations was determined. As has been suggested in previous nucleation studies, the calculation of the free energy of the critical cluster (in particular, the representation of the surface energy) has the strongest impact upon the model results, and is the term most likely to be in error. It was demonstrated that the integral model can represent the data well if alternate expressions for the cluster surface tension (as a function of composition) are chosen. From this study, it seems reasonable to suggest that such a correction to the theory is in order, since

the analysis presented here has shown that the discrepancy observed between the data and the simulations cannot be accounted for by the model approximations. However, this suggestion cannot be formulated as a conclusion, because there is some possibility that the experimental design biased the measured number concentrations.

The key problems in designing an experimental apparatus for studying binary nucleation of acid-water systems, and in interpreting the observations, can now be summarized. First, a moderate nucleation rate is desired to minimize coagulational and diffusional losses and to ensure the applicability of steady-state nucleation theory. However, the time lags for achievement of the steady-state cluster concentration can be considerable at moderate nucleation rates, especially if the acid vapor concentration is low, because of the low saturation vapor pressure of the acid species. If the time lag is on the same order as, or longer than, other time scales in the apparatus (such as that for mixing), the interpretation of the data in terms of classical nucleation theory becomes difficult.

Although some of these effects were hypothesized before the experiment was attempted, obtaining evidence for these through experimental observation has been valuable in confirming their importance and in suggesting revised experiments that will provide less ambiguity in the data interpretation. Investigation of binary nucleation phenomena, particularly of the highly nonideal aqueous acid binary systems, is a difficult task, and there is a great need for careful, controlled experiments at atmospheric-type conditions.

The validity of interpreting experimental binary nucleation data using the classical theory and macroscopic solution properties is also subject to question. Although modifications can be made to the inputs to the theory to produce agreement with the experimental results, it is necessary to first eliminate all possible biasing due to the experimental design. If this can be achieved, the accuracy of the binary nucleation theory can be evaluated, and a great contribution to the understanding of binary nucleation phenomena can be realized.

V. Conclusions

Two important contributions to the study of binary nucleation phenomena have been made. First, the binary nucleating capability of methanesulfonic acid and water, heretofore only postulated theoretically, was demonstrated. Undersaturated acid vapor in the presence of moderate (less than 60%) relative humidity was found to generate observed aerosol concentrations up to about 10^5 cm^{-3}. Trends predicted by binary nucleation theory—an increase in particle formation with increasing relative humidity at constant relative acidity, for example—were also confirmed.

The second contribution is the demonstration of the feasibility of using a mixing-type nucleation experiment for the study of binary nucleation phenomena; this apparatus was fairly easily adapted to the demanding conditions of an acidic environment, a major consideration when dealing with such corrosive materials. Analysis of the data also provided greater insight into the energetic vs. kinetic aspects of nucleation theory, and led to the identification of weak points in the design of the experiment. A key result of this work will be the application of the knowledge obtained to the improvement of the device, and its application to other binary systems, particularly those of atmospheric interest.

References

Bartz, H., Fissan, H., Helsper, C., Kousaka, Y., Okuyama, K., Fukushima, N., Keady, P.B., Kerrigan, S., Fruin, S.A., McMurry, P.H., Pui, D.Y.H., and Stolzenburg, M.R. (1985) *J. Aer. Sci.* **16**(5), 443.

Clegg, S.L. and Brimblecombe, P. (1985) *Env. Tech. Lett.* **6**, 269.

Cox (1973) *J. Aer. Sci.* **4**, 473.

Dahneke, B. (1983) *Theory of Dispersed Multiphase Flow*, R.E. Meyer, ed., Academic Press, New York.

Flageollet-Daniel, C., Garnier, J.P., and Mirabel, P. (1983) *J. Chem. Phys.* **78**(5), 2600.

Friedlander, S.K. (1977) *Smoke, Dust and Haze: Fundamentals of Aerosol Behavior*, J. Wiley and Sons, New York.

Frisch, H.L. and Carlier, C.C. (1971) *J. Chem. Phys.* **54**, 4326.

Hoppel, W.A. (1987) *Atm. Env.* **21**, 2703.

Huang, D. and Seinfeld, J.H., to be published.

Kreidenweis, S.M., Okuyama, K., Kousaka, Y., Flagan, R.C., and Seinfeld, J.H. (1988) accepted for publication, *J. Chem. Phys.*

Kreidenweis, S.M. and Seinfeld, J.H. (1988) *Atm. Env.* **22**(2), 283.

Mirabel, P. and Clavelin, C. (1978b) *J. Chem. Phys.* **68**(11), 5020.

Okuyama, K., Kousaka, Y., and Warren, D.R. (1987) *Aer. Sci. Tech.* **6**(1), 15.

Rasmussen, D. (1982) *J. Crystal Growth* **56**, 45.

Rasmussen, D. (1986) *J. Chem. Phys.* **85(4)**, 2272.

Schelling, F.J. and Reiss, H. (1981) *J. Coll. Int. Sci.* **83**(1), 246.

Spiegel, G.H., Zahoransky, R.A., and Wittig, S.L.K. (1986) *Shock waves and shock tubes*, D. Bershader and R. Hanson. eds., Stanford University Press.

Warren, D.R., Okuyama, K., Kousaka, Y., Seinfeld, J.H., and Flagan, R.C. (1987) *J. Coll. Int. Sci.* **116**(2), 563.

Warren, D.R. and Seinfeld, J.H. (1985) *Aer. Sci. Tech.* **4**, 31.

Weast, R.C. (1977) *CRC Handbook of Chemistry and Physics*, 58th Ed., R.C. Weast, ed., CRC Press, West Palm Beach.

Wilemski, G. (1975) *J. Chem. Phys* **62**(9), 3772.

Wilemski, G. (1984) *J. Chem. Phys* **80**(3), 1370.

Wilemski, G. (1987) *J. Chem. Phys* **91**(10), 2492.

Zahoransky, R.A. and Peters, F. (1985) *J. Chem. Phys.* **83**(12), 6425.

Figure Captions

Figure 1. Schematic of experimental apparatus.

Figure 2. Schematic of water bubbler.

Figure 3. Schematic of acid bubbler.

Figure 4. Variation of number concentrations, acidified flow only, with flow rate through acid bubbler.

Figure 5. Measured number concentration, $RA_{nom} = 30\%$.

Figure 6. Measured number concentration, $RA_{nom} = 50\%$.

Figure 7. Measured number concentration, $RA_{nom} = 60\%$.

Figure 8. Measured number concentration, $RH_{nom} = 15\%$.

Figure 9. Measured number concentration, $RH_{nom} = 40\%$.

Figure 10. Measured number concentration, $RH_{nom} = 50\%$.

Figure 11. Size of droplets (aqueous and dry diameters) grown for 12 s simulation time, at various RA and RH.

Figure 12. Size of critical clusters in MSA–water system: (a) diameter (nm), (b) number of molecules in critical cluster.

Figure 13. RH as a function of mixedness ratio X for experimental conditions of Table 3.

Figure 14. Variation of initial binary nucleation rate (J_B) with mixedness ratio X.

Figure 15. Conversion χ as a function of CSTR and PFR residence times.

Figure 16. Total number concentration N as a function of CSTR and PFR residence times.

Figure 17. Rates of condensation (R_c) and nucleation (R_J) as a function of PFR residence time.

Figure 18. Time lag to reach steady-state for binary nucleation in the MSA–water system as a function of nucleation rate for $RH = 36\%$ and $RA = 34\%$.

Figure 19. Model predictions ($*$) and measured N, $RA_{nom} = 30\%$.

Figure 20. Model predictions ($*$) and measured N, $RA_{nom} = 50\%$.

Figure 21. Model predictions (∗) and measured N, $RA_{nom} = 60\%$.

Figure 22. Model predictions (∗) and measured N, $RH_{nom} = 15\%$.

Figure 23. Model predictions (∗) and measured N, $RH_{nom} = 40\%$.

Figure 24. Model predictions (∗) and measured N, $RH_{nom} = 50\%$.

Figure 25. Measured N and model predictions using Hoppel's correlation for surface tension (∗) and using Eqn. (44) for surface tension (×), $RA_{nom} = 30\%$.

Figure 26. Measured N and model predictions using Hoppel's correlation for surface tension (∗) and using Eqn. (44) for surface tension (×), $RA_{nom} = 50\%$.

Figure 27. Measured N and model predictions using Hoppel's correlation for surface tension (∗) and using Eqn. (44) for surface tension (×), $RA_{nom} = 60\%$.

Figure 28. Measured N and model predictions using Hoppel's correlation for surface tension (∗) and using Eqn. (44) for surface tension (×), $RH_{nom} = 15\%$.

Figure 29. Measured N and model predictions using Hoppel's correlation for surface tension (∗) and using Eqn. (44) for surface tension (×), $RH_{nom} = 40\%$.

Figure 30. Measured N and model predictions using Hoppel's correlation for surface tension (∗) and using Eqn. (44) for surface tension (×), $RH_{nom} = 50\%$.

Figure 31. Values of $(\ln S^*)/\sigma^*$ for experimental conditions.

Figure 32. Formation free energy, $\Delta G^*/kT$, for experimental conditions.

Figure 33. Predicted binary nucleation rates, R_{J_b}, for experimental conditions.

Figure 34. Measured N and model predictions for experimental RH (∗) and for RH from Eqn. (60) (×), $RH_{nom} = 15\%$.

Figure 35. Measured N and model predictions for experimental RH (∗) and for RH from Eqn. (60) (×), $RH_{nom} = 40\%$.

Figure 36. Measured N and model predictions for experimental RH $(*)$ and for RH from Eqn. (60) $(\times)$, $RH_{nom} = 50\%$.

Figure 37. Time lag for experimental conditions.

Figure 38. Time lag for experimental conditions; approximate nucleation rates indicated.

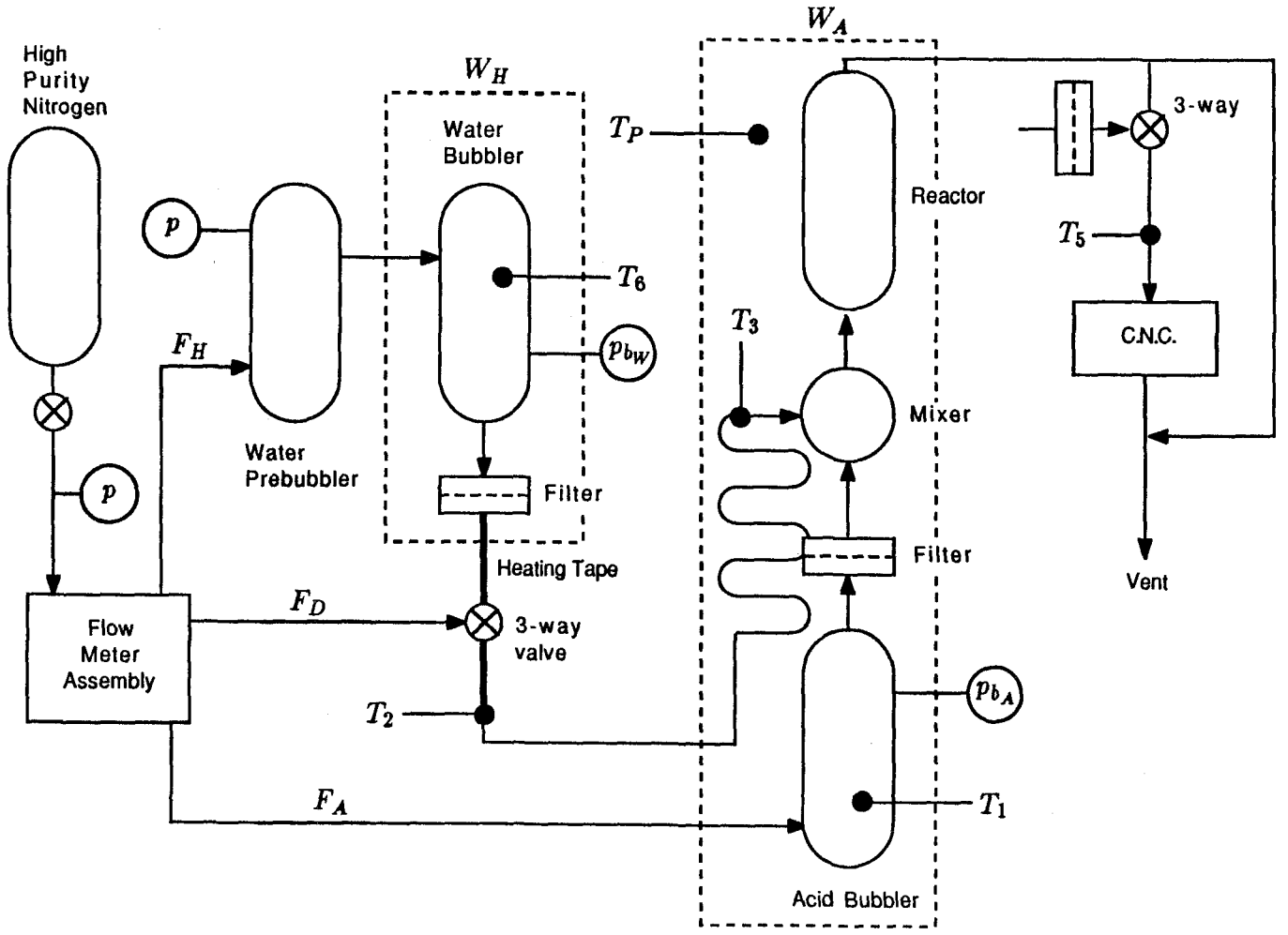
High
Purity
Nitrogen
W_H
Water
Bubbler
W_A
T_P
Reactor
3-way
T_5
C.N.C.
p
T_6
p_{b_W}
F_H
T_3
Mixer
Water
Prebubbler
Filter
Heating Tape
Filter
Vent
F_D
Flow
Meter
Assembly
3-way
valve
T_2
p_{b_A}
F_A
T_1
Acid Bubbler

Figure 1

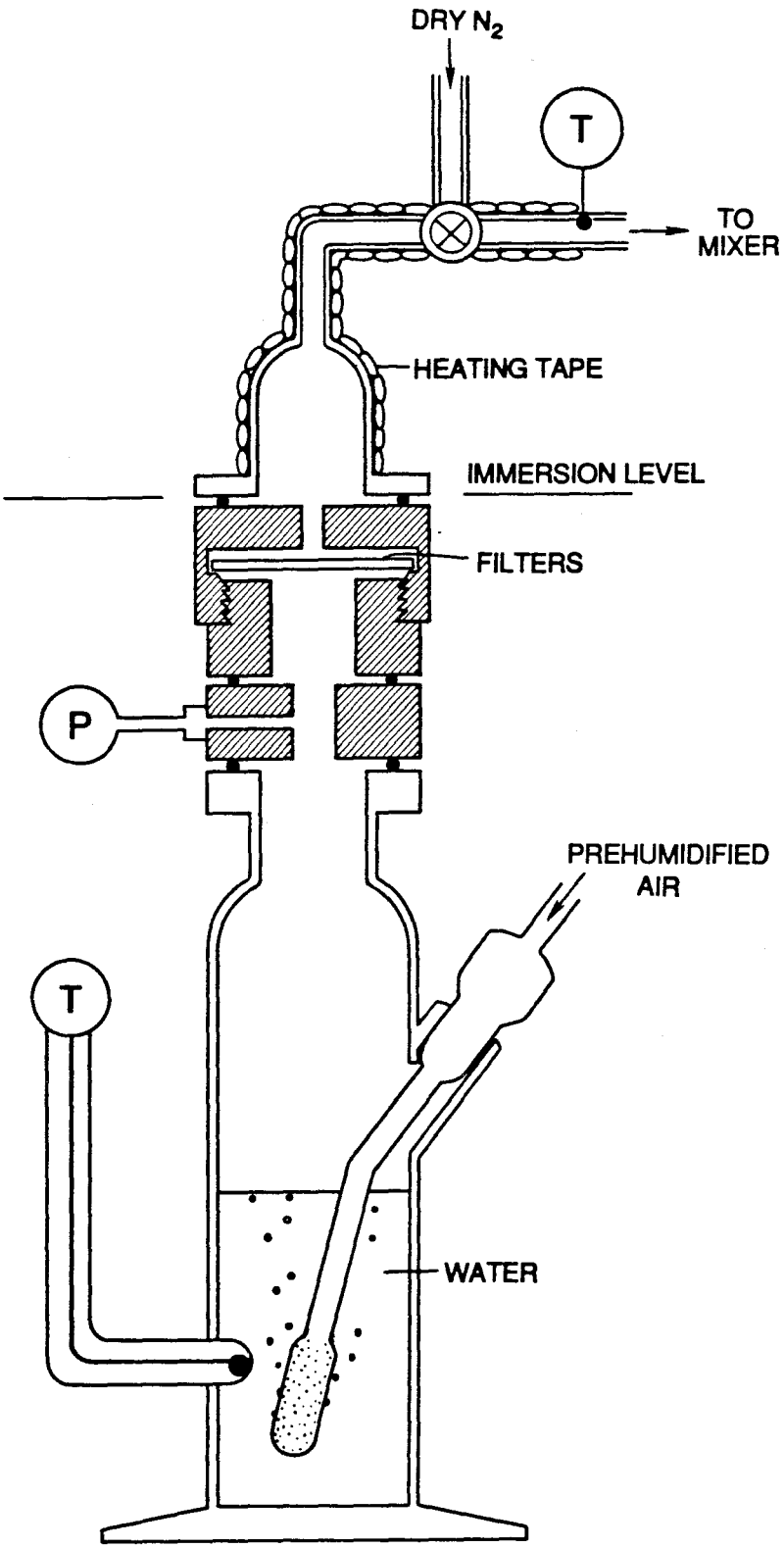
DRY N_2
T
TO MIXER
HEATING TAPE
IMMERSION LEVEL
FILTERS
P
PREHUMIDIFIED AIR
T
WATER

Figure 2

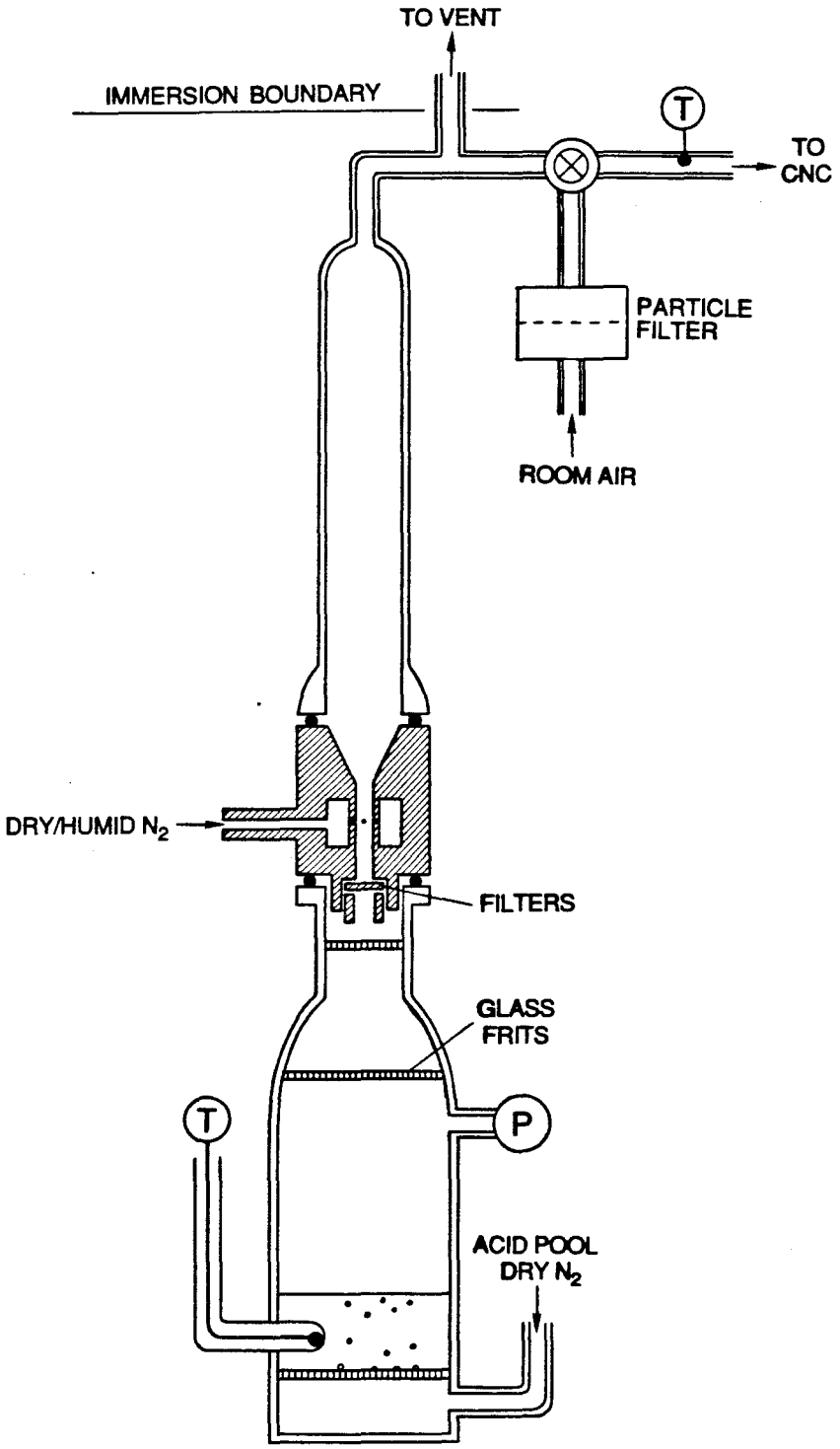
TO VENT
IMMERSION BOUNDARY
T
TO CNC
PARTICLE FILTER
ROOM AIR
DRY/HUMID N_2
FILTERS
GLASS FRITS
T
P
ACID POOL DRY N_2

Figure 3

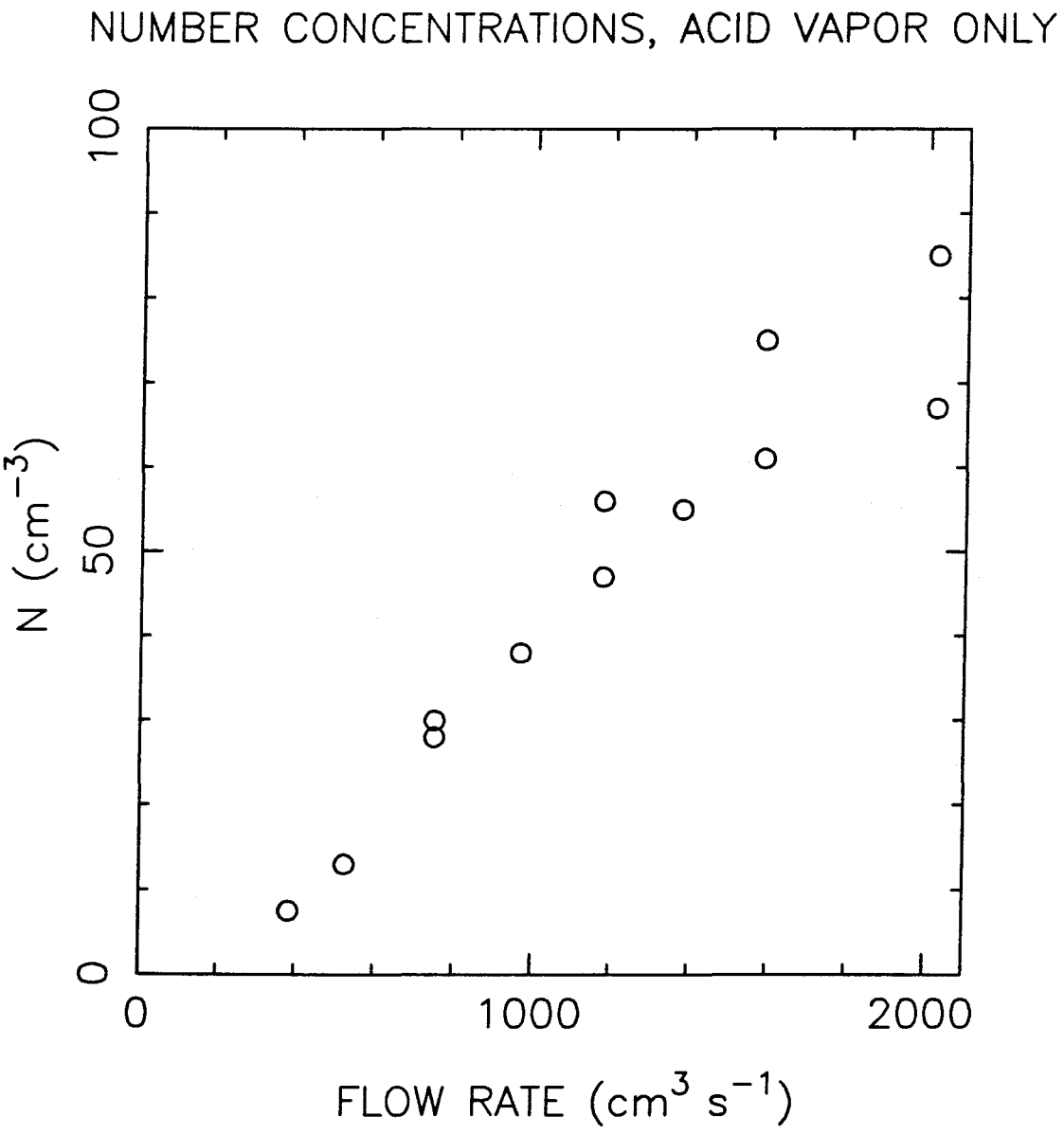
NUMBER CONCENTRATIONS, ACID VAPOR ONLY
N (cm^{-3})
100
50
0
0
1000
2000
FLOW RATE (cm^3 s^{-1})

Figure 4

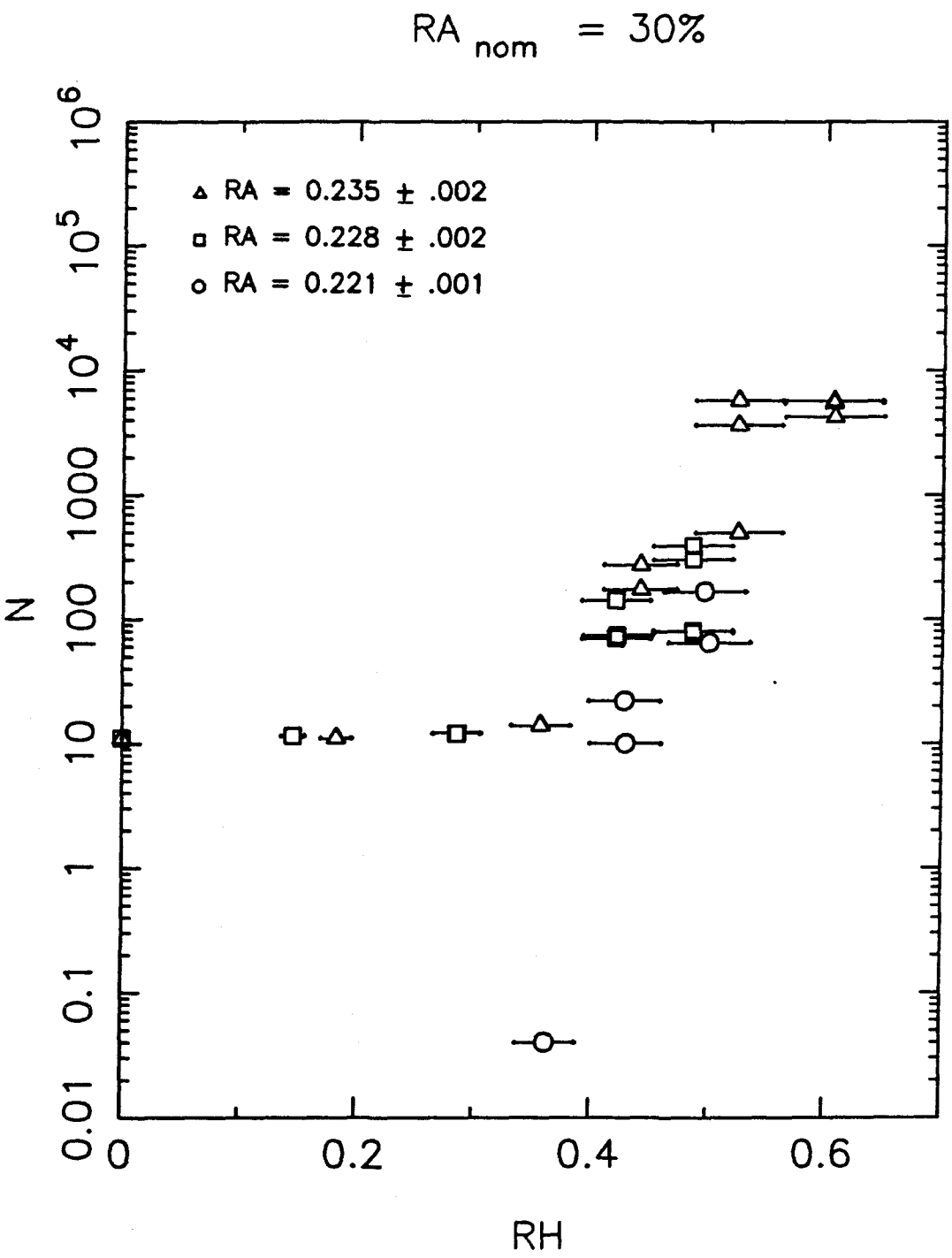
RA nom = 30%
RA = 0.235 ± .002
RA = 0.228 ± .002
RA = 0.221 ± .001
N
RH
0.01
0.1
1
10
100
1000
10^4
10^5
10^6
0
0.2
0.4
0.6

Figure 5

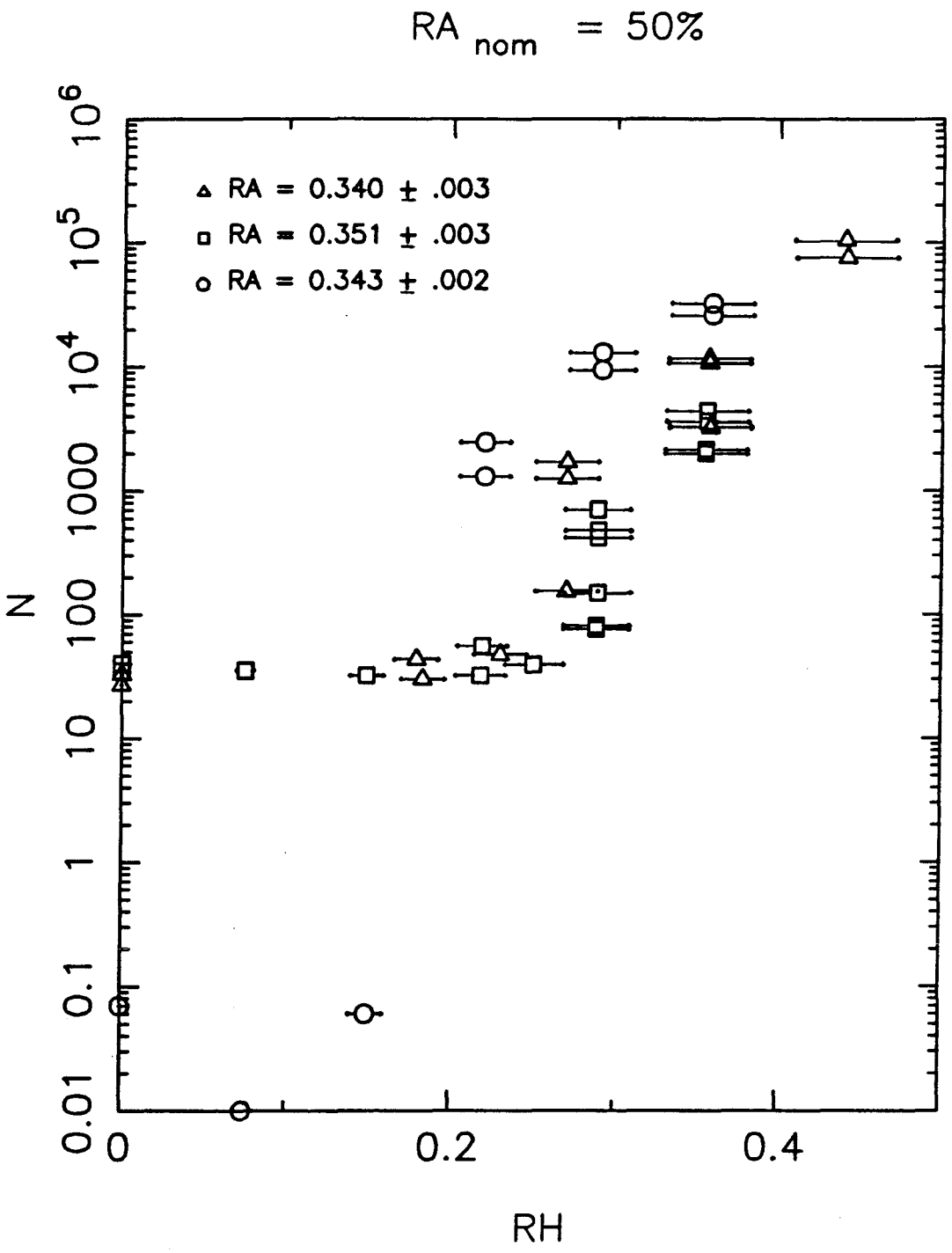
RA nom = 50%
RA = 0.340 ± .003
RA = 0.351 ± .003
RA = 0.343 ± .002
N
RH
0.01
0.1
1
10
100
1000
10^4
10^5
10^6
0
0.2
0.4

Figure 6

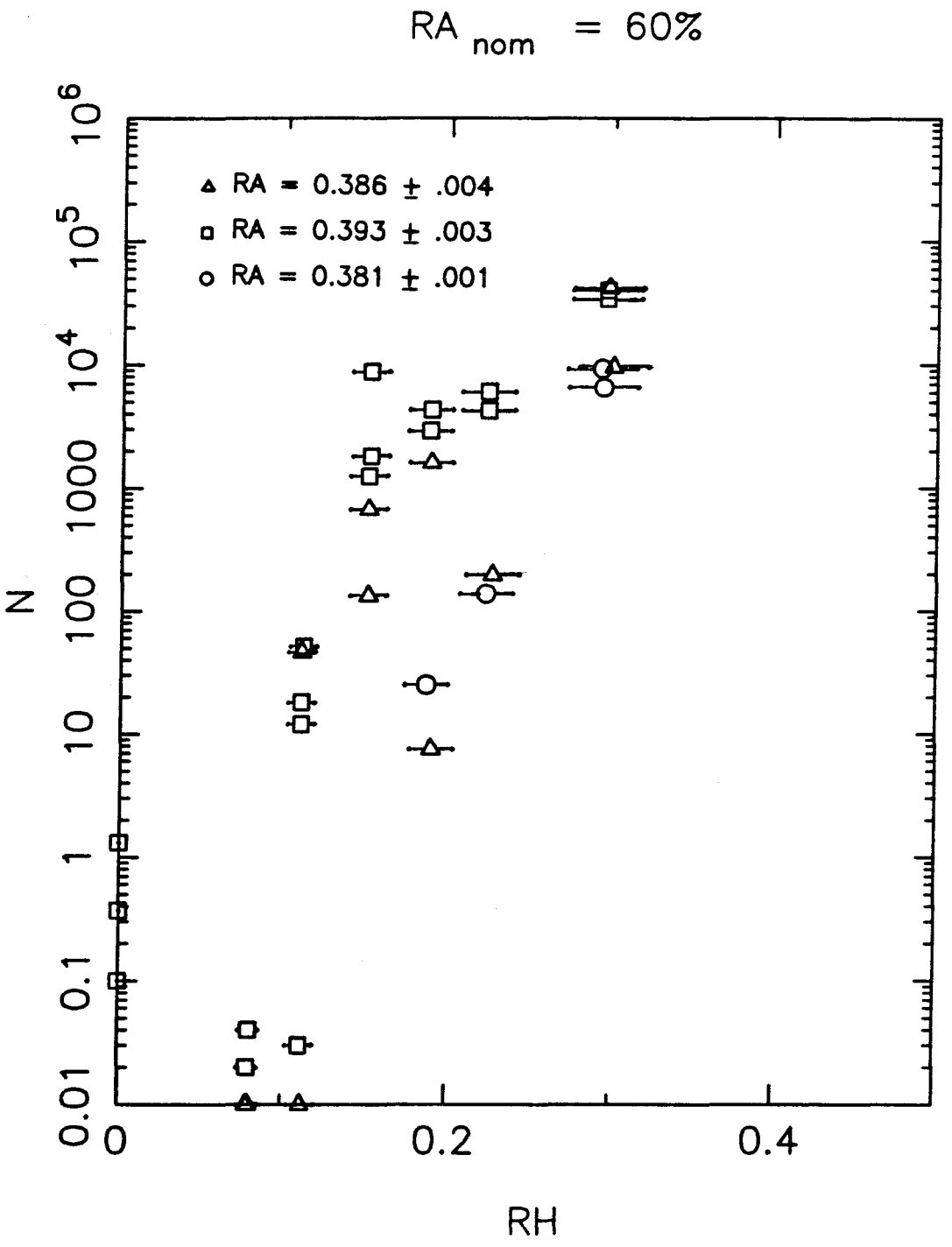
RA nom = 60%
RA = 0.386 ± .004
RA = 0.393 ± .003
RA = 0.381 ± .001
N
0.01
0.1
1
10
100
1000
10^4
10^5
10^6
0
0.2
0.4
RH

Figure 7

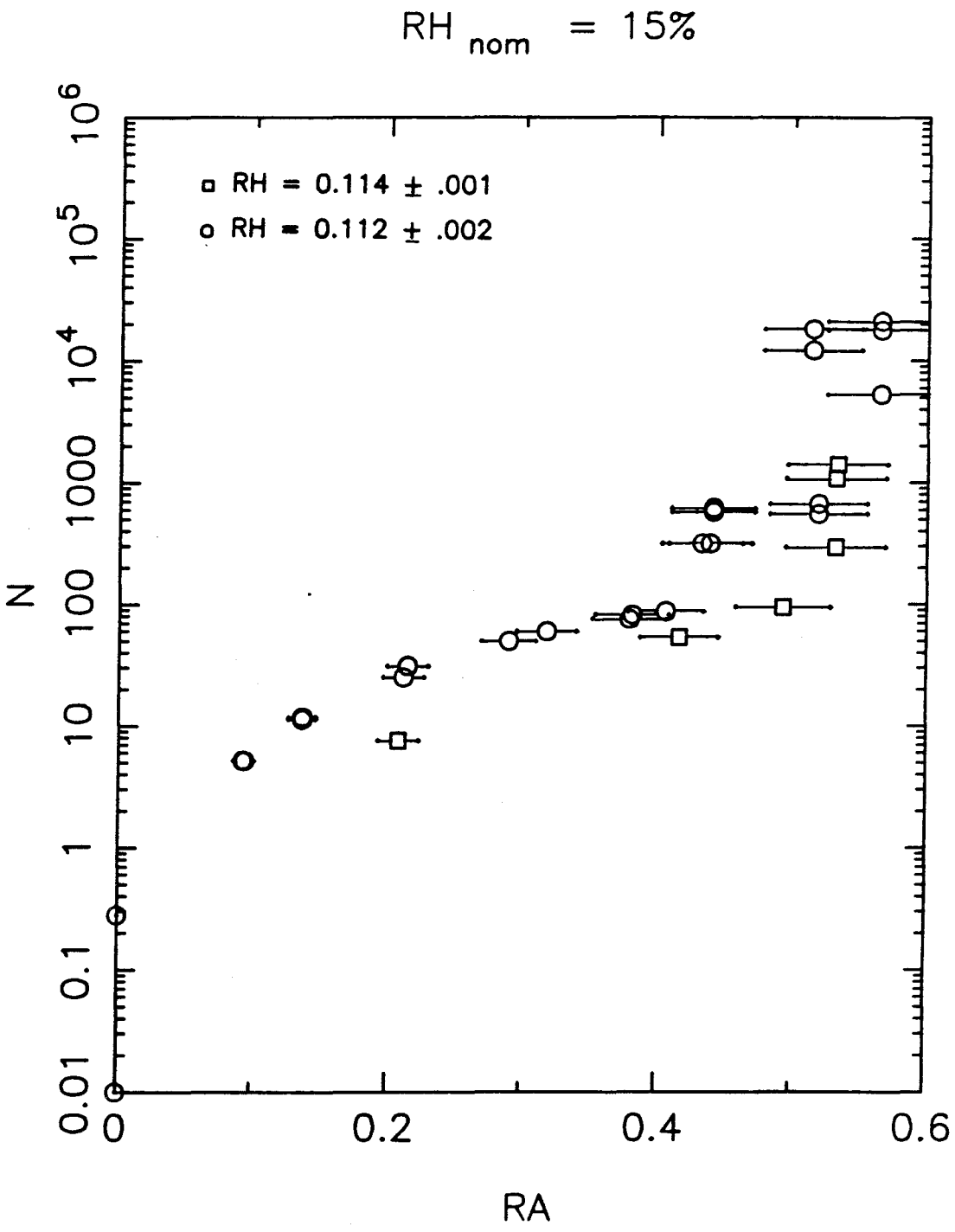
RH nom = 15%
RH = 0.114 ± .001
RH = 0.112 ± .002
N
RA
0.01
0.1
1
10
100
1000
10^4
10^5
10^6
0
0.2
0.4
0.6

Figure 8

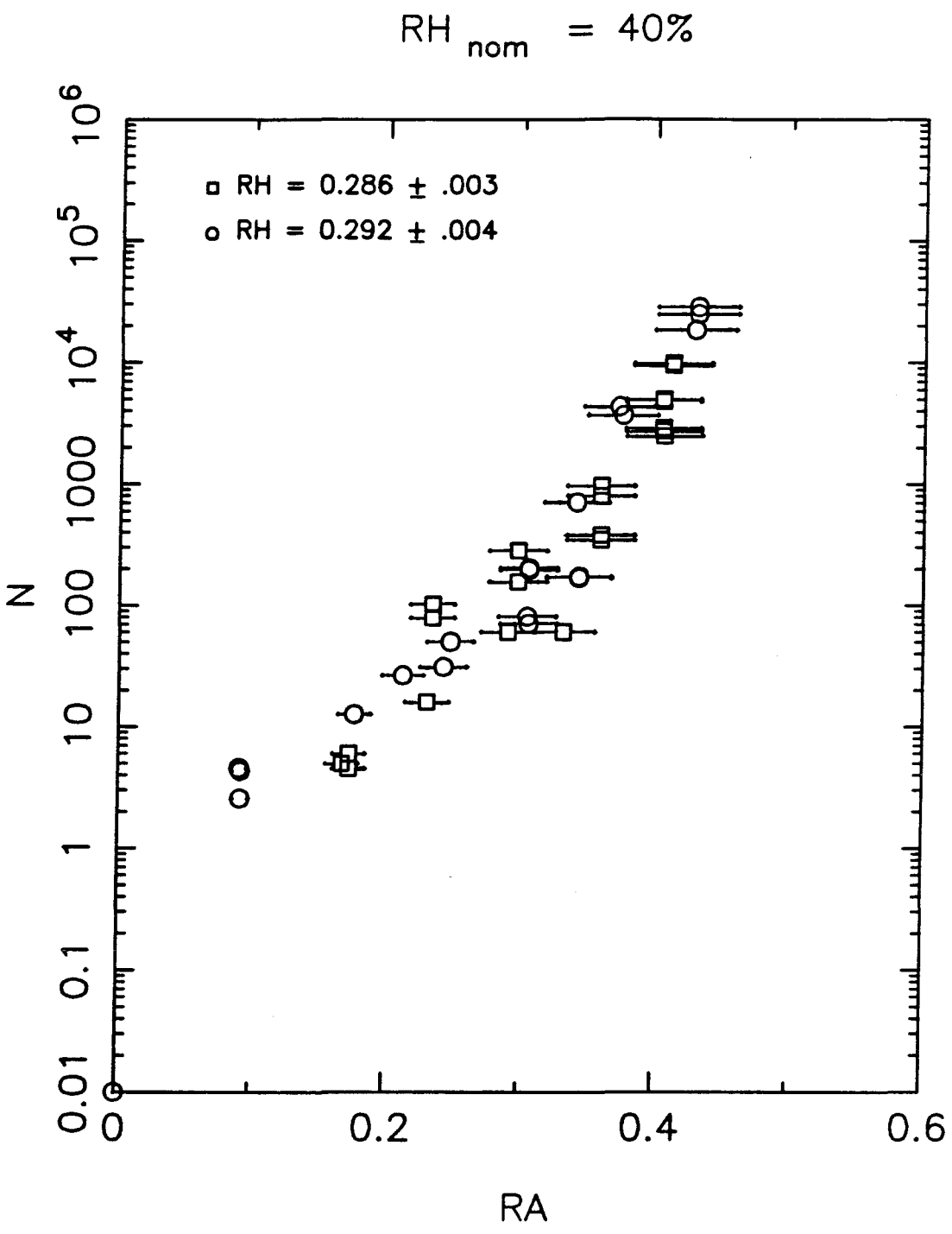
RH nom = 40%
RH = 0.286 ± .003
RH = 0.292 ± .004
N
RA
0.01
0.1
1
10
100
1000
10^4
10^5
10^6
0
0.2
0.4
0.6

Figure 9

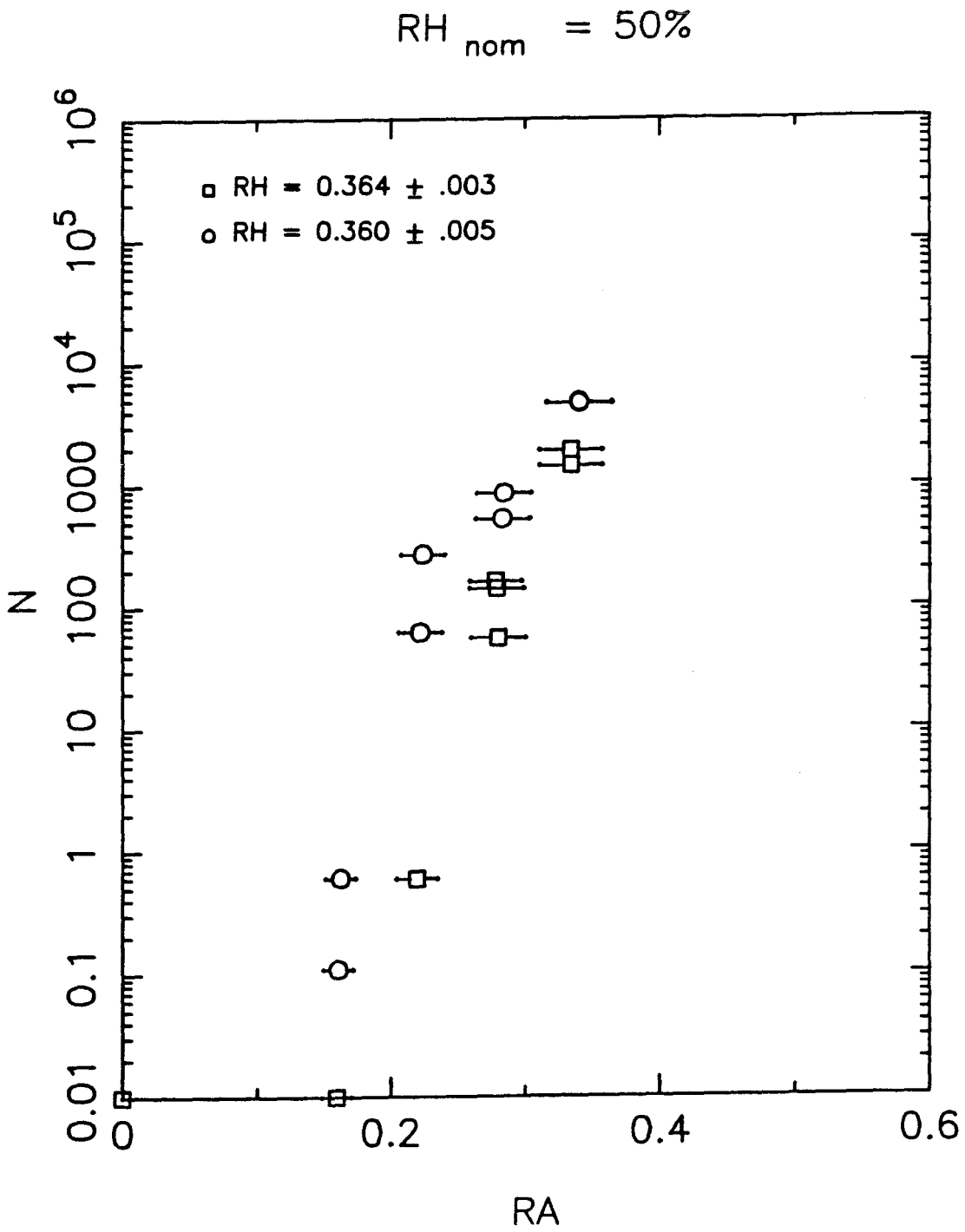
RH nom = 50%
RH = 0.364 ± .003
RH = 0.360 ± .005
N
0.01
0.1
1
10
100
1000
10^4
10^5
10^6
0
0.2
0.4
0.6
RA

Figure 10

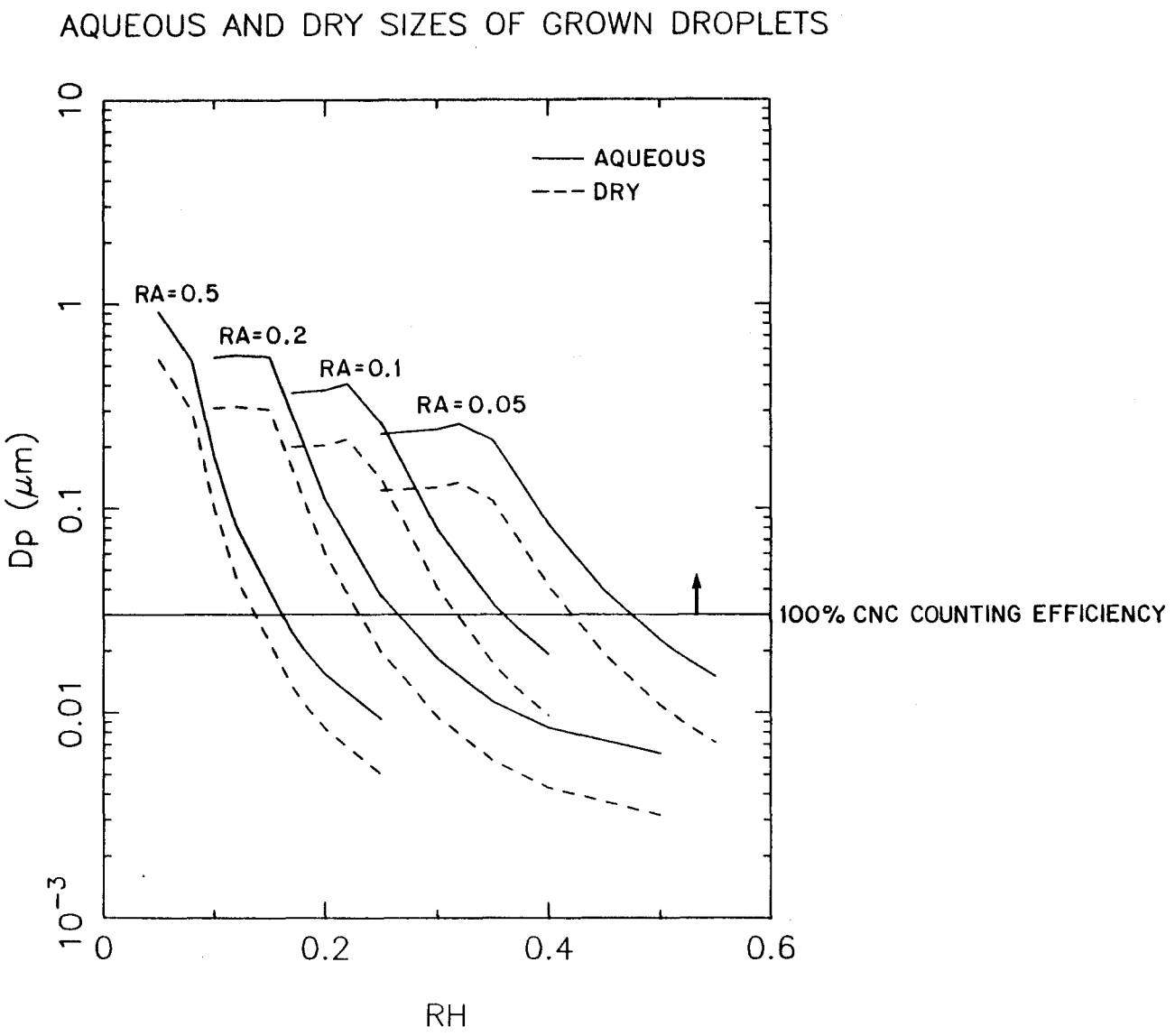
AQUEOUS AND DRY SIZES OF GROWN DROPLETS
AQUEOUS
DRY
RA=0.5
RA=0.2
RA=0.1
RA=0.05
100% CNC COUNTING EFFICIENCY
Dp (μm)
10
1
0.1
0.01
10⁻³
0
0.2
0.4
0.6
RH

Figure 11

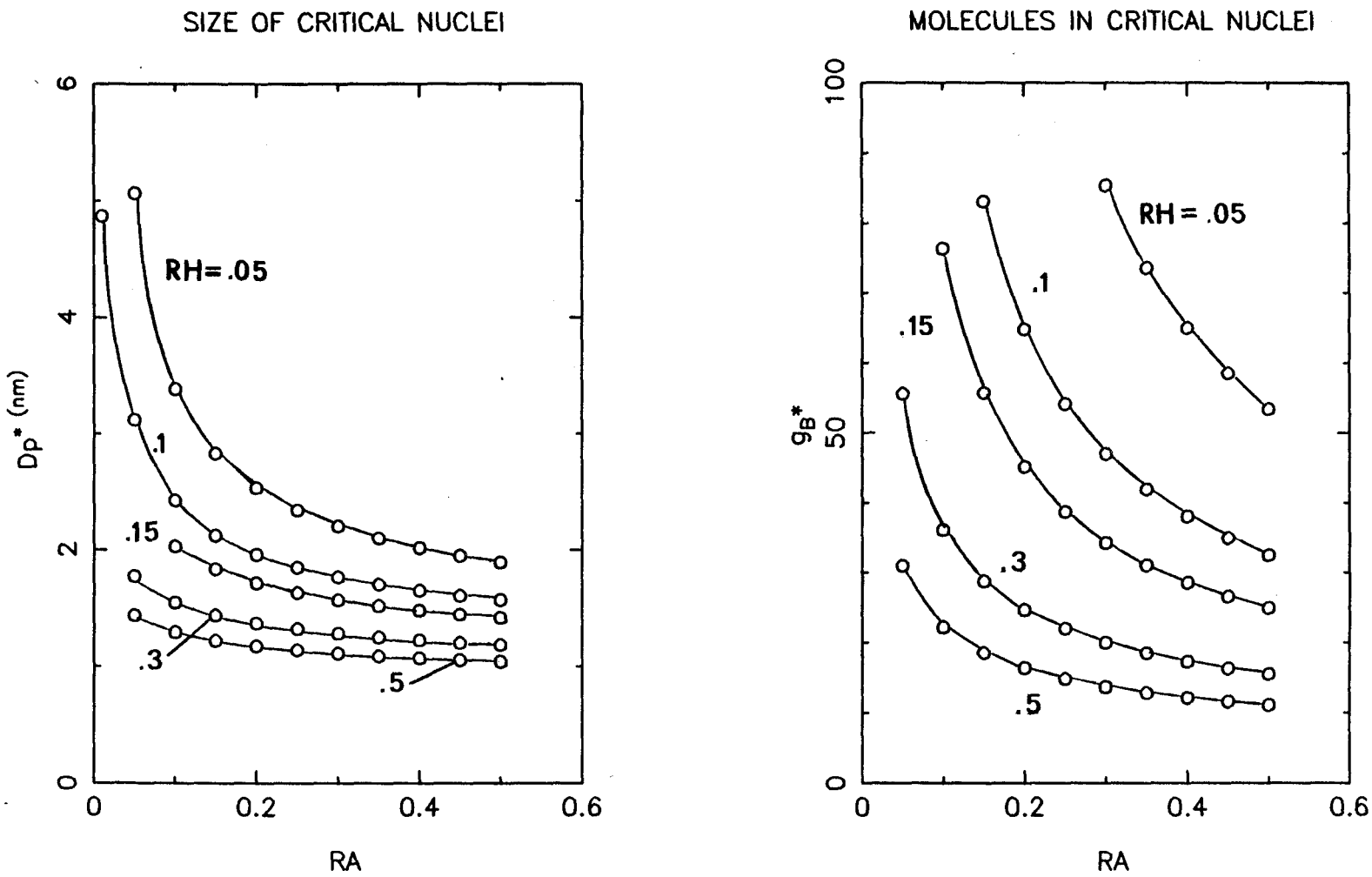
SIZE OF CRITICAL NUCLEI
Dp* (nm)
RH=.05
.1
.15
.3
.5
RA
MOLECULES IN CRITICAL NUCLEI
gB*
RH = .05
.1
.15
.3
.5
RA

Figure 12

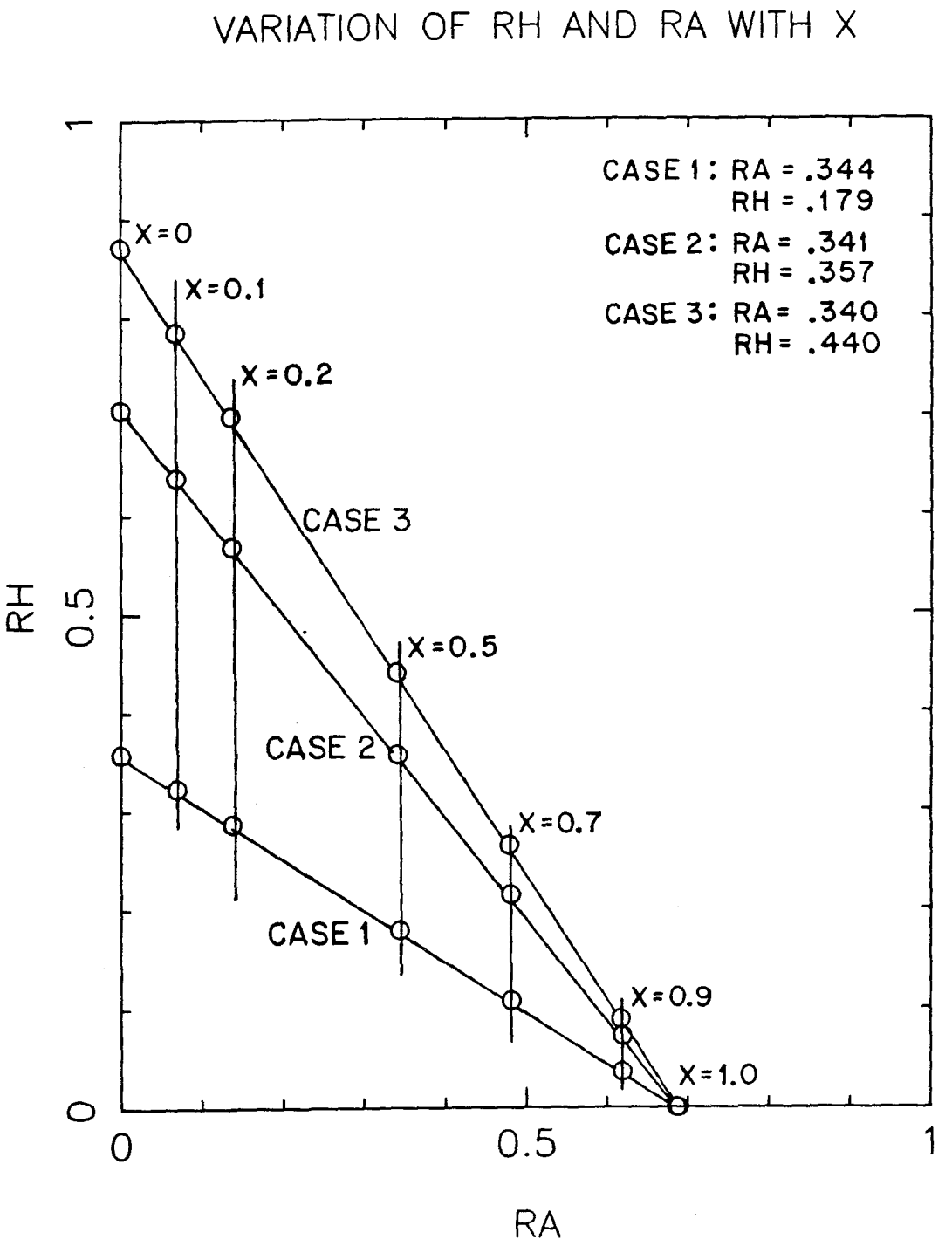
VARIATION OF RH AND RA WITH X
CASE 1: RA = .344
RH = .179
CASE 2: RA = .341
RH = .357
CASE 3: RA = .340
RH = .440
X=0
X=0.1
X=0.2
X=0.5
X=0.7
X=0.9
X=1.0
CASE 3
CASE 2
CASE 1
RH
RA
0
0.5
1
0
0.5
1

Figure 13

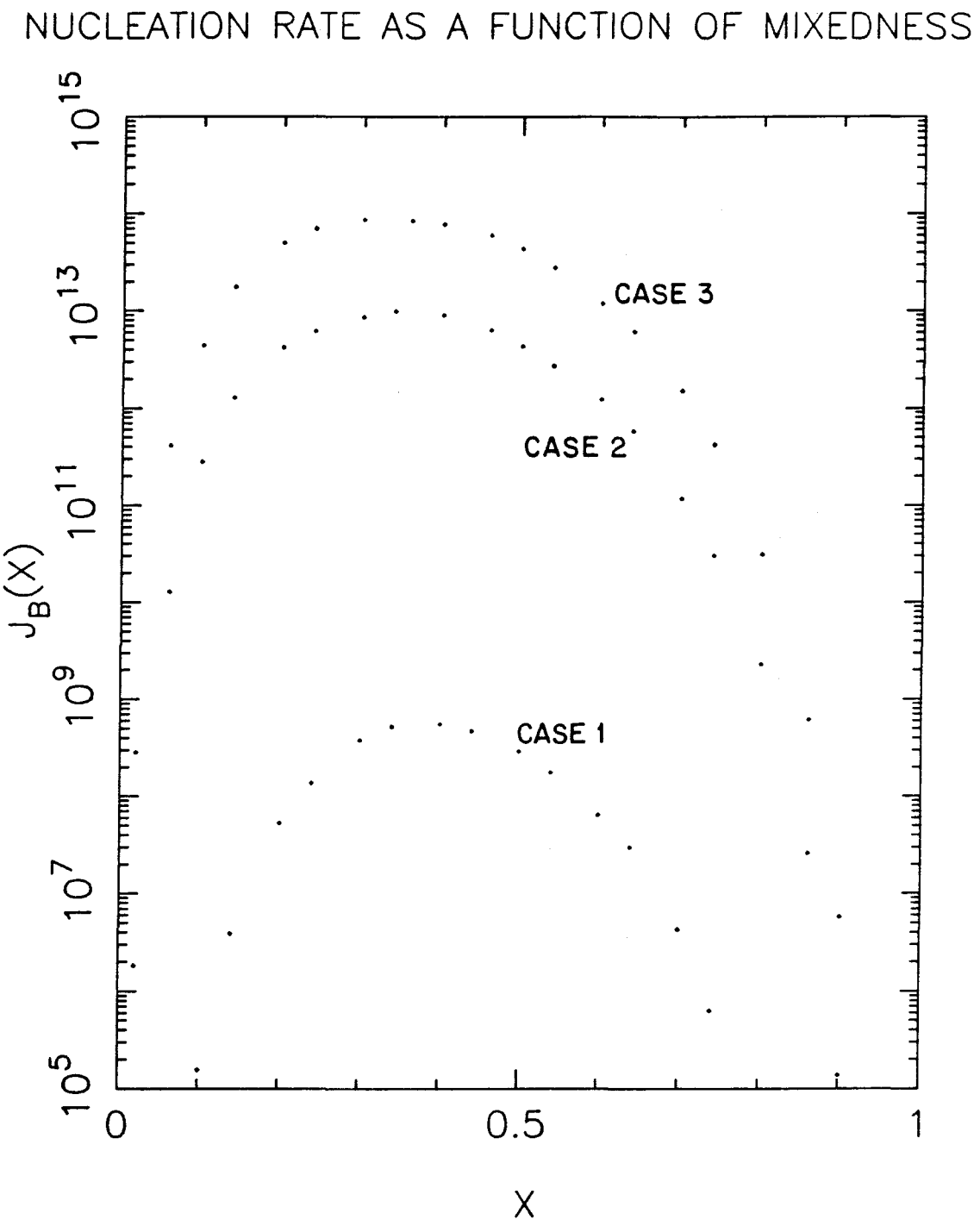
NUCLEATION RATE AS A FUNCTION OF MIXEDNESS
10^{15}
10^{13}
10^{11}
10^{9}
10^{7}
10^{5}
$J_B(X)$
CASE 3
CASE 2
CASE 1
0
0.5
1
X

Figure 14

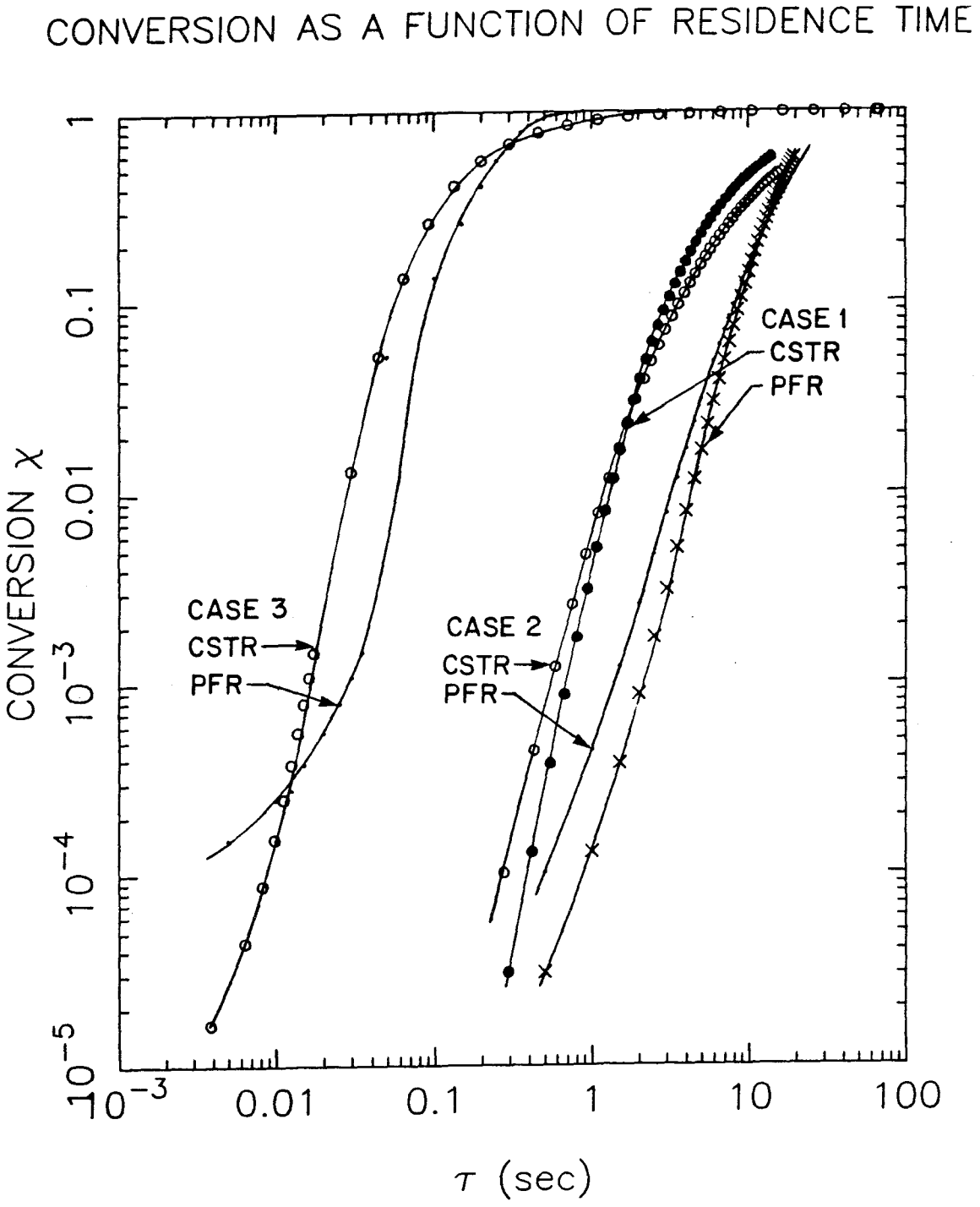
CONVERSION AS A FUNCTION OF RESIDENCE TIME
CONVERSION χ
1
0.1
0.01
10^-3
10^-4
10^-5
10^-3
0.01
0.1
1
10
100
τ (sec)
CASE 1
CSTR
PFR
CASE 2
CSTR
PFR
CASE 3
CSTR
PFR

Figure 15

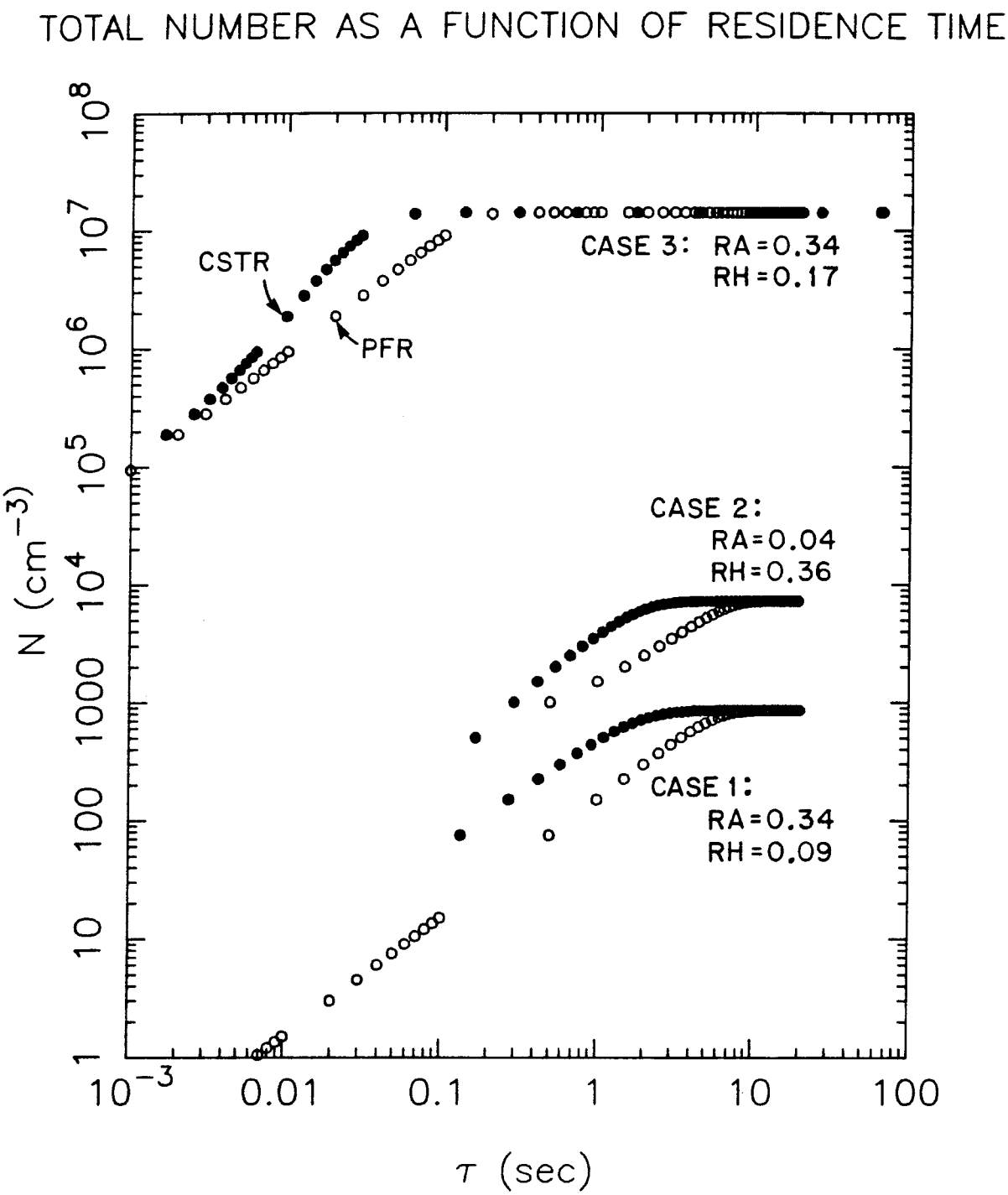
TOTAL NUMBER AS A FUNCTION OF RESIDENCE TIME
N (cm^{-3})
τ (sec)
CSTR
PFR
CASE 3: RA=0.34
RH=0.17
CASE 2:
RA=0.04
RH=0.36
CASE 1:
RA=0.34
RH=0.09

Figure 16

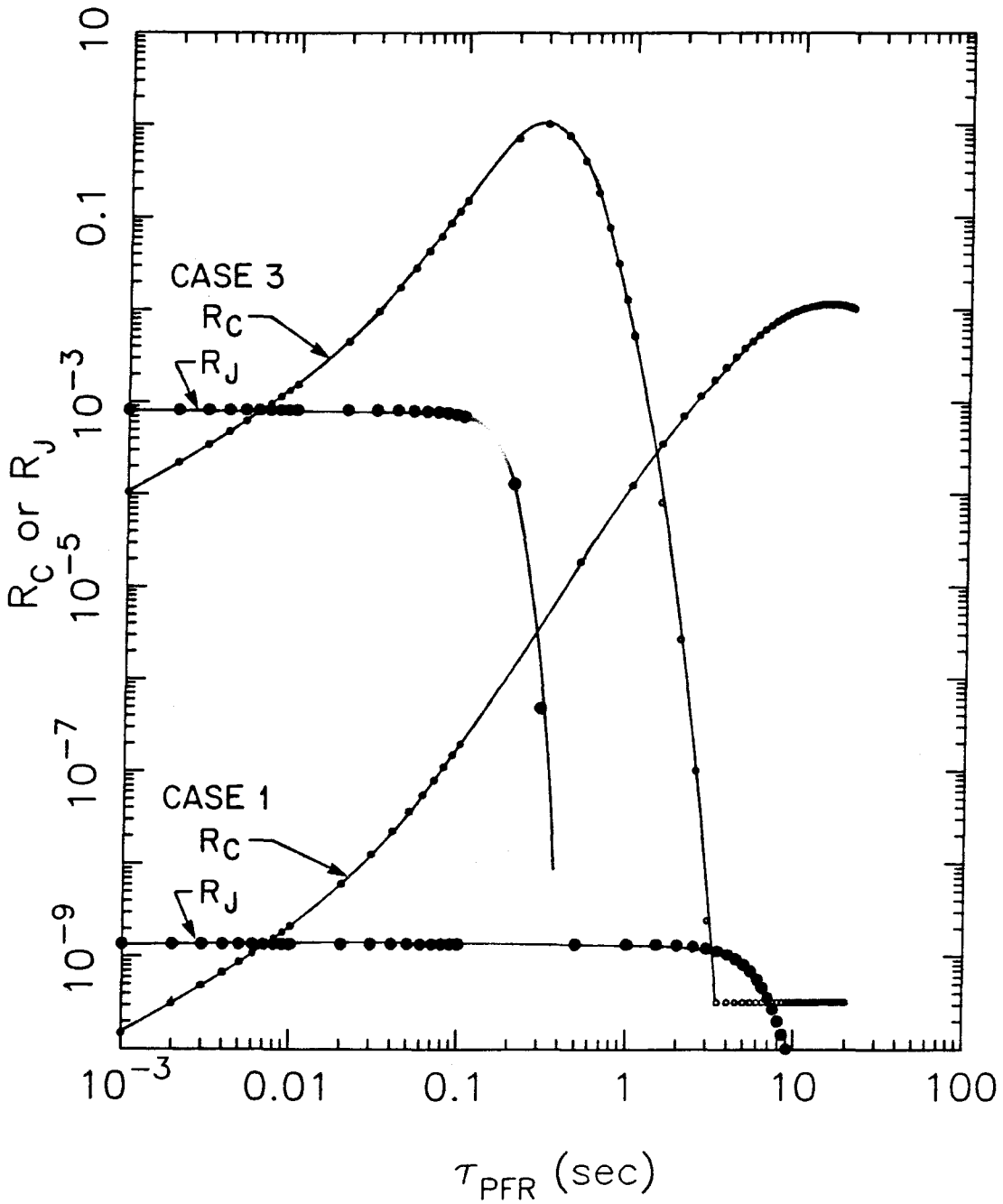
RELATIVE RATES OF NUCLEATION AND CONDENSATION
CASE 3
R_C
R_J
CASE 1
R_C
R_J
R_C or R_J
10
0.1
10^{-3}
10^{-5}
10^{-7}
10^{-9}
10^{-3}
0.01
0.1
1
10
100
τ_{PFR} (sec)

Figure 17

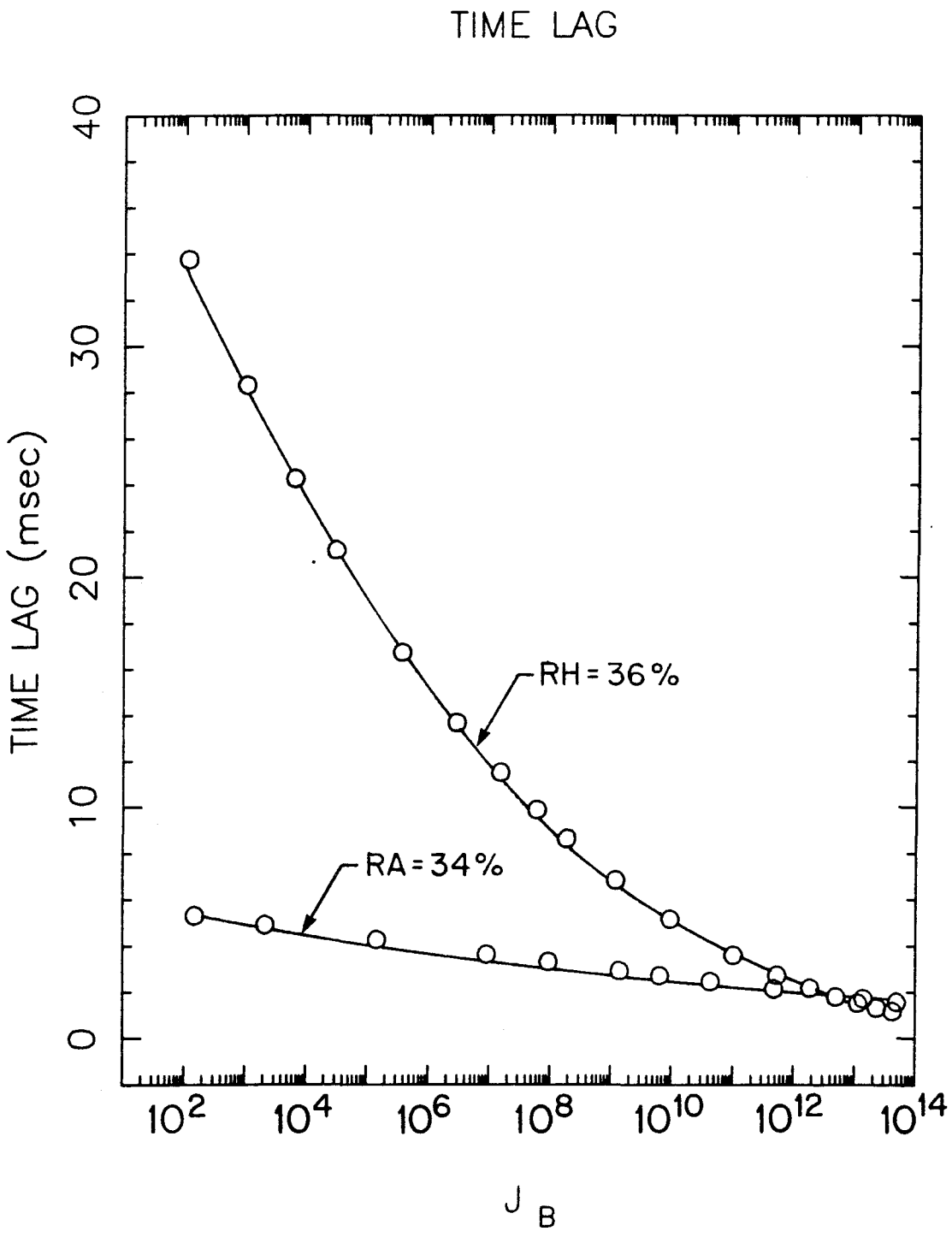
TIME LAG
TIME LAG (msec)
0
10
20
30
40
RH = 36%
RA = 34%
10^2
10^4
10^6
10^8
10^{10}
10^{12}
10^{14}
J_B

Figure 18

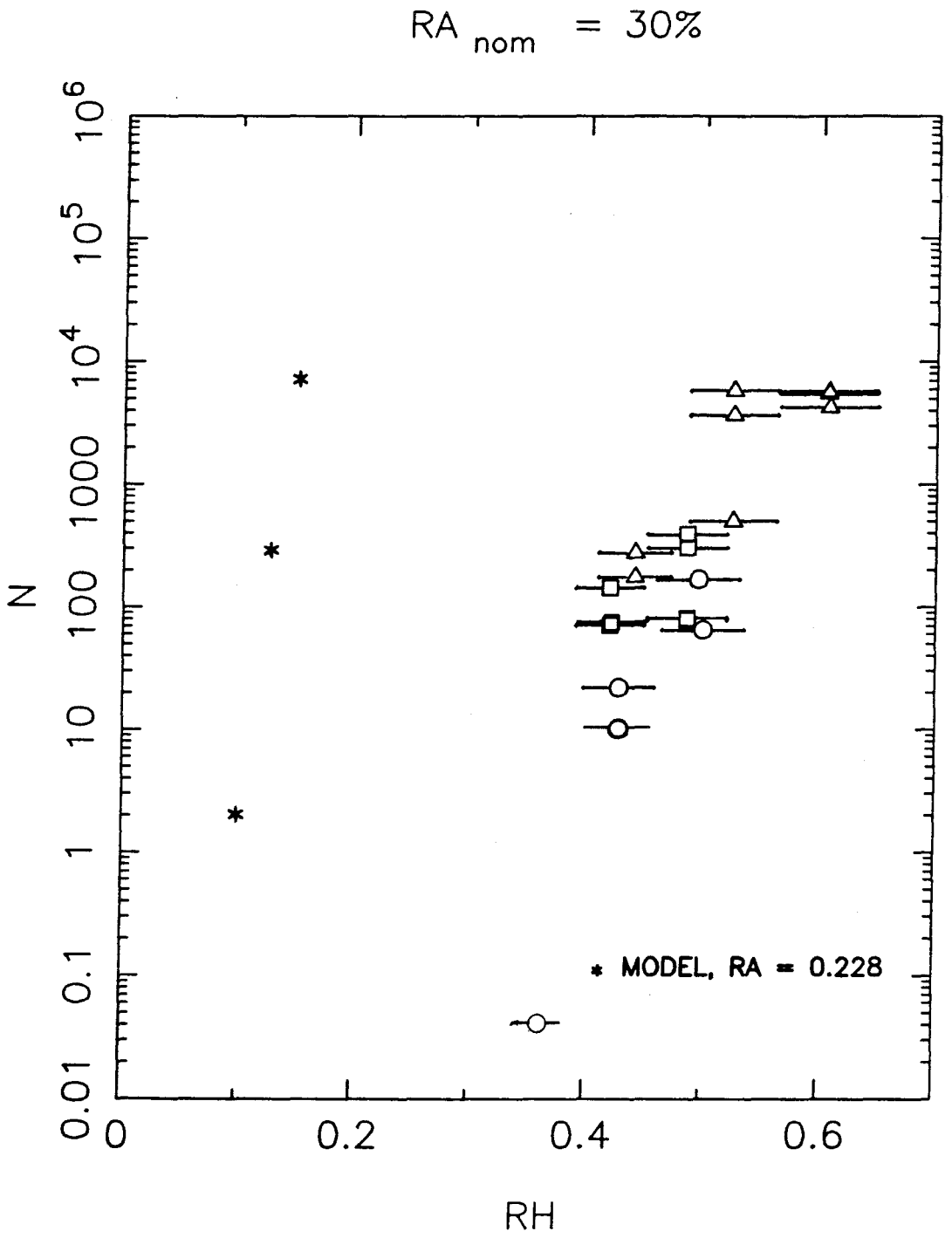
RA nom = 30%
N
RH
0.01
0.1
1
10
100
1000
10^4
10^5
10^6
0
0.2
0.4
0.6
* MODEL, RA = 0.228

Figure 19

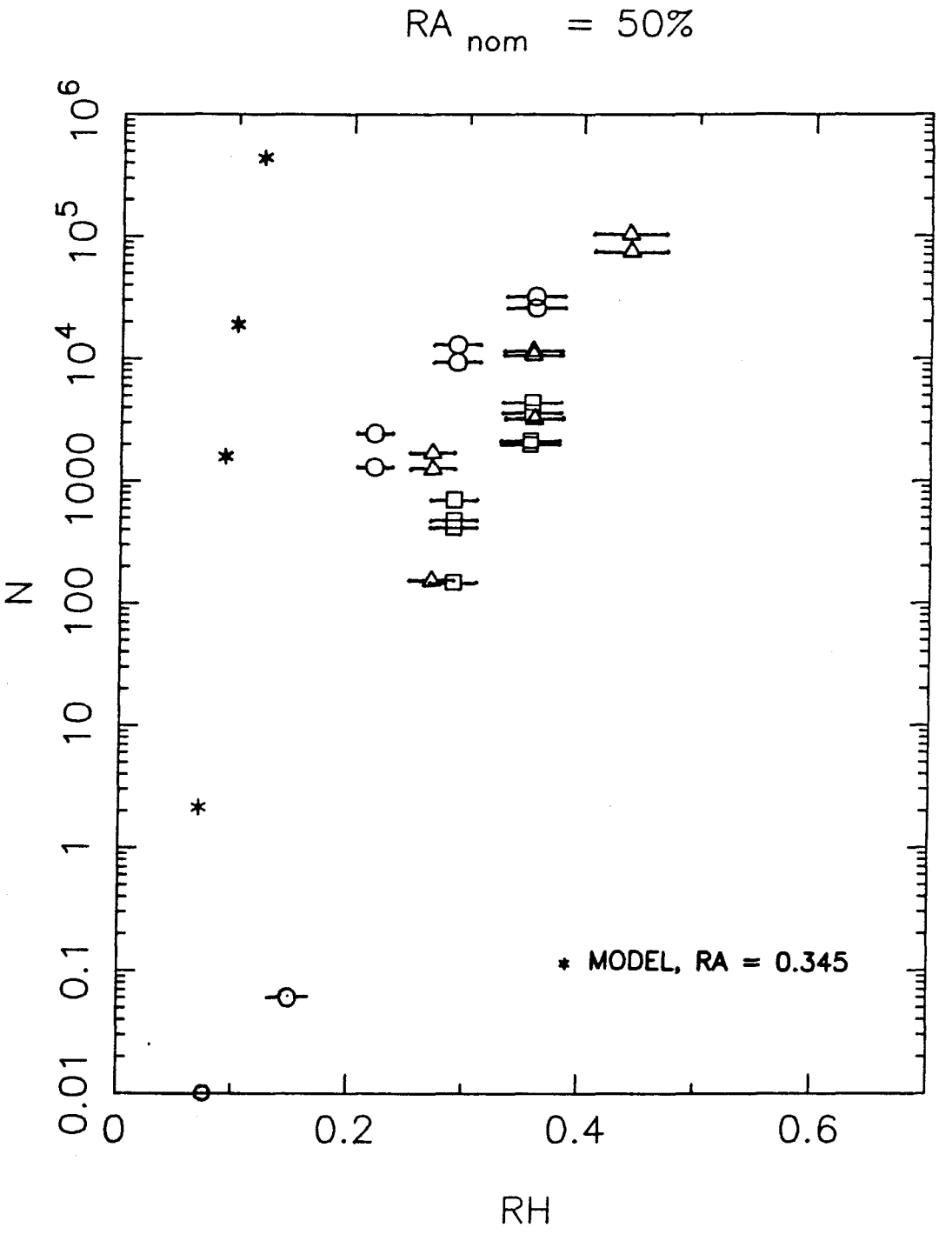
RA nom = 50%
N
RH
0.01
0.1
1
10
100
1000
10^4
10^5
10^6
0
0.2
0.4
0.6
* MODEL, RA = 0.345

Figure 20

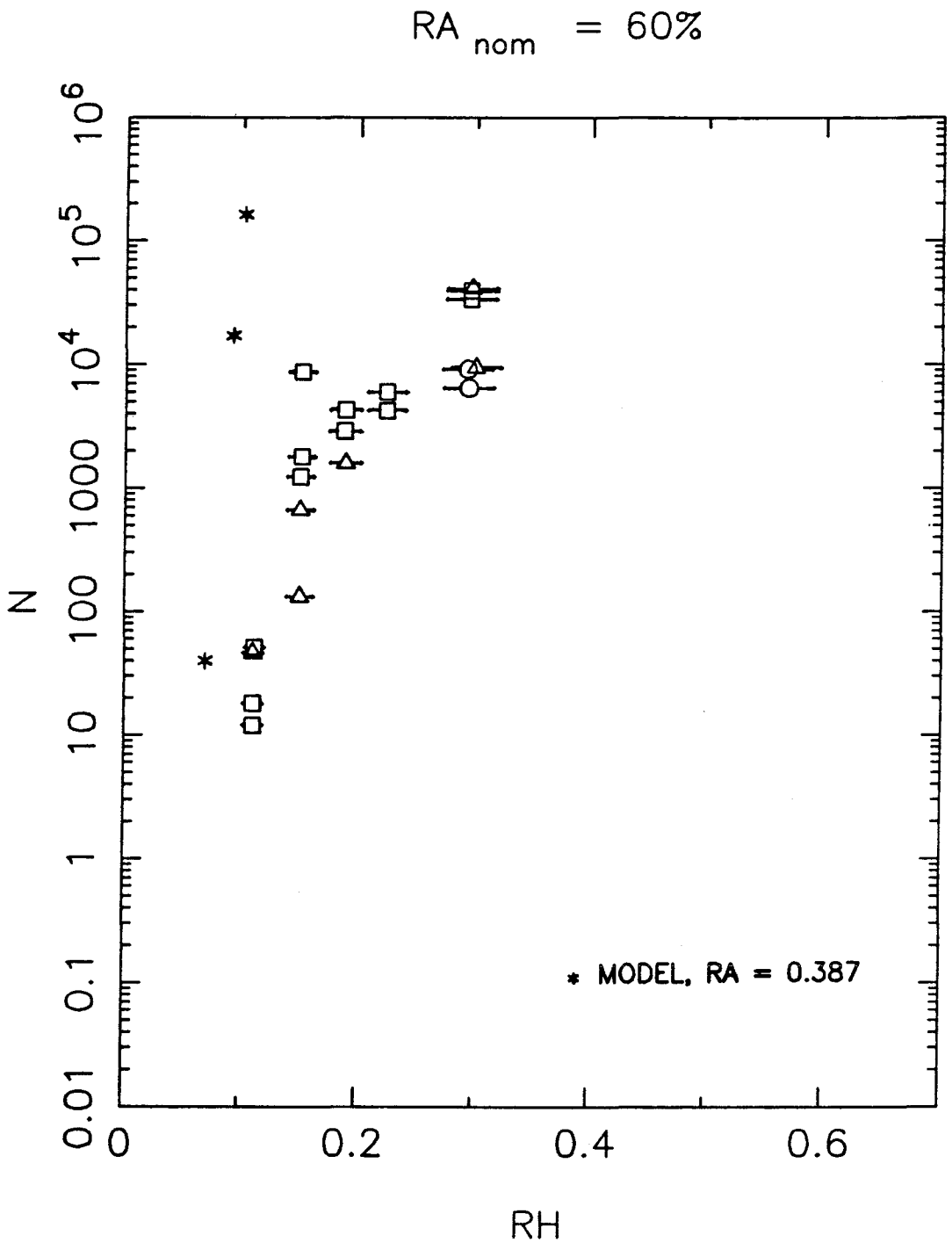
RA nom = 60%
N
RH
0.01
0.1
1
10
100
1000
10^4
10^5
10^6
0
0.2
0.4
0.6
* MODEL, RA = 0.387

Figure 21

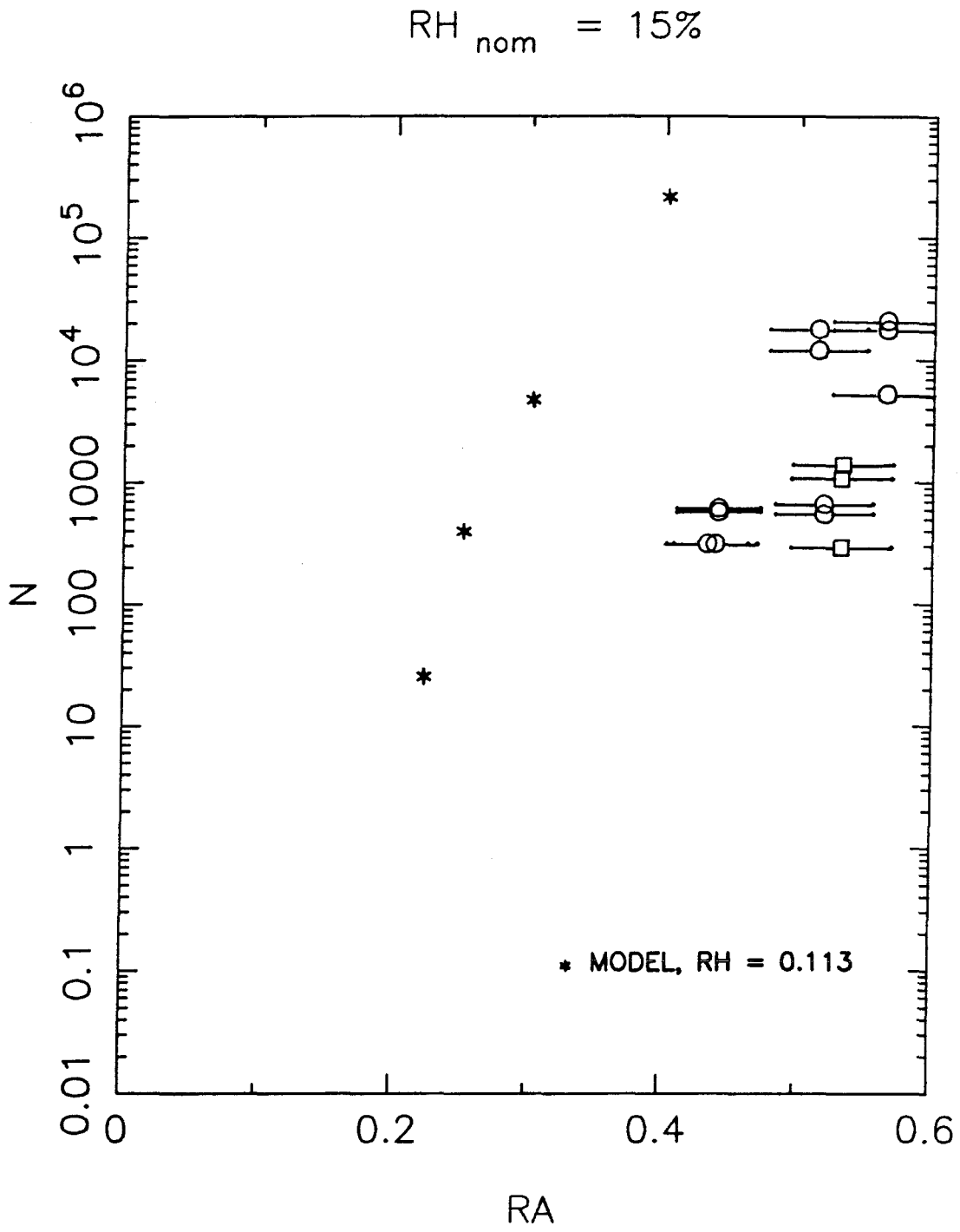
RH nom = 15%
N
0.01
0.1
1
10
100
1000
10^4
10^5
10^6
0
0.2
0.4
0.6
RA
* MODEL, RH = 0.113

Figure 22

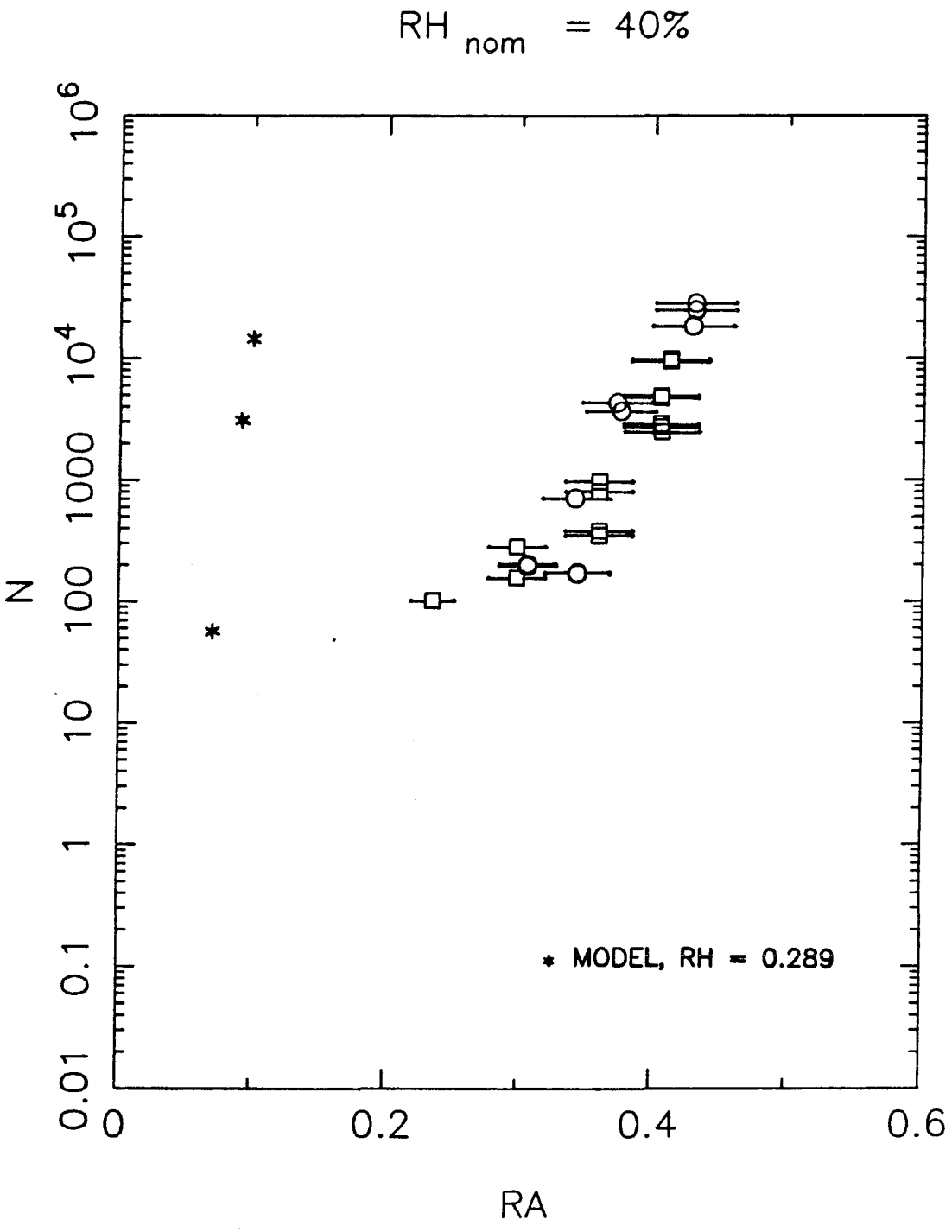
RH nom = 40%
N
RA
0.01
0.1
1
10
100
1000
10^4
10^5
10^6
0
0.2
0.4
0.6
* MODEL, RH = 0.289

Figure 23

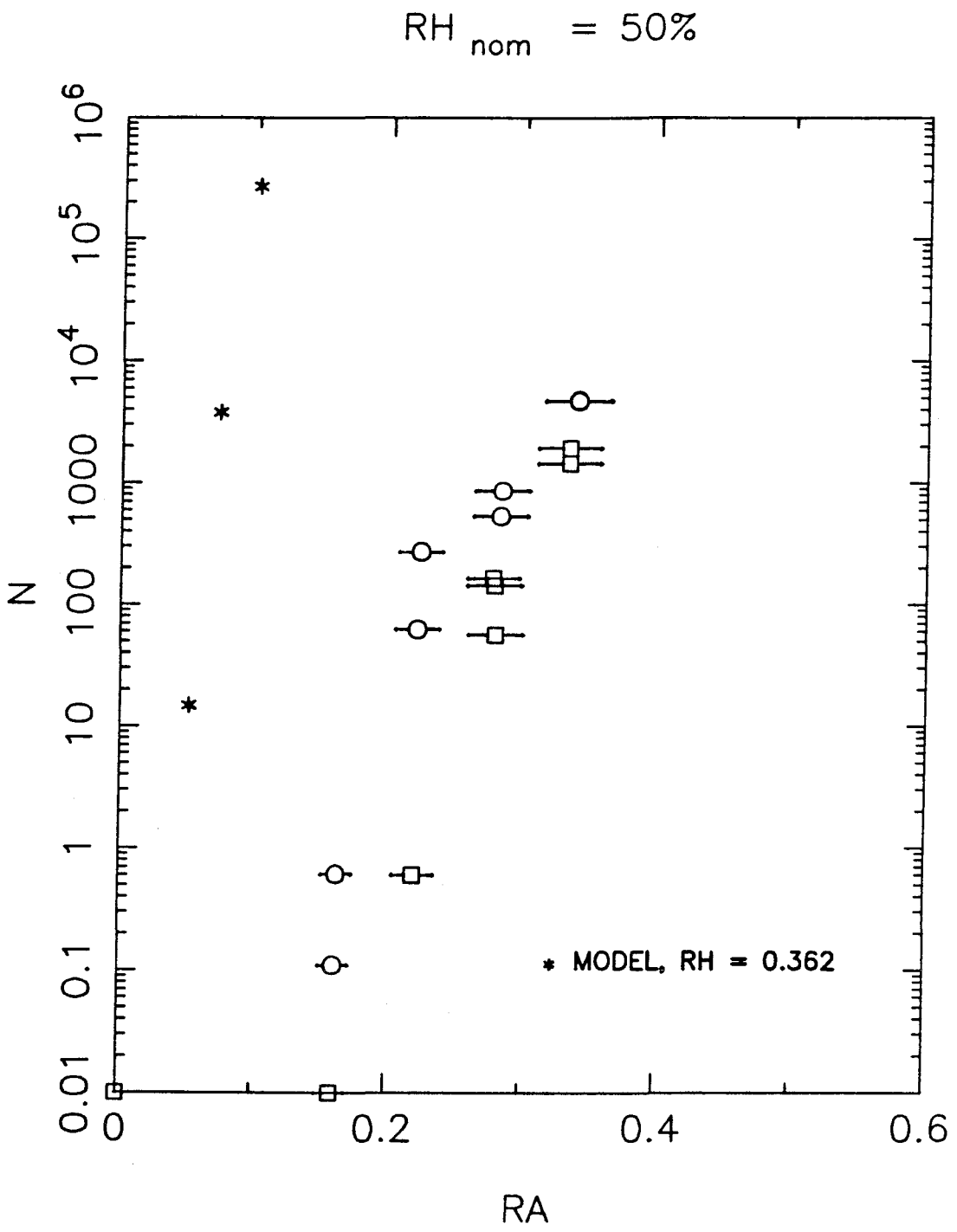
RH nom = 50%
N
RA
0.01
0.1
1
10
100
1000
10^4
10^5
10^6
0
0.2
0.4
0.6
* MODEL, RH = 0.362

Figure 24

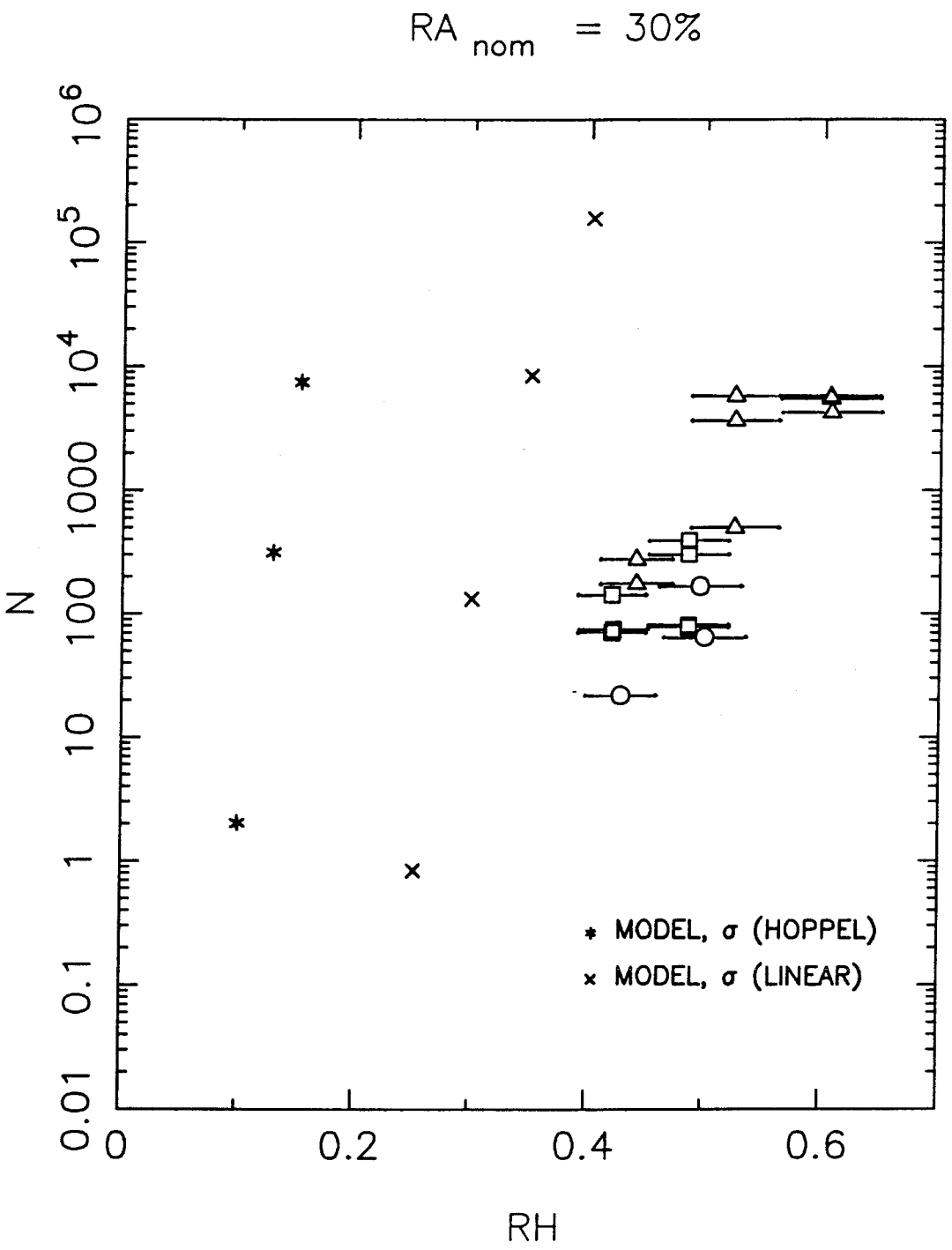
RA nom = 30%
N
RH
0.01
0.1
1
10
100
1000
10^4
10^5
10^6
0
0.2
0.4
0.6
* MODEL, σ (HOPPEL)
× MODEL, σ (LINEAR)

Figure 25

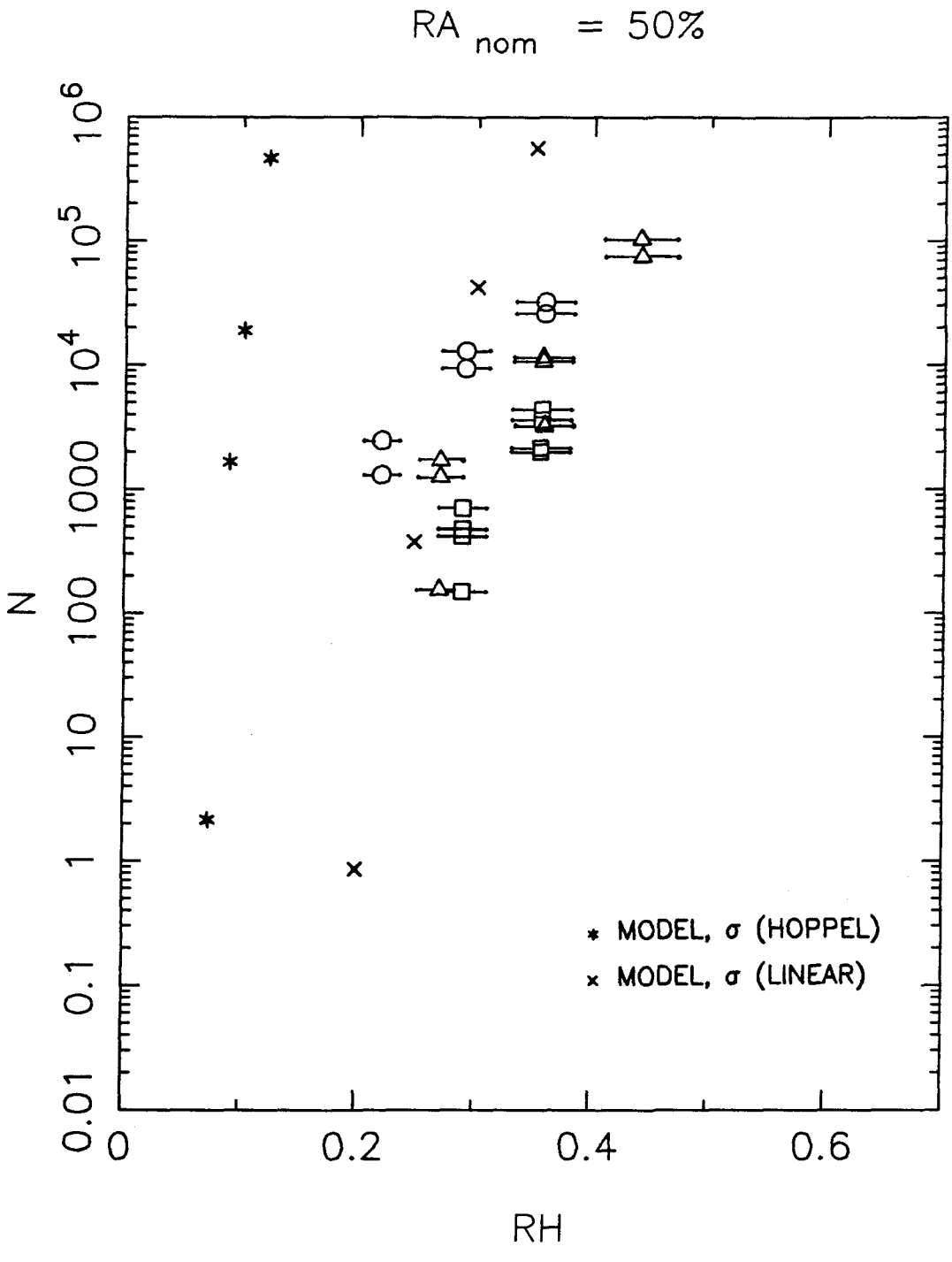
RA nom = 50%
N
RH
0.01
0.1
1
10
100
1000
10^4
10^5
10^6
0
0.2
0.4
0.6
* MODEL, σ (HOPPEL)
× MODEL, σ (LINEAR)

Figure 26

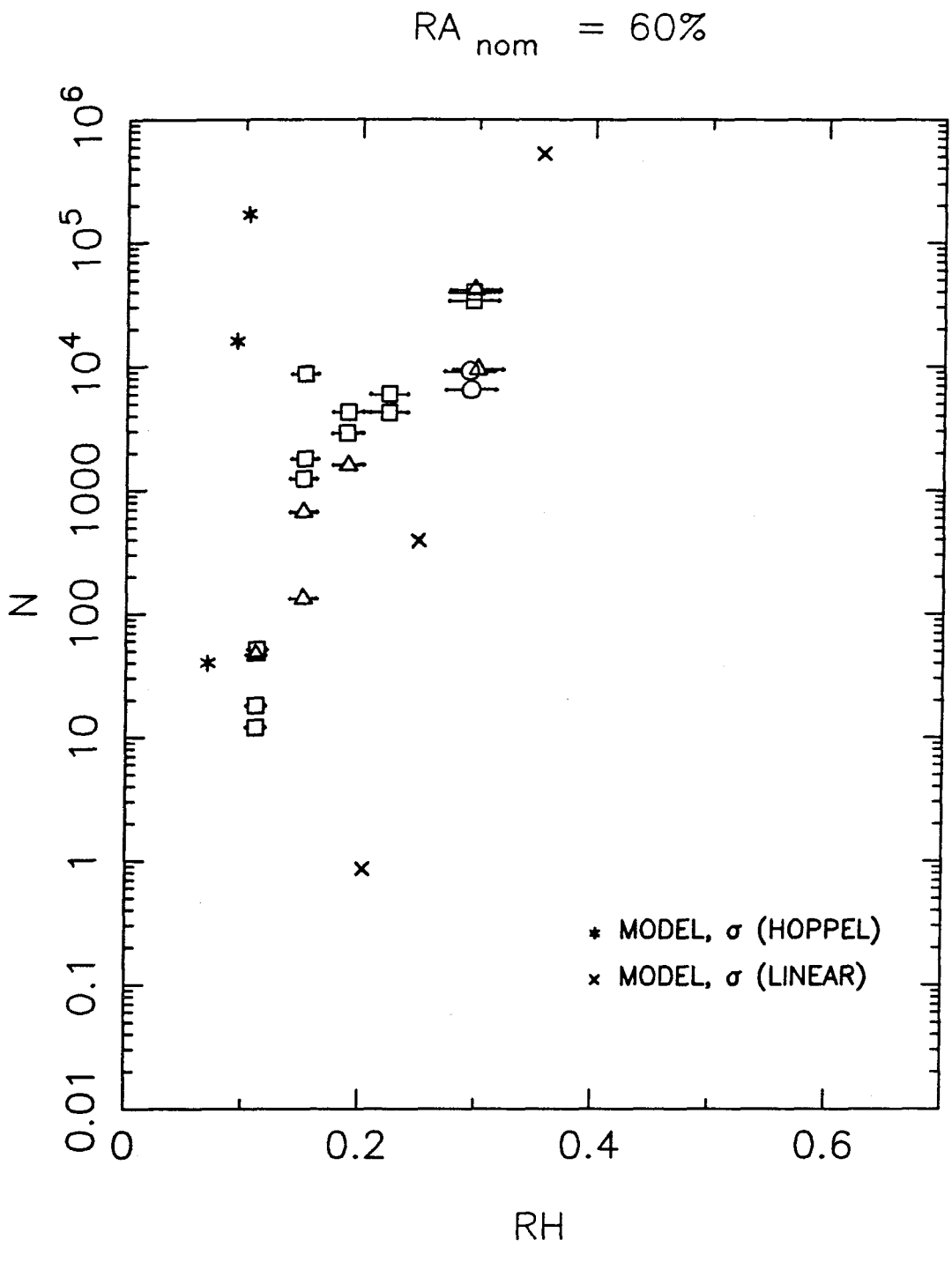
RA nom = 60%
N
RH
0.01
0.1
1
10
100
1000
10^4
10^5
10^6
0
0.2
0.4
0.6
* MODEL, σ (HOPPEL)
× MODEL, σ (LINEAR)

Figure 27

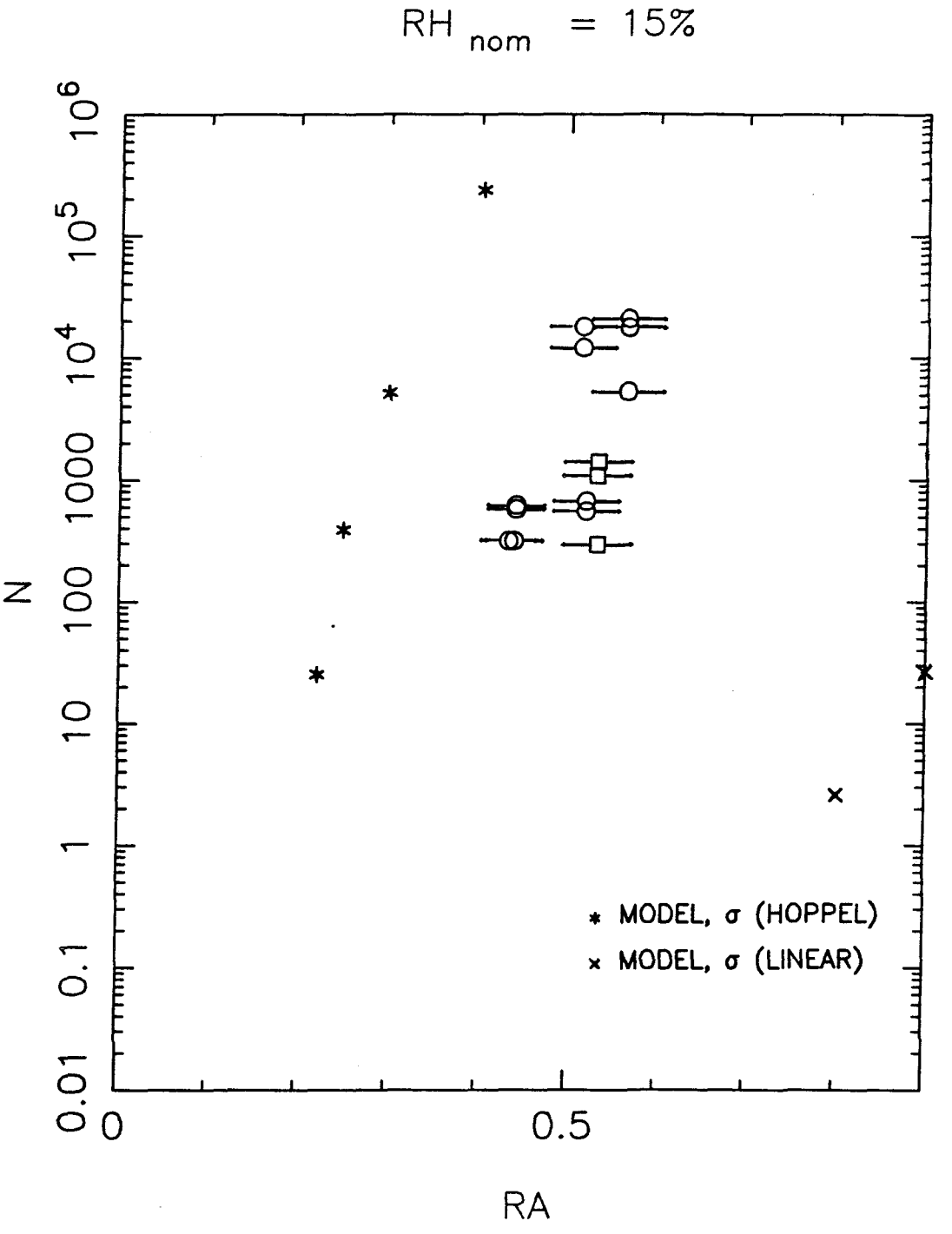
RH nom = 15%
N
0.01
0.1
1
10
100
1000
10^4
10^5
10^6
0
0.5
RA
* MODEL, σ (HOPPEL)
× MODEL, σ (LINEAR)

Figure 28

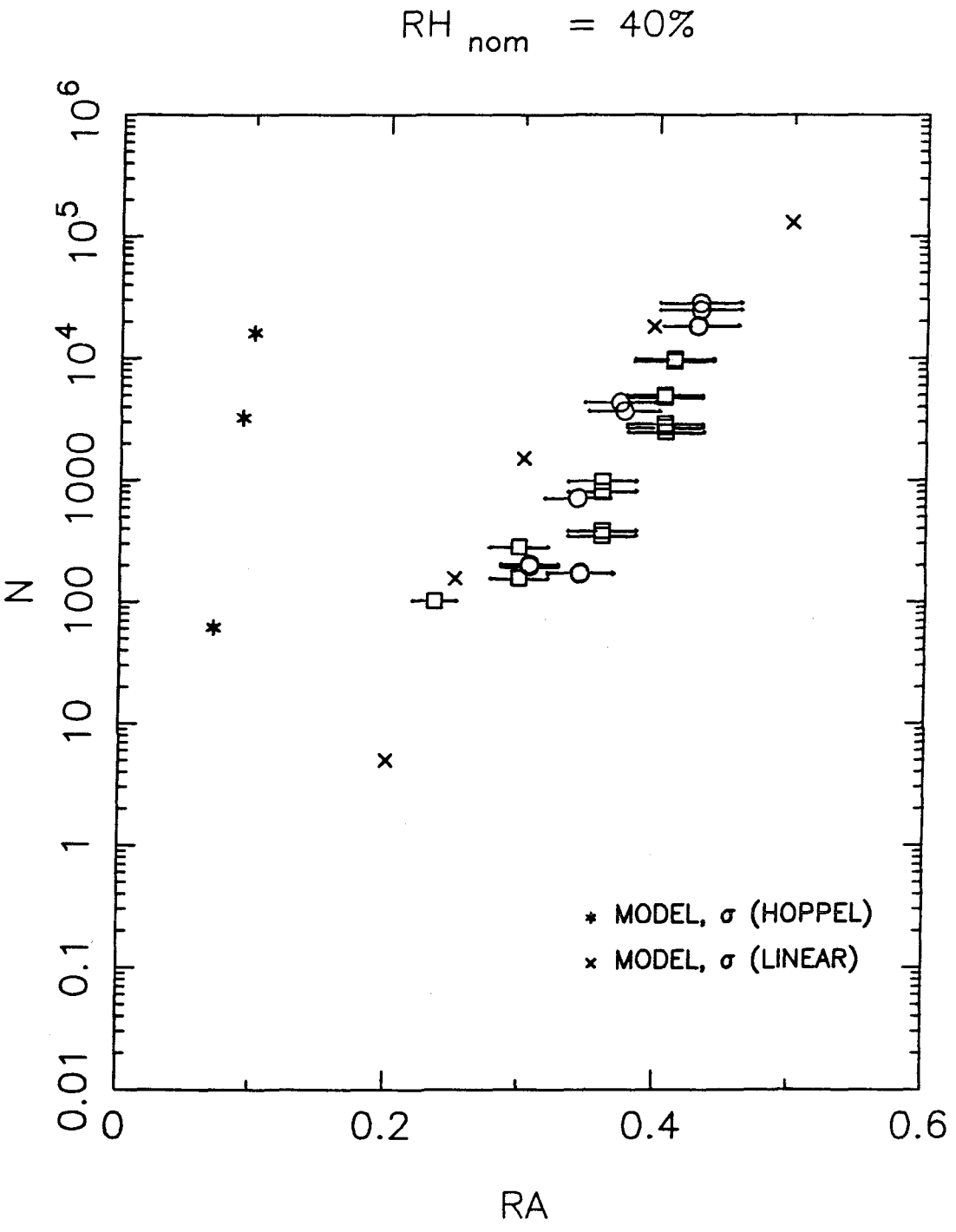
RH nom = 40%
N
RA
0.01
0.1
1
10
100
1000
10^4
10^5
10^6
0
0.2
0.4
0.6
* MODEL, σ (HOPPEL)
× MODEL, σ (LINEAR)

Figure 29

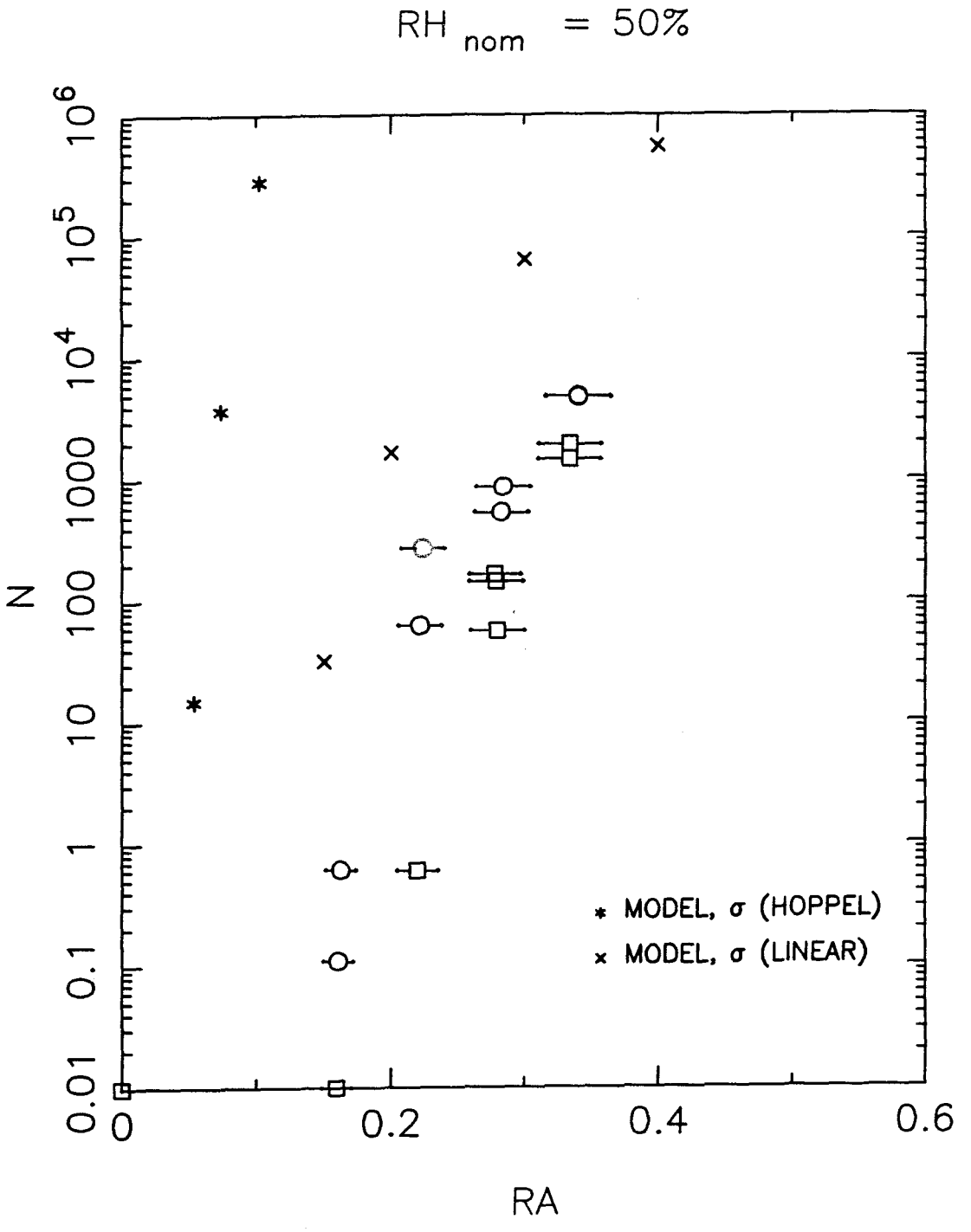
RH nom = 50%
N
RA
0.01
0.1
1
10
100
1000
10^4
10^5
10^6
0
0.2
0.4
0.6
* MODEL, σ (HOPPEL)
× MODEL, σ (LINEAR)

Figure 30

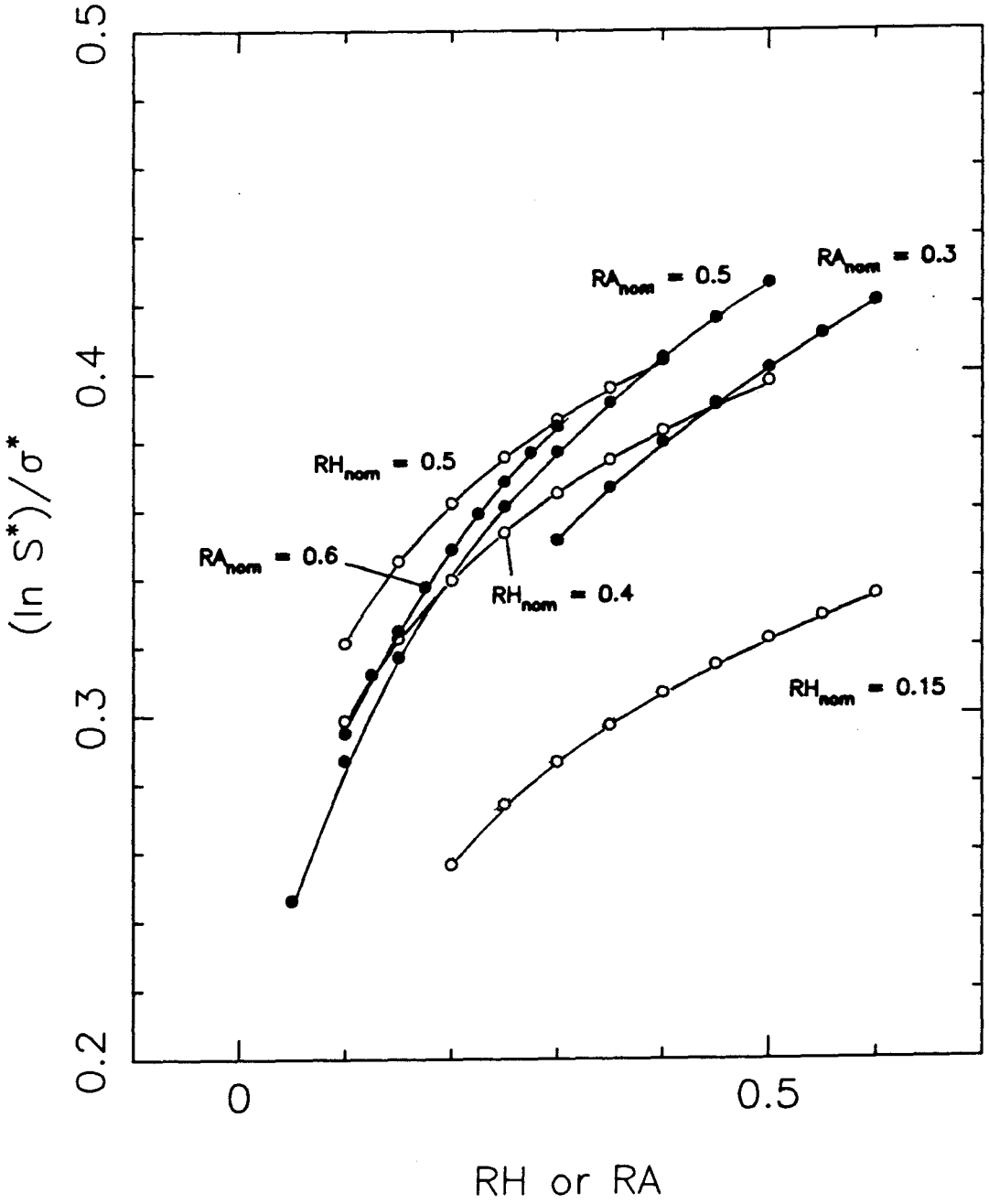
0.5
0.4
0.3
0.2
(ln S*)/σ*
0
0.5
RH or RA
RA_nom = 0.5
RA_nom = 0.3
RH_nom = 0.5
RA_nom = 0.6
RH_nom = 0.4
RH_nom = 0.15

Figure 31

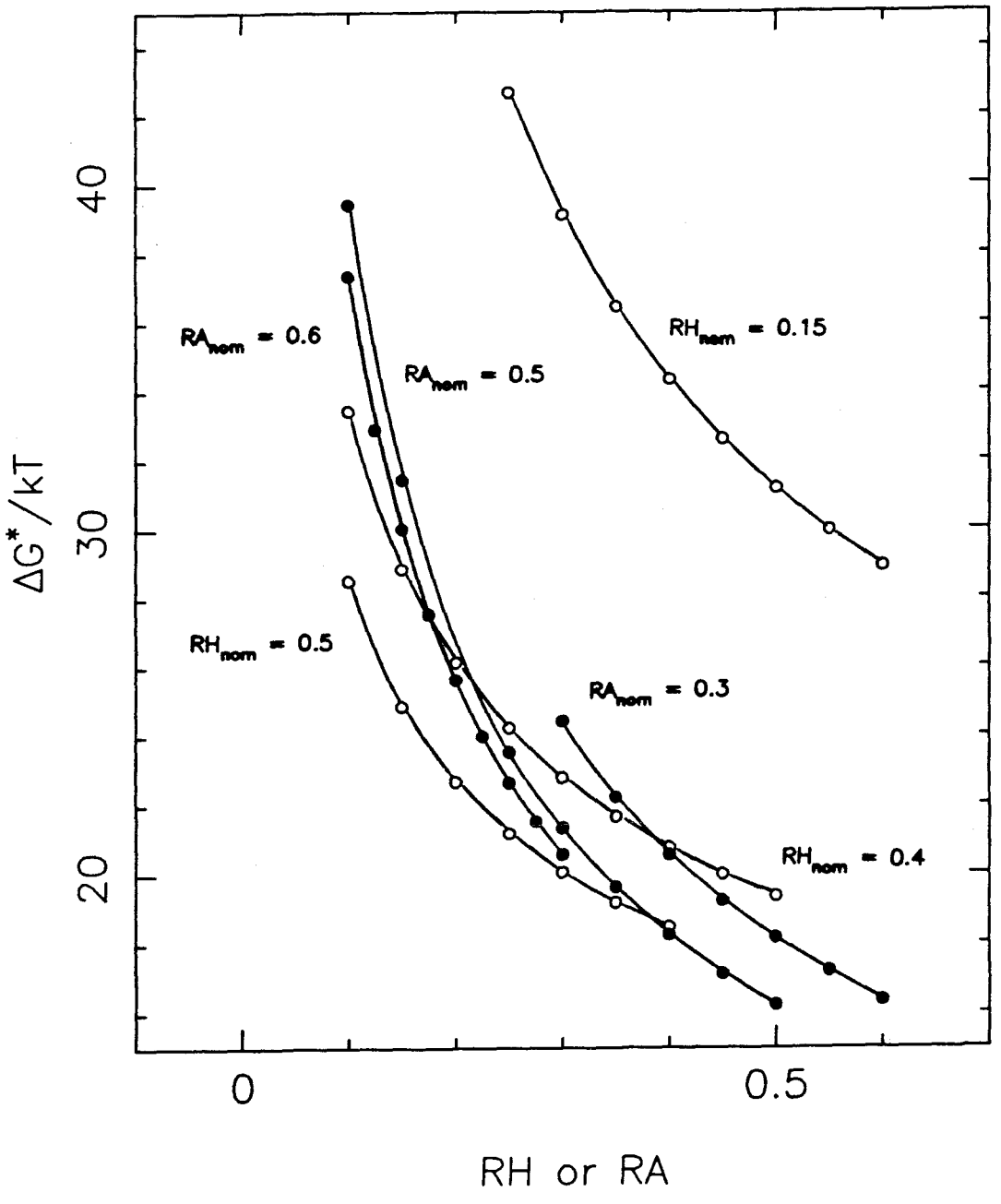
40
30
20
ΔG*/kT
0
0.5
RH or RA
RA_nom = 0.6
RA_nom = 0.5
RH_nom = 0.15
RH_nom = 0.5
RA_nom = 0.3
RH_nom = 0.4

Figure 32

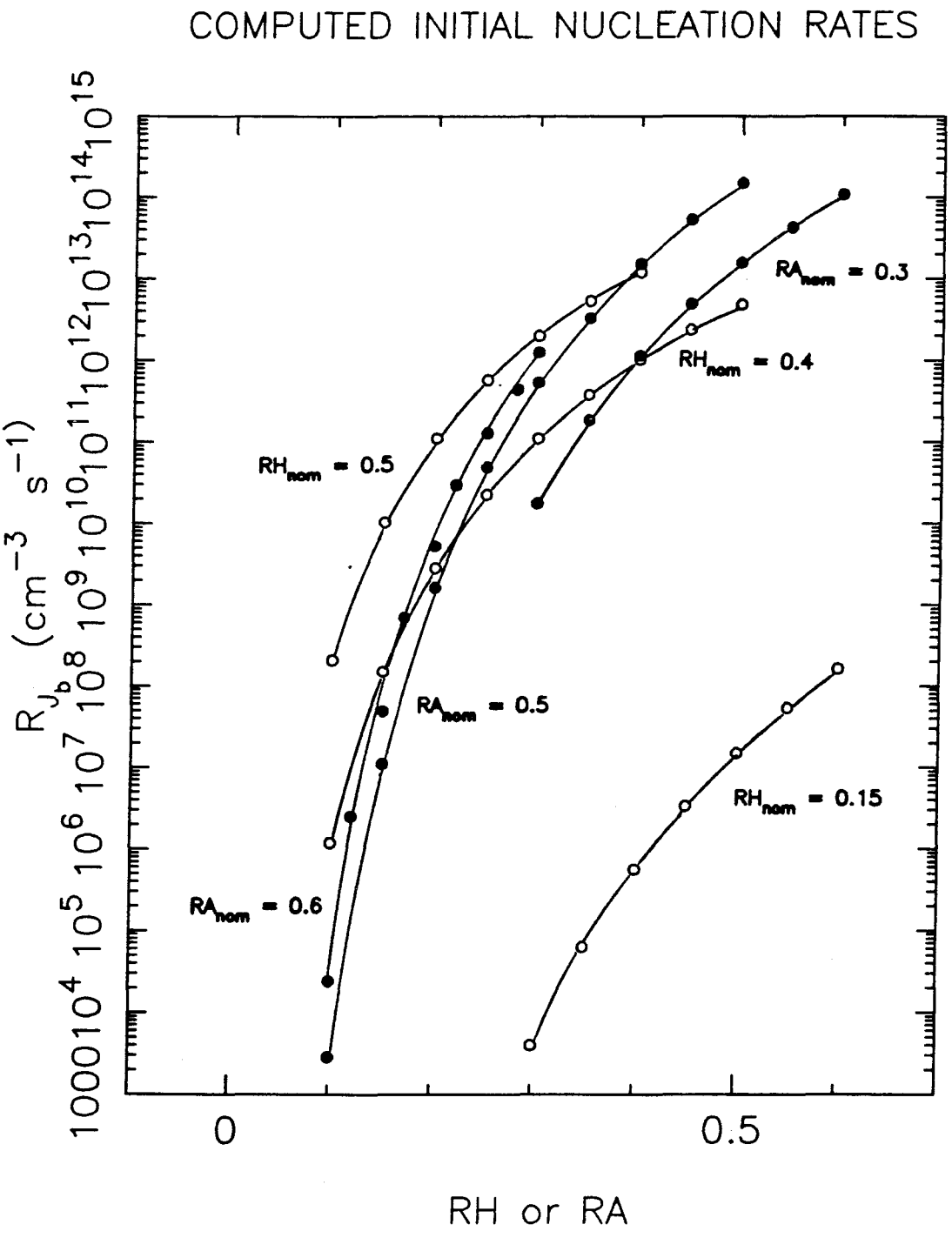
COMPUTED INITIAL NUCLEATION RATES
R_{J_b} (cm^{-3} s^{-1})
100010^4 10^5 10^6 10^7 10^8 10^9 10^{10}10^{11}10^{12}10^{13}10^{14}10^{15}
RH$_{nom}$ = 0.5
RA$_{nom}$ = 0.3
RH$_{nom}$ = 0.4
RA$_{nom}$ = 0.5
RH$_{nom}$ = 0.15
RA$_{nom}$ = 0.6
0
0.5
RH or RA

Figure 33

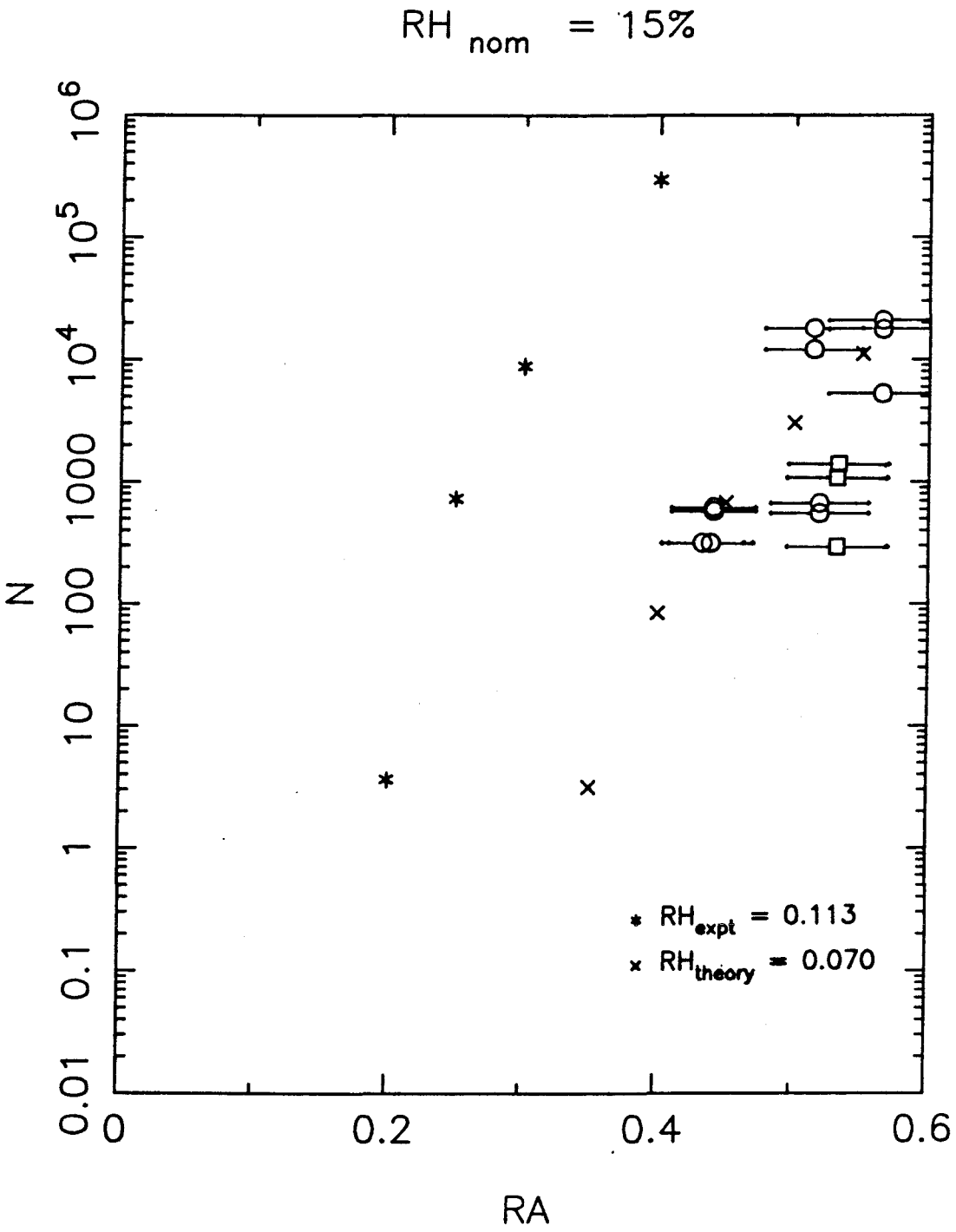
RH nom = 15%
N
RA
0.01
0.1
1
10
100
1000
10^4
10^5
10^6
0
0.2
0.4
0.6
* RH_expt = 0.113
x RH_theory = 0.070

Figure 34

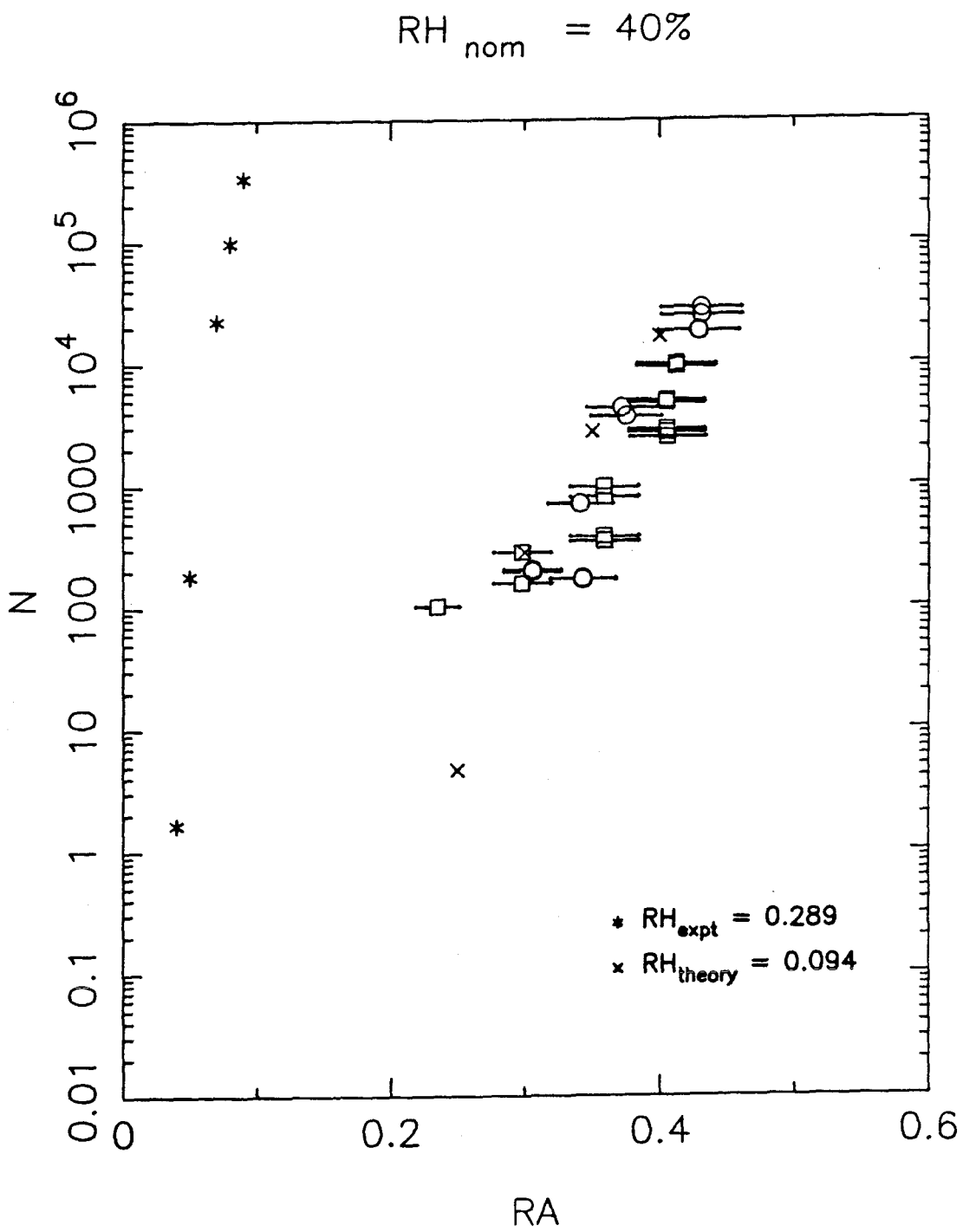
RH nom = 40%
N
RA
0.01
0.1
1
10
100
1000
10^4
10^5
10^6
0
0.2
0.4
0.6
* RH_expt = 0.289
x RH_theory = 0.094

Figure 35

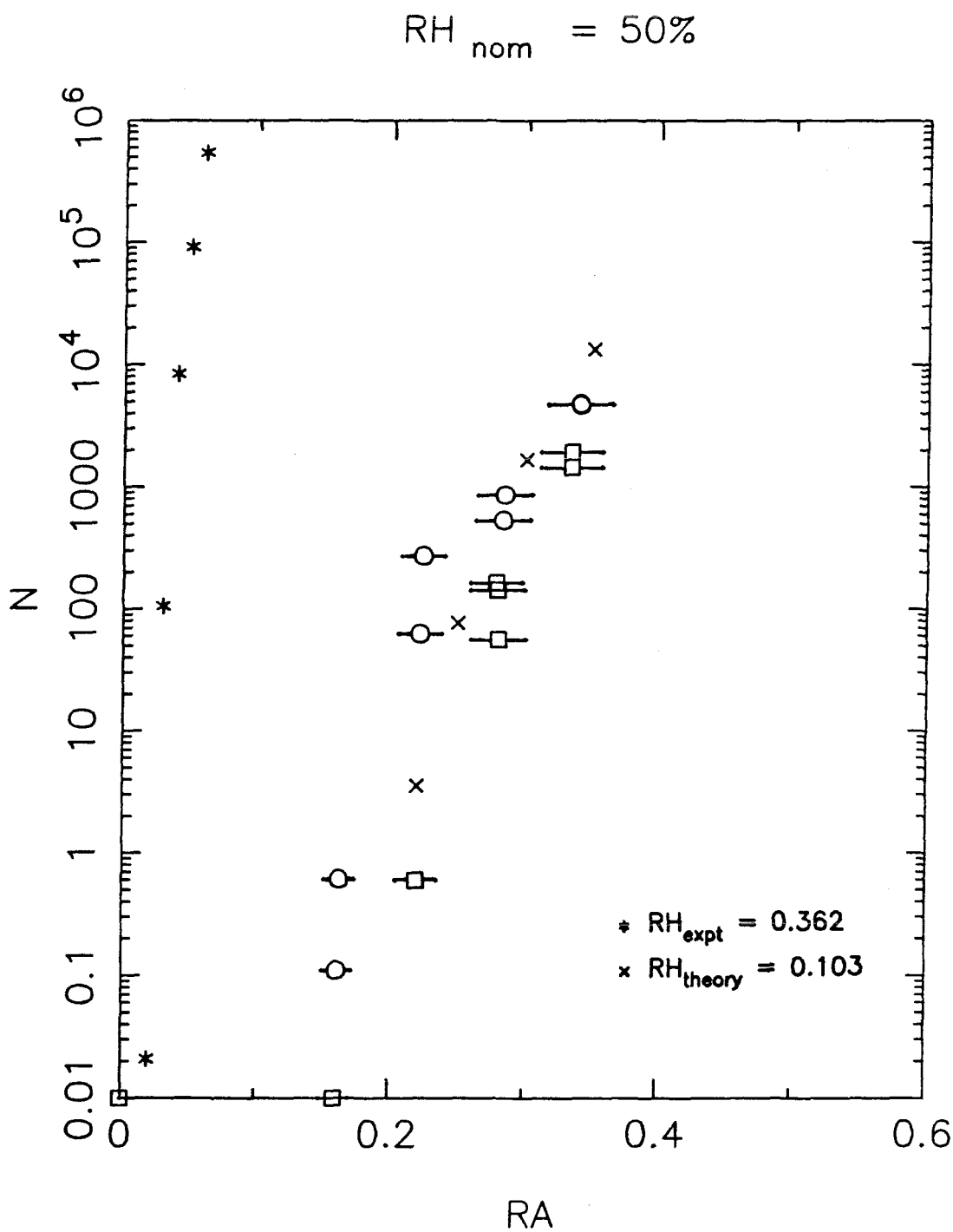
RH nom = 50%
N
RA
0.01
0.1
1
10
100
1000
10^4
10^5
10^6
0
0.2
0.4
0.6
RH_expt = 0.362
RH_theory = 0.103

Figure 36

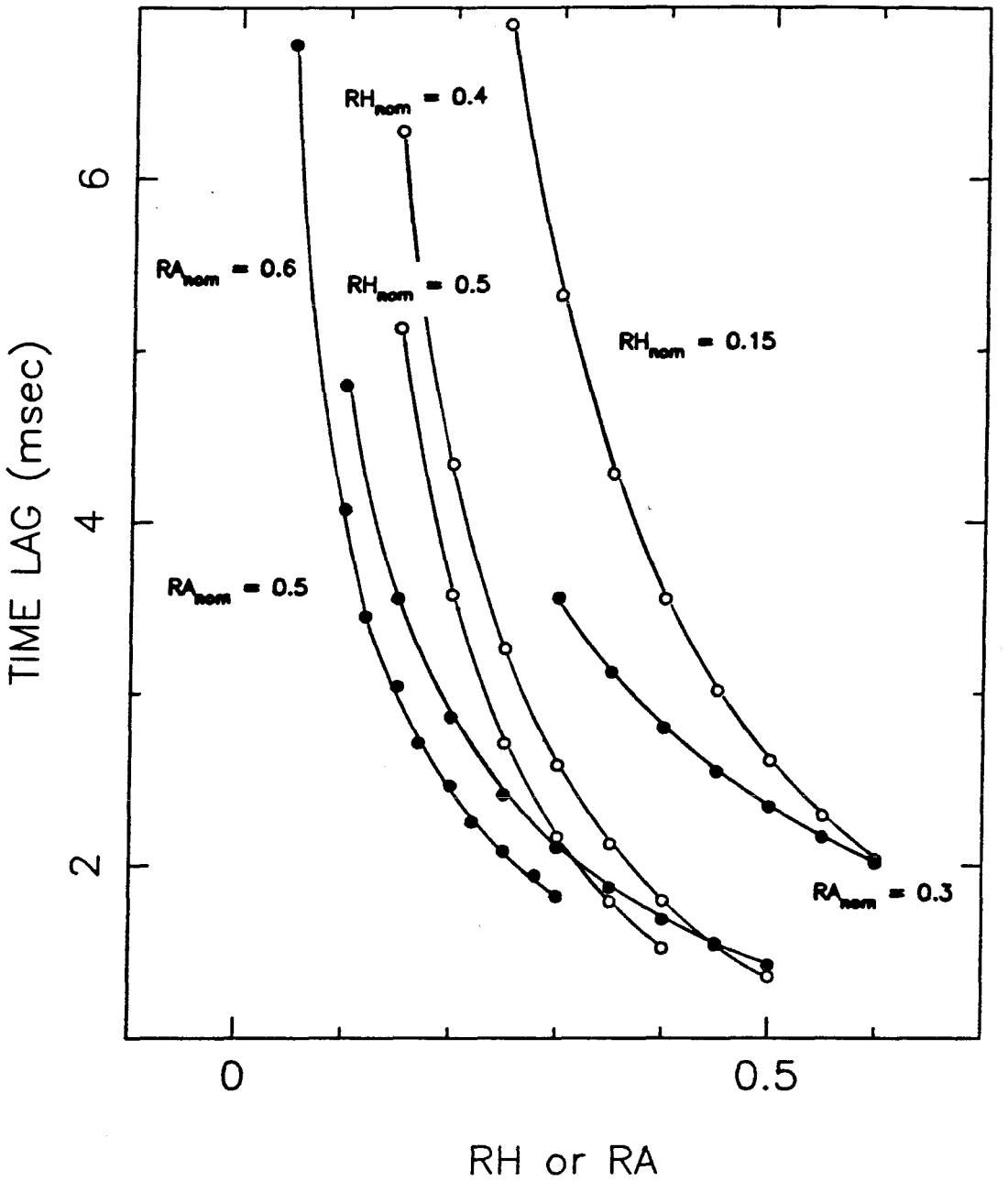
TIME LAG (msec)
2
4
6
0
0.5
RH or RA
RH_nom = 0.4
RH_nom = 0.5
RH_nom = 0.15
RA_nom = 0.6
RA_nom = 0.5
RA_nom = 0.3

Figure 37

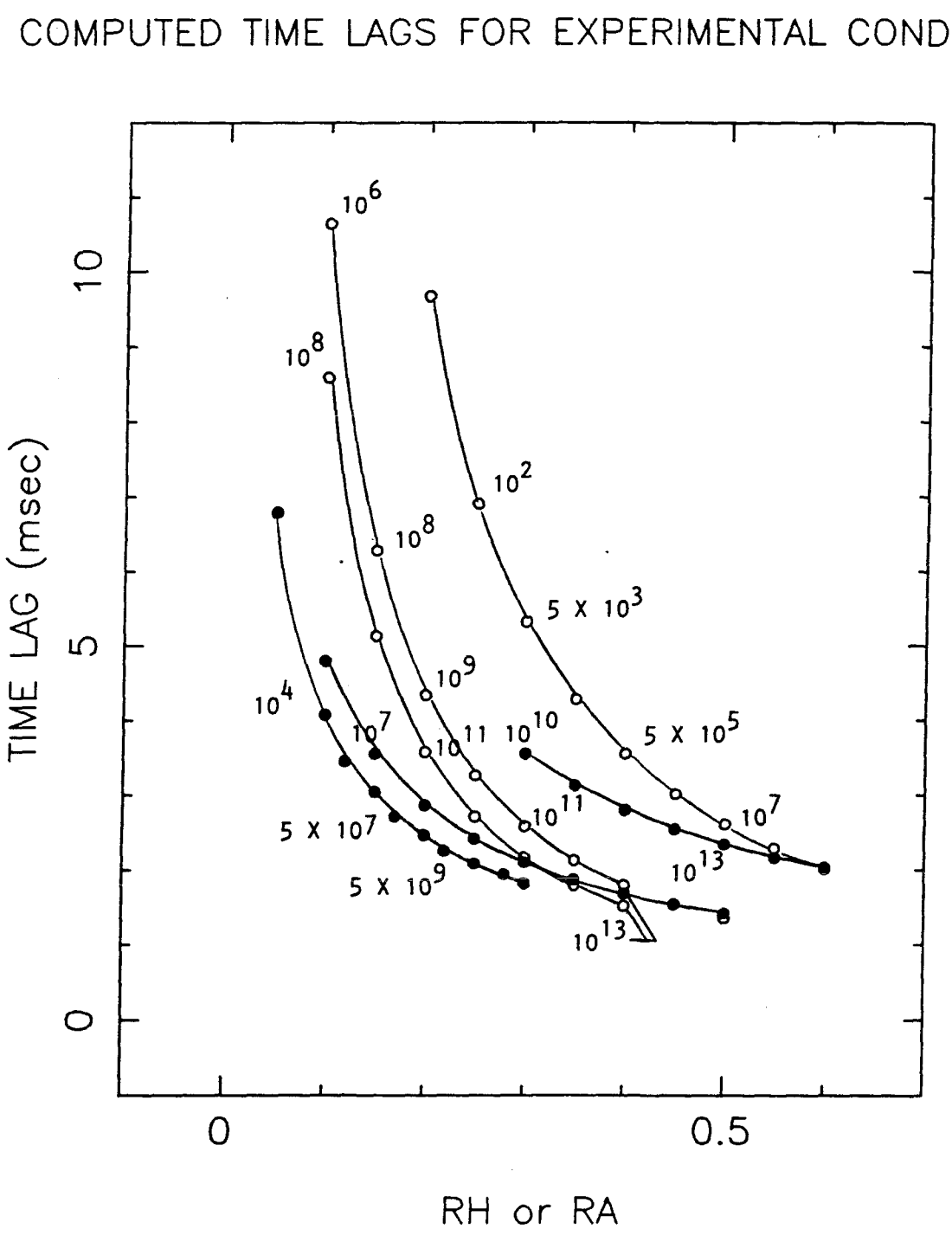
COMPUTED TIME LAGS FOR EXPERIMENTAL CONDITIONS
TIME LAG (msec)
0
5
10
0
0.5
RH or RA
10^6
10^8
10^8
10^2
5 X 10^3
10^9
10^4
10^7
10^11
10^10
5 X 10^5
10^11
10^7
5 X 10^7
10^13
5 X 10^9
10^13

Figure 38

Chapter VI

Suggestions for Future Work

Suggested modifications to the experimental apparatus

Over the course of the experiments described in the previous chapter, and during the analysis of the experimental results, a number of difficulties with the current design of the apparatus were recognized. These will be listed and discussed, with recommendations for appropriate modifications. Also, two possibly important sources of error in the data were identified, and some proposals will be made to alleviate these.

One of the biggest problems in performing an experiment that is as sensitive to temperature fluctuations as the one discussed in this work is in maintaining constant temperatures throughout all parts of the apparatus, particularly near room temperature. Initial attempts at such temperature control involved very small temperature elevations in the bubblers, which were partially immersed in the reserviors of the constant-temperature recirculating baths, and used insulation on all lines and a water jacket (pumped from one bath) on the reactor to maintain temperatures near 25°C. All variations on this scheme met with failure; gases are the flowing fluids, and these do not retain heat very well at all. (Temperatures were observed to drop to room temperature within a few centimeters from the heating point, with or without insulation.)

Since room temperatures were of primary interest, an attempt was made to simply allow the lines to equilibrate with the room air, and by measuring temperatures at the necessary points enough information would be obtained to calculate what the RH and RA were. This was not practical, however, in that the room temperature fluctated throughout the day, and the fluctuations were not even similar in different parts of the apparatus. This problem was especially severe in the hood, where the experiment was initially set up for safety reasons.

Finally, it was concluded that the only way to obtain satisfactory temperature control would be to immerse the equipment in water-filled tanks maintained at constant temperature by the recirculating baths. (This setup has the additional advantage of increased safety, since, if the acid bubbler were to break or

leak, a large volume of water would immediately dilute the acid; furthermore, in case of an explosion due to overpressurization, the water would absorb the impact and prevent harm from flying glass and acid.) By using separate tanks for the water bubbler and for the acid bubbler/mixer/reactor combination, different temperatures could be chosen for each, with a resulting wider range of relative humidity attainable. Note that water baths were sufficient for the temperatures used in these experiments, since the acid and water vapors were highly undersaturated and all temperatures were below 30°C., but if temperatures close to 100°C. are desired, a different fluid (or an entirely different temperature control scheme) must be used. Although these tanks did an excellent job of maintaining constant temperature, they did present some difficulties.

First, many of the glass pieces are joined together using O-ring seals. Under water, these have the potential for allowing leakage of bath water into the system; the same is true for Teflon fittings and valves. Although it was attempted to keep the system pressurized at all times, a relatively large gas flow through the small openings of some of the fittings acted like an aspirator to suck water (or room air) in, if there was a small leak in the fitting. These leaks are extremely difficult to find using conventional methods like soap bubbles (Snoop), because these methods can detect only leaks out of the system. In several cases, initial zero particle counts on dry air could not be achieved, the source of particles could not be determined, and the experiment had to be restarted (sometimes replacing the acid sample, if contamination was suspected); leakage of bath water may have been the cause.

A second inconvenience presented by this method of temperature control is that removal of pieces for inspection or cleaning was very cumbersome. The tanks used were opaque polypropylene; the one used for the acid bubbler/mixer/reactor setup contained over 55 liters (14 gallons) of water that had to be drained each time the pieces were removed. This tank was also quite narrow and deep, and rested on the floor; since the sides were opaque, it was

not possible to view the apparatus (particularly the acid bubbler, located at the bottom of the tank). Since incoming lines, thermistor wires, and pressure tap lines were all attached to the acid bubbler, the entire unit had to be removed and all these lines disconnected so that the acid bubbler could be transferred to the hood for inspection. This is not only cumbersome, but potentially unsafe.

These comments suggest that a revised method of temperature control should have the following features:

1. Enough mass of water (or other heating fluid) to do an efficient job of temperature control, but using the minimum fluid possible in the interests of convenience when the bath must be drained or pieces removed. (The baths should have plugs for gravity draining.) A companion requirement is for some method of circulation to keep the bath well-mixed at all times (a simple stirrer was used for these experiments, but the method chosen will depend on the final geometry.)
2. At least two baths so that the temperatures inside each bubbler can be varied independently.
3. Clear walls (preferably at eye level) to allow for viewing of the apparatus.
4. A method for removing pieces individually without exposing the entire system to room air (that is, ways of sealing off each part, that could potentially need to be examined, replaced or refilled, before removal, and of removing the same without disturbing the rest of the setup.)
5. Some thought must be given to the prevention of any possible contamination by bath water. This feature works against the suggestions in item 4, since the more joints that one builds into the apparatus, the more potential spots for leakage. If O-ring seals are used (and it seems inevitable that they must), the pieces joined together should be held rigidly, so that a tight initial seal cannot be loosened by torquing of one of the pieces during handling. (The same can be said of Teflon fittings, since these can only be made finger-tight.) This again has its counterpoint, since the more rigid the setup is,

the greater the chance of breakage during handling (because of no "give" in the parts).

What is suggested by the above items is a set of at least two tanks, similar to aquarium tanks (either glass or high-quality clear plastic), with the experimental equipment fixed to a rack that can be lowered into or raised out of each tank. (This assumes experiments will be done near room temperature; if the water tanks are at a significantly higher or lower temperature, probably too much heat will be lost from an aquarium-style tank.) The tanks can again be heated by copper coils through which constant-temperature water is pumped from one or more of the Neslab baths, with a suitable stirring device for mixing. The design of the temperature-control scheme can be worked out first (as long as the approximate dimensions are known) and the performance checked with thermistors placed in different parts of the tanks.

Next, the design of the bubblers needs to be revised. The acid bubbler in particular was proven to be very inconvenient. Although the glass frits helped contain the acid when fittings were popped, these were to a large extent the cause of the high pressures inside this bubbler, especially when they became wetted. The port added on to this bubbler for the determination of the pressure could not be separately closed off, which caused problems when the acid bubbler had to be removed from the system. Neither bubbler could be completely sealed from room air after filling, although they were quickly transferred to the apparatus and flushed with nitrogen afterwards to minimize this contact. Both methods of bubbling gas through the liquid pool – the supporting frit method and the inserted tube with fritted outlet – have different advantages; for small liquid levels, the supporting frit is probably the better choice, but the removable tube is easier to clean. Last, filter holders that are integral parts of the bubbler – for example, the holder that was fitted onto the mouth of the water bubbler – are useful in some ways, but it may be advantageous to be able to remove the filter holder separately to check the filter.

These considerations suggest a revised bubbler design that allows for direct filling and immediate sealing from the ambient. (The filling process can be done in a nitrogen-flushed glove box to lessen the chances of contamination further.) The bubbler should not contain any additional frits after the bubbling section, with entrained particle filtration in a separate section downstream. Provided no large pressure drops occur between the bubbler and the filter, the pressure can be measured immediately before the filter so that no tap is required on the bubbler itself. The thermistor well should be carefully designed for convenient handling. The method of bubbling gas through the pool must depend on the substance being evaporated (and the quantity of material that can be used per experiment, which determines the depth of the pool).

The lengths of lines after the bubblers should be kept to a minimum to avoid vapor losses on tubing walls. However, they must also provide a long enough contact time with the bath water to attain the desired temperature. Perhaps testing of thermal control at the highest flow rates that will be used can suggest the optimum length to achieve both goals. If vapor-carrying carrier gas is brought out of a tank, heating tape should be used on the exposed section so that no condensation occurs. Finally, the relative humidity should be monitored at least at the beginning and end of each set of measurements (in the absence of acid vapor) to ensure that good control is maintained.

Although mixing appears to be adequate in this system, it may be advantageous to raise somewhat the total flow rate through the system (perhaps to 3 liters per minute). The volume of the reactor would have to be adjusted accordingly to maintain the residence time desired. Raising the flow rates will aid in mixing and will also allow a little more flexibility in flow combinations (since the minimum dependable flow rate is about 200 cm^3 min^{-1}).

It was mentioned at the beginning of this discussion that two possibly important sources of error in the data were identified. These are the possibility of vapor losses before nucleation and growth can occur, and the loss of counting

efficiency in the CNC for small particles. Ways to alleviate the first of these have been mentioned above, including shorter lines, no frits, and more frequent monitoring of the relative humidity. A prebubbler for the acid stream as well as for the humid stream will help the mass transfer during the final stage. An additional consideration might be the replacement of some of the longer connecting Teflon lines with shorter glass tubing; this is also in keeping with the suggestion for more rigid assembly of the pieces. The second concern (CNC efficiency) can only be addressed by a measurement of the particle sizes produced in the apparatus to determine if a large number of particles lie at the low end of the size spectrum and may be undetected by the CNC. More discussion on measurement of sizes follows.

Appendix

List of equipment used

Pressure gauges: Magnehelic (Dwyer Corp.)

Constant temperature recirculating refrigerated baths: Neslab

Multimeter: Hewlett-Packard

Particle detection: TSI Model 3020 Condensation Nuclei Counter

Rotameters: Matheson Corp.

Dew point meter: EGG Model 911

Filter efficiencies

The efficiencies of and pressure drops across the Teflon filters used to remove entrained particles are shown in Figure 1.

Characteristics of the CNC

The characteristics of the CNC used have been discussed by Agarwal and Sem (1980), Bartz *el al.* (1985), and Wen and Kasper (1986). A schematic of the instrument (reproduced from Agarwal and Sem) is shown in Figure 1. The inlet flow rate (controlled by an internal pump) is 300 cm^3 min^{-1}. Counting efficiency as measured by Wen and Kasper is reproduced in Figure 3.

Thermistor configuration and calibration

For measurement of the temperatures inside the water and acid bubblers, the thermistor was placed inside a glass tubing with a small amount of silicone heat sink compound for good thermal contact with the glass. At the top of the tubing, the thermistor wire is run into a Teflon fitting making a seal with the glass and then through a length of Teflon tubing inserted into the other end of the fitting (see Figure 4a), sealing the glass tubing from contact with bath water.

The other thermistors used were encased in stainless steel machined 1/4 " O.D. casings, with silicone heat sink compound again used for thermal contact between the thermistor and its casing. The casing was then fit into a Teflon tee which had been drilled out to admit the casing to be inserted so that its lower tip

just protruded into the flow passing through the fitting (see Figure 4b). Tygon tubing joined to the stainless steel casings with silicone rubber provided a seal from air and moisture. The thermistors are driven by a 20 V power supply.

The thermistors, encased in the same configurations as they were to be used in during the experiment, and a thermometer with divisions of 0.1 °C. on a scale of -1 to 51 ° C., were immersed in the reservior of the Neslab bath so that the sensors were located close together, but not touching. The bath setpoint was selected, and at steady state the voltage output of each thermistor, as measured by a multimeter, and the thermometer reading were recorded. (The ambient temperature probe of the dew point meter was also calibrated in this procedure, its voltage output being read from the instrument back panel.) At least two readings were taken at each bath temperature setting. The data for each thermistor were then correlated by least-squares method to give a polynomial for temperature as a function of measured voltage (Table 1).

Flowmeter calibration

Each of the flows was calibrated by passing nitrogen through the system with all bubblers filled as in the experiment. The volumetric flow rate at the lab temperature and pressure was measured by a bubble flowmeter, converted to STP, and plotted as a function of the rotameter or Magnehelic reading. The calibration curve for each flowmeter was also fitted to a polynomial as shown in Table 2. All flow calibrations were checked periodically during the course of the experiments and found to be stable and reproducible to generally within one or two percent.

In the case of the humid stream, a correction was made for the volume due to water vapor. It was assumed that the volumetric flow measured by the bubble meter represented dry nitrogen saturated with water vapor at the pressure and temperature inside the water bubbler (which were also recorded during the

calibration). The dry nitrogen flow rate was then calculated from

$$F_H = \frac{F_{measured}}{1 + Y_W}$$

where Y_W is as defined in the description of the experimental apparatus. This correction is negligible for the acid vapor and was not made.

Preparation of the acid bubbler

Since nucleation is an extremely sensitive phenomenon, care was taken in this experiment to avoid contamination of the liquids and vapors used. The acid bubbler was baked out in a glass kiln for several hours before its first use, flushed overnight with nitrogen, and fitted with the mixer, reactor tube, pressure tap and thermistor. It was then filled with methanesulfonic acid (Aldrich, Assay $> 99.5\%$) by the following procedure. The acid was poured into a glass bottle and sealed from outside air. A clean, pressurized air line was fitted onto the inlet of this bottle and the outlet was clamped to the acid bubbler fill inlet. The bottle was slowly pressurized and the acid allowed to flow onto the frit inside the bubbler. After completion of the transfer, the bubbler was sealed off and the bottle removed and sealed off as well. The bubbler was then immediately connected to its inlet and outlet lines in the apparatus and leak tested before filling the constant-temperature tank containing it.

The acid was changed several times during the course of the experiments, using the following procedure. All fittings and the mixer and reactor were removed, allowing the used acid to be poured from the pressure tap. Milli-Q water was then used to rinse the central chamber. After most of the acid had been removed in this manner, a deionized water line was fitted onto the air inlet and the bubbler was continuously flushed with water for several hours. This process was followed by replacing the water line with a purified, filtered air line and flushing with air for several hours. The cycle of water/air flushing was repeated at least three times. Finally, the purified air was used to flush and dry the bubbler over a period of about 48 hours, and was followed by a briefer flushing with nitrogen

before filling with a new acid sample as described above. The parts removed were cleaned and dried thoroughly before replacement.

To further reduce the possibility of contamination while the experiment was not in use, a small dry, purified, and filtered air flow was used to continuously flush the system (blown through the dilution air lines). Before the start of an experiment, this bleed stream was replaced with the dry nitrogen for at least an hour, and the particle counts were checked with the CNC before any vapors were added to the system. In most cases an excellent zero particle count was measured, and in no instance was an experiment performed unless this zero was obtained.

Table 1

Thermistor calibrations

Thermistor	Formula
Acid bubbler thermistor 1	$T_1 = -0.2856V^3 + 1.998V^2$ $+5.527V + 2.829$
After heating tape thermistor 2	$T_2 = 9.901V + 0.3082$
Humid+dry into mixer thermistor 3	$T_3 = -0.2779V^3 + 1.728V^2$ $+6.561V + 4.957$
Into CNC thermistor 5	$T_5 = -0.3280V^3 + 2.313V^2$ $+4.675V + 3.967$
Water bubbler thermistor 6	$T_6 = -0.3275V^3 + 2.280V^2$ $+4.952V + 3.196$
W_A EGG probe	$T_p = -0.06378V^3 + 1.088V^2$ $+3.995V - 28.87$

Uncertainty in temperature reading: 0.04°C.

Table 2

Flowmeter calibrations

Flowmeter	Flowrate ($cm^3\ min^{-1}$)
Flowmeter 1 (acid)	$F1A = -229.278(s/100)^3$ $+788.173(s/100)^2$ $-315.091(s/100) + 76.5939$
Flowmeter 1 (humid)	$F1H = -229.278(s/100)^3$ $+788.173(s/100)^2$ $-315.091(s/100) + 76.5939$
Flowmeter 3 (acid)	$F3A = -0.0157x^3$ $+0.9347x^2 + 1.8063x + 64.0232$
Flowmeter 4 (dry)	$F4D = -0.01579x^3$ $-0.3353x^2 + 93.9314x - 13.7095$
Flowmeter 4 (humid)	$F4H = 0.1168x^3$ $-1.1336x^2 + 115.48x + 42.88$
Flowmeter 5 (dry)	$F5D = -0.1649s^3$ $+0.8608s^2 + 66.84s + 91.80$

Table 2, continued

Flowmeter 6 (humid)	$F6H = 0.007518s^3$
	$-0.7493s^2 + 98.507s + 108.06$
Flowmeter 7 (acid)	$F7A = 0.001237s^3$
	$-0.2570s^2 + 53.087s - 216.7$

---

s = float position

x = Magnehelic reading

Uncertainty in humid flows: 3%

Uncertainty in all other flows: 1.5%

References

Agarwal, J.K. and Sem, G.J. (1980) *J. Aer. Sci.* **11**, 343.

Bartz, H., Fissan, H., Helsper, C., Kousaka, Y., Okuyama, K., Fukushima, N., Keady, P.B., Kerrigan, S., Fruin, S.A., McMurry, P.H., Pui, D.Y.H., and Stolzenburg, M.R. (1985) *J. Aer. Sci.* **16**(5), 443.

Wen, H.Y. and Kasper, G. (1986) *J. Aer. Sci.* **17**(6), 947.

Figure Captions

Figure 1. Pressure drop across and efficiency of Teflon filters. Courtesy of K. Okuyama.

Figure 2. Schematic of CNC. (Agarwal and Sem, 1980.)

Figure 3. Counting efficiency of CNC. (Wen and Kaspar, 1986.)

Figure 4. Configurations used for thermistors. (Teflon fittings partially shown.)

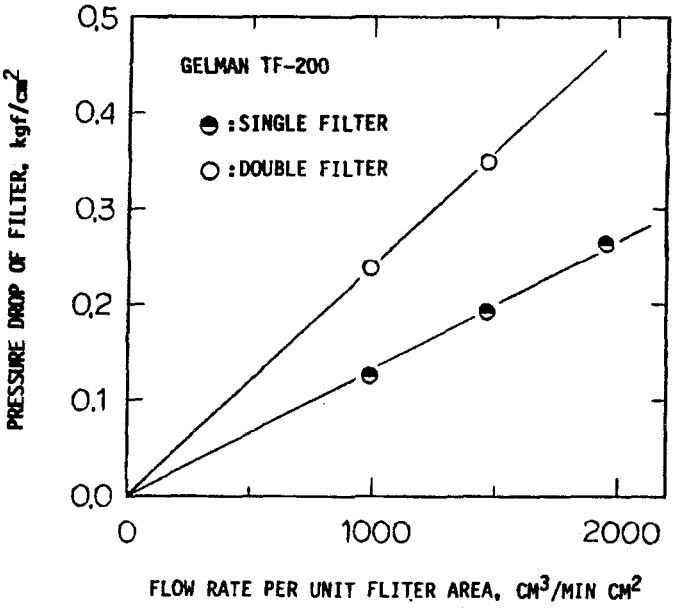
GELMAN TF-200
● :SINGLE FILTER
○ :DOUBLE FILTER
PRESSURE DROP OF FILTER, kgf/cm²
0.5
0.4
0.3
0.2
0.1
0.0
0
1000
2000
FLOW RATE PER UNIT FLITER AREA, CM³/MIN CM²

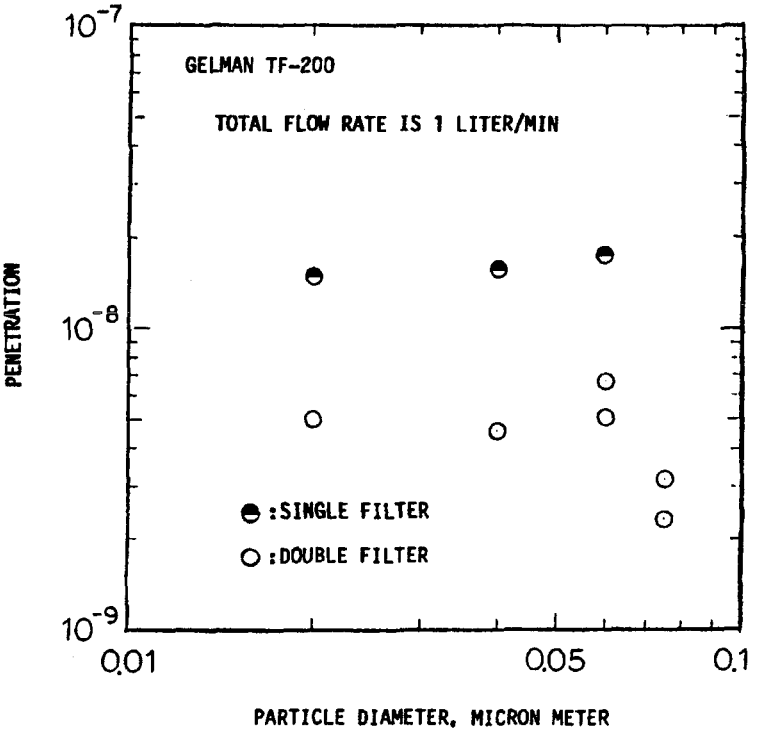
GELMAN TF-200
TOTAL FLOW RATE IS 1 LITER/MIN
● :SINGLE FILTER
○ :DOUBLE FILTER
PENETRATION
10⁻⁷
10⁻⁸
10⁻⁹
0.01
0.05
0.1
PARTICLE DIAMETER, MICRON METER

Figure 1

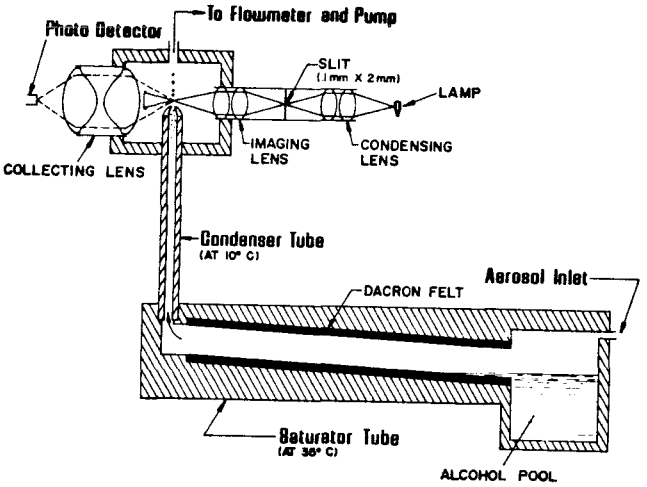

Figure 2

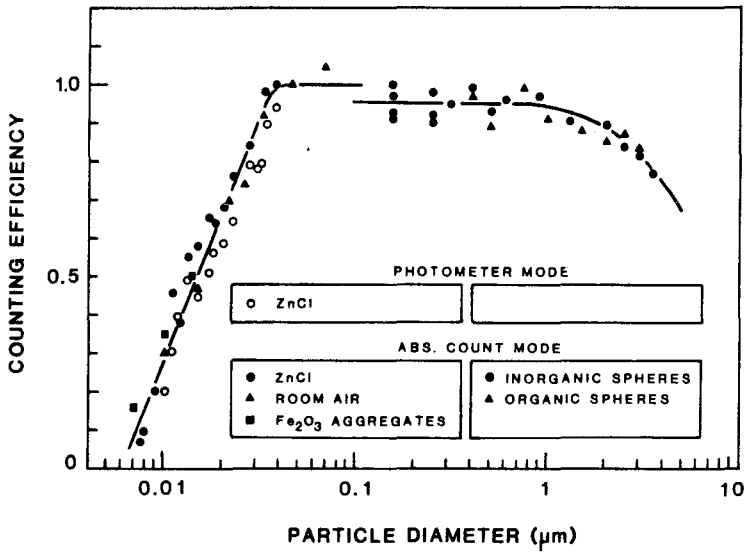

Figure 3

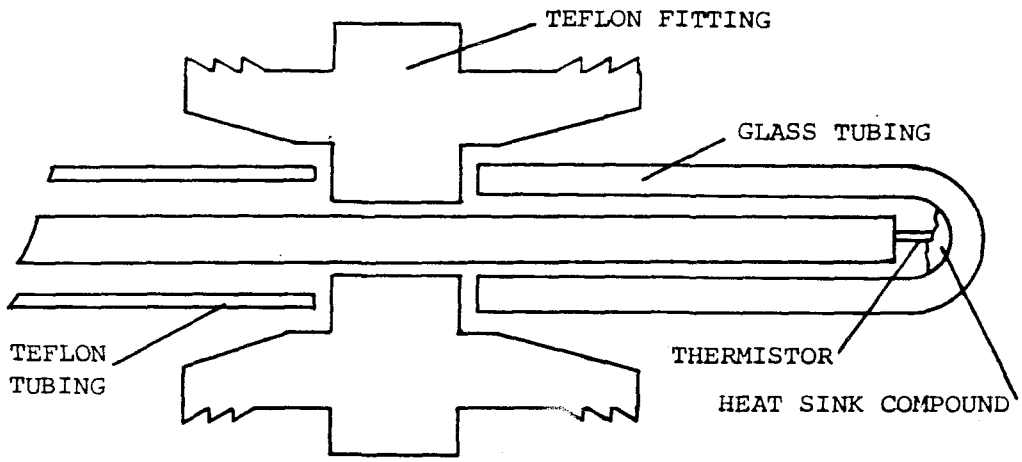

FIGURE 4A

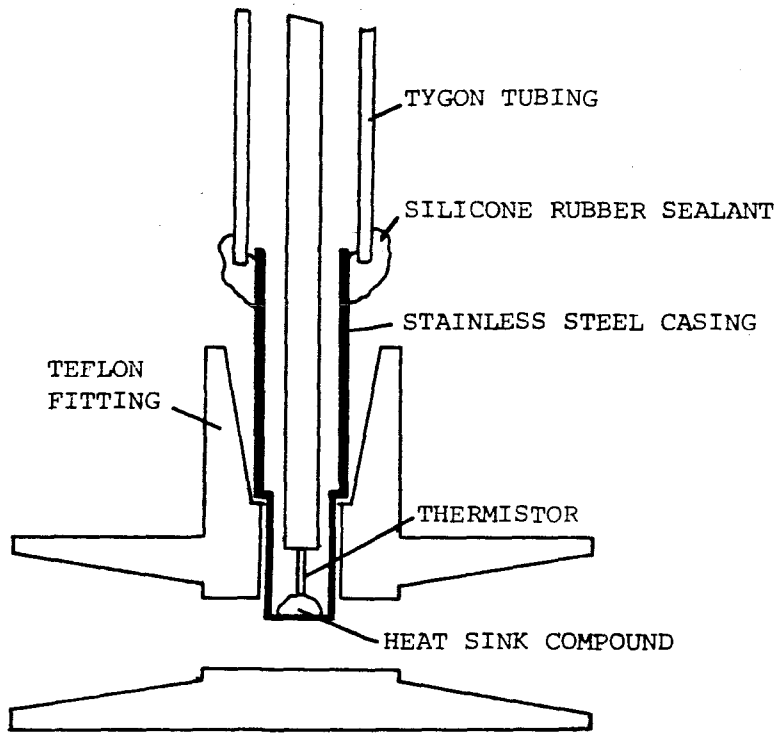

FIGURE 4B

```
c program labanal.for to analyze laboratory data
c
c first, read in expt ID:
c
      write(*,10)
 10   format(1x,'Enter date and expt number: ')
      read(*,*) date,exptno
c
      write(*,20)
 20   format(1x,'Enter 1 if acid constant or 2 if humid constant: ')
      read(*,*) iconst
c
      write(*,25)
 25   format(1x,'Enter lab pressure in inches mercury: ')
      read(*,*) plabi
      plab=plabi*25.4
c
      write(20,35)date,exptno,plab
      write(30,35)date,exptno,plab
      write(40,35)date,exptno,plab
      write(21,35)date,exptno,plab
      write(31,35)date,exptno,plab
 35   format('Date: ',f8.2,2x,'Expt.#: ',f8.2,2x,'Plab: ',f8.2/)
c
      write(*,30)
 30   format(1x,'Enter flow setting of const species in ccm: ')
      read(*,*) flow
c
      if (iconst.eq.1)then
      acid=flow
      write(*,40)
 40   format(/1x, 'enter data: ',/1x)
      go to 100
      endif
c
      if (iconst.eq.2)then
      humid=flow
      write(*,40)
      go to 200
      endif
c
c loop to read in flows, thermistor readings, pressures, and CNC data
c
 100  do 1000 j=1,1000
c
      write(*,50)
 50   format(1x,'Enter time: ')
      read(*,*) time
      write(*,60)
 60   format(1x,'Enter dry flow: ')
      read(*,*)dry
      write(*,70)
 70   format(1x,'Enter humid flow: ')
      read(*,*)humid
      write(*,80)
 80   format(1x,'Enter water bubbler pressure (psig): ')
      read(*,*) pbwi
      pbw=(pbwi*760./14.7)+plab
      write(*,90)
 90   format(1x,'Enter acid bubbler pressure (psig): ')
      read(*,*) pbai
      pba=(pbai*760./14.7)+plab
      write(*,110)
 110  format(1x,'Enter thermistor readings (1,2,3,P,5,6): ')
      read(*,*)t1,t2,t3,tp,t5,t6
      write(*,120)
```

```
 120    format(1x,'Enter CNC reading: ')
        read(*,*)cnc
        write(*,130)
 130    format(1x,'Enter CNC +/- reading: ')
        read(*,*)cncvar
c
c write out input data:
c
        write(21,140)time,acid,humid,dry,pbwi,pbai
        write(31,141)time,t1,t2,t3,tp,t5,t6
c
c Now have all data read in. Next,
c compute the temperatures from thermistor readings:
c
        call therm(t1,t2,t3,tp,t5,t6)
c
c Compute the saturation vapor pressures needed at the appropriate
c temperatures:
c
c Saturation water pressure inside bubbler:
c
        call pwat(t6,pw6)
c
c saturation water pressure at reheater temperature:
c
        call pwat(tp,pwr)
c
c acid vapor pressure inside bubbler:
c
        call pacid(t1,pa1)
c
c acid vapor pressure at reheater temperature:
c
        call pacid(tp,par)
c
c Ready to compute the relative acidity and relative humidity:
c
        y=pw6/(pbw-pw6)
        ftot=((1.+y)*humid)+dry+acid
        rh=plab*y*humid/(pwr*ftot)
        ra=plab*pal*acid/(pba*par*ftot)
c
c Correct CNC reading less than 1000 for coincidence error:
c
        cnc=cnc*exp(cnc*5.*35.e-6)
c
c write out data:
c
        write(20,140)time,acid,humid,dry,ftot,pbw,pba
        write(30,141)time,t1,t2,t3,tp,t5,t6
        write(40,142)time,rh,ra,cnc,cncvar
c
        write(*,142)time,rh,ra,cnc,cncvar
c
 140    format(7f8.2)
 141    format(7f8.3)
 142    format(f7.2,2x,2f8.3,2f12.2)
c
 1000   continue
c
c nearly identical loop for water constant:
c
 200    do 2000 j=1,1000
c
        write(*,50)
        read(*,*) time
```

```
        write(*,60)
        read(*,*)dry
        write(*,71)
 71     format(1x,'Enter acid flow: ')
        read(*,*)acid
        write(*,80)
        read(*,*) pbwi
        pbw=(pbwi*760./14.7)+plab
        write(*,90)
        read(*,*) pbai
        pba=(pbai*760./14.7)+plab
        write(*,110)
        read(*,*)t1,t2,t3,tp,t5,t6
        write(*,120)
        read(*,*)cnc
        write(*,130)
        read(*,*)cncvar
c
c write out input data:
c
        write(21,140)time,acid,humid,dry,pbwi,pbai
        write(31,141)time,t1,t2,t3,tp,t5,t6
c
        call therm(t1,t2,t3,tp,t5,t6)
c
        call pwat(t6,pw6)
c
        call pwat(tp,pwr)
c
        call pacid(t1,pa1)
c
        call pacid(tp,par)
c
c Ready to compute the relative acidity and relative humidity:
c
        y=pw6/(pbw-pw6)
        ftot=((1.+y)*humid)+dry+acid
        rh=plab*y*humid/(pwr*ftot)
        ra=plab*pa1*acid/(pba*par*ftot)
c
c Correct CNC reading less than 1000 for coincidence error:
c
        cnc=cnc*exp(cnc*5.*35.e-6)
c
c write out data:
c
        write(20,140)time,acid,humid,dry,ftot,pbw,pba
        write(30,141)time,t1,t2,t3,tp,t5,t6
        write(40,142)time,rh,ra,cnc,cncvar
c
        write(*,142)time,rh,ra,cnc,cncvar
c
 2000   continue
c
        stop
        end
c
c subroutine to compute acid vapor pressure:
c
        subroutine pacid(t,pa)
c
        tkel=273.15+t
        plog=(-8006.48/tkel)+(2.14237*(alog(tkel)))+7.45208
        pa=exp(plog)
c
        return
```

```
      end
c
c subroutine to compute water vapor pressure: use interpolation
c
      subroutine pwat(t,pw)
c
      if(t.ge.19.8.and.t.lt.20.0)call
     1  vle(19.8,20.0,t,17.319,17.535,pw)
c
      if(t.ge.20.0.and.t.lt.20.2)call
     1  vle(20.0,20.2,t,17.535,17.753,pw)
      if(t.ge.20.2.and.t.lt.20.4)call
     1  vle(20.2,20.4,t,17.753,17.974,pw)
      if(t.ge.20.4.and.t.lt.20.6)call
     1  vle(20.4,20.6,t,17.974,18.197,pw)
      if(t.ge.20.6.and.t.lt.20.8)call
     1  vle(20.6,20.8,t,18.197,18.422,pw)
      if(t.ge.20.8.and.t.lt.21.0)call
     1  vle(20.8,21.0,t,18.422,18.650,pw)
c
      if(t.ge.21.0.and.t.lt.21.2)call
     1  vle(21.0,21.2,t,18.650,18.880,pw)
      if(t.ge.21.2.and.t.lt.21.4)call
     1  vle(21.2,21.4,t,18.880,19.113,pw)
      if(t.ge.21.4.and.t.lt.21.6)call
     1  vle(21.4,21.6,t,19.113,19.349,pw)
      if(t.ge.21.6.and.t.lt.21.8)call
     1  vle(21.6,21.8,t,19.349,19.587,pw)
      if(t.ge.21.8.and.t.lt.22.0)call
     1  vle(21.8,22.0,t,19.587,19.827,pw)
c
      if(t.ge.22.0.and.t.lt.22.2)call
     1  vle(22.0,22.2,t,19.827,20.070,pw)
      if(t.ge.22.2.and.t.lt.22.4)call
     1  vle(22.2,22.4,t,20.070,20.316,pw)
      if(t.ge.22.4.and.t.lt.22.6)call
     1  vle(22.4,22.6,t,20.316,20.565,pw)
      if(t.ge.22.6.and.t.lt.22.8)call
     1  vle(22.6,22.8,t,20.565,20.815,pw)
      if(t.ge.22.8.and.t.lt.23.0)call
     1  vle(22.8,23.0,t,20.815,21.068,pw)
c
      if(t.ge.23.0.and.t.lt.23.2)call
     1  vle(23.0,23.2,t,21.068,21.324,pw)
      if(t.ge.23.2.and.t.lt.23.4)call
     1  vle(23.2,23.4,t,21.324,21.583,pw)
      if(t.ge.23.4.and.t.lt.23.6)call
     1  vle(23.4,23.6,t,21.583,21.845,pw)
      if(t.ge.23.6.and.t.lt.23.8)call
     1  vle(23.6,23.8,t,21.845,22.110,pw)
      if(t.ge.23.8.and.t.lt.24.0)call
     1  vle(23.8,24.0,t,22.110,22.377,pw)
c
      if(t.ge.24.0.and.t.lt.24.2)call
     1  vle(24.0,24.2,t,22.377,22.648,pw)
      if(t.ge.24.2.and.t.lt.24.4)call
     1  vle(24.2,24.4,t,22.648,22.922,pw)
      if(t.ge.24.4.and.t.lt.24.6)call
     1  vle(24.4,24.6,t,22.922,23.198,pw)
      if(t.ge.24.6.and.t.lt.24.8)call
     1  vle(24.6,24.8,t,23.198,23.476,pw)
      if(t.ge.24.8.and.t.lt.25.0)call
     1  vle(24.8,25.0,t,23.476,23.756,pw)
c
      if(t.ge.25.0.and.t.lt.25.2)call
     1  vle(25.0,25.2,t,23.756,24.039,pw)
```

```
      if(t.ge.25.2.and.t.lt.25.4)call
     1  vle(25.2,25.4,t,24.039,24.326,pw)
      if(t.ge.25.4.and.t.lt.25.6)call
     1  vle(25.4,25.6,t,24.326,24.617,pw)
      if(t.ge.25.6.and.t.lt.25.8)call
     1  vle(25.6,25.8,t,24.617,24.912,pw)
      if(t.ge.25.8.and.t.lt.26.0)call
     1  vle(25.8,26.0,t,24.912,25.209,pw)
c
      return
      end
c
c interpolation subroutine
c
      subroutine vle(s1,s2,sm,w1,w2,wm)
c
      wm=w1-((s1-sm)*(w1-w2)/(s1-s2))
c
      return
      end
c
c subroutine that computes thermistor temps from calibration curves
c Note: thermistor2 was replaced and recalibrated during experiments.
c       Data presentation reflects this.
c
      subroutine therm(t1,t2,t3,tp,t5,t6)
c
      t1= (t1*10.1317) +
     1     0.713495
c
      t2= (t2*9.90123) +
     1    .308175
c
      t3= ((t3**3)*(-.277944))+
     1    ((t3**2)*1.72787) +
     1    (t3*6.56104) +
     1     4.95704
c
      tp= ((tp**3)*(-.0637771)) +
     1    ((tp**2)*1.0882) +
     1    (tp*3.99484) +
     1     (-28.867)
c
      t5= ((t5**3)*(-.32795)) +
     1    ((t5**2)*2.31285) +
     1    (t5*4.67537) +
     1     3.96667
c
      t6= ((t6**3)*(-.327525)) +
     1    ((t6**2)*2.27982) +
     1    (t6*4.95167) +
     1     3.19595
c
      return
      end
```

RA=30%

Date: 3.21 Expt #: 2 Plab: 734.82

time	acid	humid	dry	Pbw,g	Pba,g
5.34	594.80	.00	1401.90	.00	3.60
5.47	594.80	401.60	989.30	.58	3.60
6.18	594.80	807.90	606.90	.78	3.60
6.34	594.80	1195.20	198.00	.94	3.60
6.52	594.80	1401.80	.00	1.05	3.60
7.08	594.80	1401.80	.00	1.05	3.60
7.22	594.80	1195.20	198.00	.94	3.60
7.40	594.80	1195.20	198.00	.94	3.60
7.59	594.80	807.90	606.90	.78	3.60
8.15	594.80	1401.80	.00	1.03	3.60
8.36	594.80	1401.80	.00	1.03	3.60

time	ther1	ther2	ther3	probe	ther5	ther6
5.34	2.52	2.73	2.24	6.47	2.60	2.07
5.47	2.52	2.76	2.24	6.47	2.56	2.06
6.18	2.52	2.83	2.24	6.47	2.53	2.06
6.34	2.52	2.86	2.24	6.47	2.51	2.06
6.52	2.54	2.91	2.24	6.47	2.52	2.06
7.08	2.52	2.91	2.24	6.47	2.52	2.06
7.22	2.52	2.87	2.24	6.47	2.54	2.06
7.40	2.52	2.85	2.24	6.47	2.50	2.06
7.59	2.52	2.81	2.24	6.47	2.51	2.06
8.15	2.52	2.88	2.24	6.47	2.49	2.06
8.36	2.52	2.88	2.24	6.47	2.48	2.06

Date: 3.21 Expt.#: 2.00 Plab: 734.82

time	acid	water	dry	total	Pbw	Pba
5.34	594.80	.00	1401.90	1996.70	734.82	920.94
5.47	594.80	401.60	989.30	1995.27	764.81	920.94
6.18	594.80	807.90	606.90	2028.58	775.15	920.94
6.34	594.80	1195.20	198.00	2015.78	783.42	920.94
6.52	594.80	1401.80	.00	2028.94	789.11	920.94
7.08	594.80	1401.80	.00	2028.94	789.11	920.94
7.22	594.80	1195.20	198.00	2015.78	783.42	920.94
7.40	594.80	1195.20	198.00	2015.76	783.42	920.94
7.59	594.80	807.90	606.90	2028.56	775.15	920.94
8.15	594.80	1401.80	.00	2028.96	788.07	920.94
8.36	594.80	1401.80	.00	2028.94	788.07	920.94

Date: 3.21 Expt.#: 2.00 Plab: 734.82

time	t1	t2	t3	tp	t5	t6
5.34	24.89	27.36	25.18	25.22	25.95	20.26
5.47	24.89	27.67	25.19	25.23	25.63	20.24
6.18	24.88	28.28	25.19	25.23	25.24	20.24
6.34	24.89	28.59	25.20	25.23	25.12	20.24
6.52	25.03	29.08	25.21	25.24	25.14	20.24
7.08	24.90	29.16	25.21	25.25	25.20	20.24
7.22	24.90	28.73	25.22	25.25	25.34	20.24
7.40	24.90	28.50	25.21	25.25	25.00	20.23
7.59	24.90	28.09	25.21	25.24	25.06	20.22
8.15	24.89	28.80	25.21	25.25	24.88	20.23
8.36	24.90	28.87	25.21	25.24	24.82	20.22

Date: 3.21 Expt.#: 2.00 Plab: 734.82

time	RH	RA	CNC	+/-
5.34	.000	.230	11.00	.00
5.47	.146	.230	11.50	.00
6.18	.286	.226	12.00	.00
6.34	.421	.228	74.00	3.00
6.52	.486	.229	392.00	44.00
7.08	.486	.226	305.00	39.00
7.22	.420	.228	140.00	10.00
7.40	.420	.228	70.00	6.00
7.59	.285	.226	12.00	.00
8.15	.486	.226	80.00	3.00
8.36	.486	.226	77.00	4.00

RA=30%

Date: 3.22 Expt #: 2 Plab: 734.82

time	acid	humid	dry	Pbw,g	Pba,g
6.33	594.80	.00	1401.90	.00	3.00
6.50	594.80	401.60	989.30	.58	3.00
7.20	594.80	1401.80	.00	1.05	3.00
7.30	594.80	1401.80	.00	1.05	3.00
7.46	594.80	1195.20	198.00	.95	3.00
7.58	594.80	1195.20	198.00	.95	3.00
8.17	594.80	1004.20	405.30	.87	3.00
8.30	594.80	1004.20	405.30	.87	3.00
8.47	594.80	807.90	606.90	.78	3.00
9.10	594.80	1195.20	198.00	.95	3.00
9.25	594.80	1401.80	.00	1.05	3.00

time	ther1	ther2	ther3	probe	ther5	ther6
6.33	2.53	2.69	2.24	6.47	2.53	2.42
6.50	2.53	2.67	2.24	6.47	2.49	2.42
7.20	2.52	2.84	2.24	6.47	2.50	2.42
7.30	2.52	2.85	2.24	6.47	2.50	2.42
7.46	2.52	2.83	2.24	6.47	2.51	2.42
7.58	2.52	2.83	2.24	6.47	2.51	2.42
8.17	2.52	2.81	2.24	6.47	2.51	2.42
8.30	2.52	2.80	2.24	6.47	2.49	2.42
8.47	2.52	2.78	2.24	6.47	2.49	2.42
9.10	2.52	2.82	2.24	6.47	2.51	2.42
9.25	2.52	2.83	2.24	6.47	2.50	2.42

Date: 3.22 Expt.#: 2.00 Plab: 734.82

time	acid	humid	dry	total	Pbw	Pba
6.33	594.80	.00	1401.90	1996.70	734.82	889.92
6.50	594.80	401.60	989.30	1997.73	764.81	889.92
7.20	594.80	1401.80	.00	2037.15	789.11	889.92
7.30	594.80	1401.80	.00	2037.13	789.11	889.92
7.46	594.80	1195.20	198.00	2022.81	783.94	889.92
7.58	594.80	1195.20	198.00	2022.81	783.94	889.92
8.17	594.80	1004.20	405.30	2033.73	779.80	889.92
8.30	594.80	1004.20	405.30	2033.73	779.80	889.92
8.47	594.80	807.90	606.90	2033.42	775.15	889.92
9.10	594.80	1195.20	198.00	2022.83	783.94	889.92
9.25	594.80	1401.80	.00	2037.15	789.11	889.92

Date: 3.22 Expt.#: 2.00 Plab: 734.82

time	t1	t2	t3	tp	t5	t6
6.33	24.95	26.97	25.25	25.30	25.28	23.92
6.50	24.94	26.70	25.24	25.28	24.93	23.90
7.20	24.91	28.42	25.22	25.26	24.95	23.86
7.30	24.91	28.49	25.21	25.25	25.01	23.85
7.46	24.90	28.37	25.21	25.25	25.04	23.86
7.58	24.89	28.33	25.20	25.24	25.09	23.86
8.17	24.89	28.12	25.19	25.24	25.07	23.87
8.30	24.89	28.03	25.20	25.24	24.94	23.87
8.47	24.89	27.86	25.19	25.24	24.94	23.87
9.10	24.89	28.20	25.20	25.24	25.11	23.87
9.25	24.88	28.30	25.19	25.24	25.02	23.86

Date: 3.22 Expt.#: 2.00 Plab: 734.82

time	RH	RA	CNC	+/-
6.33	.000	.238	11.00	.00
6.50	.183	.238	11.00	.00
7.20	.606	.233	5500.00	500.00
7.30	.606	.233	5700.00	400.00
7.46	.525	.235	5800.00	700.00
7.58	.525	.235	3660.00	200.00
8.17	.441	.234	278.00	35.00
8.30	.441	.234	170.00	25.00
8.47	.357	.234	14.00	.00
9.10	.525	.235	500.00	30.00
9.25	.607	.233	4250.00	50.00

RA=30%

Date: 4.15 Expt.#: 1.00 Plab: 731.27

time	acid	humid	dry	Pbw,g	Pba,g
11.28	594.80	211.40	1196.70	0.50	4.10
11.49	594.80	1195.20	198.00	0.95	4.10
12.06	594.80	1401.80	0.00	1.03	4.15
12.21	594.80	1195.20	198.00	0.95	4.15
1.23	594.80	1004.20	405.30	0.87	4.15
1.48	594.80	1401.80	0.00	1.03	4.15

Date: 4.15 Expt.#: 1.00 Plab: 731.27

time	ther1	ther2	ther3	probe	ther5	ther6
11.280	2.361	2.507	2.213	6.439	2.492	2.064
11.490	2.358	2.696	2.209	6.436	2.602	2.062
12.060	2.355	2.728	2.207	6.434	2.574	2.062
12.210	2.353	2.683	2.206	6.433	2.540	2.063
1.230	2.347	2.590	2.199	6.426	2.510	2.064
1.480	2.346	2.815	2.198	6.425	2.567	2.064

Date: 4.15 Expt.#: 1.00 Plab: 731.27

time	acid	humid	dry	total	Pbw	Pba
11.28	594.80	211.40	1196.70	2007.99	757.12	943.24
11.49	594.80	1195.20	198.00	2015.87	780.38	943.24
12.06	594.80	1401.80	0.00	2029.11	784.52	945.82
12.21	594.80	1195.20	198.00	2015.89	780.38	945.82
1.23	594.80	1004.20	405.30	2027.88	776.25	945.82
1.48	594.80	1401.80	0.00	2029.16	784.52	945.82

Date: 4.15 Expt.#: 1.00 Plab: 731.27

time	t1	t2	t3	tp	t5	t6
11.280	24.634	25.131	24.926	24.947	24.905	20.249
11.490	24.604	27.002	24.886	24.917	26.014	20.228
12.060	24.574	27.319	24.866	24.897	25.732	20.228
12.210	24.553	26.873	24.855	24.887	25.390	20.238
1.230	24.493	25.952	24.785	24.816	25.087	20.249
1.480	24.482	28.180	24.774	24.806	25.661	20.249

Date: 4.15 Expt.#: 1.00 Plab: 731.27

time	RH	RA	CNC	+/-
11.28	0.078	0.223	0.00	0.00
11.49	0.428	0.222	22.00	0.00
12.06	0.496	0.220	165.00	15.00
12.21	0.429	0.221	10.00	0.00
1.23	0.362	0.220	0.04	0.00
1.48	0.500	0.220	65.00	0.00

RA=50%

Date: 3.22 Expt #: 1 Plab: 734.82

time	acid	humid	dry	Pbw,g	Pba,g
1.43	1011.60	.00	1009.60	.00	5.70
2.04	1011.60	396.10	606.90	.44	5.75
2.24	1011.60	605.70	405.30	.53	5.75
2.35	1011.60	605.70	405.30	.53	5.75
2.52	1011.60	807.90	198.00	.63	5.75
3.05	1011.60	807.90	198.00	.63	5.75
3.20	1011.60	1004.20	.00	.73	5.80
3.32	1011.60	1004.20	.00	.73	5.80
4.11	1011.60	407.90	606.90	.44	5.85
4.13	1011.60	512.30	495.60	.47	5.85
4.48	1011.60	605.70	405.30	.54	5.90
5.07	1011.60	807.90	198.00	.64	5.95
5.15	1011.60	807.90	198.00	.64	5.95
5.38	1011.60	1004.20	.00	.72	6.00
5.48	1011.60	1004.20	.00	.72	6.00
6.04	1011.60	.00	1009.60	.00	6.05

time	ther1	ther2	ther3	probe	ther5	ther6
1.43	2.52	2.69	2.24	6.46	2.54	2.41
2.04	2.52	2.79	2.24	6.47	2.61	2.41
2.24	2.53	2.83	2.24	6.47	2.63	2.41
2.35	2.53	2.83	2.25	6.47	2.64	2.41
2.52	2.52	2.85	2.25	6.48	2.65	2.41
3.05	2.53	2.86	2.25	6.48	2.66	2.42
3.20	2.53	2.93	2.25	6.48	2.61	2.42
3.32	2.53	2.94	2.25	6.48	2.58	2.42
4.11	2.53	2.81	2.25	6.48	2.62	2.42
4.13	2.53	2.81	2.25	6.48	2.55	2.42
4.48	2.53	2.83	2.25	6.48	2.53	2.42
5.07	2.53	2.87	2.25	6.48	2.58	2.42
5.15	2.53	2.89	2.25	6.48	2.59	2.42
5.38	2.53	2.90	2.25	6.48	2.55	2.42
5.48	2.53	2.90	2.25	6.48	2.58	2.42
6.04	2.53	2.78	2.25	6.48	2.55	2.42

Date: 3.22 Expt.#: 1.00 Plab: 734.82

time	acid	humid	dry	total	Pbw	Pba
1.43	1011.60	.00	1009.60	2021.20	734.82	1029.52
2.04	1011.60	396.10	606.90	2026.51	757.57	1032.10
2.24	1011.60	605.70	405.30	2040.73	762.22	1032.10
2.35	1011.60	605.70	405.30	2040.73	762.22	1032.10
2.52	1011.60	807.90	198.00	2041.52	767.39	1032.10
3.05	1011.60	807.90	198.00	2041.54	767.39	1032.10
3.20	1011.60	1004.20	.00	2045.47	772.56	1034.69
3.32	1011.60	1004.20	.00	2045.49	772.56	1034.69
4.11	1011.60	407.90	606.90	2038.73	757.57	1037.27
4.13	1011.60	512.30	495.60	2034.95	759.12	1037.27
4.48	1011.60	605.70	405.30	2040.77	762.74	1039.86
5.07	1011.60	807.90	198.00	2041.57	767.91	1042.44
5.15	1011.60	807.90	198.00	2041.57	767.91	1042.44
5.38	1011.60	1004.20	.00	2045.55	772.05	1045.03
5.48	1011.60	1004.20	.00	2045.53	772.05	1045.03
6.04	1011.60	.00	1009.60	2021.20	734.82	1047.61

Date: 3.22 Expt.#: 1.00 Plab: 734.82

time	t1	t2	t3	t4	t5	t6

1.43	24.86	26.96	25.17	25.19	25.36	23.84
2.04	24.88	27.91	25.20	25.23	26.09	23.81
2.24	24.93	28.31	25.24	25.28	26.26	23.83
2.35	24.97	28.31	25.27	25.31	26.39	23.83
2.52	24.89	28.54	25.29	25.34	26.46	23.84
3.05	25.01	28.60	25.31	25.35	26.58	23.85
3.20	25.01	29.29	25.30	25.34	26.05	23.85
3.32	25.00	29.45	25.29	25.34	25.75	23.86
4.11	25.00	28.13	25.30	25.35	26.20	23.89
4.13	25.00	28.12	25.30	25.35	25.52	23.89
4.48	25.00	28.31	25.28	25.33	25.27	23.88
5.07	24.98	28.72	25.28	25.33	25.80	23.88
5.15	24.99	28.88	25.28	25.33	25.88	23.88
5.38	24.98	29.03	25.27	25.32	25.44	23.88
5.48	24.98	29.02	25.27	25.32	25.83	23.87
6.04	24.98	27.79	25.27	25.32	25.52	23.91

Date: 3.22 Expt.#: 1.00 Plab: 734.82

time	RH	RA	CNC	+/-
1.43	.000	.346	33.00	.00
2.04	.179	.344	43.00	.00
2.24	.270	.341	1700.00	150.00
2.35	.270	.341	1250.00	150.00
2.52	.357	.338	11600.00	200.00
3.05	.357	.341	10700.00	600.00
3.20	.440	.340	104000.00	1000.00
3.32	.440	.340	105000.00	2000.00
4.11	.183	.340	30.00	.00
4.13	.230	.340	47.00	.00
4.48	.270	.339	150.00	10.00
5.07	.358	.337	3200.00	100.00
5.15	.358	.338	3300.00	60.00
5.38	.441	.336	76000.00	500.00
5.48	.441	.336	74800.00	500.00
6.04	.000	.340	27.00	.00

RA=50%

Date: 4.12 Expt.#: 1.00 Plab: 731.77

time	acid	humid	dry	Pbw,g	Pba,g
5.12	1011.60	0.00	1009.60	0.00	5.80
5.20	1011.60	199.10	802.00	0.33	5.80
5.30	1011.60	605.70	405.30	0.51	5.80
5.42	1011.60	605.70	405.30	0.51	5.80
5.55	1011.60	807.90	198.00	0.63	5.80
6.05	1011.60	807.90	198.00	0.63	5.80
6.20	1011.60	1004.20	0.00	0.70	5.80
6.30	1011.60	1004.20	0.00	0.70	5.80
6.43	1011.60	407.90	606.90	0.42	5.80

Date: 4.12 Expt.#: 1.00 Plab: 731.77

time	ther1	ther2	ther3	probe	ther5	ther6
5.120	2.380	2.540	2.231	6.456	2.596	2.079
5.200	2.380	2.591	2.231	6.456	2.602	2.077
5.300	2.381	2.649	2.232	6.458	2.593	2.077
5.420	2.381	2.691	2.233	6.458	2.634	2.076
5.550	2.382	2.691	2.234	6.460	2.614	2.075
6.050	2.383	2.709	2.234	6.460	2.629	2.075
6.200	2.383	2.705	2.234	6.460	2.629	2.074
6.300	2.383	2.702	2.234	6.460	2.566	2.074
6.430	2.383	2.646	2.235	6.460	2.579	2.074

Date: 41288.00 Expt.#: 1.00 Plab: 731.77

time	acid	humid	dry	total	Pbw	Pba
5.12	1011.60	0.00	1009.60	2021.20	731.77	1031.64
5.20	1011.60	199.10	802.00	2017.59	748.84	1031.64
5.30	1011.60	605.70	405.30	2037.29	758.14	1031.64
5.42	1011.60	605.70	405.30	2037.28	758.14	1031.64
5.55	1011.60	807.90	198.00	2036.91	764.35	1031.64
6.05	1011.60	807.90	198.00	2036.91	764.35	1031.64
6.20	1011.60	1004.20	0.00	2039.79	767.96	1031.64
6.30	1011.60	1004.20	0.00	2039.79	767.96	1031.64
6.43	1011.60	407.90	606.90	2036.34	753.49	1031.64

Date: 41288.00 Expt.#: 1.00 Plab: 731.77

time	t1	t2	t3	tp	t5	t6
5.120	24.827	25.457	25.109	25.118	25.953	20.401
5.200	24.827	25.962	25.109	25.118	26.014	20.381
5.300	24.837	26.537	25.119	25.138	25.923	20.381
5.420	24.837	26.952	25.129	25.138	26.335	20.371
5.550	24.847	26.952	25.139	25.159	26.134	20.361
6.050	24.857	27.131	25.139	25.159	26.285	20.361
6.200	24.857	27.091	25.139	25.159	26.285	20.350
6.300	24.857	27.061	25.139	25.159	25.651	20.350
6.430	24.857	26.507	25.149	25.159	25.782	20.350

Date: 41288.00 Expt.#: 1.00 Plab: 731.77

time	RH	RA	CNC	+/-
5.12	0.000	0.345	0.07	0.00
5.20	0.074	0.346	0.01	0.00
5.30	0.220	0.342	2450.00	250.00
5.42	0.220	0.342	1300.00	100.00

5.55	0.291	0.342	13000.00	1500.00
6.05	0.291	0.342	9400.00	1000.00
6.20	0.359	0.342	32300.00	2000.00
6.30	0.359	0.342	26000.00	2000.00
6.43	0.149	0.342	0.06	0.00

RA=60%

Date: 4.15 Expt.#: 2.00 Plab: 731.27

time	acid	humid	dry	Pbw,g	Pba,g
10.00	1198.40	807.90	0.00	0.56	7.20
10.15	1198.40	807.90	0.00	0.56	7.20
10.31	1198.40	507.60	303.90	0.42	7.25
10.45	1198.40	605.70	198.00	0.46	7.30

Date: 4.15 Expt.#: 2.00 Plab: 731.27

time	ther1	ther2	ther3	probe	ther5	ther6
10.000	2.374	2.612	2.224	6.449	2.553	2.060
10.150	2.369	2.634	2.219	6.445	2.541	2.060
10.310	2.365	2.638	2.216	6.442	2.584	2.061
10.450	2.362	2.643	2.213	6.440	2.597	2.061

Date: 4.15 Expt.#: 2.00 Plab: 731.27

time	acid	humid	dry	total	Pbw	Pba
10.00	1198.40	807.90	0.00	2025.63	760.22	1103.51
10.15	1198.40	807.90	0.00	2025.63	760.22	1103.51
10.31	1198.40	507.60	303.90	2022.17	752.98	1106.10
10.45	1198.40	605.70	198.00	2016.70	755.05	1108.68

Date: 4.15 Expt.#: 2.00 Plab: 731.27

time	t1	t2	t3	t4	t5	t6
10.000	24.766	26.170	25.038	25.048	25.521	20.208
10.150	24.715	26.388	24.987	25.007	25.400	20.208
10.310	24.675	26.428	24.957	24.977	25.833	20.218
10.450	24.645	26.477	24.926	24.957	25.963	20.218

Date: 4.15 Expt.#: 2.00 Plab: 731.27

time	RH	RA	CNC	+/-
10.00	0.293	0.381	9200.00	500.00
10.15	0.294	0.381	6500.00	600.00
10.31	0.187	0.380	25.00	0.00
10.45	0.223	0.380	135.00	25.00

RA=60%

Date: 4.14 Expt.#: 1.00 Plab: 731.77

time	acid	humid	dry	Pbw,g	Pba,g
11.20	1198.40	211.40	607.30	0.27	6.95
11.35	1198.40	293.70	499.60	0.28	6.95
11.50	1198.40	401.60	391.10	0.35	7.00
12.01	1198.40	401.60	391.10	0.35	7.00
12.15	1198.40	507.60	303.90	0.40	7.00
12.25	1198.40	807.90	0.00	0.56	7.02
2.13	1198.40	807.90	0.00	0.56	7.10
2.32	1198.40	605.70	198.00	0.46	7.15
2.49	1198.40	507.60	303.90	0.43	7.15
3.10	1198.40	293.70	499.60	0.30	7.15
3.25	1198.40	211.40	607.30	0.27	7.15

Date: 4.14 Expt.#: 1.00 Plab: 731.77

time	ther1	ther2	ther3	probe	ther5	ther6
11.200	2.372	2.289	2.222	6.446	2.497	2.062
11.350	2.367	2.370	2.217	6.440	2.452	2.063
11.500	2.362	2.421	2.212	6.435	2.450	2.061
12.010	2.359	2.446	2.210	6.433	2.463	2.061
12.150	2.355	2.463	2.206	6.429	2.428	2.061
12.250	2.352	2.522	2.203	6.427	2.461	2.060
2.130	2.336	2.489	2.187	6.412	2.416	2.061
2.320	2.336	2.467	2.188	6.413	2.461	2.061
2.490	2.337	2.468	2.188	6.414	2.462	2.062
3.100	2.338	2.444	2.188	6.414	2.464	2.062
3.250	2.338	2.439	2.189	6.415	2.473	2.062

Date: 41488.00 Expt.#: 1.00 Plab: 731.77

time	acid	humid	dry	total	Pbw	Pba
11.20	1198.40	211.40	607.30	2022.26	745.73	1091.09
11.35	1198.40	293.70	499.60	1998.87	746.25	1091.09
11.50	1198.40	401.60	391.10	2000.85	749.87	1093.68
12.01	1198.40	401.60	391.10	2000.85	749.87	1093.68
12.15	1198.40	507.60	303.90	2022.18	752.45	1093.68
12.25	1198.40	807.90	0.00	2025.61	760.73	1094.71
2.13	1198.40	807.90	0.00	2025.63	760.73	1098.85
2.32	1198.40	605.70	198.00	2016.69	755.56	1101.43
2.49	1198.40	507.60	303.90	2022.16	754.01	1101.43
3.10	1198.40	293.70	499.60	1998.86	747.28	1101.43
3.25	1198.40	211.40	607.30	2022.26	745.73	1101.43

Date: 41488.00 Expt.#: 1.00 Plab: 731.77

time	t1	t2	t3	t4	t5	t6
11.200	24.746	22.972	25.017	25.018	24.956	20.228
11.350	24.695	23.774	24.967	24.957	24.502	20.238
11.500	24.645	24.279	24.916	24.907	24.481	20.218
12.010	24.614	24.527	24.896	24.887	24.613	20.218
12.150	24.574	24.695	24.855	24.846	24.259	20.218
12.250	24.543	25.279	24.825	24.826	24.592	20.208
2.130	24.381	24.952	24.683	24.675	24.138	20.218
2.320	24.381	24.735	24.673	24.685	24.592	20.218
2.490	24.391	24.744	24.673	24.695	24.603	20.228
3.100	24.401	24.507	24.673	24.695	24.623	20.228

3.250 24.401 24.457 24.683 24.705 24.714 20.228

Date: 41488.00 Expt.#: 1.00 Plab: 731.77

time	RH	RA	CNC	+/-
11.20	0.079	0.387	0.01	0.00
11.35	0.111	0.392	46.00	0.00
11.50	0.151	0.391	666.00	25.00
12.01	0.151	0.390	130.00	10.00
12.15	0.189	0.386	1600.00	100.00
12.25	0.297	0.385	41500.00	2500.00
2.13	0.300	0.383	9500.00	150.00
2.32	0.227	0.383	190.00	20.00
2.49	0.190	0.382	7.50	0.00
3.10	0.112	0.387	0.01	0.00
3.25	0.080	0.382	0.01	0.00

RA=60%

Date: 4.06 Expt.#: 1.00 Plab: 732.28

time	acid	humid	dry	Pbw,g	Pba,g
1.46	1198.40	401.60	391.10	0.37	6.60
1.59	1198.40	293.70	499.60	0.34	6.60
2.13	1198.40	211.40	607.30	0.28	6.60
2.44	1198.40	0.00	799.20	0.00	6.60
2.51	1198.40	0.00	799.20	0.00	6.60
2.56	1198.40	0.00	799.20	0.00	6.60
3.12	1198.40	293.70	499.60	0.34	6.65
3.24	1198.40	293.70	499.60	0.34	6.65
3.36	1198.40	401.60	391.10	0.36	6.65
3.46	1198.40	401.60	391.10	0.36	6.65
3.53	1198.40	211.40	607.30	0.28	6.65
4.11	1198.40	507.60	303.90	0.42	6.65
4.20	1198.40	507.60	303.90	0.42	6.65
4.34	1198.40	807.90	0.00	0.56	6.65
4.51	1198.40	807.90	0.00	0.56	6.65
5.04	1198.40	605.70	198.00	0.47	6.70
5.15	1198.40	605.70	198.00	0.47	6.70
5.25	1198.40	293.70	499.60	0.32	6.70

Date: 4.06 Expt.#: 1.00 Plab: 732.28

time	ther1	ther2	ther3	probe	ther5	ther6
1.460	2.351	2.856	2.204	6.430	2.638	2.073
1.590	2.353	2.855	2.205	6.432	2.666	2.074
2.130	2.354	2.854	2.208	6.435	2.667	2.075
2.440	2.357	2.844	2.211	6.439	2.690	2.077
2.510	2.358	2.842	2.212	6.440	2.701	2.078
2.560	2.359	2.844	2.212	6.441	2.702	2.078
3.120	2.360	2.863	2.214	6.442	2.703	2.076
3.240	2.361	2.872	2.214	6.443	2.704	2.076
3.360	2.362	2.893	2.215	6.443	2.701	2.077
3.460	2.362	2.903	2.215	6.444	2.702	2.076
3.530	2.363	2.899	2.216	6.445	2.715	2.077
4.110	2.364	2.925	2.216	6.445	2.715	2.076
4.200	2.364	2.937	2.217	6.446	2.734	2.076
4.340	2.364	2.969	2.217	6.447	2.719	2.076
4.510	2.365	2.976	2.217	6.447	2.697	2.076
5.040	2.365	2.984	2.217	6.447	2.698	2.076
5.150	2.366	2.970	2.218	6.448	2.711	2.076
5.250	2.366	2.943	2.218	6.448	2.695	2.077

Date: 4688.00 Expt.#: 1.00 Plab: 732.28

time	acid	humid	dry	total	Pbw	Pba
1.46	1198.40	401.60	391.10	2000.90	751.41	1073.51
1.59	1198.40	293.70	499.60	1998.89	749.86	1073.51
2.13	1198.40	211.40	607.30	2022.30	746.76	1073.51
2.44	1198.40	0.00	799.20	1997.60	732.28	1073.51
2.51	1198.40	0.00	799.20	1997.60	732.28	1073.51
2.56	1198.40	0.00	799.20	1997.60	732.28	1073.51
3.12	1198.40	293.70	499.60	1998.90	749.86	1076.09
3.24	1198.40	293.70	499.60	1998.90	749.86	1076.09
3.36	1198.40	401.60	391.10	2000.94	750.89	1076.09
3.46	1198.40	401.60	391.10	2000.93	750.89	1076.09
3.53	1198.40	211.40	607.30	2022.31	746.76	1076.09
4.11	1198.40	507.60	303.90	2022.27	754.00	1076.09
4.20	1198.40	507.60	303.90	2022.27	754.00	1076.09

4.34	1198.40	807.90	0.00	2025.80	761.23	1076.09
4.51	1198.40	807.90	0.00	2025.80	761.23	1076.09
5.04	1198.40	605.70	198.00	2016.81	756.58	1078.68
5.15	1198.40	605.70	198.00	2016.81	756.58	1078.68
5.25	1198.40	293.70	499.60	1998.91	748.83	1078.68

Date: 4688.00 Expt.#: 1.00 Plab: 732.28

time	t1	t2	t3	t4	t5	t6
1.460	24.533	28.586	24.835	24.856	26.375	20.340
1.590	24.553	28.576	24.845	24.877	26.656	20.350
2.130	24.564	28.566	24.876	24.907	26.666	20.361
2.440	24.594	28.467	24.906	24.947	26.896	20.381
2.510	24.604	28.447	24.916	24.957	27.006	20.391
2.560	24.614	28.467	24.916	24.967	27.016	20.391
3.120	24.624	28.655	24.936	24.977	27.026	20.371
3.240	24.634	28.745	24.936	24.987	27.036	20.371
3.360	24.645	28.952	24.947	24.987	27.006	20.381
3.460	24.645	29.051	24.947	24.997	27.016	20.371
3.530	24.655	29.012	24.957	25.007	27.146	20.381
4.110	24.665	29.269	24.957	25.007	27.146	20.371
4.200	24.665	29.388	24.967	25.018	27.335	20.371
4.340	24.665	29.705	24.967	25.028	27.186	20.371
4.510	24.675	29.774	24.967	25.028	26.966	20.371
5.040	24.675	29.853	24.967	25.028	26.976	20.371
5.150	24.685	29.715	24.977	25.038	27.106	20.371
5.250	24.685	29.447	24.977	25.038	26.946	20.381

Date: 4688.00 Expt.#: 1.00 Plab: 732.28

time	RH	RA	CNC	+/-
1.46	0.152	0.396	8700.00	1300.00
1.59	0.112	0.396	51.00	4.00
2.13	0.080	0.391	0.04	0.00
2.44	0.000	0.395	1.31	0.00
2.51	0.000	0.395	0.37	0.00
2.56	0.000	0.395	0.10	0.00
3.12	0.111	0.394	18.00	0.00
3.24	0.111	0.394	12.00	0.00
3.36	0.152	0.394	1800.00	150.00
3.46	0.151	0.394	1240.00	70.00
3.53	0.079	0.390	0.02	0.00
4.11	0.189	0.390	4300.00	400.00
4.20	0.188	0.390	2900.00	300.00
4.34	0.296	0.389	40000.00	2000.00
4.51	0.296	0.389	34000.00	3000.00
5.04	0.224	0.390	6000.00	300.00
5.15	0.224	0.390	4250.00	450.00
5.25	0.111	0.393	0.03	0.00

RH=15%

Date: 3.19 Expt #: 1 Plab: 736.35

time	acid	humid	dry	Pbw,g	Pba,g
6.25	.00	303.30	1698.00	.00	.00
6.45	502.80	303.30	1206.30	.56	2.20
7.00	1198.40	303.30	495.60	.30	5.50
7.12	1497.30	303.30	198.00	.23	6.60
7.25	1708.30	303.30	.00	.20	7.30
7.40	1708.30	303.30	.00	.20	7.60
8.55	1708.30	303.00	.00	.20	7.60

time	ther1	ther2	ther3	probe	ther5	ther6
6.25	2.49	2.78	2.20	6.43	2.64	2.07
6.45	2.48	2.83	2.20	6.43	2.77	2.06
7.00	2.49	2.85	2.21	6.43	2.89	2.06
7.12	2.49	2.85	2.21	6.43	2.87	2.06
7.25	2.49	2.82	2.21	6.43	2.85	2.06
7.40	2.48	2.78	2.20	6.43	2.76	2.06
8.55	2.49	2.81	2.21	6.43	2.86	2.06

Date: 3.19 Expt.#: 1.00 Plab: 736.35

time	acid	humid	dry	total	Pbw	Pba
6.25	.00	303.30	1698.00	2008.84	736.35	736.35
6.45	502.80	303.30	1206.30	2019.61	765.30	850.09
7.00	1198.40	303.30	495.60	2004.64	751.86	1020.70
7.12	1497.30	303.30	198.00	2005.97	748.24	1077.57
7.25	1708.30	303.30	.00	2018.99	746.69	1113.76
7.40	1708.30	303.30	.00	2018.98	746.69	1129.27
8.55	1708.30	303.00	.00	2018.67	746.69	1129.27

Date: 3.19 Expt.#: 1.00 Plab: 736.35

time	t1	t2	t3	tp	t5	t6
6.25	24.62	27.81	24.83	24.86	26.44	20.29
6.45	24.49	28.33	24.80	24.84	27.66	20.22
7.00	24.53	28.53	24.86	24.89	28.87	20.21
7.12	24.55	28.48	24.87	24.90	28.72	20.20
7.25	24.54	28.19	24.87	24.91	28.44	20.19
7.40	24.52	27.83	24.85	24.89	27.57	20.19
8.55	24.55	28.17	24.87	24.91	28.60	20.19

Date: 3.19 Expt.#: 1.00 Plab: 736.35

time	RH	RA	CNC	+/-
6.25	.117	.000	.00	.00
6.45	.112	.208	7.55	.00
7.00	.114	.416	53.00	.00
7.12	.115	.493	93.00	.00
7.25	.114	.532	294.00	.00
7.40	.114	.532	1081.00	.00
8.55	.114	.533	1400.00	.00

RH=15%

Date: 3.08 Expt #: 1 Plab:736.09

time	acid	humid	dry	Pbw,g	Pba,g
6.22	.00	303.30	1698.00	.83	.00
6.30	.00	303.30	1698.00	.83	.00
6.43	202.00	303.30	1494.30	.70	1.02
6.52	202.00	303.30	1494.30	.70	1.02
7.03	302.80	303.30	1390.40	.66	1.42
7.09	302.80	303.30	1390.40	.66	1.42
7.20	502.80	303.30	1206.30	.57	2.20
7.23	502.80	303.30	1206.30	.57	2.20
7.32	707.60	303.30	1009.60	.48	2.80
7.40	796.20	303.30	907.10	.46	3.40
7.52	1011.60	303.30	694.50	.37	4.40
8.00	1198.40	303.30	495.60	.30	4.95
8.05	1198.40	303.30	495.60	.30	4.95
8.16	1011.60	303.30	694.00	.36	4.50
8.25	1095.40	303.30	606.90	.33	4.75
8.33	1198.40	303.30	495.60	.30	5.00
8.41	1497.30	303.30	198.00	.23	6.10
8.47	1497.30	303.30	198.00	.23	6.10
8.58	1689.10	303.30	.00	.18	6.90
9.05	1689.10	303.30	.00	.18	6.90
9.17	1497.30	303.30	198.00	.23	6.30
9.22	1497.30	303.30	198.00	.23	6.30
9.31	1689.10	303.30	.00	.18	6.95
9.46	1198.40	303.30	495.60	.30	5.30
9.55	502.80	303.30	1206.30	.55	2.40
10.00	.00	303.30	1698.00	.83	.00

time	ther1	ther2	ther3	probe	ther5	ther6
6.22	2.55	2.53	2.24	6.46	2.41	2.06
6.30	2.55	2.53	2.24	6.46	2.46	2.06
6.43	2.54	2.53	2.24	6.46	2.46	2.06
6.52	2.54	2.51	2.23	6.46	2.44	2.06
7.03	2.54	2.52	2.23	6.45	2.43	2.06
7.09	2.54	2.53	2.23	6.45	2.43	2.06
7.20	2.54	2.53	2.23	6.45	2.44	2.06
7.23	2.54	2.54	2.23	6.45	2.45	2.06
7.32	2.54	2.54	2.23	6.45	2.46	2.06
7.40	2.54	2.53	2.23	6.45	2.46	2.06
7.52	2.53	2.53	2.23	6.45	2.45	2.06
8.00	2.54	2.52	2.23	6.45	2.43	2.06
8.05	2.53	2.53	2.23	6.45	2.46	2.06
8.16	2.53	2.53	2.23	6.45	2.45	2.06
8.25	2.53	2.53	2.23	6.45	2.45	2.06
8.33	2.53	2.54	2.23	6.45	2.45	2.06
8.41	2.53	2.52	2.23	6.45	2.45	2.07
8.47	2.53	2.52	2.23	6.45	2.45	2.07
8.58	2.53	2.49	2.23	6.45	2.46	2.07
9.05	2.53	2.49	2.23	6.45	2.46	2.07
9.17	2.53	2.49	2.23	6.45	2.44	2.07
9.22	2.53	2.51	2.23	6.45	2.45	2.07
9.31	2.53	2.49	2.23	6.45	2.46	2.07
9.46	2.53	2.50	2.23	6.45	2.44	2.07
9.55	2.53	2.52	2.23	6.45	2.44	2.07
10.00	2.53	2.53	2.23	6.45	2.45	2.71
10.00	2.53	2.53	2.23	6.45	2.45	2.07

Date: 3.08 Expt.#: 1.00 Plab: 736.09

time	acid	humid	dry	total	Pbw	Pba

6.22	.00	303.30	1698.00	2008.38	779.00	736.09
6.30	.00	303.30	1698.00	2008.39	779.00	736.09
6.43	202.00	303.30	1494.30	2006.75	772.28	788.83
6.52	202.00	303.30	1494.30	2006.76	772.28	788.83
7.03	302.80	303.30	1390.40	2003.68	770.21	809.51
7.09	302.80	303.30	1390.40	2003.67	770.21	809.51
7.20	502.80	303.30	1206.30	2019.62	765.56	849.83
7.23	502.80	303.30	1206.30	2019.62	765.56	849.83
7.32	707.60	303.30	1009.60	2027.76	760.91	880.85
7.40	796.20	303.30	907.10	2013.87	759.87	911.87
7.52	1011.60	303.30	694.50	2016.71	755.22	963.57
8.00	1198.40	303.30	495.60	2004.65	751.60	992.01
8.05	1198.40	303.30	495.60	2004.66	751.60	992.01
8.16	1011.60	303.30	694.00	2016.22	754.70	968.75
8.25	1095.40	303.30	606.90	2012.94	753.15	981.67
8.33	1198.40	303.30	495.60	2004.66	751.60	994.60
8.41	1497.30	303.30	198.00	2006.00	747.98	1051.47
8.47	1497.30	303.30	198.00	2006.00	747.98	1051.47
8.58	1689.10	303.30	.00	1999.84	745.40	1092.83
9.05	1689.10	303.30	.00	1999.84	745.40	1092.83
9.17	1497.30	303.30	198.00	2006.02	747.98	1061.81
9.22	1497.30	303.30	198.00	2006.02	747.98	1061.81
9.31	1689.10	303.30	.00	1999.85	745.40	1095.41
9.46	1198.40	303.30	495.60	2004.69	751.60	1010.11
9.55	502.80	303.30	1206.30	2019.66	764.53	860.17
10.00	.00	303.30	1698.00	2008.42	779.00	736.09

Date: 3.08 Expt.#: 1.00 Plab: 736.09

time	t1	t2	t3	tp	t5	t6
6.22	25.22	25.40	25.20	25.20	24.10	20.21
6.30	25.20	25.39	25.19	25.17	24.56	20.23
6.43	25.10	25.33	25.16	25.14	24.61	20.24
6.52	25.07	25.11	25.15	25.12	24.39	20.25
7.03	25.05	25.23	25.13	25.10	24.29	20.25
7.09	25.04	25.31	25.12	25.09	24.32	20.24
7.20	25.04	25.37	25.12	25.08	24.42	20.24
7.23	25.03	25.41	25.11	25.08	24.45	20.24
7.32	25.04	25.42	25.11	25.08	24.56	20.23
7.40	25.03	25.40	25.11	25.08	24.56	20.23
7.52	25.02	25.34	25.11	25.08	24.49	20.23
8.00	25.03	25.28	25.11	25.08	24.33	20.23
8.05	25.02	25.32	25.11	25.08	24.58	20.24
8.16	25.01	25.35	25.10	25.07	24.45	20.24
8.25	25.02	25.37	25.11	25.08	24.53	20.25
8.33	25.00	25.43	25.10	25.07	24.52	20.25
8.41	25.00	25.21	25.10	25.07	24.52	20.26
8.47	25.01	25.23	25.10	25.07	24.52	20.26
8.58	25.01	24.99	25.10	25.07	24.61	20.28
9.05	25.00	24.96	25.10	25.07	24.60	20.28
9.17	25.00	24.99	25.10	25.06	24.39	20.30
9.22	25.00	25.12	25.09	25.07	24.52	20.30
9.31	25.01	24.92	25.10	25.06	24.61	20.30
9.46	25.01	25.05	25.09	25.06	24.40	20.31
9.55	25.00	25.24	25.08	25.06	24.43	20.31
10.00	25.01	25.37	25.08	25.06	24.44	20.31

Date: 3.08 Expt.#: 1.00 Plab: 736.09

time	RH	RA	CNC	+/-
6.22	.108	.000	.01	.00
6.30	.108	.000	.01	.00

6.43	.110	.094	5.15	.00
6.52	.110	.093	5.20	.00
7.03	.110	.137	11.30	.00
7.09	.110	.137	11.80	.00
7.20	.110	.215	30.70	.00
7.23	.110	.215	31.00	.00
7.32	.110	.290	49.40	.00
7.40	.111	.318	59.30	.00
7.52	.112	.381	80.60	.00
8.00	.113	.441	618.00	35.00
8.05	.113	.441	575.00	35.00
8.16	.112	.379	74.40	.00
8.25	.113	.406	85.90	.00
8.33	.113	.439	300.00	25.00
8.41	.114	.519	555.00	32.00
8.47	.114	.519	666.00	50.00
8.58	.115	.565	20900.00	2300.00
9.05	.115	.565	17700.00	1900.00
9.17	.114	.514	18000.00	3000.00
9.22	.114	.514	12100.00	1000.00
9.31	.115	.565	5270.00	670.00
9.46	.114	.433	310.00	.00
9.55	.111	.212	25.00	.00
10.00	.110	.000	.00	.00
10.00	.110	.000	.28	.00

RH=40%

Date: 3.09 Expt #: 1 Plab: 736.09

time	acid	humid	dry	Pbw,g	Pba,g
12.24	.00	807.90	1206.30	1.06	.00
12.30	.00	807.90	1206.30	1.06	.00
12.39	202.00	807.90	1009.60	.95	1.02
12.47	202.00	807.90	1009.60	.95	1.02
1.00	409.10	807.90	802.00	.85	1.83
1.14	502.80	807.90	694.50	.79	2.25
1.25	594.80	807.90	606.90	.76	2.50
1.36	796.20	807.90	405.30	.67	3.90
1.44	796.20	807.90	405.30	.67	3.90
2.13	1011.60	807.90	198.00	.60	4.50
2.23	1198.40	807.90	.00	.55	5.15
2.30	1198.40	807.90	.00	.55	5.15
2.45	1011.60	807.90	198.00	.59	4.65
2.58	905.00	807.90	290.70	.64	4.30
3.12	1198.40	807.90	.00	.56	5.25
3.22	1198.40	807.90	.00	.56	5.25
3.43	796.20	807.90	405.30	.67	3.90
3.46	796.20	807.90	405.30	.67	3.90
3.56	905.00	807.90	290.70	.65	4.20
4.00	905.00	807.90	290.70	.65	4.20
4.12	594.80	807.90	606.90	.76	2.80
4.16	594.80	807.90	606.90	.76	2.80
4.29	202.00	807.90	1009.60	.94	1.02
4.40	.00	807.90	1206.30	1.05	.00

time	ther1	ther2	ther3	probe	ther5	ther6
12.24	2.54	2.52	2.23	6.45	2.58	2.07
12.30	2.54	2.62	2.23	6.45	2.61	2.07
12.39	2.53	2.59	2.23	6.45	2.49	2.07
12.47	2.53	2.58	2.23	6.45	2.71	2.07
1.00	2.53	2.58	2.23	6.45	2.47	2.07
1.14	2.53	2.59	2.23	6.45	2.47	2.07
1.25	2.53	2.59	2.23	6.45	2.47	2.07
1.36	2.53	2.59	2.23	6.45	2.46	2.07
1.44	2.53	2.59	2.23	6.45	2.46	2.07
2.13	2.53	2.53	2.22	6.44	2.43	2.07
2.23	2.52	2.53	2.22	6.44	2.44	2.07
2.30	2.53	2.54	2.22	6.44	2.46	2.07
2.45	2.53	2.65	2.22	6.44	2.45	2.07
2.58	2.52	2.65	2.22	6.44	2.43	2.07
3.12	2.52	2.62	2.22	6.44	2.43	2.07
3.22	2.52	2.61	2.22	6.44	2.44	2.07
3.43	2.52	2.55	2.21	6.44	2.44	2.07
3.46	2.52	2.54	2.21	6.44	2.45	2.07
3.56	2.52	2.56	2.21	6.44	2.47	2.07
4.00	2.52	2.57	2.21	6.43	2.48	2.07
4.12	2.52	2.66	2.21	6.44	2.53	2.07
4.16	2.52	2.68	2.21	6.44	2.56	2.07
4.29	2.52	2.70	2.22	6.44	2.58	2.07
4.40	2.52	2.72	2.22	6.44	2.62	2.07

Date: 3.09 Expt.#: 1.00 Plab: 736.09

time	acid	humid	dry	total	Pbw	Pba
12.24	.00	807.90	1206.30	2032.88	790.89	736.09
12.30	.00	807.90	1206.30	2032.88	790.89	736.09
12.39	202.00	807.90	1009.60	2038.33	785.21	788.83

12.47	202.00	807.90	1009.60	2038.33	785.21	788.83
1.00	409.10	807.90	802.00	2037.97	780.04	830.70
1.14	502.80	807.90	694.50	2024.25	776.94	852.42
1.25	594.80	807.90	606.90	2028.69	775.38	865.34
1.36	796.20	807.90	405.30	2028.61	770.73	937.72
1.44	796.20	807.90	405.30	2028.62	770.73	937.72
2.13	1011.60	807.90	198.00	2036.81	767.11	968.75
2.23	1198.40	807.90	.00	2025.68	764.53	1002.35
2.30	1198.40	807.90	.00	2025.67	764.53	1002.35
2.45	1011.60	807.90	198.00	2036.82	766.60	976.50
2.58	905.00	807.90	290.70	2022.86	769.18	958.40
3.12	1198.40	807.90	.00	2025.65	765.04	1007.52
3.22	1198.40	807.90	.00	2025.64	765.04	1007.52
3.43	796.20	807.90	405.30	2028.57	770.73	937.72
3.46	796.20	807.90	405.30	2028.58	770.73	937.72
3.56	905.00	807.90	290.70	2022.78	769.70	953.23
4.00	905.00	807.90	290.70	2022.78	769.70	953.23
4.12	594.80	807.90	606.90	2028.64	775.38	880.85
4.16	594.80	807.90	606.90	2028.64	775.38	880.85
4.29	202.00	807.90	1009.60	2038.31	784.69	788.83
4.40	.00	807.90	1206.30	2032.89	790.38	736.09

Date: 3.09 Expt.#: 1.00 Plab: 736.09

time	t1	t2	t3	tp	t5	t6
12.24	25.07	25.23	25.08	25.05	25.80	20.31
12.30	25.06	26.21	25.09	25.06	26.08	20.31
12.39	25.01	25.97	25.09	25.06	24.94	20.32
12.47	25.00	25.84	25.08	25.05	27.10	20.32
1.00	24.99	25.89	25.08	25.05	24.68	20.33
1.14	24.99	25.91	25.07	25.04	24.72	20.33
1.25	24.98	25.95	25.07	25.04	24.69	20.33
1.36	24.95	25.91	25.07	25.04	24.62	20.33
1.44	24.95	25.92	25.06	25.03	24.56	20.34
2.13	24.93	25.35	25.03	25.00	24.26	20.34
2.23	24.91	25.36	25.02	25.00	24.39	20.34
2.30	24.92	25.44	25.02	25.00	24.55	20.33
2.45	24.92	26.51	25.01	24.99	24.53	20.34
2.58	24.90	26.51	25.00	24.98	24.33	20.34
3.12	24.88	26.25	24.98	24.96	24.30	20.33
3.22	24.86	26.18	24.97	24.94	24.34	20.32
3.43	24.83	25.55	24.95	24.93	24.42	20.30
3.46	24.83	25.50	24.95	24.92	24.48	20.31
3.56	24.83	25.62	24.93	24.92	24.68	20.29
4.00	24.83	25.71	24.94	24.91	24.77	20.29
4.12	24.83	26.61	24.94	24.93	25.33	20.29
4.16	24.83	26.83	24.95	24.94	25.54	20.29
4.29	24.85	27.02	24.97	24.97	25.77	20.29
4.40	24.90	27.20	24.99	24.99	26.19	20.31

Date: 3.09 Expt.#: 1.00 Plab: 736.09

time	RH	RA	CNC	+/-
12.24	.284	.000	.01	.00
12.30	.284	.000	.01	.00
12.39	.285	.092	2.58	.00
12.47	.285	.092	4.35	.00
1.00	.288	.177	12.68	.67
1.14	.291	.213	26.50	1.00
1.25	.291	.248	49.80	1.20
1.36	.293	.306	190.00	10.00
1.44	.293	.306	197.00	19.00

2.13	.294	.375	3700.00	.14
2.23	.296	.431	25000.00	1400.00
2.30	.296	.431	28500.00	3700.00
2.45	.294	.372	4360.00	120.00
2.58	.295	.341	717.00	75.00
3.12	.297	.429	18400.00	2500.00
3.22	.297	.429	18600.00	2300.00
3.43	.294	.305	80.00	.00
3.46	.294	.306	70.00	.00
3.56	.295	.343	165.00	5.00
4.00	.295	.343	168.00	10.00
4.12	.292	.243	31.00	.00
4.16	.292	.243	31.00	.00
4.29	.286	.091	4.57	.00
4.40	.285	.000	.01	.00

RH=40%

Date: 3.20 Expt #: 1 Plab: 734.82

time	acid	humid	dry	Pbw,g	Pba,g
4.58	.00	807.90	1206.30	1.07	.00
5.08	409.10	807.90	802.00	.87	1.83
5.20	409.10	807.90	802.00	.87	1.83
5.31	594.80	807.90	606.90	.78	3.00
5.39	594.80	807.90	606.90	.78	3.00
5.53	796.20	807.90	405.30	.70	4.00
6.07	796.20	807.90	405.30	.70	4.00
6.22	1011.60	807.90	198.00	.63	4.90
6.33	1011.60	807.90	198.00	.63	4.90
6.44	1198.40	807.90	.00	.56	5.65
6.57	1198.40	807.90	.00	.56	5.65
7.15	594.80	807.90	606.90	.78	3.30
7.33	905.00	807.90	290.70	.66	4.40
7.48	1011.60	807.90	198.00	.63	4.90
8.05	1011.60	807.90	198.00	.63	4.90
8.38	1198.40	807.90	.00	.56	5.90
8.47	1198.40	807.90	.00	.56	5.90
8.55	796.20	807.90	405.30	.70	4.40
9.08	409.10	807.90	802.00	.87	2.25
9.15	1198.40	807.90	.00	.56	5.90
9.26	1198.40	807.90	.00	.56	5.90
9.33	1198.40	807.90	.00	.56	5.90

time	ther1	ther2	ther3	probe	ther5	ther6
4.58	2.51	2.50	2.22	6.44	2.61	2.04
5.08	2.51	2.58	2.22	6.45	2.58	2.04
5.20	2.51	2.73	2.22	6.45	2.65	2.04
5.31	2.51	2.71	2.22	6.45	2.67	2.04
5.39	2.51	2.71	2.22	6.45	2.66	2.04
5.53	2.51	2.70	2.23	6.45	2.53	2.04
6.07	2.51	2.68	2.23	6.45	2.46	2.04
6.22	2.51	2.69	2.22	6.45	2.46	2.04
6.33	2.51	2.69	2.22	6.45	2.46	2.04
6.44	2.51	2.69	2.23	6.45	2.46	2.04
6.57	2.51	2.68	2.22	6.45	2.46	2.04
7.15	2.51	2.70	2.22	6.45	2.48	2.04
7.33	2.51	2.69	2.22	6.45	2.46	2.04
7.48	2.51	2.72	2.23	6.45	2.48	2.04
8.05	2.51	2.74	2.22	6.45	2.52	2.04
8.38	2.51	2.71	2.23	6.45	2.50	2.04
8.47	2.51	2.73	2.23	6.45	2.53	2.04
8.55	2.51	2.73	2.23	6.45	2.53	2.05
9.08	2.51	2.73	2.23	6.45	2.52	2.04
9.15	2.51	2.85	2.23	6.45	2.57	2.04
9.26	2.51	2.89	2.23	6.46	2.59	2.04
9.33	2.51	2.89	2.23	6.46	2.46	2.04

Date: 3.20 Expt.#: 1.00 Plab: 734.82

time	acid	humid	dry	total	Pbw	Pba
4.58	.00	807.90	1206.30	2032.51	790.14	734.82
5.08	409.10	807.90	802.00	2037.57	779.80	829.43
5.20	409.10	807.90	802.00	2037.57	779.80	829.43
5.31	594.80	807.90	606.90	2028.29	775.15	889.92
5.39	594.80	807.90	606.90	2028.28	775.15	889.92
5.53	796.20	807.90	405.30	2028.19	771.01	941.62
6.07	796.20	807.90	405.30	2028.21	771.01	941.62
6.22	1011.60	807.90	198.00	2036.41	767.39	988.16

6.33	1011.60	807.90	198.00	2036.41	767.39	988.16
6.44	1198.40	807.90	.00	2025.31	763.77	1026.93
6.57	1198.40	807.90	.00	2025.30	763.77	1026.93
7.15	594.80	807.90	606.90	2028.32	775.15	905.43
7.33	905.00	807.90	290.70	2022.47	768.94	962.30
7.48	1011.60	807.90	198.00	2036.42	767.39	988.16
8.05	1011.60	807.90	198.00	2036.42	767.39	988.16
8.38	1198.40	807.90	.00	2025.34	763.77	1039.86
8.47	1198.40	807.90	.00	2025.34	763.77	1039.86
8.55	796.20	807.90	405.30	2028.27	771.01	962.30
9.08	409.10	807.90	802.00	2037.64	779.80	851.15
9.15	1198.40	807.90	.00	2025.34	763.77	1039.86
9.26	1198.40	807.90	.00	2025.34	763.77	1039.86
9.33	1198.40	807.90	.00	2025.34	763.77	1039.86

Date: 3.20 Expt.#: 1.00 Plab: 734.82

time	t1	t2	t3	tp	t5	t6
4.58	24.75	25.06	25.01	25.00	26.10	19.97
5.08	24.73	25.82	25.04	25.04	25.83	19.98
5.20	24.73	27.32	25.02	25.02	26.55	19.98
5.31	24.72	27.15	25.02	25.02	26.68	19.99
5.39	24.73	27.13	25.03	25.03	26.56	19.98
5.53	24.75	27.09	25.06	25.05	25.26	19.99
6.07	24.75	26.80	25.06	25.04	24.62	20.00
6.22	24.75	26.92	25.05	25.04	24.54	20.01
6.33	24.74	26.93	25.05	25.04	24.60	20.01
6.44	24.75	26.90	25.06	25.04	24.63	20.02
6.57	24.75	26.85	25.05	25.04	24.54	20.01
7.15	24.75	27.00	25.05	25.05	24.81	20.01
7.33	24.74	26.92	25.05	25.05	24.55	20.01
7.48	24.74	27.23	25.06	25.05	24.80	20.02
8.05	24.75	27.47	25.05	25.06	25.19	20.02
8.38	24.75	27.16	25.06	25.07	25.02	20.05
8.47	24.76	27.30	25.07	25.08	25.33	20.05
8.55	24.77	27.32	25.07	25.09	25.28	20.06
9.08	24.76	27.31	25.08	25.10	25.22	20.05
9.15	24.79	28.54	25.09	25.10	25.68	20.05
9.26	24.80	28.91	25.10	25.12	25.88	20.05
9.33	24.79	28.91	25.11	25.12	24.58	20.05

Date: 3.20 Expt.#: 1.00 Plab: 734.82

time	RH	RA	CNC	+/-
4.58	.279	.000	.00	.00
5.08	.281	.173	4.55	.00
5.20	.282	.173	5.99	.00
5.31	.285	.235	100.00	.00
5.39	.284	.235	78.00	3.00
5.53	.286	.298	270.00	20.00
6.07	.286	.298	153.00	12.00
6.22	.287	.359	970.00	72.00
6.33	.287	.359	812.00	36.00
6.44	.290	.412	9500.00	600.00
6.57	.290	.412	9900.00	1000.00
7.15	.285	.231	16.00	.00
7.33	.288	.332	60.00	.00
7.48	.287	.359	360.00	30.00
8.05	.286	.359	330.00	30.00
8.38	.290	.405	4800.00	500.00
8.47	.289	.405	5000.00	300.00
8.55	.286	.291	60.00	.00

9.08	.281	.168	4.99	.00
9.15	.289	.406	2500.00	200.00
9.26	.289	.405	2750.00	250.00
9.33	.289	.405	2900.00	100.00

RH=50%

Date: 4.13 Expt.#: 1.00 Plab: 731.77

time	acid	humid	dry	Pbw,g	Pba,g
1.21	0.00	1004.20	1009.60	1.19	0.00
1.40	409.10	1004.20	606.90	0.95	2.75
1.50	594.80	1004.20	405.30	0.87	3.80
2.22	796.20	1004.20	198.00	0.77	4.85
2.38	1011.60	1004.20	0.00	0.72	5.90
2.50	1011.60	1004.20	0.00	0.72	5.90
3.07	796.20	1004.20	198.00	0.77	4.93
3.23	594.80	1004.20	405.30	0.86	3.95
3.36	409.10	1004.20	606.90	0.95	2.90
3.45	0.00	1004.20	1009.60	1.18	0.00

Date: 4.13 Expt.#: 1.00 Plab: 731.77

time	ther1	ther2	ther3	probe	ther5	ther6
1.210	2.357	2.639	2.200	6.426	2.474	2.067
1.400	2.349	2.655	2.201	6.427	2.574	2.066
1.500	2.349	2.708	2.202	6.427	2.574	2.066
2.220	2.352	2.746	2.204	6.431	2.541	2.066
2.380	2.354	2.706	2.206	6.432	2.590	2.067
2.500	2.355	2.696	2.207	6.433	2.605	2.068
3.070	2.356	2.704	2.208	6.434	2.581	2.069
3.230	2.356	2.754	2.209	6.435	2.590	2.069
3.360	2.357	2.714	2.209	6.435	2.589	2.069
3.450	2.359	2.732	2.209	6.436	2.553	2.070

Date: 41388.00 Expt.#: 1.00 Plab: 731.77

time	acid	humid	dry	total	Pbw	Pba
1.21	0.00	1004.20	1009.60	2036.90	793.30	731.77
1.40	409.10	1004.20	606.90	2043.66	780.89	873.95
1.50	594.80	1004.20	405.30	2027.89	776.75	928.24
2.22	796.20	1004.20	198.00	2022.15	771.58	982.52
2.38	1011.60	1004.20	0.00	2039.65	769.00	1036.81
2.50	1011.60	1004.20	0.00	2039.67	769.00	1036.81
3.07	796.20	1004.20	198.00	2022.20	771.58	986.66
3.23	594.80	1004.20	405.30	2027.95	776.24	935.99
3.36	409.10	1004.20	606.90	2043.71	780.89	881.71
3.45	0.00	1004.20	1009.60	2036.96	792.78	731.77

Date: 41388.00 Expt.#: 1.00 Plab: 731.77

time	t1	t2	t3	tp	t5	t6
1.210	24.594	26.438	24.795	24.816	24.724	20.279
1.400	24.513	26.596	24.805	24.826	25.732	20.269
1.500	24.513	27.121	24.815	24.826	25.732	20.269
2.220	24.543	27.497	24.835	24.866	25.400	20.269
2.380	24.564	27.101	24.855	24.877	25.893	20.279
2.500	24.574	27.002	24.866	24.887	26.044	20.289
3.070	24.584	27.081	24.876	24.897	25.802	20.299
3.230	24.584	27.576	24.886	24.907	25.893	20.299
3.360	24.594	27.180	24.886	24.907	25.883	20.299
3.450	24.614	27.358	24.886	24.917	25.521	20.310

Date: 41388.00 Expt.#: 1.00 Plab: 731.77

time	RH	RA	CNC	+/-
1.21	0.353	0.000	0.00	0.00
1.40	0.357	0.163	0.61	0.00
1.50	0.362	0.224	260.00	40.00
2.22	0.365	0.284	365.00	65.00
2.38	0.363	0.340	4800.00	300.00
2.50	0.363	0.340	4700.00	200.00
3.07	0.365	0.283	530.00	30.00
3.23	0.361	0.222	62.00	3.00
3.36	0.356	0.161	0.11	0.00
3.45	0.352	0.000	0.00	0.00

RH=50%

Date: 4.14 Expt.#: 2.00 Plab: 731.01

time	acid	humid	dry	Pbw,g	Pba,g
3.53	796.20	1004.20	198.00	0.77	5.20
4.46	1011.60	1004.20	0.00	0.73	6.23
5.07	796.20	1004.20	198.00	0.78	5.25
5.25	594.80	1004.20	405.30	0.87	4.15
5.49	409.10	1004.20	606.90	0.97	3.02
6.19	796.20	1004.20	198.00	0.78	5.10
6.34	1011.60	1004.20	0.00	0.73	6.23
7.00	0.00	1004.20	1009.60	1.23	0.00

Date: 4.14 Expt.#: 2.00 Plab: 731.01

time	ther1	ther2	ther3	probe	ther5	ther6
3.530	2.337	2.491	2.188	6.414	2.418	2.061
4.460	2.335	2.559	2.187	6.414	2.470	2.060
5.070	2.336	2.560	2.188	6.414	2.428	2.061
5.250	2.336	2.582	2.188	6.414	2.433	2.061
5.490	2.337	2.603	2.189	6.416	2.512	2.061
6.190	2.339	2.645	2.192	6.419	2.546	2.062
6.340	2.340	2.623	2.192	6.419	2.483	2.061
7.000	2.347	2.572	2.193	6.419	2.456	2.062

Date: 4.14 Expt.#: 2.00 Plab: 731.01

time	acid	humid	dry	total	Pbw	Pba
3.53	796.20	1004.20	198.00	2022.10	770.82	999.86
4.46	1011.60	1004.20	0.00	2039.55	768.75	1053.11
5.07	796.20	1004.20	198.00	2022.08	771.34	1002.44
5.25	594.80	1004.20	405.30	2027.84	775.99	945.57
5.49	409.10	1004.20	606.90	2043.58	781.16	887.15
6.19	796.20	1004.20	198.00	2022.10	771.34	994.69
6.34	1011.60	1004.20	0.00	2039.57	768.75	1053.11
7.00	0.00	1004.20	1009.60	2036.79	794.60	731.01

Date: 4.14 Expt.#: 2.00 Plab: 731.01

time	t1	t2	t3	tp	t5	t6
3.530	24.391	24.972	24.673	24.695	24.158	20.218
4.460	24.371	25.645	24.663	24.695	24.683	20.208
5.070	24.381	25.655	24.673	24.695	24.259	20.218
5.250	24.381	25.873	24.673	24.695	24.310	20.218
5.490	24.391	26.081	24.683	24.715	25.107	20.218
6.190	24.412	26.497	24.714	24.745	25.450	20.228
6.340	24.422	26.279	24.714	24.745	24.815	20.218
7.000	24.493	25.774	24.724	24.745	24.542	20.228

Date: 4.14 Expt.#: 2.00 Plab: 731.01

time	RH	RA	CNC	+/-
3.53	0.367	0.279	140.00	10.00
4.46	0.365	0.334	1930.00	30.00
5.07	0.367	0.278	160.00	15.00
5.25	0.364	0.220	0.60	0.00
5.49	0.358	0.160	0.01	0.00
6.19	0.366	0.280	56.00	0.00
6.34	0.364	0.334	1450.00	50.00
7.00	0.353	0.000	0.01	0.00